

Electronic Thesis and Dissertation Repository

12-2-2021 2:30 PM

In Situ Study of Geological Fluid Inclusions Using ^{23}Na Nuclear Magnetic Resonance Spectroscopy

Stephen Pilar, *The University of Western Ontario*

Supervisor: Flemming, Roberta L., *The University of Western Ontario*

Co-Supervisor: Blamey, Nigel J.F., *The University of Western Ontario*

A thesis submitted in partial fulfillment of the requirements for the Master of Science degree in Geology

© Stephen Pilar 2021

Follow this and additional works at: <https://ir.lib.uwo.ca/etd>

 Part of the [Environmental Chemistry Commons](#), [Geochemistry Commons](#), and the [Geology Commons](#)

Recommended Citation

Pilar, Stephen, "In Situ Study of Geological Fluid Inclusions Using ^{23}Na Nuclear Magnetic Resonance Spectroscopy" (2021). *Electronic Thesis and Dissertation Repository*. 8353.
<https://ir.lib.uwo.ca/etd/8353>

This Dissertation/Thesis is brought to you for free and open access by Scholarship@Western. It has been accepted for inclusion in Electronic Thesis and Dissertation Repository by an authorized administrator of Scholarship@Western. For more information, please contact wlsadmin@uwo.ca.

Abstract

²³Na Magic Angle Spinning Solid State Nuclear Magnetic Resonance (MAS SS NMR) spectroscopy has been used to study natural geological samples of halite, fluorite, and quartz to evaluate the efficacy of NMR spectroscopy for in situ fluid inclusion analysis. NaCl calibration standards yielded a strong linear correlation ($R^2=0.9919$) for salinity, albeit only over a ~1 ppm breadth of chemical shift. Fluid inclusions were successfully identified in all three types of minerals studied using MAS NMR. Chemical analysis with Inductively Coupled Plasma -- Mass Spectrometry (ICP-MS) was employed to quantify elemental contaminants in halite samples. Powder X-Ray Diffraction (pXRD) analysis was used to verify the mineral identity of the samples and identify any contaminant mineral phases. This research was successful in producing reasonable estimates for fluid salinity within halite samples. Quartz and fluorite samples showed evidence of further influence beyond salinity affecting the chemical shift of fluid peaks. This research was successful as a proof of concept for NMR analysis of fluid inclusions, however, further study is needed to understand the effects of pressure and fluid composition on fluid inclusion behaviour in order for NMR to be a useful technique to identify formation conditions of geological samples.

Keywords

Magic Angle Spinning Solid State Nuclear Magnetic Resonance (MAS SS NMR), sodium-23, Halite, Hansonburg Fluorite, Gonzales Fluorite, Snowbird Quartz, Fluid Inclusions, Salinity, Powder X-Ray Diffraction

Summary for Lay Audience

This research seeks to lay the foundation for using sodium-23 Nuclear Magnetic Resonance (^{23}Na NMR) spectroscopy to study microscopic capsules of fluids that have been trapped inside naturally occurring rocks and minerals. These naturally preserved fluids can hold important information about the formation of the mineral, such as the temperature and pressure of formation and the types of fluids involved in its mineralization. Hydrothermal alteration can also be recorded, so changes over time could be monitored to better understand the geological history of the area. These are important to understand when trying to model the processes that contributed to a geological system, and these can be very useful when identifying areas that have a high potential for hosting minerals of economic interest. Current techniques that are used to study fluid inclusions are very time-consuming and labour-intensive, leading to expensive analyses that sometimes require a month or more to complete. By understanding the capabilities of NMR spectroscopy for studying geological samples and their fluid inclusions, there exists the potential to greatly reduce the time needed for sample characterization. Preparation of samples for NMR analysis is fast and efficient, as is the analysis itself; NMR spectroscopy can be completed within hours with the appropriate understanding and resources, instead of weeks or more with standard fluid inclusion analysis. This research investigates the potential for studying fluid inclusions in situ and non-destructively using ^{23}Na NMR spectroscopy within natural samples of halite, fluorite, and quartz.

Co-Authorship Statement

This thesis was compiled under the guidance and mentorship of Dr. Roberta Flemming and Dr. Nigel Blamey. Their feedback and suggestions were instrumental in the completion of this research.

Nuclear Magnetic Resonance data was collected by Dr. Mat Willans at the J.B. Stothers NMR facility at the University of Western Ontario. Due to Covid restrictions, training for use of the spectrometer was not possible, however, all of the data were processed and interpreted by the author (Stephen Pilar).

Acknowledgments

I would like to thank both of my co-supervisors Dr. Roberta Flemming and Dr. Nigel Blamey for their steadfast support and enthusiasm for my thesis and helping me pull everything together on time. The past two years have been unprecedented in countless ways and while things were far from ordinary, you both always kept a positive outlook and made the best out of everything. Thank you for giving me the opportunity to further pursue my education and welcoming me into the geology department at Western, it's a wonderful community to be a part of.

Thank you to Mat Willans for his expertise and guidance with NMR spectroscopy; this project was far from routine, and it would not have been possible without your invaluable wealth of knowledge and willingness to try something a little bit off-beat.

To my gaggle of fellow graduate students: you were the heart of my Masters experience. Nikol, your support has been unmatched and your encouragement throughout the entirety of my university career has brought me farther than I ever imagined I would go; thank you for believing in me, even when I failed to. James, Nico, Steph, Russel, Ian, Dave, Lindsay, Chris, Matt, Mere, and Jason, I hate to see everyone go separate ways, but I wish you all the best wherever life takes you. If knowing me has been even a fraction as enriching as it has been getting to know all of you, I consider that an achievement; you are all incredible people and I love you all dearly.

To my family: we have already moved separate ways, but we will never let distance keep us apart. Mom, Dad, Alex, and Martin, thank you all for supporting me, not just through the past 2 years of my life, but the past 25 of them. You are all a part of who I am, and I couldn't be prouder of that fact; my success is just as much yours as it is my own. I know there is nothing we wouldn't do for each other, and if the need ever arises you can count on me to be there for each of you in kind. I love you all more than anything and I always will.

My sincerest thanks to all of you. Cheers.

Stephen

Table of Contents

Abstract.....	ii
Summary for Lay Audience.....	iii
Co-Authorship Statement.....	iv
Acknowledgments.....	v
Table of Contents.....	vi
List of Tables.....	x
List of Abbreviations and Symbols.....	x
List of Figures.....	xii
List of Appendices.....	xvii
Chapter 1.....	1
1 Introduction and Literature Review.....	1
1.1 Background.....	1
1.2 Literature Review.....	3
1.2.1 Fluid Inclusions and Microthermometry.....	3
1.2.2 Nuclear Magnetic Resonance Spectroscopy.....	6
1.2.3 Atomic Scale Nuclear Magnetic Resonance Theory.....	6
1.2.4 Chemical Shielding and Chemical Shift.....	9
1.2.5 Magnetic Dipole and Coupling Effects.....	11
1.2.6 Quadrupolar Nuclei and Associated Effects.....	12
1.2.7 Standard NMR Analysis.....	14
1.3 Powder X-Ray Diffraction.....	17
1.4 Inductively Coupled Plasma - Mass Spectroscopy.....	23
1.5 References.....	24

Chapter 2.....	26
2 Methods and Sample Selection	26
2.1 Calibration Curve Dilution Scheme.....	26
2.2 Inductively Coupled Plasma - Mass Spectroscopy.....	27
2.3 Nuclear Magnetic Resonance Spectroscopy.....	29
2.3.1 Calibration Curve Standard Acquisition.....	30
2.3.2 Solid State NMR Acquisition	30
2.3.3 Variable Temperature NMR Acquisition.....	30
2.3.4 Raw NMR Data Processing	31
2.4 Powder X-Ray Diffraction.....	31
2.4.1 pXRD Data Acquisition.....	31
2.4.2 pXRD Data Processing	32
2.5 Sample Selection and Geological Background.....	32
2.5.1 Dana 711 Halite	33
2.5.2 Dana 730 Halite	33
2.5.3 Dana 1922 Halite	34
2.5.4 Dana 3137 Halite	34
2.5.5 Dana 5477 Halite	34
2.5.6 Dana 5490 Halite	35
2.5.7 South African Halite	35
2.5.8 Salton Sea Halite.....	35
2.5.9 TronaCA Halite.....	36
2.5.10 DeLaval Blue Halite	37
2.5.11 Bonaire Halite	37
2.5.12 Snowbird Quartz	38

2.5.13 Hansonburg Fluorite	39
2.5.14 Gonzales Fluorite	40
2.6 Preparation of Hygroscopic Standards.....	40
2.7 References.....	41
Chapter 3.....	43
3 Analysis of Halite.....	43
3.1 Introduction.....	43
3.2 Geological Deposition of Halite	43
3.2.1 Halite Formation	44
3.3 Methods.....	47
3.4 Results.....	49
3.4.1 ²³ Na NMR Results for Halite	49
3.4.2 pXRD Results for Halite.....	53
3.4.3 ICP-MS Results for Halite	55
3.5 Discussion of Halite Results	55
3.5.1 ²³ Na NMR Discussion.....	56
3.5.2 ICP-MS Discussion.....	61
3.5.3 pXRD Discussion.....	63
3.6 Conclusion	67
3.7 References.....	68
Chapter 4.....	70
4 Analysis of Fluorite.....	70
4.1 Introduction.....	70
4.2 Geological Deposition of Fluorite	70
4.3 Methods.....	72

4.4 Results.....	73
4.4.1 pXRD Results for Fluorite.....	73
4.4.2 ²³ Na NMR Results for Fluorite.....	75
4.5 Discussion.....	80
4.5.1 ²³ Na NMR Discussion.....	80
4.5.2 pXRD Discussion.....	84
4.6 Conclusions.....	85
4.7 References.....	86
Chapter 5.....	89
5 Analysis of Quartz.....	89
5.1 Introduction to the Study of Snowbird Quartz.....	89
5.2 Geological Context for the Snowbird Region.....	89
5.3 Methods.....	90
5.3.1 pXRD Methods.....	90
5.3.2 ²³ Na NMR Methods.....	91
5.4 Results.....	92
5.4.1 ²³ Na NMR Results for Quartz.....	92
5.4.2 pXRD Results.....	93
5.5 Discussion.....	94
5.6 Conclusion.....	100
5.7 References.....	100
Chapter 6.....	102
6 Overview of Research and Suggested Future Work.....	102
6.1 Studying Fluid Inclusions with NMR Spectroscopy.....	102
6.2 Potential Future Work.....	103

6.3 Unexplained Results	106
6.3.1 X-ray Burn on Powder X-ray Diffraction Samples	106
6.3.2 Complex NMR Peaks in Snowbird Quartz.....	106
6.4 References.....	108
Appendices.....	109
Curriculum Vitae	170

List of Tables

Table 3-1: Summary of data collected for 12 Halite samples.....	50
Table 4-1: ^{23}Na NMR Parameters for acquisition of Hansonburg and Gonzales Fluorite.	73
Table 5-1: Acquisition parameters for Variable Temperature ^{23}Na MAS NMR spectroscopy of the Snowbird Quartz sample.....	91

List of Abbreviations and Symbols

ASR: Alkali-Silica Reaction

CSA: Chemical Shift Anisotropy

EFG: Electric Field Gradient

FID: Free Induction Decay

FT: Fourier Transform

FWHM: Full-Width Half-Maximum

ICDD: International Centre for Diffraction Data

ICP-MS: Inductively Coupled Mass Spectrometry

IR: Infrared Radiation

MAS: Magic Angle Spinning

MRI: Magnetic Resonance Imaging

MVT: Mississippi Valley Type

NMR: Nuclear Magnetic Resonance

PPB/PPM: Parts Per Billion/Parts Per Million

pXRD: Powder X-ray Diffraction

RF: Radio Frequency

RGR: Rio Grande Rift

S/N: Signal to Noise Ratio

VT: Variable Temperature

B_0 : Static external magnetic field vector

B_1 : Applied radiofrequency

C_Q : Quadrupolar coupling constant

γ : Gyromagnetic ratio

η : Assymetry of electric field gradient

\hbar : Reduced Planck Constant ($6.626 \times 10^{-34} \text{ J}\cdot\text{s}/2\pi$)

I : Nuclear spin quantum number

k : Boltzmann Constant ($1.380 \times 10^{-23} \text{ m}^2\cdot\text{Kg}/\text{s}^2\cdot\text{K}$)

μ : Nuclear Magnetic Moment

m: Nuclear magnetic quantum number

r: Internuclear radius

List of Figures

Fig. 1-1: Examples of Primary (P), Secondary (S), and Pseudo-Secondary (PS) fluid inclusion patterns that can be found.....	3
Fig. 1-2: (Top) phase change of vapour and liquid phases upon heating to T_h , and (bottom), melting of a frozen fluid inclusion to determine T_m	5
Fig. 1-3: Net angular momentum of a rotating nucleus.....	7
Fig. 1-4: Energy diagram of the Zeeman splitting interaction when a spin-1/2 nucleus is placed within an external magnetic field (B_0).....	8
Fig. 1-5: Typical NMR spectrum with three samples plotted.....	10
Fig. 1-6: Schematic of an MAS probe oriented at 54.7° with respect to B_0	11
Fig. 1-7: The symmetrical charge distribution of a spin-1/2 nucleus (left) compared to the asymmetrical charge distributions that can be found in quadrupolar nuclei (right).	13
Fig. 1-8: Energy diagram for a spin-3/2 nucleus under the influence of B_0 , with additional energy changes from an EFG.....	13
Fig. 1-9: Lineshapes that are produced by quadrupolar nuclei based on their asymmetry (η_Q) values from 0 to 1.	14
Fig. 1-10: A typical 90° pulse sequence.....	15
Fig. 1-11: Production of an X-ray in a cobalt atom via ejection of a core electron (left) and subsequent transition of a valence electron, releasing energy in the form of X-radiation (right).	19

Fig. 1-12: Monochromatic X-rays diffracting at a Bragg's angle upon leaving the lattice in phase with each other and constructively interfering.	20
Fig. 1-13: Schematic of a typical θ - 2θ powder X-ray diffractometer.....	21
Fig. 1-14: Powder X-Ray diffraction pattern of laboratory reagent-grade halite with intensity plotted over the range of 2θ	22
Fig. 1-15: A depiction of an extremely simplified ICP-MS instrument with a quadrupolar filter.....	24
Fig. 2-1: Illustrated dilution scheme used for NaCl calibration curve standards.....	27
Fig. 2-2: Halite samples prepared for ICP-MS and pXRD analysis. Vial samples were retained for pXRD, bagged samples were delivered to ACTLabs.....	28
Fig. 2-3: Coarsely ground halite samples prepared for NMR analysis.....	29
Fig. 2-4: Hand sample of the Dana 711 halite	33
Fig. 2-5: Hand sample of the Dana 730 orange halite.	33
Fig. 2-6: Drill core sample of the Dana 1922 red halite sample.	34
Fig. 2-7: Sample of the Dana 3137 Pugwash halite sample	34
Fig. 2-8: Sub sample of the Dana 5477 pink hopper halite.	34
Fig. 2-9: Sub sample of the Dana 5490 white hopper halite sample.	35
Fig. 2-10: Coarsely ground sample of the South African halite. No sample image was collected prior to processing.	35
Fig. 2-11: Parent and sub samples of the Salton Sea brown halite sample.....	35
Fig. 2-12: Photo of the TronaCA pink hopper halite sample.....	36
Fig. 2-13: Photo of the blue halite sample from New Mexico, U.S.A.....	37

Fig. 2-14: Two mineral samples from the Bonaire halite	37
Fig. 2-15: Bulk sample and sub-samples of quartz from the Snowbird region in New Mexico, U.S.A.....	38
Fig. 2-16: Two of the largest and cleanest subsamples taken from the Hansonburg fluorite sample collection.	39
Fig. 2-17: Hand sample of the Gonzales fluorite sample from New Mexico, U.S.A.	40
Fig. 2-18: Rehydration of Na_2SO_4 to $\text{Na}_2\text{SO}_4 \cdot 0.445 \text{H}_2\text{O}$ via ambient atmospheric absorption.	41
Fig. 3-1: Evaporite sequence and composition for a standard isolated basin of seawater	44
Fig. 3-2: Formation of crystalline halite in a saturated brine at the liquid/air boundary	45
Fig. 3-3: Cornet-style (left) and Chevron-style (right) mineralization that is common for subaqueous halite deposition.	46
Fig. 3-4: Coarsely ground halite samples for NMR analysis.....	47
Fig. 3-5: Static ^{23}Na NMR spectrum of DC-5477 halite showing the characteristic peak shape and distribution seen in static (top) and MAS (bottom) halite analysis.....	49
Fig. 3-6: ^{23}Na MAS NMR spectrum of South African (left) and Dana 5477 (right) halite samples.....	51
Fig. 3-7: ^{23}Na MAS NMR of TronaCA (left) and Dana 5490 (right) halite samples	52
Fig. 3-8: Powder X-ray Diffraction patterns for Dana 711 (left) and Dana 730 (right) halite samples, exhibiting trace amounts of giniite/anhydrite and anhydrate, respectively.	54
Fig. 3-9: Calibration curve of the NaCl fluid standards from 0.25 M to 6.16 M with halite samples plotted with their estimated salinity.....	57

Fig. 3-10: Exaggerated ^{23}Na MAS NMR stack plot of the Dana 5477 halite sample (bottom) versus the thenardite and hydrated thenardite spectra (middle and top, respectively).	58
Fig. 3-11: pXRD pattern for TronaCA with partial matches for quartz, trona and natron. The latter two sodium carbonates could contribute to the NMR spectrum.....	60
Fig. 3-12: ^{23}Na MAS NMR spectra for the ASR gel sample suite analyzed by Tambelli et al., (2006) (left) in comparison to the signal observed in the TronaCA sample in this research (right).	61
Fig. 3-13: Powder X-ray Diffraction pattern for Dana-3137 halite	65
Fig. 3-14: Powder X-ray Diffraction pattern for Dana 5477 halite, with a strong peak match for traces of thenardite (Na_2SO_4).	66
Fig. 4-1: Powder X-ray Diffraction pattern of the Gonzales fluorite sample with matching ICDD mineral cards for fluorite and gypsum applied (left) and a powder X-ray Diffraction pattern for the Hansonburg fluorite sample exhibiting excellent ICDD card matches for fluorite and quartz mineralization (right).....	74
Fig. 4-2: ^{23}Na MAS NMR spectrum for the Gonzales fluorite sample.	75
Fig. 4-3: Static ^{23}Na NMR spectra of Hansonburg fluorite. Initial spectrum collected in a borosilicate rotor without MAS compared to a similar static acquisition in a ZrO_2 rotor.....	76
Fig. 4-4: Static ^{23}Na NMR of the Hansonburg fluorite in a ZrO_2 rotor with a relatively narrow peak atop a very broad peak near -2 ppm, 24000 scans overnight (left). Zoomed and exaggerated MAS ^{23}Na NMR stack plot of the Hansonburg fluorite sample under various scan parameters (right).....	77
Fig. 4-5: Left, ^{23}Na NMR spectrum of Hansonburg fluorite spinning at 8 kHz.	79
Fig. 4-6: Variable temperature ^{23}Na MAS NMR zoomed stack plot for Hansonburg fluorite.	80

Fig. 4-7: Hansonburg fluorite observed ^{23}Na MAS NMR liquid peak plotted using the solvated NaCl calibration curve to extrapolate molarity	82
Fig. 4-8: Change in Hansonburg fluorite liquid peak chemical shift with increasing temperature, modelled with a quadratic approximation.	83
Fig. 4-9: Hansonburg fluorite plotted on the linear regression to estimate salinity of the fluid signal produced by ^{23}Na MAS NMR	84
Fig. 5-1: ^{23}Na MAS NMR spectrum of the Snowbird quartz sample at ambient temperature in the laboratory	92
Fig. 5-2: Stack plot of the Snowbird Quartz sample acquired using Variable Temperature ^{23}Na MAS NMR.	93
Fig. 5-3: Powder X-ray Diffraction pattern for Snowbird quartz with mineral match for quartz (ICDD Card #01-085-0797).....	94
Fig. 5-4: Zoomed in portion of the Snowbird quartz ^{23}Na MAS NMR spectrum spinning at 11 kHz.....	96
Fig. 5-5: Plot of each peak present in the Snowbird quartz sample and the relative shift with increasing temperature.	97
Fig. 5-6: Stacked plot of the Snowbird quartz VT ^{23}Na MAS NMR spectra highlighting the most intense ‘fluid’ peak used for estimating salinity.	97
Fig. 5-7: Estimated salinity of the Snowbird quartz fluid signal at varying temperatures based on the standard NaCl calibration curve.....	98
Fig. 6-1: Potential factors influencing the ^{23}Na NMR chemical shift of geological fluid inclusions, as well as shift range if known.	105
Fig. 6-2: X-ray burn on a selection of samples after pXRD analysis. From left to right: DC-5477, Salton Sea, DeLaval Blue, 99.9% AnalR, Gonzales Fluorite.....	106

Fig. 6-3: Exaggerated and zoomed Snowbird quartz ^{23}Na NMR spectrum showing the unidentified peak shape between -1 and 3 ppm. 107

List of Appendices

Appendix A: Inductively Coupled Plasma – Mass Spectrometry Data..... 109

Appendix B: ^{23}Na Nuclear Magnetic Resonance Spectroscopy Data 125

Appendix C: Powder X-ray Diffraction Data 154

Chapter 1

1 Introduction and Literature Review

A brief overview of the following chapters will be introduced, as will the background for this research and the objectives that directed it. A literature review will follow, introducing the fundamental theory behind the various techniques employed throughout the following chapters.

1.1 Background

The study of fluid inclusions is an important aspect for understanding the temperature, pressure, and chemical conditions that were responsible for forming mineral assemblages found today in a variety of geological environments. One of the most oft-employed techniques for interpreting fluid inclusions is microthermometry, which can provide a reliable estimate for the internal conditions of inclusions suites when properly analyzed. The full characterization of a sample using microthermometry, however, generally requires weeks of labour-intensive microscope work and can oftentimes yield subjective results which can vary from researcher to researcher.

In order to remove operator bias and produce quantitative results from fluid inclusion research, Nuclear Magnetic Resonance (NMR) spectroscopy was chosen as a potential analytical tool to study fluid inclusions in situ. NMR spectroscopy, although much more complex than microthermometry in terms of instrument operation, shows potential for rapidly performing quantitative measurements in a fraction of the time required for microthermometry work; instead of a timescale of weeks to months for a single sample, NMR can provide results within hours or days and with significantly less sample preparation. Because NMR spectroscopy uses electromagnetic radiation in the radio frequency (RF) spectrum, it allows for whole sample penetrative analysis on samples that are optically opaque or otherwise difficult to interpret petrographically without altering the sample. Perhaps most importantly, NMR spectroscopy is highly selective and the applied RF pulse will only interact with one type of nucleus at a time, such as ^1H or ^{13}C , while essentially ignoring any other nuclei that may be present. This would result in a ^1H

NMR spectrum only providing information about the nuclear environment surrounding the hydrogen within the sample, while other nuclei such as carbon or sodium could only influence the spectrum indirectly through their effects on the hydrogen atom. Depending on the local chemical environment immediately surrounding the selected nucleus, different frequencies are observed on the NMR spectrum and these can be used to elucidate chemical structure and differentiate between unique bonding sites and local electronic environments. Understanding the potential benefits and limitations of NMR spectroscopy for fluid inclusion research is an important step in developing this new methodology. The goal of this research is to lay a foundation for the use of ^{23}Na NMR spectroscopy as a viable method for routine analysis of fluid inclusions in geological samples.

The objectives for reaching this goal were as follows:

1. Determine if ^{23}Na NMR spectroscopy is capable of detecting saline fluid inclusions in a variety of geological samples.
2. Determine the effect of salinity on the chemical shift of solvated NaCl using ^{23}Na NMR Spectroscopy of calibrated solutions.
3. Experimentally estimate the salinity of naturally occurring fluids within geological samples using ^{23}Na NMR.
4. Evaluate the effect of contaminants on the viability of ^{23}Na MAS NMR spectroscopy for geological samples.
5. Attempt to observe phase changes and changes in internal pressure in fluid inclusions using Variable Temperature ^{23}Na MAS NMR.
6. Integrate the effects of concentration, pressure/temperature, and composition on ^{23}Na NMR spectroscopy to evaluate the analytical value of NMR for fluid inclusion study.

1.2 Literature Review

1.2.1 Fluid Inclusions and Microthermometry

Fluid inclusions are small volumes of liquid or gas that are trapped within a mineral crystal upon formation or following alteration by hydrothermal processes and metamorphic recrystallization. Fluid inclusions can range in size from millimetres in diameter, which can be visible to the naked eye, down to micrometres, requiring high-powered microscopes to observe them (Roedder, 1972). The content of these inclusions reflects key conditions that were present when the formation or alteration took place and can be considered as a subsample of the fluids that were present and responsible for the crystallization of the mineral in which they are encapsulated.

To differentiate between fluids trapped during initial crystallization from those produced via recrystallization, fluid inclusions are subdivided into three separate categories: primary inclusions, secondary inclusions, and pseudo-secondary inclusions (Fig. 1-1) (Roedder, 1972).

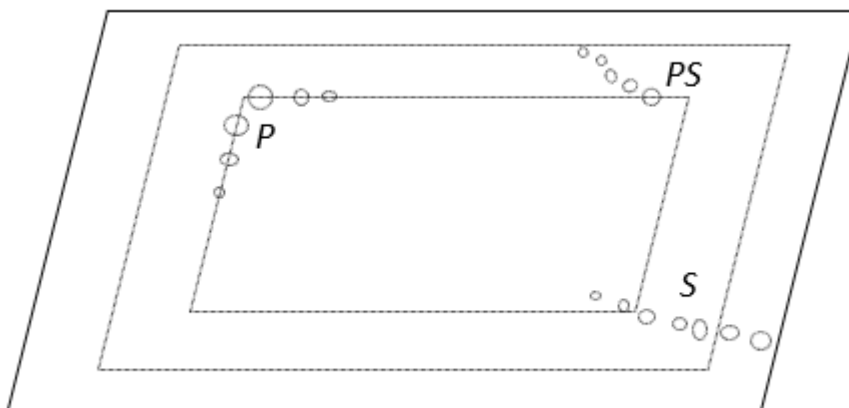


Fig. 1-1: Examples of Primary (P), Secondary (S), and Pseudo-Secondary (PS) fluid inclusion patterns that can be found.

Primary fluid inclusions are created during the initial formation of a mineral and remain unaltered by subsequent hydrothermal or metamorphic events. These form as a result of imperfections in the crystal lattice as the mineral forms, usually in environments with a

fluid that is highly saturated. Under such conditions, rapid deposition is common, causing uneven crystal growth. Fluid inclusions are also commonly formed at nucleation points where lattice development is interrupted, eventually trapping the surrounding fluids (Crawford & Hollister, 1986).

Secondary fluid inclusions are formed as a result of fractures or voids in a mineral becoming infilled with fluids which then recrystallize and close the fracture to form pockets of fluid that are not directly associated with the conditions present when the mineral first formed. These can often be identified by trails of fluid inclusions that formed along an open fracture that has been recrystallized closed. Because fracturing and recrystallization can happen many times over the course of a mineral's geological lifespan, many generations of fluid inclusions with different fluids compositions and internal pressures are possible within the same host mineral and each represent a discrete geological event that has influenced the development of the assemblage (Goldstein et al., 2003).

The final type of fluid inclusions are called pseudo-secondary; these are formed from fractures being filled and recrystallized in the same manner as secondary fluid inclusions, but at the same time that the initial mineral was forming. Although these inclusions may closely resemble secondary type inclusions based on their physical appearance and distribution in the mineral, they share the same composition as primary fluid inclusions elsewhere in the sample and also behave similarly upon microthermometric analysis.

Microthermometry is the practice of preparing a small wafer of sample and varying the temperature on a thermally controlled microscope stage to monitor phase changes within the inclusions. Samples are cut and polished to approximately 100-300 microns thick, although thickness depends heavily on the size and distribution of the inclusions being studied and must be done carefully to avoid damaging the fluid inclusions (Goldstein et al., 2003). A high-powered microscope is often required to see fluid inclusions and resolve the internal solid, liquid, and vapor phases. By varying the temperature of the sample, the equilibrium between the phases found inside of the fluid inclusions can be manipulated to estimate the relative salinity, the potential formation temperatures, and the

pressure experienced when the fluid inclusion was formed. As noted previously, there may be many generations of fluid inclusions produced over the geologic history of a sample with each suite of fluid inclusions preserving information on the conditions present during their respective formation events.

Modern microthermometry stages use liquid nitrogen pumps and thermocouples to precisely control the temperature of the sample stage. A temperature range of -196°C to 600°C can be achieved with a high degree of accuracy by varying the flow of liquid nitrogen and adjusting the voltage delivered to the thermocouple (Hurai et al., 2015). Phase changes can be studied as the fluids inside the inclusions freeze and homogenize when cooled and heated, respectively.

The homogenization temperature of a fluid inclusion is indicative of the minimum temperature of deposition, as it is the lowest temperature at which the fluid was homogenous and could flow freely in order to be incorporated in the inclusion. At increased temperatures, gaseous phases will begin to shrink as pressure increases and the gas is forced to dissolve into the incompressible liquid phase, known as a gas to liquid ($G \rightarrow L$) phase transition (Hurai et al., 2015). Upon further heating, the solubility of the fluid increases allowing for the dissolution of any solid phases present in the inclusion, this is known as a solid to liquid ($S \rightarrow L$) phase transition or the point of homogenization when associated with a multi-phase system (Fig. 1-2). This is the temperature at which the triple point of the solution is reached and there is only one discernable phases within the inclusion, generally denoted as the T_h (Hurai et al., 2015).

Freezing analysis is most useful for estimating the salinity of the fluid inclusions and it is generally examined by fully freezing the sample and slowly raising the temperature until the last ice phase is completely melted. Since this temperature is denoted by the temperature when the last frozen phase melts, it is known as the melting temperature,

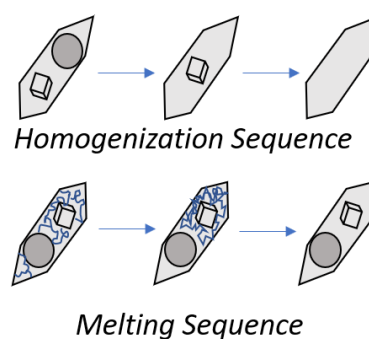


Fig. 1-2: (Top) phase change of vapour and liquid phases upon heating to T_h , and (bottom), melting of a frozen fluid inclusion to determine T_m

T_m . With this technique, salt content is assumed to be pure NaCl and the depression of the freezing temperature is used as an indicator for NaCl content in the fluid. If melting temperatures fall beyond the typical ranges for an H₂O-NaCl system, other phase diagrams that incorporate additional salts such as KCl and CaCl₂, or common gas phases such as CO₂ can be used to better characterize the sample (Hurai et al., 2015).

1.2.2 Nuclear Magnetic Resonance Spectroscopy

NMR spectroscopy is a powerful analytical technique that has been widely utilized across many different disciplines since the first successful experiments were carried out in the 1940s. After the first successful acquisition of NMR signals in pioneering studies at Harvard and Stanford, formal investigation and understanding of NMR-active nuclei began to develop in the mid-1950s as the effect of molecular motion and relaxation times became better understood within solids, liquids, and gases (Andrew & Szczesniak, 1995). In the following decades, NMR research progressed quickly as commercial spectrometers became available and continued to improve with the advent of more powerful magnets and improved computing technology. This has allowed for the development of faster spectral processing, new acquisition techniques, higher spectral resolution, and multi-dimensional spectroscopy which has expanded the utility of the technique to a broad range of disciplines. Nuclear magnetic resonance techniques are used for a variety of modern applications such as medical research in the form of Magnetic Resonance Imaging (MRI) instruments and even mobile instruments for in-situ borehole analysis of hydrocarbon deposits in oil and gas exploration (Liao et al., 2021).

The following passages are attributed to information retrieved from “NMR and Chemistry: An Introduction to Modern NMR Spectroscopy, 4th Edition” by Akitt and Mann (Akitt & Mann, 2000) unless otherwise stated.

1.2.3 Atomic Scale Nuclear Magnetic Resonance Theory

Fundamentally, NMR spectroscopy relies on the natural intrinsic magnetic properties of an atomic nuclei, its corresponding susceptibility to interactions with external magnetic fields, and the electromagnetic perturbation it experiences. Where most fields of chemistry focus on the activity and interaction of electrons for explaining and predicting

chemical behaviour, the function of electrons in NMR spectroscopy are predominantly considered in terms of their effect on the local magnetic field they produce with respect to the nucleus in question. This is to say electrons play a secondary role to the activity of the nucleus itself, as the nucleus predominantly dictates the conditions that must be met to properly probe the desired nuclei.

The magnetic susceptibility of a nucleus, or whether a nucleus is NMR active or not, depends on the net polarization of the constituents of an atom's nucleus. Both protons and neutrons possess spin states that can pair together to create an overall net-zero spin state when opposing spins are coupled. The overall result is zero nuclear magnetization if there is an even number of protons and neutrons, but in the event of an odd number of protons or neutrons, there will be a net magnetic moment present in the nucleus. This intrinsic spin possessed by the nucleus creates a magnetic dipole moment that behaves in a similar fashion to a macroscopic bar magnet, with the net spin of the nucleus following the right-hand rule and creating a net magnetic moment orthogonal to the plane of rotation.

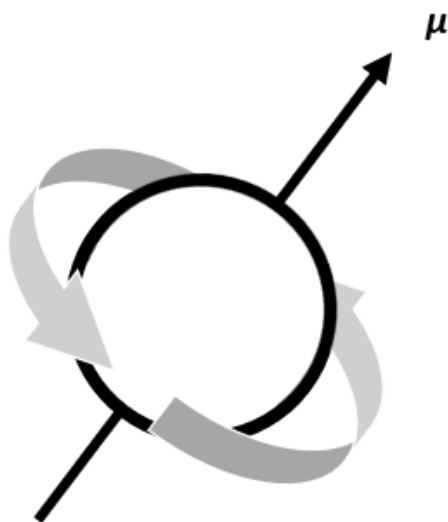


Fig. 1-3: Net angular momentum of a rotating nucleus.

Mathematically, the magnitude of a nuclear spin is calculated as $\hbar\sqrt{I(I+1)}$, where \hbar is the reduced Planck's constant ($\frac{h}{2\pi}$) and I is the quantized angular momentum (Fig. 1-3) (where $I = 0, \frac{1}{2}, \frac{3}{2}, \dots, \frac{9}{2}$). The direction of this nuclear spin is defined by quantum number m , which will take values between $-I$ and $+I$, formally written as $m = -I, -I + 1, \dots, I - 1, +I$. These values for m represent the discrete energy levels accessible to a particular nucleus, with the total number of components defined as $\mu = 2I + 1$. These discrete states are degenerate

in the absence of an external magnetic field, but will split into evenly spaced, non-

degenerate energy states due to the Zeeman interaction when introduced to an external magnetic field, B_0 , with the energy separation between these states (ΔE) being dependent on the strength of the magnetic field applied to the nucleus. The energy separation between adjacent energy levels can be calculated as $\Delta E = -\frac{m\mu}{I} B_0$.

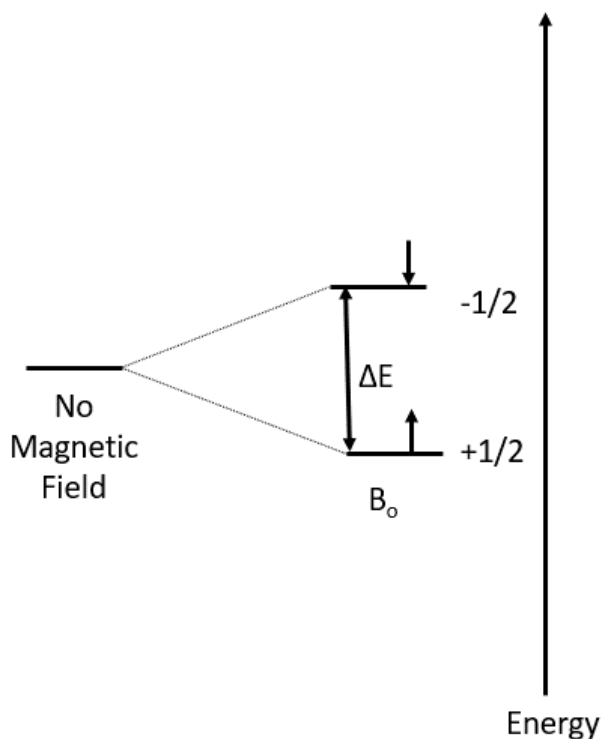


Fig. 1-4: Energy diagram of the Zeeman splitting interaction when a spin-1/2 nucleus is placed within an external magnetic field (B_0).

This energy (ΔE) is also equivalent to the energy needed to interact with and excite the nucleus during NMR spectroscopy to induce an imbalance in spin state population and produce a signal upon relaxation. When an $I = \frac{1}{2}$ nucleus is placed within an external magnetic field, it will begin to precess around B_0 with alignment of the spin either parallel or anti-parallel to the external field (Fig. 1-4). This phenomenon is described by the Zeeman interaction, with the lower energy state (+1/2) aligning with B_0 and the higher energy state (-1/2) aligning against the field. The population of nuclear spins occupying each energy state is defined by a Boltzman distribution

$$\frac{N_{Upper}}{N_{Lower}} = e^{\left(-\frac{2\mu B_0}{kT}\right)}$$

(N= population of each energy level, k= Boltzman constant, and T is

temperature in Kelvin). In general, the differences in the populations of each state is negligible at ambient conditions and each energy state is assumed to have an equivalent number of nuclei in each state.

We can calculate the corresponding frequency required to excite a particular nucleus to promote it to the higher energy spin state using the relationship $E = h\nu$; since the energy

gap is dependent on the field strength of B_0 , the three most relevant parameters of NMR spectroscopy can be summarized through the following relationship: $E = h\nu = -\frac{m\mu}{I} B_0$. Due to this elegant mathematical relationship, the convention of defining a spectrometer based on the frequency required for interacting with a hydrogen nucleus (i.e. 400 MHz, 600 MHz, etc..) instead of magnetic field strength (Tesla) was adopted, as it offers a more intuitive understanding of the magnet strength with respect to nuclear resonance (as well as clearly stating the Larmor frequency for proton NMR). The Larmor frequency is a nucleus-dependent property that defines the frequency at which a nucleus will precess within a magnetic field of a given strength, thus resonance frequency of a nucleus is directly related to the strength of the spectrometer.

The susceptibility of a particular nucleus is defined by its gyromagnetic ratio, defined as $\gamma = \frac{\mu}{\hbar I}$. The greater the ratio value is, the more NMR active the nucleus will be. The gyromagnetic ratio is commonly used in place of the quantum number notation, as it is a constant for each individual isotope and can easily be used to compare the sensitivity of different nuclei commonly used in NMR spectroscopy.

1.2.4 Chemical Shielding and Chemical Shift

Each nucleus has its own characteristic Larmor frequency at which it precesses in an external magnetic field, but there are also localized magnetic interactions that can influence this frequency. Each nucleus is surrounded by the electrons bound to the nucleus, each with their own spin and associated local magnetic field. These small, localized magnetic fields will align anti-parallel to B_0 , affecting the frequency that is required to interact with the nucleus. This is known as chemical shielding and is highly dependent on the bonding environment of the electrons and their orientation relative to B_0 . If a nucleus is considered in isolation, the electrons decrease the effective magnetic field experienced by the nucleus, shielding it from the effects of B_0 . If the electron density is shifted away from the nucleus, this effect is less pronounced and it becomes deshielded, as it is no longer as heavily influenced by the local electron magnetic field.

Chemical shift values are conventionally reported as δ_{ppm} with respect to a chemically stable laboratory standard that produces consistent NMR signals, the signal from various

experimental samples will shift to higher or lower ppm values depending on their local environment. As previously noted, local bonding environments with electrons can dramatically affect the degree of chemical shift since it changes the spatial orientation of the electrons with respect to the nucleus, thereby changing the influence of the local magnetic field. The more shielding around a nucleus (anti-parallel local magnetic fields), the lower the radio frequency pulse required to influence the nucleus.

The chemical shift of an NMR signal can be used to determine local bonding environments based on the degree of shielding and deshielding produced from each unique nuclear environment. In relatively simple molecules, this effect is extremely useful in elucidating structure, especially with relative deshielding of protons in ^1H NMR where chemical shift is highly diagnostic of bond order on adjacent atoms.

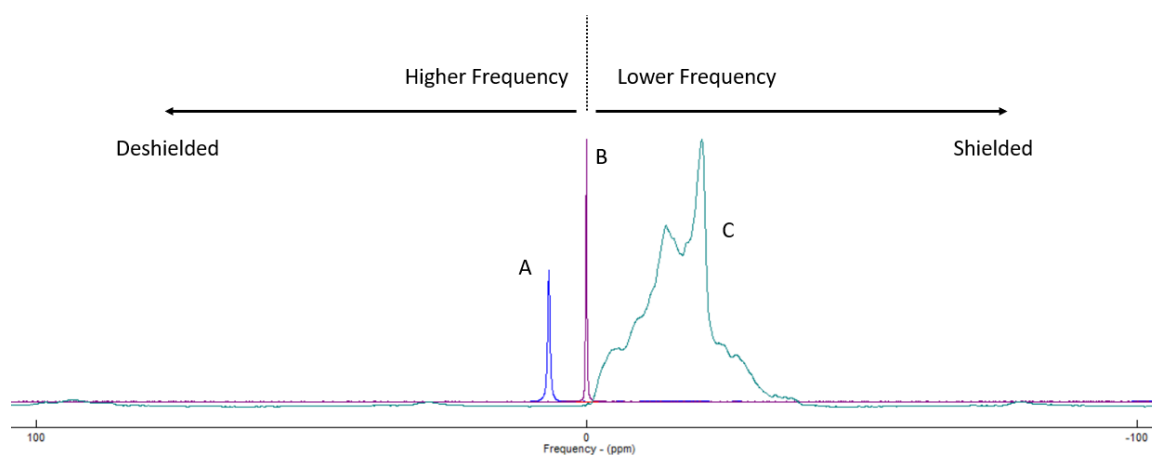


Fig. 1-5: Typical NMR spectrum with three samples plotted: A is a deshielded crystalline halite signal, B is a 1 M NaCl liquid standard, and C is crystalline sample of thenardite (Na_2SO_4) experiencing a shielding effect and shifting to a lower frequency.

1.2.5 Magic Angle Spinning of Solid Samples

When atoms are molecularly or ionically bound together (such as in organic molecules or in a crystal lattice) the electrons are localized in their respective bonding environments and no longer produce an isotropic effect on the nucleus.

Instead, the electron density is held in the bond and the orientation of the electron's magnetic field is restricted, making the shielding effects anisotropic and dependent on the orientation of the molecule with respect to B_0 . In solvated samples, this is not an issue, since the rapid tumbling of the molecules via Brownian motion is constantly reorienting, however this is not the case with static solid-state samples

where movement is heavily restricted. In powdered crystalline samples, this results in a broad signal that is attributed to the overlapping of the infinite number of possible orientations for each grain with respect to B_0 . Fortunately, this effect can be minimized by rapidly spinning the powder sample at the 'magic angle' to minimize peak broadening from static crystalline samples. This functions in two distinct ways: 1) it re-introduces rapid reorientation of the sample, and 2) when spun at a high enough frequency on an angle with respect to B_0 , anisotropic effects that are present around the nuclei can be averaged out to produce a narrow signal.

This technique is known as Magic Angle Spinning (MAS) and it is routinely used to resolve solid-state spectra collected from crystalline samples. The so-called 'magic angle' requires the sample be tilted to 54.7° with respect to B_0 (Fig. 1-6). The 'magic angle' is effective because anisotropic effects on the nuclei (such as first-order quadrupolar, chemical shift anisotropy, and dipolar coupling interactions) share the same sensitivity to spatial orientation. The dipolar interaction can be modelled as $B_z = \frac{K\mu}{r^3} (3\cos^2\theta - 1)$, which, when evaluated at an angle of $\theta = 54.7^\circ$ results in the expression approaching zero

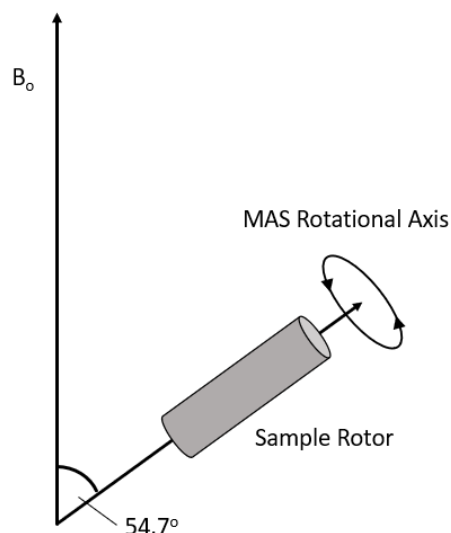


Fig. 1-6: Schematic of an MAS probe oriented at 54.7° with respect to B_0 .

and effectively removing the interaction. A similar phenomenon can be seen in first-order quadrupolar interaction as well as CSA interactions, both of which contain the $(3\cos^2\theta - 1)$ term when their hamiltonian equations are solved with respect to the laboratory frame of reference at an angle of $\theta = 54.7^\circ$. This means that by manipulating the angle of the sample with respect to B_0 (combined with rapid rotation), it is possible to remove a significant amount of the anisotropic line broadening that is introduced in solid-state NMR. As the anisotropic components (CSA, dipolar, and quadrupolar interactions) are averaged to zero, only the isotropic interaction is available for analysis.

1.2.6 Quadrupolar Nuclei and Associated Effects

This research relies on the sodium-23 nucleus for studying a variety of samples. sodium-23 is a good candidate for NMR analysis because it has a natural abundance of 100% and has a nuclear spin of $I = 3/2$ so it is NMR active. However, the nuclear spin of $3/2$ means that ^{23}Na is a quadrupolar nucleus that has more than two discrete energy states when placed within an external magnetic field. The Zeeman splitting of a quadrupolar nucleus results in a number of extra energy levels equivalent to $2I+1$; in the case of ^{23}Na ($I=3/2$), the resulting number of discrete energy levels is four ($+3/2, +1/2, -1/2, -3/2$). For most quadrupolar nuclei, the electrical field of the nucleus is no longer uniform and spherical, resulting in an electric field gradient (EFG) (Fig. 1-7).

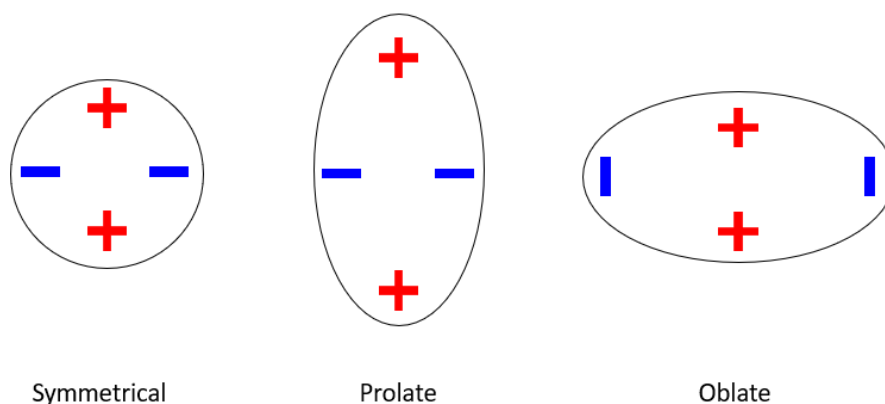


Fig. 1-7: The symmetrical charge distribution of a spin-1/2 nucleus (left) compared to the asymmetrical charge distributions that can be found in quadrupolar nuclei (right)

The imbalanced local magnetic environment of such nuclei gives rise to a variable distribution in energy levels when the Zeeman interaction is induced by the external magnetic field (B_0) which disrupts the energy separation between spin states so that they are no longer equally energetically spaced. This results in some transitions being favoured over others, as there is a lower energy threshold for the transition to take place.

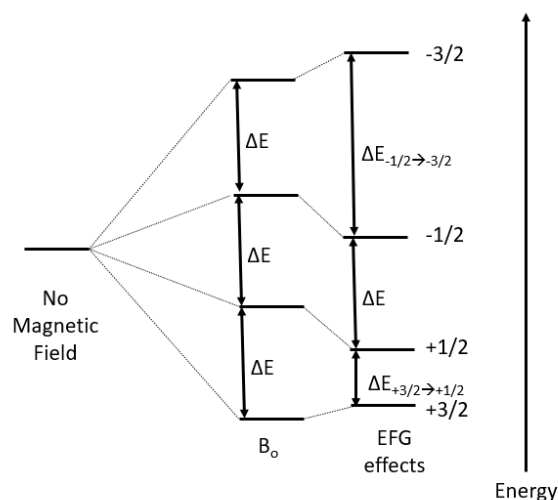


Fig. 1-8: Energy diagram for a spin-3/2 nucleus under the influence of B_0 , with additional energy changes from an EFG

This produces a quadrupolar interaction (quantified by the electric quadrupolar moment value) that can distort the NMR signal produced by the nuclei as the asymmetrical charge distribution within the nucleus creates inequalities in the energy separations between Zeeman states and consequently redistributing the population found within each spin state when under the influence of B_0 (Fig. 1-8). This unequal distribution of charge density about the nucleus results in line broadening and quadrupolar

lineshapes developing in the NMR spectrum (Fig.1-9). The asymmetrical charge distribution is denoted as η_Q , which takes a value between zero and one to model the degree of asymmetry. This manifests as distorted spectral signals which can then be deconvoluted using software (such as DMFit) that can compute the specific parameters that give rise to a quadrupolar signal once it is fitted to the experimental data. Quadrupolar deconvolution is a necessary aspect of understanding the local magnetic environment of quadrupolar nuclei and can help determine the changes in EFG with respect to the external magnetic field.

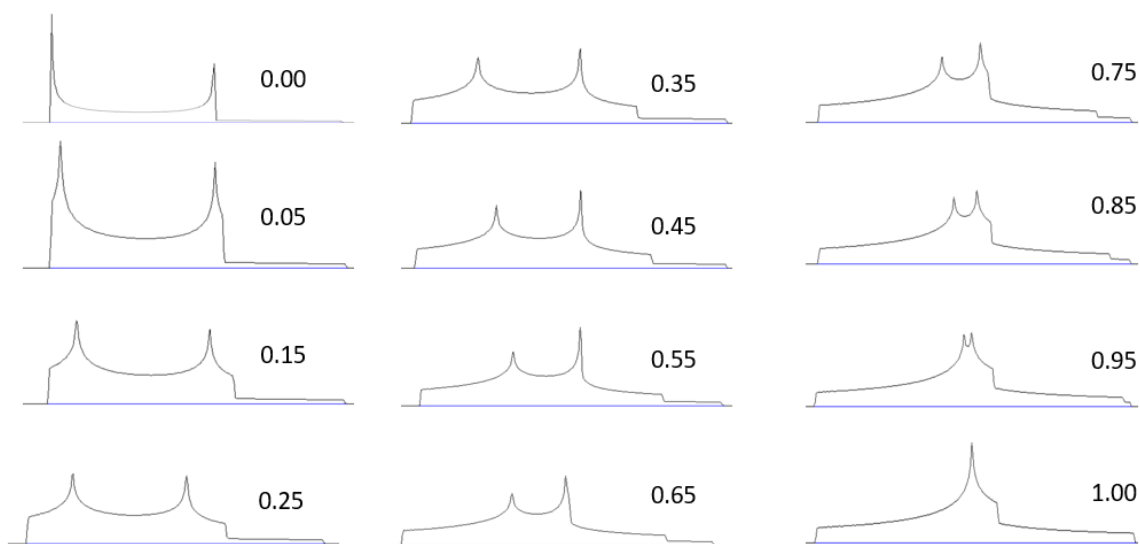


Fig. 1-9: Spectral line shapes that are characteristic of quadrupolar nuclei based on their asymmetry (η_Q) values from 0 to 1, where 0 = perfect axial symmetry about the nucleus. Line shapes were modelled for a ^{23}Na nuclei at a spectrometer frequency of 105.84 MHz and a $C_Q = 1$ MHz using DMFit. Line shapes are independent of chemical shift (PPM) and signal intensity, these are omitted for clarity.

1.2.7 Standard NMR Analysis

In order to be able to detect spin-state transitions, a significant imbalance in the population needs to be induced so a stronger signal can be produced as a large population of nuclei relax back to the lower energy state and restore equilibrium. This change in equilibrium is achieved by pulsing the nuclei with an RF pulse that can push them out of their low energy state, then relaxation can be observed through the released RF energy as the excited nuclei return to their original energy states. If the full energy difference between the two spin states ($-1/2 \rightarrow +1/2$) is applied, the nuclei will be occupying their second lowest energy state available in the system which would result in slower and less homogenous relaxation times. This is not ideal when attempting to collect representative spectral information, so instead the nuclei are usually forced to precess in the least favourable orientation relative to B_0 . If B_0 is defined as the z-axis within the frame of the

experiment, a transition from $+1/2$ to $-1/2$ would be a 180° rotation, or π radians, from their initial orientation. The most unstable, highest energy precession for these nuclei, then, would occur midway between these two states and orthogonal to B_0 . Such a change in precession would tilt the nuclei by 90° or $\pi/2$ radians from their initial orientation resulting in an unfavourably high energy orientation once the RF pulse has been turned off (Fig. 1-10). This RF pulse is defined as B_1 , which induces another magnetic field to probe the sample.

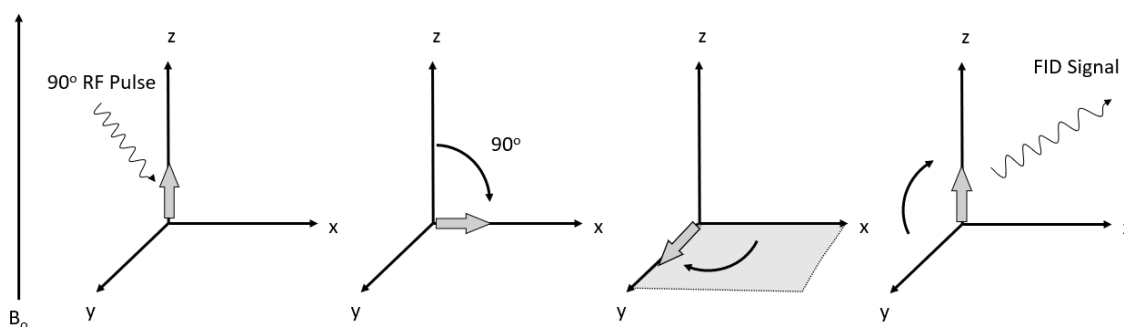


Fig. 1-10: A typical 90° pulse sequence. The incident RF pulse creates an orthogonal magnetic field (B_1) along the XY plane. The nuclei then precess in the XY plane before decaying back to alignment along B_0 .

Depending on the length of the RF pulse from the probe, the orientation of the nucleus can rotate through a full 360° relative to B_0 and will continue to cycle while the RF probe is active. Once the pulse is stopped, the artificially induced local magnetic field is removed and the nucleus is allowed to decay back to equilibrium from the excited state induced by B_1 .

The traditional 90° pulse technique produces the strongest NMR signal when decaying but it generally necessitates the longest delay between consecutive scans (recycle delay). This results from the fact that all of the nuclei within the sample must be allowed to return to equilibrium with B_0 before the next pulse can begin. Relaxation times can vary widely (from milliseconds to minutes) based on dipole-dipole and quadrupole interactions, as well as spin-rotation and chemical shift anisotropy within a particular chemical environment. Solid samples tend to have very long relaxation times owing to

their tightly bound crystal structure which can significantly increase the amount of time needed to return to equilibrium (Bakmutov, 2015). A shorter pulse that tips the nucleus less than 90° can allow for a faster relaxation within the sample, but also results in a weaker signal being emitted upon relaxation. The ideal tip angle for any given experiment becomes a balancing act between strength of the emitted signal and number of acquisitions that need to be collected; sometimes it is beneficial to perform fewer scans at a 90° tip angle and wait longer between pulses, other times (such as with solid samples) it may be more efficient to use shorter pulse widths (tip angle $<90^\circ$) and collect more acquisitions within the same time frame.

Single pulse experiments (as were used in this research) are extremely useful in simple chemical environments, however multiple pulse sequences can be designed to manipulate the nuclei to eliminate undesirable interactions in more complex samples. Such complex techniques can eliminate nuclear coupling, increase sensitivity via spin transfer, and offer additional information on bonding environments. The experiments in this research did not employ any complex pulse sequences, all experiments were completed by using single pulses with varying pulse widths (i.e. tip angles) and relaxation times.

The coil that is used to induce the excitation of the nuclei plays a role in both the perturbation of the spin states as well as the detection of signal upon relaxation back to ground state. After the short incident pulse is produced, the coil then acts as a receiver to collect the signal that is produced from spin decaying back to normal. This signal is collected as a Free Induction Decay (FID) spectrum, measuring the intensity of the signal over time while the signal decays, free from any external magnetic fields apart from B_0 . Once the FID data are collected, the Fourier transform calculation can be used to separate the various frequencies that have been combined to form the signal decay spectrum and create a plot displaying the intensity of each signal against its frequency. Although the signal is collected as a frequency (conventionally in Hz), the experimentally observed frequency (Hz) is divided by the Larmor frequency of the nucleus at the magnetic field of the spectrometer (in MHz). For example, the natural resonant frequency of ^{23}Na at 9.398 Tesla is 105.84 MHz and reported in parts per million ($1 \text{ Hz} / 1 \text{ MHz} = 1 \text{ ppm}$). This convention makes it easier to interpret chemical shifts and also standardizes chemical

shifts across different spectrometers so characteristic chemical shifts are universally diagnostic regardless of what spectrometer was used to collect them. The practice of using ppm as the conventional notation for chemical shift also allows reference samples to arbitrarily be set to 0.0 ppm and all chemical shifts can be referenced as a deviation from the standard (δ ppm); when using a standard, the chemical shift can be calculated as

$$\delta = \frac{[\nu_{Sample} - \nu_{Ref}] \times 10^6}{\nu_{Ref}} \text{ (Bakhmutov, 2015).}$$

1.3 Powder X-Ray Diffraction

X-Ray diffraction is an extremely powerful tool for non-destructively analyzing a variety of crystalline, and polycrystalline solids which can offer valuable information on crystal structure, mineral phases, physical deformation, chemical composition (indirectly), and more (Suryanarayana & Norton, 1998). Although the process itself is non-destructive, the preparation for powder X-ray diffraction requires that the sample be crushed to a fine powder before being affixed to a mount. The advantage of powdering the sample is that all of the phases that may be present in the sample become homogeneously distributed and can usually be identified after a single analysis (Suryanarayana & Norton, 1998). It also ensures that the crystallites are in random distribution and all of the lattice planes in each mineral are in diffraction condition simultaneously giving a complete powder pattern; this is useful for identification using the International Center Diffraction Data (ICDD) database of powder X-ray diffraction patterns.

Using X-ray radiation has several advantages over other analytical methods that use lower energy electromagnetic radiation such as IR, UV-Vis, or Raman spectroscopy since the much shorter wavelength of the incident rays can interact directly on the same scale as the interatomic distances found in most chemical bonding environments. X-ray radiation lies within the range of 10^{-2} Å to 100 Å in wavelength, which means X-ray radiation can cover the breadth of most interatomic distances that generally fall in the order of 1-10 Å (Lee, 2017).

In order to produce a consistent and monochromatic source of X-rays, a tube is used to house a cathode and an anode source under vacuum. As an electric current with a high

enough voltage is applied to the anode, the electrons are forced to jump the vacant gap to the cathode, and with enough current, this can form a cohesive beam of high energy electrons flowing between the two terminals. In order to produce X-rays, this beam can be interrupted with a number of suitable metals that have appropriate electron configurations and produce X-rays of the desired energy (and wavelength). Some metals that are employed for this purpose are copper, molybdenum, iron, cobalt, and chromium (Lee, 2017). To further explain the process, cobalt will be used as an example.

When the high-energy electron beam encounters a sheet of cobalt metal, there are two possible outcomes: electrons can pass through (likely with a small loss of kinetic energy) and continue to the cathode, or they can hit another electron in the metal and eject it from its orbital, creating a vacancy (Fig. 1-11). When an electron is ejected from an atom in the core orbitals of a Co nucleus, another electron is energetically obligated to fill the vacancy to return the electron configuration to the lowest possible energy state (Lee, 2017). This key process of vacancy filling is where the X-ray radiation is produced, as the higher energy outer electron must release the amount of energy equal to the energy separation between the inner and outer orbital states. As the transition takes place, a high energy photon is emitted with a high enough frequency to be classified as X-ray radiation which can then be allowed to interact with the sample in the X-ray diffractometer (Suryanarayana & Norton, 1998).

To better distinguish between energy levels in electron orbital shells, conventional names have been given to each energy shell. The core electrons are considered to be in the K shell of electrons, the next energy level above the core electrons is the L shell, and the outer-most electron shell is called the M shell.

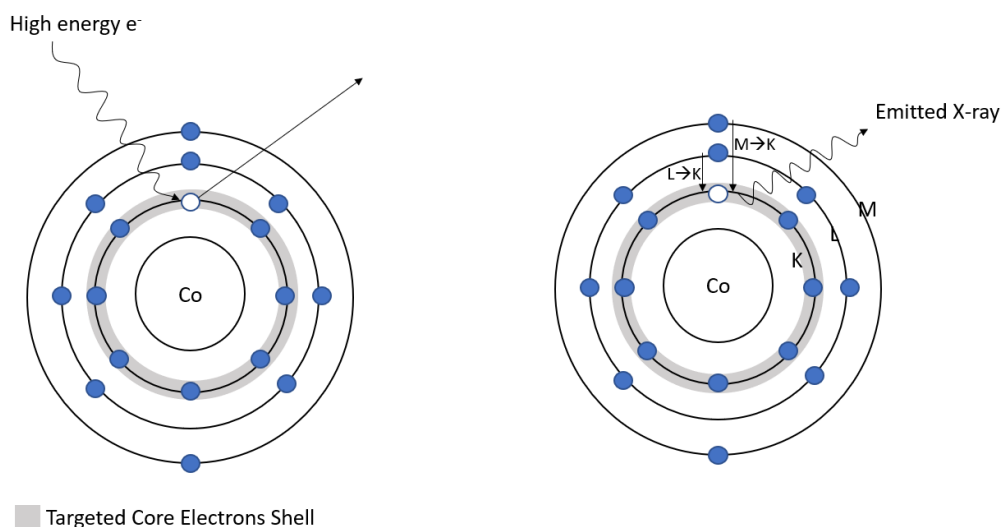


Fig. 1-11: Simplified Bohr-Rutherford diagrams illustrating the production of an X-ray in a cobalt atom. Initial ejection of a core electron (left) and subsequent transition of a valence electron, releasing energy in the form of X-radiation (right).

Both of these X-ray transitions create characteristic metal peaks and are the X-ray frequencies that are used for sample analysis (Lee, 2017; Waseda et al., 2011). The K_{α} emission produced by the $L \rightarrow K$ transition has twice the intensity of K_{β} (produced by the $M \rightarrow K$ transition) and is therefore often selected as the wavelength for X-ray analysis of the sample ($\lambda_{\text{Co } K_{\alpha}} = 1.78897 \text{ \AA}$). Core electrons found in orbitals below the K shell require significantly more energy to liberate and are not considered under standard X-ray production conditions.

When an incident X-ray contacts the surface of a crystal lattice, the X-ray may inelastically scatter back, bouncing off the top few layers of the crystal with a loss of energy in a process known as diffraction. If this happens at just the right angle where the perpendicular distance between adjacent lattice planes (d-spacing) is equivalent to a multiple of the X-ray's wavelength, the diffracting X-rays can constructively interfere and produce an amplified signal much stronger than random inelastically scattered X-rays (Fig. 1-12). This relationship is described by Bragg's Law: $2d\sin\theta = n\lambda$ where d is the interplanar spacing between lattice layers, θ is the angle of incidence, n is the multiple of wavelengths equivalent to the interplanar distance, and λ is the incident wavelength of X-

ray radiation (Waseda et al., 2011). By varying the incident X-ray angle, a characteristic diffraction pattern can be collected that corresponds to all of the angles that satisfy Bragg's Law for all of the corresponding lattice planes (with associated d-spacings) in a specific crystal structure. This diffraction pattern can be used as a "fingerprint" for identifying the same crystal pattern in new samples by comparison to existing standard samples.

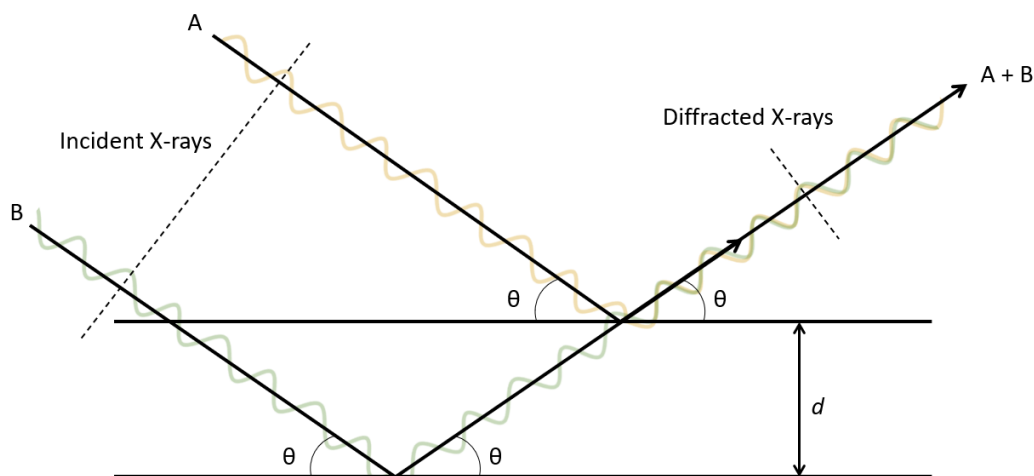


Fig. 1-12: Monochromatic X-rays diffracting at a Bragg's angle upon leaving the lattice in phase with each other and constructively interfering.

As mentioned earlier, a powdered sample will have crystal grains oriented such that all lattice planes satisfy the Bragg diffraction condition and will produce a complete diffraction pattern. For θ - 2θ geometry, the X-ray source is fixed, but both the sample and the detector must rotate about the centre of diffraction by θ and 2θ , respectively, to collect the diffraction pattern while maintaining a corresponding equivalence between the angle of incidence (θ) and the angle of diffraction (θ) relative to the surface of the sample.

The angle of incidence is decided by random grain orientation with respect to the X-ray source and the angle of diffraction is equivalent to the angle of rotation for the detector. These two angles are inherently equivalent, thus pXRD often refers to the angle of collection in terms of 2θ (signal will not be detected if this parameter is not satisfied),

removing the need to account for random orientation of the powdered crystalline grains (Fig. 1-13).

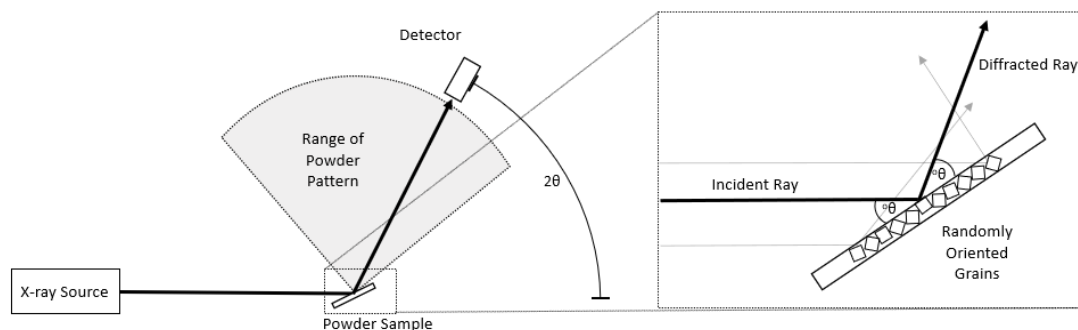


Fig. 1-13: Schematic of a typical θ - 2θ powder X-ray diffractometer where the detector rotates by 2θ while the sample rotates by θ , to collect the full powder diffraction pattern. This enables the angle of incidence and the angle of diffraction from the sample to remain equal at every position. Random grain orientation of the sample illustrates how angle of incidence varies with a stationary powder distribution.

Quality pXRD analysis requires that the X-ray beam be monochromatic and the spatial relations between the X-ray source, sample, and detector are all properly calibrated. Mineral databases such as the International Centre for Diffraction Data (ICDD) are relied upon for producing and maintaining high quality reference patterns for mineral identification. An example of an ICDD card match to a sample is shown in Fig. 1-14.

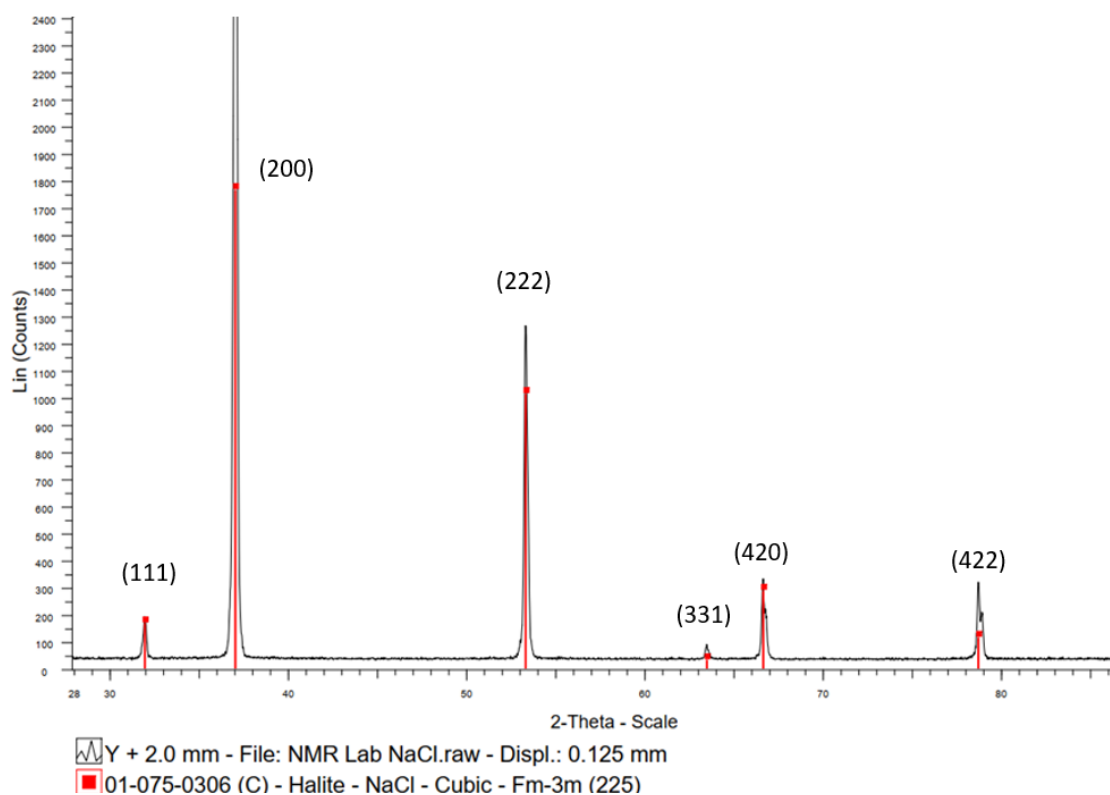


Fig. 1-14: Powder X-Ray diffraction pattern of laboratory reagent-grade halite with intensity plotted over the range of 2θ . This is a best match to ICDD card number 07-75-0306 for halite. Miller indices are noted above their corresponding peaks with respect to 2θ .

Because this technique solely relies on the diffraction of X-rays from the sample, it contains no intrinsic chemical information about the material. The diffraction patterns are a strictly structural phenomenon and can therefore be very similar between unique samples that have very similar crystal structures, such as cubic minerals with similar lattice dimensions (i.e. isomorphous phases). This possibility needs to be taken into account when identifying a particular mineral phase strictly using a pXRD pattern and subsequent supplementary analysis using other complementary analytical techniques is advisable.

1.4 Inductively Coupled Plasma - Mass Spectroscopy

Inductively Coupled Plasma - Mass Spectrometry (ICP-MS) analysis is a common technique used to identify sample composition at the elemental level, although it is possible to use the technique for larger mass samples and deduce fragments of molecules with the appropriate analytical methods. In the case of this research ICP-MS analysis was used to identify the trace chemical composition within solvated samples, so this technique will be covered in more depth. The fundamental principles remain the same, however, for most mass spectrometry instruments: 1) ionize the sample, 2) separate each individual constituent by their respective mass, and 3) count the number of each respective ion. As per the name of the technique, these instruments produce a plasma by flowing argon gas through a chamber surrounded by a coil that is used to induce a magnetic field across the gas. This excites the electrons in the argon gas and liberates them, forming $\text{Ar}^+ + e^-$ and $\text{Ar}^{2+} + 2e^-$ species that are responsible for ionizing the sample and carrying it through to the mass spectrometer (Hoffmann & Stroobant, 2007). Temperatures produced by the plasma can be as high as 10000 K, ionizing nearly 100% of the sample within milliseconds before it proceeds to the vacuum chamber for separation. The removal of atmosphere from within the spectrometer is necessary to minimize collisions that might impact the analysis of the free ions. In this step, the ions are separated over the course of their movement from the plasma chamber to the detector. There are several methods that spectrometers rely on for separating ions, such as a time-of-flight separation that allows lighter ions to reach a detector faster than heavier ones over the course of the analysis. More commonly, spectrometers utilize a quadrupolar rod system that selectively hinders the transit of ions based on their mass to charge (m/z) ratio. By carefully varying the voltage applied to the quadrupolar rods, more massive particles are allowed to pass through the quadrupoles with minimal impact on their trajectory, while lighter ions will be removed from the ion beam (cations drawn towards the anodes and anions drawn towards the cathodes). This creates a selective filter once the appropriate quadrupolar charge settings are implemented around the ion beam and each ion can be counted in isolation. An example of a simplified ICP-MS instrument can be seen in Fig. 1-15.

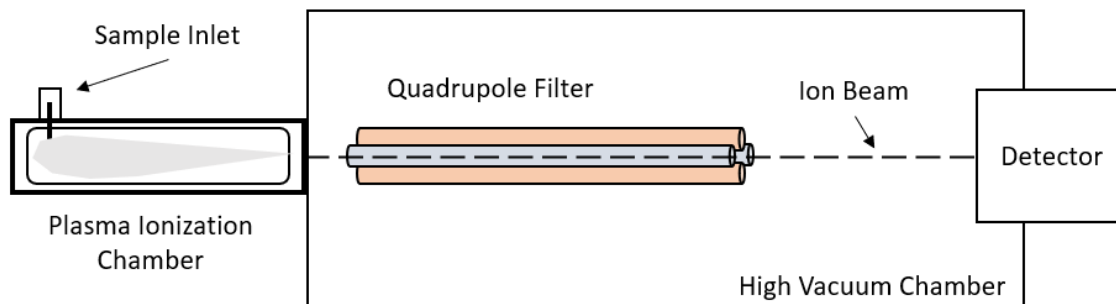


Fig. 1-15: A depiction of an extremely simplified ICP-MS instrument with a quadrupolar filter.

As the ions are separated (regardless of separation method), they impinge on a detector at the end of the instrument where their ionic charge registers and can be counted to determine concentration. Despite being called mass spectrometry, the mass is never directly measured as part of the analysis, either the mass is inferred by time of flight or selected based on the mass to charge ratio of the ion and counted accordingly. The output of a mass spectrometry analysis is a dataset comprised of the relative concentration of an element within the sample based on the number of charged particles at each particular mass to charge ratio that is detected. Depending on the sensitivity of the instrument, the result may be reported in terms of parts per million (ppm) or parts per billion (ppb) as a representative concentration for the bulk sample.

1.5 References

Akitt, J. W., & Mann, B. E. (2000). *NMR and chemistry: An introduction to modern NMR spectroscopy* (4th ed). S. Thornes.

Andrew, E. R., & Szczesniak, E. (1995). A historical account of NMR in the solid state. *Progress in Nuclear Magnetic Resonance Spectroscopy*, 28(1), 11–36.

[https://doi.org/10.1016/0079-6565\(95\)01018-1](https://doi.org/10.1016/0079-6565(95)01018-1)

Bakhmutov, V. I. (2015). *NMR Spectroscopy in Liquids and Solids*. CRC Press.

Crawford, M. L., & Hollister, L. S. (1986). Metamorphic Fluids: The Evidence from Fluid Inclusions. In J. V. Walther & B. J. Wood (Eds.), *Fluid—Rock Interactions during Metamorphism* (Vol. 5, pp. 1–35). Springer New York. https://doi.org/10.1007/978-1-4612-4896-5_1

Goldstein, R. H., Samson, I., Anderson, A., & Marshall, D. (2003). Petrographic analysis of fluid inclusions. *Fluid Inclusions: Analysis and Interpretation*, 32, 9–53.

Hoffmann, E. de, & Stroobant, V. (2007). *Mass spectrometry: Principles and applications* (3rd ed). J. Wiley.

Hurai, V., Huraiová, M., Slobodník, M., & Thomas, R. (2015). Chapter 1—General Characteristics of Geofluids. In V. Hurai, M. Huraiová, M. Slobodník, & R. Thomas (Eds.), *Geofluids* (pp. 1–22). Elsevier. <https://doi.org/10.1016/B978-0-12-803241-1.00001-0>

Lee, M. (2017). *X-Ray diffraction for materials research: From fundamentals to applications*. CRC Press.

Liao, G., Luo, S., & Xiao, L. (2021). Borehole Nuclear Magnetic Resonance Study at the China University of Petroleum. *Journal of Magnetic Resonance*, 324, 106914. <https://doi.org/10.1016/j.jmr.2021.106914>

Roedder, E. (1972). *Composition of fluid inclusions* (No. 440-JJ). <https://pubs.er.usgs.gov/publication/pp440JJ>

Suryanarayana, C., & Norton, M. G. (1998). *X-Ray Diffraction*. Springer US. <https://doi.org/10.1007/978-1-4899-0148-4>

Waseda, Y., Matsubara, E., & Shinoda, K. (2011). *X-Ray Diffraction Crystallography*. Springer Berlin Heidelberg. <https://doi.org/10.1007/978-3-642-16635-8>

Chapter 2

2 Methods and Sample Selection

This chapter will cover sample selection and the methods used for sample analysis throughout the dissertation. Methods include: ^{23}Na Magic Angle Spinning Solid State Nuclear Magnetic Resonance Spectroscopy (MAS SS NMR), Variable Temperature (VT) NMR, Inductively Coupled Plasma – Mass Spectrometry, powder X-ray Diffraction, calibration curve dilution schemes, and software packages that were employed for data processing and analysis.

2.1 Calibration Curve Dilution Scheme

To determine the dependence of the ^{23}Na NMR chemical shift on concentration of NaCl in solution, a calibration curve was created by using a stepped dilution scheme of reagent grade NaCl (AnalaR brand, 99.9% pure NaCl) dissolved in pure deionized water.

Lab grade NaCl was weighed to ± 0.0001 g precision using an R200D Mettler-Toledo analytical scale. The dispensed mass of NaCl was 35.0640 g. A concentration of 6.000 M NaCl was the initial target for the primary solution by adding the NaCl to a 100 mL volumetric flask and filling the flask to the meniscus, swirling frequently to promote solvation. All glassware was rinsed three times with deionized water prior to use in mixing the solutions. At a laboratory temperature of 19.6°C, the NaCl remained beyond saturation and remained undissolved for the 6 M solution. Gentle heating in a warm water bath was used to promote dissolution but was unsuccessful. The solution was cooled to lab temperature and transferred to a 150 mL volumetric flask with a new target concentration of 4.000 M NaCl (same mass of NaCl into 150 mL H₂O). The flask for the initial 100 mL solution was rinsed and incorporated into the new 150 mL flask to ensure full transfer of dissolved NaCl. The new solution fully incorporated the NaCl and was used as the primary solution for the dilution scheme. Delivery pipettes were rinsed three times with deionized water and three times with each preceding NaCl solution prior to transferring to the next flask to ensure the most accurate concentrations with the lowest possible error. The following dilution scheme was followed to produce precise solutions

of 4.000 M NaCl, 2.000 M NaCl, 1 M NaCl, 0.500 M NaCl, and 0.250 M NaCl (Fig. 2-1).

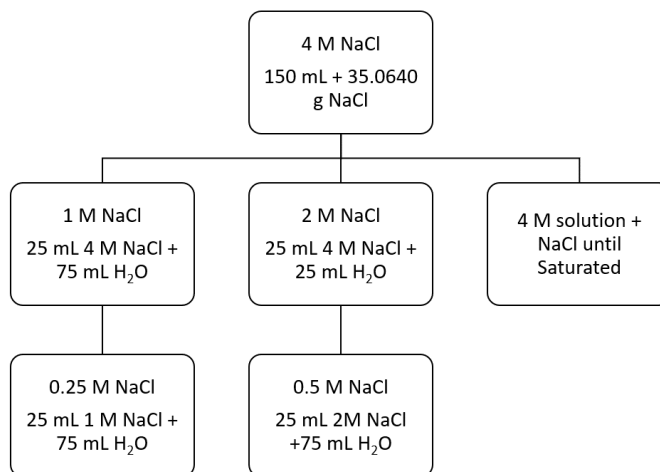


Fig. 2-1: Illustrated dilution scheme used for NaCl calibration curve standards.

A sub-sample of the initial 4.000 M solution was then brought to saturation with the addition of NaCl until solid halite remained undissolved in the flask. The calculated molarity for the saturation solution at ambient temperature (19.6°C) was 6.16 M NaCl, the maximum concentration under laboratory conditions as the solution was left to saturate.

The samples were stored under standard laboratory conditions in the volumetric flasks and sealed with ParaFilm until subsamples could be transferred for NMR analysis. A sample of pure deionized water was included in the sample suite as a control to ensure no contamination was present within the dilution scheme.

2.2 Inductively Coupled Plasma - Mass Spectroscopy

All halite samples were sent to Activation Laboratories (ACTLabs) in Ancaster, Ontario for a full chemical characterization using Inductively Coupled Plasma - Mass Spectrometry (ICP-MS). Samples were prepared for analysis at the University of Western Ontario by finely grinding the halite samples to a powder under a pure anhydrous ethanol wash to avoid loss of sample. Approximately two grams of each halite sample were

prepared as if for powder X-Ray Diffraction (pXRD) analysis (sub 5 μm grain size), then subdivided into two separate samples. A sub-sample of each halite sample powder was delivered for analysis while the other sub-sample was retained for pXRD analysis, ensuring equivalent samples for both analytical methods (Fig. 2-2).

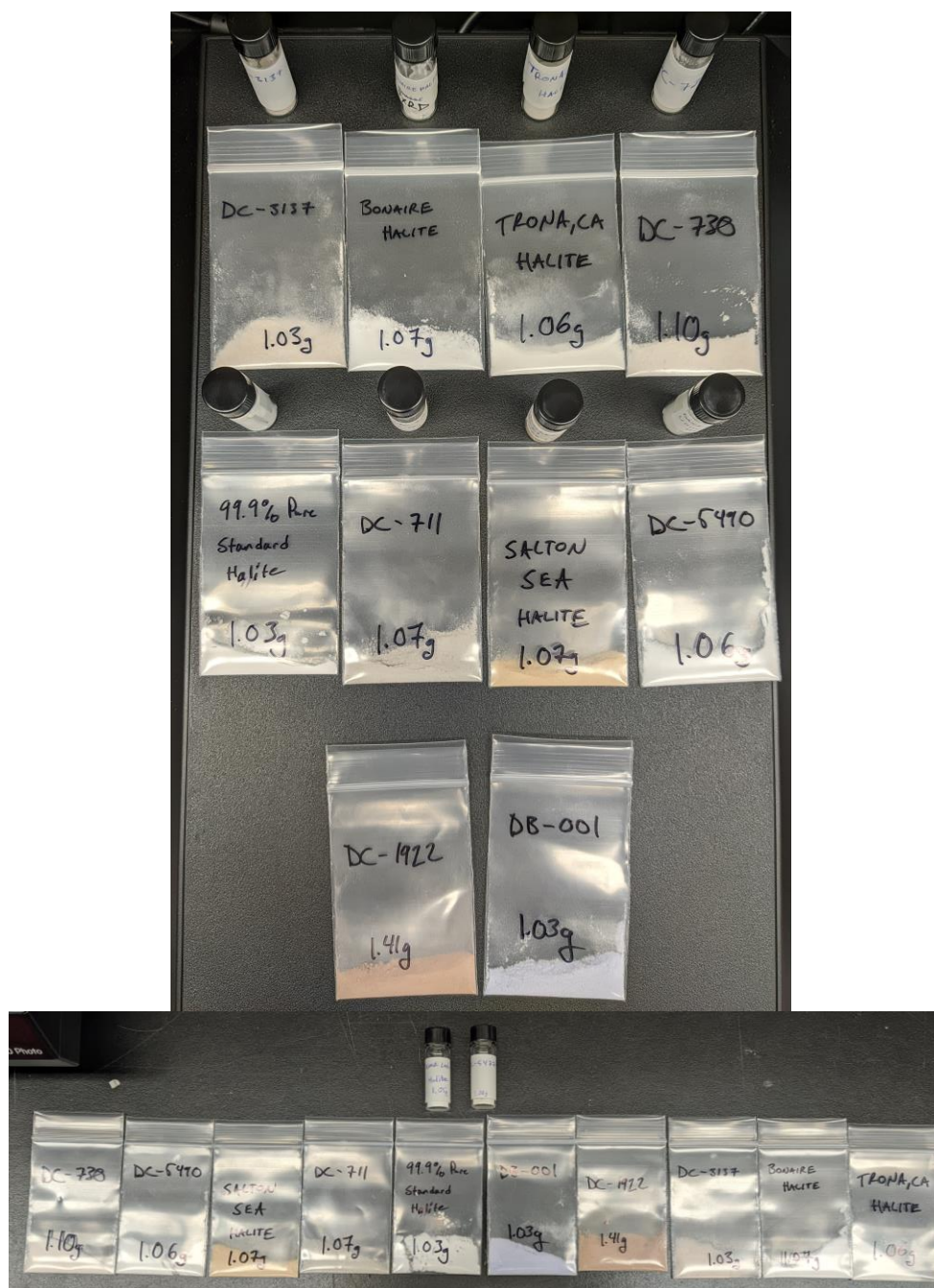


Fig. 2-2: Halite samples prepared for ICP-MS and pXRD analysis. Vial samples were retained for pXRD, bagged samples were delivered to ACTLabs.

ACTLabs Mass Spectrometry analysis was carried out by dissolving the powdered halite sample in deionized water and injecting it into the ICP-MS instrument. Information regarding the analytical error and sensitivity of the spectrometer can be found in Appendix A.

2.3 Nuclear Magnetic Resonance Spectroscopy

All NMR data were collected at the J.B. Stothers NMR Facility at the University of Western Ontario, using a Varian Infinity Plus 400 NMR spectrometer. All samples, both solid and liquid, were analyzed using a Varian triple-resonance 4.0 mm HXY MAS NMR probe and referenced with respect to a 1.0 M NaCl aqueous solution ($\delta(^{23}\text{Na}) = 0.0$ ppm). All solid geological samples were coarsely ground to approximately 1-2 mm grain size to avoid breaking fluid inclusions and packed into 4 mm ZrO_2 rotors to ensure consistent analysis free from interference introduced by borosilicate rotors, while also allowing for high-speed Magic Angle Spinning (MAS) of solid samples.



Fig. 2-3: Coarsely ground halite samples prepared for NMR analysis.

Lab grade samples such as halite and thenardite were already at a finer grain size and were analyzed without grinding. Hygroscopic standard samples of halite and thenardite were desiccated by moderate heating in a laboratory oven ($\sim 70^\circ\text{C}$ and 120°C , respectively, for a minimum of 12 hours) prior to analysis to eliminate possible effects of moisture and salt hydration.

2.3.1 Calibration Curve Standard Acquisition

For the liquid calibration standards, 40 scans were acquired per sample using a 40 kHz spectral width, with a 3.4 μs 90° pulse, 175 ms acquisition time, and a three second recycle delay between scans. All data were collected at static ambient laboratory conditions.

2.3.2 Solid State NMR Acquisition

Solid halite samples and samples of Snowbird quartz, Gonzales fluorite, Hansonburg fluorite, thenardite, and hydrated thenardite were analyzed at ambient laboratory conditions, both with a static probe (halite, Hansonburg) and an MAS probe (all samples) with a spin rate of 12.0 kHz. All spectra were acquired with a 55 kHz spectral width, a 1.7 μs 90° pulse, a 54.5 ms acquisition time, and a 45 second recycle delay to account for the slower relaxation of solid-state halite nuclei. The only variation between samples was the number of acquisitions necessary to achieve an acceptable signal to noise (S/N) ratio. Number of scans per sample varied from 20 scans of the South African Halite to 1600 scans for the Hansonburg fluorite. All acquisition data specific to individual samples can be found within the relevant chapter and are consolidated in Appendix B.

2.3.3 Variable Temperature NMR Acquisition

Variable temperature analysis was carried out on the Hansonburg fluorite sample and Snowbird quartz sample at 100°C, 150°C, 175°C, 185°C and 50°C, 100°C, 150°C, and 200°C, respectively. The Hansonburg fluorite sample was analyzed using a spin rate of 11.0 kHz with a spectral width of 25 kHz. A 1.7 μs selective 90° pulse was used with a 40.96 ms acquisition time and a 5 second recycle delay over 2140 scans.

Variable temperature analysis of the Snowbird quartz was also carried out at 11.0 kHz but with a 40 kHz spectral width, a 1.7 μs selective 90° pulse, and a 25.6 ms acquisition time. A 10 second recycle delay was used over the course of 800 to 1032 scans depending on the response of the sample at each temperature. Details for each individual acquisition period can be found in the relevant chapter and in Appendix B.

2.3.4 Raw NMR Data Processing

NMR spectra were collected in the time domain as Free Induction Decays (FIDs). These were converted to the frequency domain by Fourier transformation. Spectra were processed from the raw FID data using the NUTS Pro NMR Utility Transform Software. All spectra were zero-filled for optimal resolution before being Fourier transformed and manually phased. In the event of quadrupolar lineshapes in the data, further analysis was completed by exporting each spectrum as PPM + Intensity ASCII datasets and converted to MHz + Intensity datasets and imported to DMFit for complex peak deconvolution.

2.4 Powder X-Ray Diffraction

2.4.1 pXRD Data Acquisition

Halite samples were powdered and analyzed using powder X-Ray Diffraction on a Rigaku DMAX powder diffractometer with Bragg-Brentano geometry (theta-2theta), graphite monochromator, and scintillation counter using a cobalt X-ray source (Co $K\alpha_1$ radiation with wavelength of 1.78897 Å) operated at 40 kV and 35 mA at the University of Western Ontario. The samples were finely powdered to sub 5 μm grain size and thinly deposited on a glass sample mount by creating a slurry in anhydrous ethanol and manually distributing the powder slurry across the mount. Diffraction patterns were collected over a total scan time of approximately one hour (1h:06m:41s) with a starting angle of $10^\circ 2\theta$ and ending angle of $90^\circ 2\theta$. Each step increment was 0.02° with a dwell time of one second per step (2θ range from 10 – 90° , $0.02^\circ/\text{step}$, dwell time per step varied from 1 to 5 seconds/step). All but two halite samples were collected with these standard parameters: the DC-5477 sample (pink hopper halite exhibiting unique line shapes in NMR analysis) and the red Dana 1922 drill core halite sample with a fibrous texture were analyzed with a modified program. For the DC-5477 sample, the scan time was increased to nearly 14 hours (13 h: 53 m: 20 s), scanning from 10 – $110^\circ 2\theta$ in 0.02° increments with a dwell time of 10 seconds per step. The DC-1922 sample was scanned for just over 11 hours, scanning from 30 – $110^\circ 2\theta$ in 0.01° increments with a dwell time of 5 seconds per step. Different dwell times were allotted for the fluorite and quartz samples, with a dwell

time of 10 seconds for the Hansonburg fluorite and Snowbird quartz (total scan time of 13 h : 53 m : 20 s), while the Gonzalez fluorite was analyzed with a dwell time of three seconds per step (4 h : 10 m); the rest of the parameters were kept consistent with the majority of the halite samples, with a scan range of 10-110° 2 θ in 0.02° increments.

2.4.2 pXRD Data Processing

Data analysis was performed using the Bruker DIFFRACPLUS.EVA data processing software package on Microsoft Windows 7. Mineral phases were identified by pattern matching using a graphical interface to the International Center for Diffraction Data (ICDD) database, within the Bruker software package and assigning diffraction patterns by selecting the best-matching standard ICDD card match to the acquired data set. A sample displacement correction was sometimes necessary to account for variable sample thickness on the sample plate in some instances, while other samples required a change to the unit cell parameters of the reference card patterns to achieve the best fit. Although these changes were minimal in most cases, they are notable and worth mentioning explicitly.

2.5 Sample Selection and Geological Background

All samples that were analyzed in this research were collected from natural mineral deposits from across North America and beyond, although none was personally collected for the purposes of this work. Six halite samples were generously donated by the Richard W. Hutchinson Geoscience Collaborative Suite at the University of Western Ontario, originally curated as part of the Dana Collection. A variety of halite colours and morphologies were loaned for this research, with varying degrees of documentation available on each sample. All of the information available for the following samples has been summarized and supplemented with descriptions and images of each sub-sample used for research purposes. Four halite samples were contributed by Dr. Nigel Blamey at the University of Western Ontario, as were both fluorite samples and the quartz sample. The geological context for these samples has been included as well. Due to the nature of the research, samples were chosen without regard to provenance; halite samples were chosen for variety in colour, while the fluorite and quartz samples were chosen for their

academically published documentation of prior microthermometric analysis and their reputation of hosting fluid inclusions.

2.5.1 Dana 711 Halite

The provenance of this halite sample was documented as 'unknown origin' in the Dana collection, so little information exists about its geological context. The sample has a deep black region of halite crystals surrounded by smokey grey and clearer patches of halite. The host lithology appears to be a shale or fine-grained mudstone, but most of the host matrix material



Fig. 2-4: Hand sample of the Dana 711 halite

had been worn away from the halite sample and remained as powder in the sample box. The sample is approximately 10 cm across and exhibited typical halite cleavage across most of the sample, except for some regions where there appeared to be some conchoidal fracturing or evidence of irregular dissolution (See Fig. 2-4).

2.5.2 Dana 730 Halite

As with Dana 711, there was no recorded location information in the collection for Dana 730. The sample presents as coarse-grained halite and has a strong orange-amber colour present throughout the sample. The sub-sample taken for analysis is approximately 5 cm across and does not exhibit any cleavage, but does show conchoidal fracturing and obvious signs of surface dissolution (See Fig. 2-5).



Fig. 2-5: Hand sample of the Dana 730 orange halite.

2.5.3 Dana 1922 Halite

This sample was collected by the Adelaide Salt Company in Middlesex County, Ontario, from a depth of approximately 1300 feet. It was reportedly recovered from a vein system in the Upper Silurian Salina formation. The sample is deep red in colour and exhibits columnar growth habit, approaching an almost fibrous texture (See Fig. 2-6).

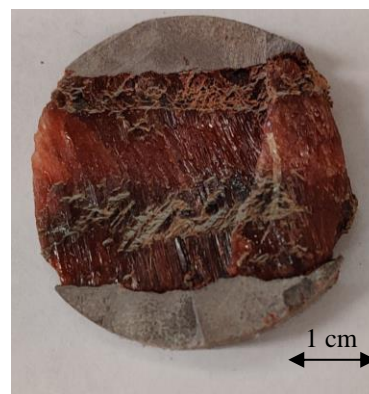


Fig. 2-6: Drill core sample of the Dana 1922 red halite sample.

2.5.4 Dana 3137 Halite

The Dana 3137 sample was collected in Pugwash, Nova Scotia, but no other information was recorded with regard to its location. The sample colour ranges from deep red-brown to light orange-pink in colour (see Fig. 2-7.) The original hand sample is coarsely crystalline, however the sub-sample exhibited finer grains along the fractured face.



Fig. 2-7: Sample of the Dana 3137 Pugwash halite sample

2.5.5 Dana 5477 Halite

The first of three hopper halite samples recovered from Trona, California, U.S.A. The Dana 5477 sample consists of two discrete shades of pink: one darker pink fraction from the top of the sample and a lighter pink fraction from below. The two pieces in Fig. 2-8 were adjacent before sub sampling, but there was too little sample to run the two fractions independently in analysis, so the two samples were ground together into a single powdered sample for subsequent analysis.

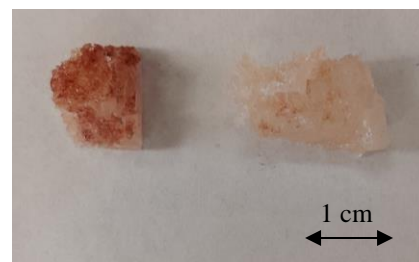


Fig. 2-8: Sub sample of the Dana 5477 pink hopper halite.

2.5.6 Dana 5490 Halite

The second of the three samples from Trona, California, U.S.A., this sample is a clean white hopper sample recovered from Searles Lake. Despite similar collection locations, this sample was nearly pure white halite, with the exception of a small brown fleck inside one of the hopper crystals (see Fig. 2-9).

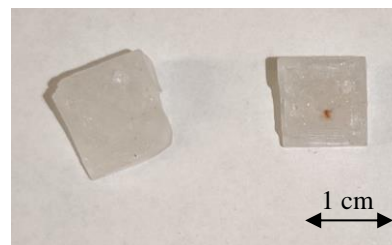


Fig. 2-9: Sub sample of the Dana 5490 white hopper halite sample.

2.5.7 South African Halite

This halite sample was produced by Marina Sea Salt, a salt producer in Port Elizabeth, South Africa. Salt mining companies in the area produce marine halite by actively evaporating sea water pumped in from the south Indian Ocean. This method consistently produces high purity halite with little variation in chemical content. The sample obtained was an unrefined modern marine evaporite; it was mostly clear with some clouding and a well-defined cubic crystal habit (see Fig. 2-10).

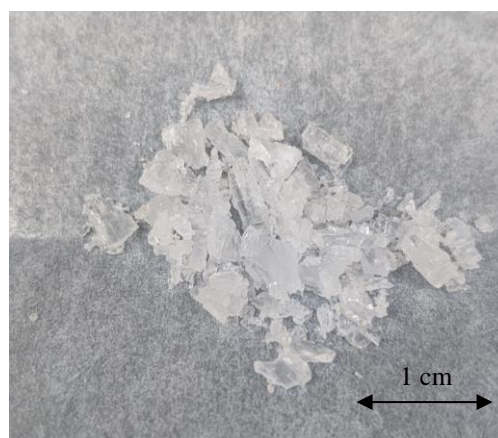


Fig. 2-10: Coarsely ground sample of the South African halite. No sample image was collected prior to processing.

2.5.8 Salton Sea Halite

The Salton Sea halite sample is a dark brown to orange coloured sample with small patches of clear halite sparsely distributed throughout. The cubic habit is clearly visible within the homogenous conglomerate which indicates that the precipitation of the sample was subaqueous and that rapid crystallization was encouraged by nucleating on the



Fig. 2-11: Parent and sub samples of the Salton Sea brown halite sample.

deposited substrate. Despite the dirty appearance of the halite, no other mineralization is apparent and the colouration appears to be from the halite and not from co-deposition of other minerals (such as sylvite). The sample was obtained from the Imperial Company in California, USA, which operates around the Salton Sea in southern California. This sample is part of the 2nd year mineralogy collection (see Fig. 2-11).

2.5.9 TronaCA Halite

This pink hopper halite specimen was subsampled from the 2nd year mineral teaching supply cabinet at the University of Western Ontario. Only the general location for the sample was kept as a matter of record, with the container maintaining that the sample was from Trona, California, U.S.A. This would place it in the same region as the hopper samples retrieved from the Searles Lake region in southern California, making it the third of the three samples from this region. The

sample is most likely a modern evaporite product from the highly saline inland lake, with the hopper morphology having resulted from rapid precipitation. The colour ranges from light pink to a deep pink with flecks of brown mineralization localized in small areas on the sample. The hopper structure is well defined, and any other colours or materials seen in the sample image (Fig. 2-12) are attributed to labelling for use in mineral identification lessons. This sample was donated to Western Earth Sciences by local collector Arnim Walter.



Fig. 2-12: Photo of the TronaCA pink hopper halite sample. The yellow colouration at the top of the left sample is remnants of putty used by the donor to mount the sample for display.

2.5.10 DeLaval Blue Halite

Originally given to Dr. Nigel Blamey by Virgil Lueth at the New Mexico Bureau of Geology and Mineral Resources, this sample of blue halite was recovered from the salt mining region of Carlsbad in New Mexico, USA. The sample exhibits a deep blue colour with some purple banding when viewed at certain angles. The colour is thought to be a product of vacant colour centres within the halite lattice caused by radiation exposure as opposed to a chemical contaminant that is common for most other coloured halite samples (see Fig.2-13). Literature sources that report on Carlsbad blue halite are likely referring to the same depositional region as the blue halite used in this study (Bickham, 2019; Minette, 1999).

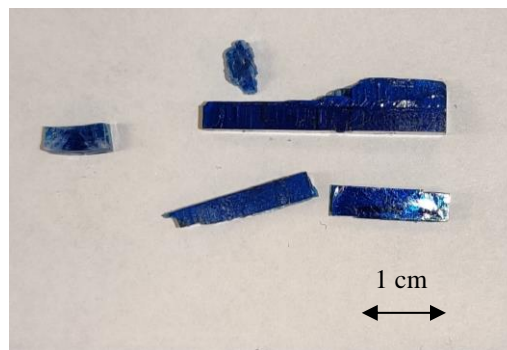


Fig. 2-13: Photo of the blue halite sample from New Mexico, U.S.A.

2.5.11 Bonaire Halite

The Bonaire halite sample was collected from the island of Bonaire in the southern Caribbean Sea which has historically been the location of commercial solar halite production due to the favourable conditions present on the island. The annual mean temperature and humidity are 27°C and 75%, respectively and the area

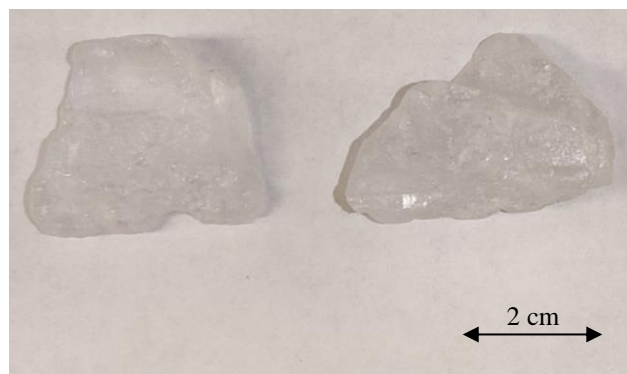


Fig. 2-14: Two mineral samples from the Bonaire halite set used for analysis in this research.

receives an average annual rainfall of approximately 50 cm. Halite crystallization ponds are allowed to naturally evaporate the inflowing seawater, facilitating the deposition of marine halite throughout the year (Handford, 1990). The samples provided were clean and transparent with no noticeable colouration or contaminants apart from minimal dark specks on the surface. The crystals did not exhibit the typical cubic crystal habit found in halite but are more massive in form with few cleavages observed on any of the individual samples (see Fig. 2-14).

2.5.12 Snowbird Quartz

The Snowbird quartz sample was collected from the Snowbird deposit near the northwestern Montana-Idaho border, U.S.A. This mineral deposit has been well documented by Michael Metz (1985) and Iain Samson (2004), particularly with respect to the fluid inclusion composition and mineralization conditions. Snowbird quartz samples have been found to contain saline liquid phases within the inclusions, with a combination of solid halite phases, vapour carbonic phases, or all three within a single fluid inclusion (Samson et al., 2004). Quartz mineralization in this area has been known to produce crystals in excess of 6 metres in diameter that are believed to have formed at temperatures between 400 and 500°C from highly saline fluids (between 33 and 50 wt.% NaCl equ.). The lithostatic pressure at the time of formation has been estimated at approximately 200 to 300 MPa based on fluid inclusion analysis and estimated depth of approximately 10 km. The samples used for this research were supplied by Dr. Nigel Blamey at the University of Western Ontario; three of the samples were between 1-3 cm in size and were of high optical clarity with few to no visible contaminants. The largest sample was approximately 5 cm across and showed evidence of weathering and did not exhibit the same clarity of the smaller samples shown in Fig. 2-15. Only the smaller samples were used for analysis to minimize the chance of contamination from other phases that may have been present either on the surface or within the weathered sample.



Fig. 2-15: Bulk sample and subsamples of quartz from the Snowbird region in New Mexico, U.S.A.

2.5.13 Hansonburg Fluorite

Perhaps the best documented of all the samples included in this work, the Hansonburg region has been well documented with a particular focus on fluid inclusions. The Hansonburg region lies within the greater Rio Grande Rift in central New Mexico, U.S.A. The Rio Grande Rift is a Mississippi Valley Type deposit where it is believed the fluorite was co-precipitated with barite and quartz within the region (Böhlke & Irwin, 1992; Hill et al., 2000; Norman et al., 1985). Although the mineralization of fluorite resulted in an array of colouration, the fluorite sample obtained for analysis is clear and colourless. The deposition of the fluorite is believed to have occurred at the temperatures of 125-210°C with a fluid salinity between 10% and 18% NaCl by mass. The pressure of mineralization is estimated to be an approximate total of 157 bars at a depth of 1.5 to 2 km from the surface. Fluid inclusion contents have been well documented by (Hill et al., 2000; Norman et al., 1985) across the Hansonburg region; this sample is best represented by the HSF-1 sample within Norman's research. As mentioned, the sample acquired is clear and colourless with a high optical clarity and no obvious cleavage or crystal habit in the bulk sample. The sample was already very coarsely crushed upon receipt, so the two largest pieces were selected for sample imaging (Fig. 2-16). The smaller pieces of fluorite were used for analysis, as their grain size was already small enough to begin analysis.

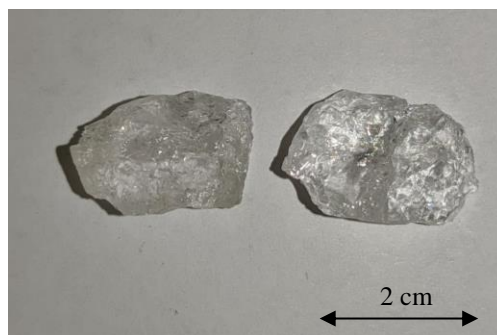


Fig. 2-16: Two of the largest and cleanest subsamples taken from the Hansonburg fluorite sample collection.

2.5.14 Gonzales Fluorite

The Gonzales fluorite sample was retrieved from the same geological area as the Hansonburg fluorite sample, offering a different system of mineralization within the greater MVT depositional region within the Rio Grande Rift (Hill et al., 2000). The Gonzales sample originated northwest from the area where the Hansonburg sample was collected, near the city of Socorro, New Mexico, U.S.A. The sample is of moderate clarity, with a slight brown tint and small flecks of brown distributed across the sample (Fig. 2-17). It is unclear whether the flecks are surficial or if they are present throughout the bulk of the mineral. Overall, the sample is roughly hexagonal in shape but with imperfect cleavage; mineral facies can be seen within the sample as a pattern of triangles that are visible when tilted under the light. But no clean cleavage is seen on the natural surface of the sample



Fig. 2-17: Hand sample of the Gonzales fluorite sample from New Mexico, U.S.A. Octahedral cleavage is visible.

2.6 Preparation of Hygroscopic Standards

Both NaCl and Na₂SO₄ laboratory standard samples were included in this research to verify the identity of minerals analyzed using NMR spectroscopy. Both mineral standards are prone to moisture absorption if left in open atmospheric conditions or outside of a moisture-controlled vessel, such as a desiccator. In order to ensure minimal moisture absorption for these samples, both halite (NaCl) and thenardite (Na₂SO₄) standards were left to desiccate in a laboratory oven at moderate to high temperatures to drive off water. The halite was left for 20 hours at 80°C while the thenardite was left for 4 days at 120°C. The initial mass of halite before drying was 10.2362 g. Over the span of the dehydration - 0.0435 g was lost for a final mass of 10.1927, equating to mass reduction of ~ -1%. An initial mass of 4.8323 g of thenardite was left to desiccate, resulting in a final mass of 4.8287 g. The total loss of water from the thenardite sample was -0.0036 g, corresponding to a mass loss of ~ -1%.

Due to the high affinity of thenardite to capture and retain moisture, a hydrated salt complex called mirabilite ($\text{Na}_2\text{SO}_4 \cdot 10 \text{H}_2\text{O}$) is quite common where thenardite naturally occurs but becomes unstable under humid conditions. At a laboratory temperature of 20°C , a relative humidity of 76.4% is required to begin forming mirabilite (Steiger & Asmussen, 2008). To rehydrate a sample of thenardite, a dry sample of 8.8657 g of Na_2SO_4 was added to a small beaker and left inside a closed beaker with deionized water adjacent to the sample (see Fig. 2-18). The sample was left for 4 days to rehydrate, gaining 0.5004 g of moisture for a final total mass

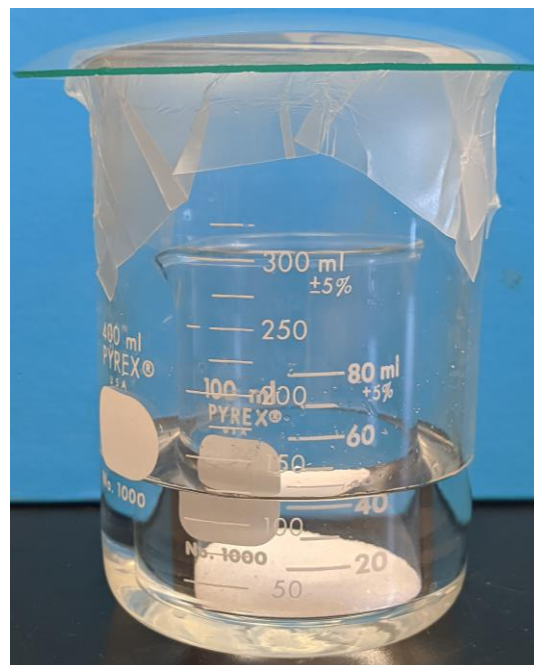


Fig. 2-18: Rehydration of Na_2SO_4 to $\text{Na}_2\text{SO}_4 \cdot 0.445 \text{H}_2\text{O}$ via ambient atmospheric absorption.

of 9.3661 g. This corresponds with a mass increase of approximately +5.6% (molar composition of $\text{Na}_2\text{SO}_4 \cdot 0.445 \text{H}_2\text{O}$) from the added moisture. The sample was left in the hydrator until taken for NMR analysis. The sample represents hydrated thenardite and can not be referred to as mirabilite as full hydration was not achieved.

2.7 References

Bickham, M. Z. (2019). *Chemical Analysis of Blue Halite* [ProQuest Dissertations Publishing]. <https://search.proquest.com/docview/2283382073?pq-origsite=primo>

Böhlke, J. K., & Irwin, J. J. (1992). Brine history indicated by argon, krypton, chlorine, bromine, and iodine analyses of fluid inclusions from the Mississippi Valley type lead-fluorite-barite deposits at Hansonburg, New Mexico. *Earth and Planetary Science Letters*, 110(1–4), 51–66. [https://doi.org/10.1016/0012-821X\(92\)90038-W](https://doi.org/10.1016/0012-821X(92)90038-W)

Handford, C. R. (1990). Halite depositional facies in a solar salt pond: A key to interpreting physical energy and water depth in ancient deposits? *Geology*, 18(8), 691–694.

Hill, G. T., Campbell, A. R., & Kyle, P. R. (2000). Geochemistry of southwestern New Mexico fluorite occurrences implications for precious metals exploration in fluorite-bearing systems. *Journal of Geochemical Exploration*, 68(1–2), 1–20.

[https://doi.org/10.1016/S0375-6742\(99\)00047-3](https://doi.org/10.1016/S0375-6742(99)00047-3)

Minette, J. W. (1999). The Carlsbad Halite Caves. *The Mineralogical Record*, 30(5), 369–369.

Norman, D. I., Ting, W., Putnam, B. R., & Smith, R. W. (1985). Mineralization of the Hansonburg Mississippi-Valley-Type Deposit, New Mexico: Insight From Composition of Gases in Fluid Inclusions. *The Canadian Mineralogist*, 17.

Samson, I. M., Wood, S. A., & Finucane, K. (2004). Fluid Inclusion Characteristics and Genesis of the Fluorite-Parasite Mineralization in the Snowbird Deposit, Montana. *Economic Geology*, 99(8), 1727–1744. <https://doi.org/10.2113/gsecongeo.99.8.1727>

Steiger, M., & Asmussen, S. (2008). Crystallization of sodium sulfate phases in porous materials: The phase diagram $\text{Na}_2\text{SO}_4\text{-H}_2\text{O}$ and the generation of stress. *Geochimica et Cosmochimica Acta*, 72(17), 4291–4306. <https://doi.org/10.1016/j.gca.2008.05.053>

Chapter 3

3 Analysis of Halite

This chapter summarizes the analysis of ten naturally-occurring geological halite samples and two lab-grade halite standards using ^{23}Na Magic Angle Spinning Solid State Nuclear Magnetic Resonance (MAS SS NMR) Spectroscopy, Inductively Coupled Plasma – Mass Spectrometry (ICP-MS), and powder X-ray Diffraction (pXRD). ICP-MS and pXRD are used to characterize and verify the chemical and mineral composition of the samples, respectively, while NMR spectroscopy is used to probe the samples for fluid inclusions and estimate their salinities in situ.

3.1 Introduction

The decision to use halite as the primary mineral for this research was made upon considering three major factors: availability, mineralogical simplicity, and abundance of fully saturated fluid inclusions. Halite is known to occur in a variety of colours including white, red, yellow, blue, orange, pink, violet, and grey, due to chemical contaminants or structural disruptions within the crystal lattice (*Minerals.Net: Halite*, 2021). It is also known to be a simple crystal structure composed solely of NaCl in an isometric face centred cubic arrangement (space group $F4/m-32/m$ or $Fm3m$), making analysis of the mineral and its inclusions as straightforward as possible (Aquilano et al., 2016; Melvin, 1991). Halite is well studied and well understood (Bloss, 1971; Smyth & Bish, 1988; Wyckoff, 1963), and the composition ensures that all fluids inside are at full saturation with NaCl, maximizing the chances of identifying sodium-rich fluids inclusions.

3.2 Geological Deposition of Halite

Halite is found primarily as the result of an evaporative deposition sequence from highly saturated, relatively isolated bodies of water where fluid exchange is minimal and evaporation can remove the water faster than it can be replenished (Schreiber & Tabakh, 2000). The fluid gradually reaches full saturation and forces crystallization from the mineral rich body of water. With the typical composition of seawater, this process begins

with the less readily soluble minerals such as carbonates and gypsum crystallizing before proceeding to halite mineralization (Fig. 3-1) (Melvin, 1991). The mineralization of magnesium and potassium salts occur towards the end of the evaporite series. This process generally creates homogenous stratigraphic layers if the system is stable over the course of the evaporation process.

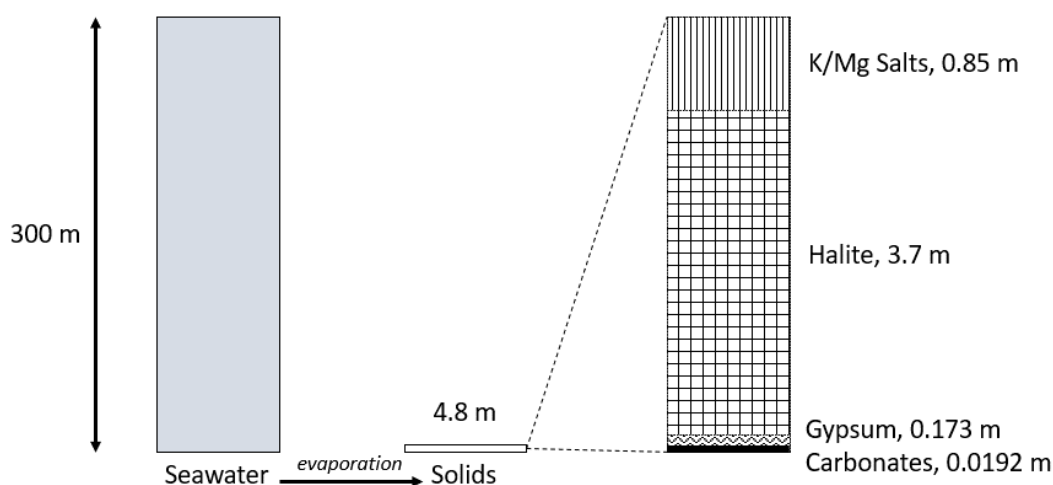


Fig. 3-1: Evaporite sequence and composition for a standard isolated basin of seawater. The thickness of each depositional layer (in metres) is proportional to the relative concentrations of each evaporite phase, as is the overall deposit thickness for the volume of seawater assuming uniform distribution. Adapted from Melvin (1991).

The ambient temperature, humidity, latitude, and local climate patterns can all play a part in determining the rate of deposition within an evaporite system. Generally, high temperature and low humidity will offer the ideal conditions for evaporating water from the system and leaving behind a highly concentrated brine.

3.2.1 Halite Formation

When appropriate conditions are achieved (high temperature/water loss, low humidity, and brine reaching maximum saturation) halite will precipitate and begin crystallizing and settling at the bottom of the basin in a process known as subaqueous cumulation (Fig. 3-2). This happens when halite crusts form at the water-air surface where a large

temperature differential or especially low humidity environment can promote surficial crystallization, a process that is common in early depositional stages and in shallow evaporite basins.

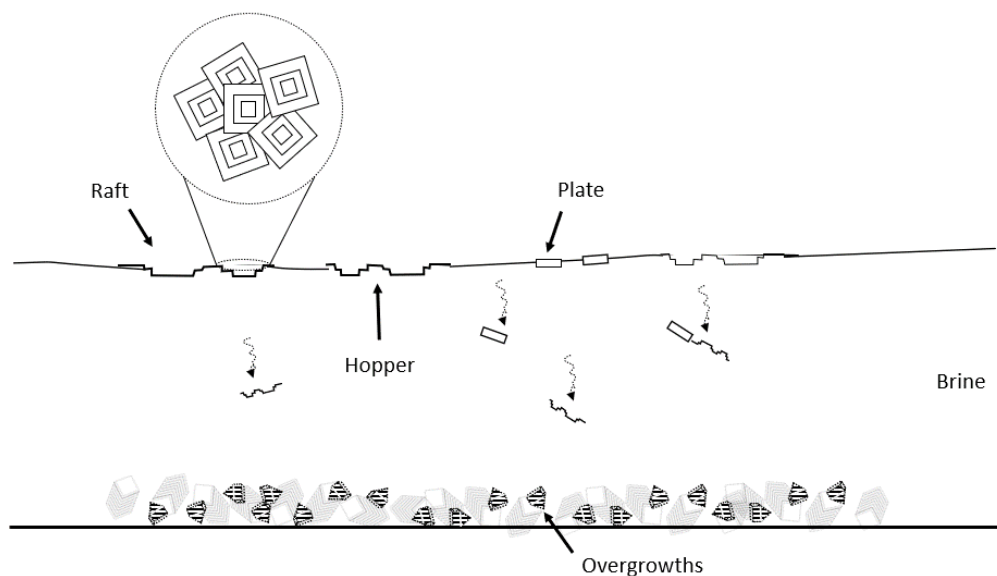


Fig. 3-2: Formation of crystalline halite in a saturated brine at the liquid/air boundary. Halite rafts are shown forming at the surface of the brine and sinking to the bottom of the basin. Adapted from (Melvin, 1991).

These halite ‘rafts’ will sink when disturbed or grow too large to maintain buoyancy. This crystallization mode predominantly produces hopper crystals which form concave structures with large surface areas that tend to remain afloat in the brine (Handford, 1990). Cubic halite tends to form predominantly at the bottom of a basin once there are halite crystals already present that can act as nucleation points and promote further crystallization. Throughout the process, orientation and temperature play a large role in determining the crystallization structure, as halite will preferentially crystallize at the vertices and edges of a crystal rather than along a crystal face (Warren, 2016). This subaqueous growth can produce all types of halite morphologies, such as cornets and chevrons (Fig. 3-3) that are common in hopper samples, as well as cubic halite crystals if deposition is slower. This is also where halite can become consolidated and cemented together into a solid depositional layer. This process is known as subaqueous bottom precipitation and is associated with more mature instances of halite deposition.

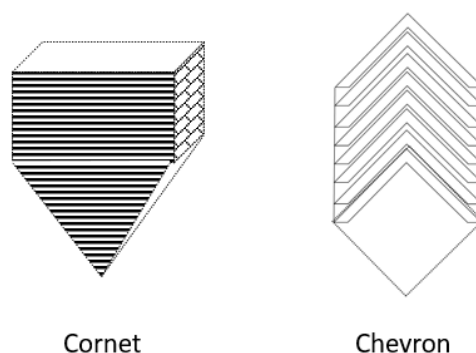


Fig. 3-3: Cornet-style (left) and Chevron-style (right) mineralization that is common for subaqueous halite deposition (Melvin, 1991).

Although less common, it is possible for halite to crystallize within a sedimentary matrix. This intrasediment deposition is much more restricted than free brine deposition as the host sediment needs to be displaced by the crystallizing halite, or fill vacancies already present, both of which place further restriction on growth direction and morphology of new halite deposition. Rapid growth of halite within sediments results in the sediment being incorporated into the halite. In an intrasediment growth environment, hopper and dendritic growth patterns are heavily favoured over cubic crystal growth (Melvin, 1991).

In some cases, highly concentrated brines can be produced from remobilization of evaporite minerals by hydrothermal activity, resulting in a more diverse assemblage of evaporites than is found in marine evaporite basins (Schreiber & Tabakh, 2000). This reworking of minerals selectively concentrates the more soluble evaporites within the brine, such as halite, thenardite, and natron (Smith, 1977) that are easily incorporated into the fluids. Searles Lake in California, U.S.A. is an example of this type of depositional system where non-marine evaporite deposits are collected and concentrated by hydrothermal redissolution and these deposits contain mineralogy that is distinctly non-marine. The deposits found in Searles Lake are heavily influenced by nearby hot spring activity, producing enriched metasomatic fluids forming an inland spring-fed series of

lakes that constitute a major source of sodium carbonates, potash, sodium sulphate, and borates eventually depositing in Searles Lake (Melvin, 1991; Smith, 1977). These types of unique evaporite systems are also seen in East Africa and Turkey and all of them share some history of chemical enrichment that is consistent with interactions involving products of local volcanism (Melvin, 1991).

3.3 Methods

All methods for analysis by NMR, pXRD, and ICP-MS were followed as outlined in detail within Chapter 2 (sections 1.2-1.4). A general overview is summarized below.

All 12 halite samples were coarsely ground to approximately 1-2 mm in grain size in preparation for analysis using ^{23}Na static and MAS NMR (Fig. 3-4).



Fig. 3-4: Coarsely ground halite samples for NMR analysis. Samples are as follows: Top: DC-711 Powdered, Salton Sea, 99.9% Reagent grade halite, coarsely ground Bonaire, fine grained Bonaire, DC-730, DeLaval Blue, DC-3137, DC-1922, and DC-711 coarsely ground. Bottom: TronaCA, DC-5490, DC-5477 (light pink), and DC-5477 (dark pink).

Samples were analyzed on a Varian Infinity Plus 400 spectrometer (γ $^{23}\text{Na} = 105.7$ MHz) at the J.B. Stothers NMR facility at The University of Western Ontario, Canada. All samples were referenced to a 1.0 M NaCl standard solution set to $\delta(^{23}\text{Na}) = 0.0$ ppm. Spin rates of 12 kHz were maintained for MAS analysis with a 55 kHz spectral width, a 1.7 μs (90°) pulse, a 54.5 ms acquisition time, and a 45 second recycle delay.

A calibration curve for NaCl was established by varying NaCl concentration in solution for comparison to the fluid peak in the natural halite samples. A dilution scheme was created from 0.25 M to 4 M + complete saturation as reported in Chapter 2. For the liquid calibration standards, 40 scans were acquired per sample using a 40 kHz spectral width, with a 3.4 μs 90° pulse, 175 ms acquisition time, and a three second recycle delay between scans. All data were collected at static ambient laboratory conditions.

The thenardite samples were both analyzed with similar parameters to the halite samples, maintaining the 1.0 M NaCl external standard with MAS spin rates of 12 kHz for thenardite and 11 kHz for hydrated thenardite. Acquisition time and recycle delay times were reduced to 12.8 ms and 10 seconds, respectively. A total of 200 acquisitions were collected for the thenardite sample while 344 acquisitions were collected for the hydrated sample.

Powder X-ray Diffraction was completed using a Rigaku DMAX powder diffractometer using a cobalt X-ray source ($\text{Co K}\alpha_1 \lambda = 1.78897 \text{ \AA}$) operated at a voltage of 40 kV and current of 35 mA. Each sample was finely powdered and analyzed for approximately one hour from 10° - 90° 2θ in 0.02° increments with a dwell time of one second/step. The Dana 5477 sample was allowed to run for nearly 14 hours as the dwell time was extended to 10 seconds/step. The DC-1922 sample was analyzed for 11 hours, with a scan range of 30 - 110° 2θ in 0.01° increments with a dwell time of 5 seconds per step.

ICP-MS analysis was completed by Activation Laboratories (ACTLabs) in Ancaster, Ontario. The samples were finely powdered for chemical analysis and delivered to the laboratory for distilled water solvation analysis.

3.4 Results

3.4.1 ^{23}Na NMR Results for Halite

Static NMR analysis produced a broad symmetrical signal spanning approximately 200 ppm (FWHM = 2500-2800 Hz) centred at approximately 7 ppm, with no evidence of any other peaks on the spectra (e.g. Fig. 3-5).

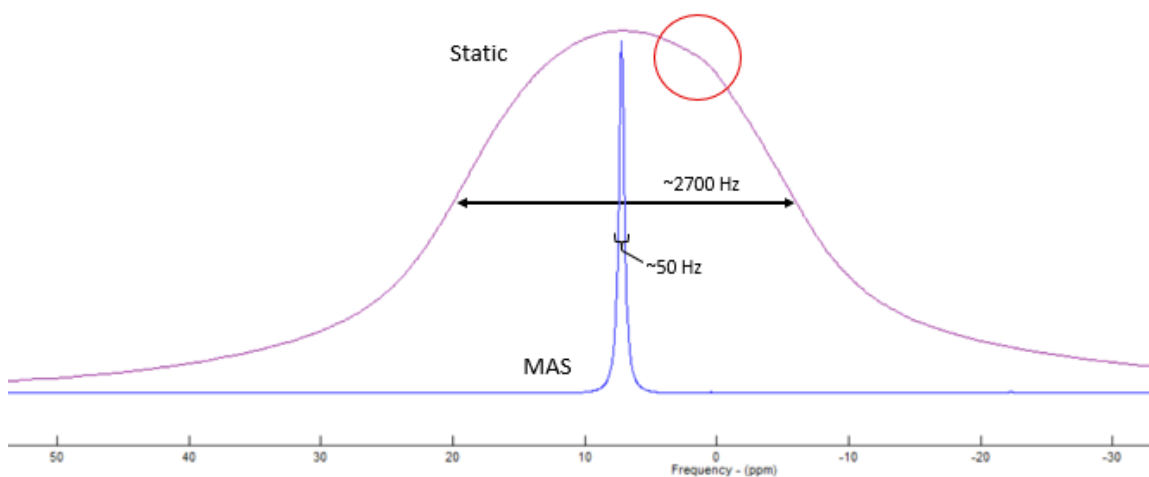


Fig. 3-5: Static ^{23}Na NMR spectrum of DC-5477 halite showing the characteristic peak shape and distribution seen in static (top) and MAS (bottom) halite analysis.

Initial analysis of the 99.9% reagent grade NaCl exhibited a small peak around 0 ppm, interpreted to be a fluid peak, in addition to the solid halite peak at 7 ppm, but upon secondary analysis following desiccation (80°C for 20 hours, 10.2362 g to 10.1927 g, - 0.042% by mass), the fluid peak was no longer present on the spectrum.

Each halite sample was also analyzed using MAS NMR with a spin rate of 12 kHz, which produced much narrower peaks (e.g. FWHM = 50-60 Hz), and, in the case of some samples, new peaks became resolved which had been previously obscured under the broad main peak. Samples that exhibited these newly resolved peaks include Dana 5477 (Fig. 3-6), Dana 5490 (Fig. 3-7), and TronaCA halite (Fig. 3-7).

Table 3-1: Summary of data collected for 12 Halite samples.

Sample	Location	Sample Colour	Deposition Type	Chemical Shift Halite Peak (static, δ ppm)	Chemical Shift Halite Peak (MAS, δ ppm)	Chemical Shift Liquid Peak (MAS, δ ppm)	Contaminant Minerals Phases (pXRD)	Elevated Element Concentrations (>500 ppm)
Bonaire	Bonaire, Neth. Antilles	Clear, colourless	Modern Marine	7.187	7.196	--	None	None
Dana 1922	Middlesex Ontario	Red	Hydrothermal Vein	7.060	7.212	--	None	None
Dana 711	Unknown	Smokey grey, clear	Unknown	6.993	7.212	--	Giniite, Anhydrite	Ca (10800 ppm)
Dana 730	Unknown	Orange	Unknown	7.187	N/A	N/A	Anhydrite	Ca (3860 ppm)
Dana 3137	Puwash, Nova Scotia	Brown	Ancient Marine	7.187	7.196	--	Anhydrite, Quartz	Ca (2030 ppm)
Dana 5477	Trona, California	Light/Dark Pink	Hydrothermal Hopper	6.993	7.212	0.413	Thenardite	K (1960 ppm)
Dana 5490	Searles Lake, California	White, colourless	Hydrothermal Hopper	7.187	7.212	0.445	None	K (884 ppm)
DeLaval Blue	Carlsbad, New Mexico	Deep blue, violet	Ancient Marine	7.187	7.196	--	None	None
99.9% Reagent	N/A	white, colourless	Laboratory Refined	N/A	7.256	0.282	None	None
Salton Sea	Salton Sea, California	Orange	Modern Inland	7.314	7.212	--	None	Pb (525 ppm)
TronaCA	Trona, California	Light Pink	Hydrothermal Hopper	6.806	7.196	0.635	Trona, Natron	K (1920 ppm)
South African	Port Elizabeth, South Africa	White, colourless	Modern Marine	N/A	7.225	0.298	None	None

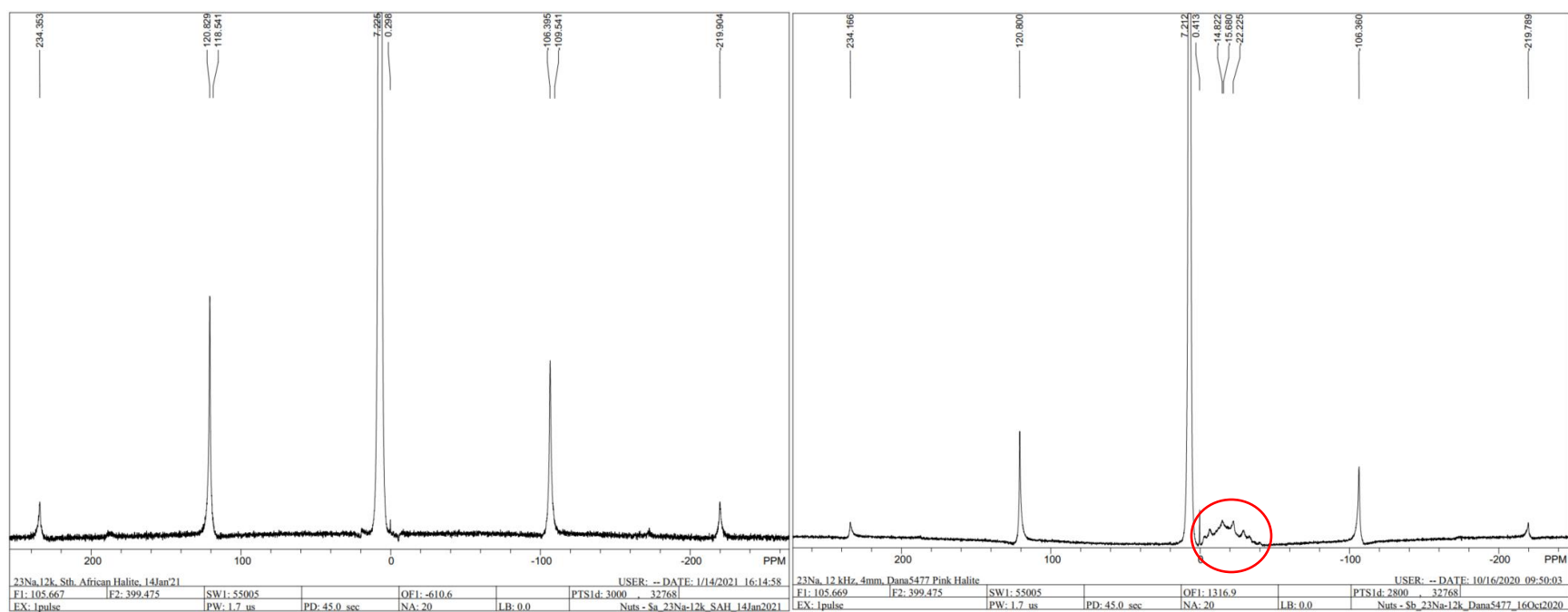


Fig. 3-6: ^{23}Na MAS NMR spectrum of South African (left) and Dana 5477 (right) halite samples. Both samples exhibit a major signal around 7 ppm interpreted to be solid halite, and a smaller peak near 0 ppm, interpreted to be fluid. In addition, the Dana 5477 sample exhibits a series of peaks to higher frequency of the solid and fluid signals, between 0 ppm and -40 ppm (circled) that do not appear on any other sample spectra. This signal is attributed to the presence of thenardite within the sample (see Section 3.5.1).

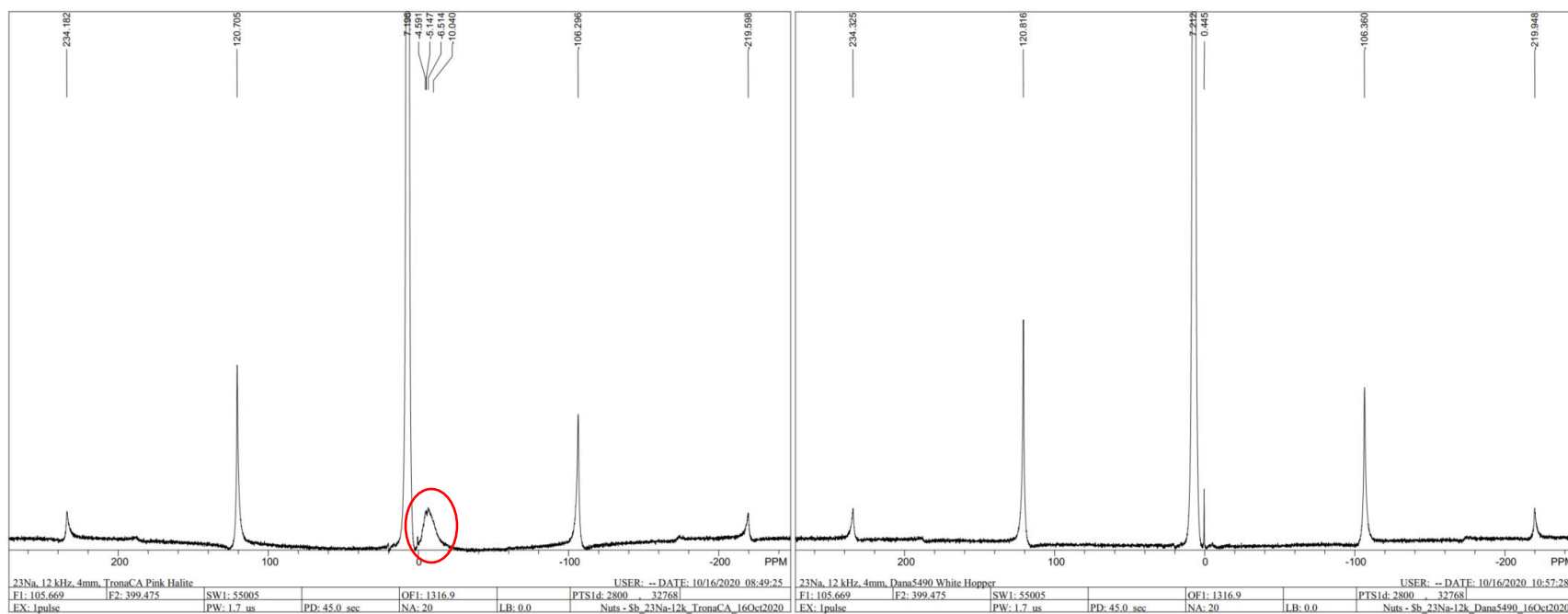


Fig. 3-7: ^{23}Na MAS NMR of TronaCA (left) and Dana 5490 (right) halite samples. Both samples exhibit both solid NaCl and fluid peaks near 7 ppm and 0 ppm, respectively. The TronaCA sample also displays an additional broad signal between 0 ppm and -20 ppm (circled).

In all cases, the newly resolved and unidentified peaks appeared at a lower δ_{ppm} than the halite and fluid peaks. The TronaCA sample (Fig. 3-7) produced a broad signal between 0 and -20 ppm that appears to have two discrete peaks; this is the only sample that produced a peak in this chemical shift region. Dana 5477 exhibited a unique grouping of 6 or 7 peaks between 0 and -40 ppm in addition to the sharp peak around 0 ppm (Fig. 3-6). These can be fitted to thenardite using quadrupolar lineshapes (see discussion section 3.5.1). The Dana 1922 sample initially produced a narrow signal at 12.993 ppm, but this appears to have been an error in processing. Subsequent attempts to reproduce the peak were unsuccessful. The original spectrum with the aberrant signal can be found in Appendix B, this spectrum was not used for analytical interpretation.

3.4.2 pXRD Results for Halite

Diffraction patterns for Dana 711 and Dana 730 are shown in Fig. 3-8. The halite samples were, as expected, predominantly pure halite with a few notable exceptions. Anhydrite (CaSO_4) was detected in the Dana 711 and Dana 730 sample with the former also showing some evidence of giniite in the diffraction pattern. Giniite ($\text{Fe}_5(\text{PO}_4)_4(\text{OH})_3 \cdot 2\text{H}_2\text{O}$) is an iron phosphate mineral whose presence may account for the smokey grey and black colouration found within the Dana 711, although the process by which it could have been included is uncertain. Most notably, the Dana 5477 sample exhibited a very strong match for thenardite as a discrete mineral phase; thenardite is a sodium sulphate mineral (Na_2SO_4) that is normally deposited from saturated brine under warm conditions alongside its hydrated phase, mirabilite ($\text{Na}_2\text{SO}_4 \cdot 10 \text{H}_2\text{O}$) which mineralizes at cooler temperatures (Herrero et al., 2015). Either or both of these phases may be attributable to the unusual signal in the NMR spectrum of Dana 5477. Thenardite has been reported in the saline lake system in Trona, California, which is the location of this hopper crystal.

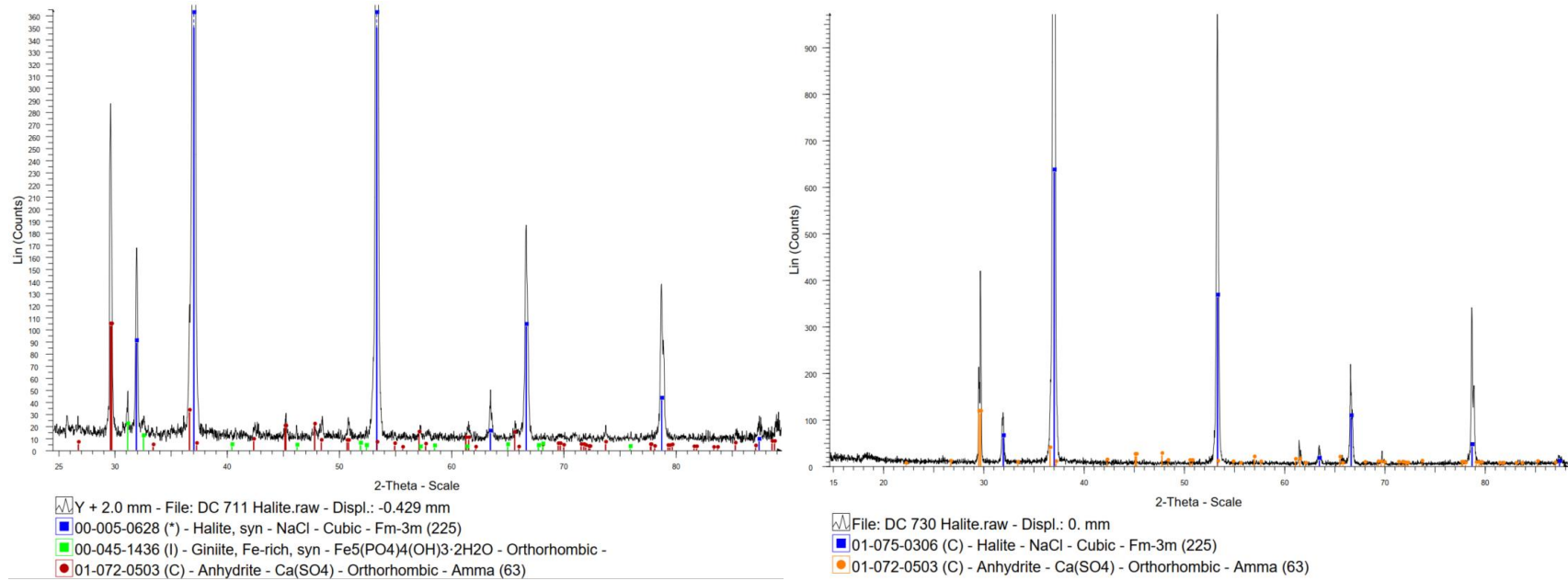


Fig. 3-8: Powder X-ray Diffraction patterns for Dana 711 (left) and Dana 730 (right) halite samples, exhibiting trace amounts of giniite/anhydrite and anhydrate, respectively.

The TronaCA sample had partial matches to natron and trona, but the match was not definitive. The rest of the samples primarily exhibited characteristic halite peaks and only required minimal sample offset correction to properly match the patterns to mineral cards. Some samples had small diffraction peaks well below the intensity of the halite peaks. In these cases, definitive mineral identification was very difficult as no satisfactory matches were found for the diffraction patterns. They are likely attributable to very minor trace amounts of mineral contamination.

3.4.3 ICP-MS Results for Halite

Based on the elemental analysis provided by the ICP-MS data, the halite samples showed no evidence of any major contamination. All samples, including reagent grade halite, showed low levels of magnesium, potassium, and calcium, but beyond these exceptions there were no notably elevated levels of any other elements. Minute amounts of aluminum, bromine, iron, and in some cases, barium and strontium were observed variably throughout the sample set, with an average of a few hundred parts per billion but never in excess of 200 ppm. This does not rule out the possibility of other minerals being present within the sample, however, it does indicate that low levels of contamination impart a negligible impact on the NMR analysis of halite. It can be stated with a fairly high degree of confidence that the fluid peak chemical shift is not influenced by the presence of any particular chemical contaminant. From the ICP-MS data, it cannot be determined whether the elemental components were present within the fluid inclusions or within the halite crystal, but regardless, neither the solid-state nor the liquid-state NaCl signals show any evidence of being influenced by chemical contaminants.

3.5 Discussion of Halite Results

The halite results will be discussed by method of analysis, generalized findings will be consolidated following the individual discussions.

3.5.1 ^{23}Na NMR Discussion

The NMR results, although generally consistent between NMR spectra, provide some very useful information for understanding how halite and fluid inclusions present themselves in NMR analysis. Overall, the solid signal for natural and synthetic halite samples is highly consistent regardless of colour, macroscopic morphology, or method of crystallization. The peak present at ~ 7.2 ppm was consistent between samples and is diagnostic of a solid halite signal when compared to the solid-state laboratory grade samples. A very narrow signal was detected in Dana 5477, Dana 5490, TronaCA, and the South African halite samples around 0.5 ppm, which is squarely in the region of NaCl liquid signals observed when building the NaCl calibration curve for salinities between 0.25 M and full saturation. Based on the relatively low intensity of the signal and narrow lineshape, this peak can be attributed to a fluid signal from within the solid halite samples with a high degree of confidence.

By using the calibration curve outlined in the methods chapter above, a linear relationship was established to estimate the salinity of these fluid signals given their experimental chemical shifts. Based on the liquid standard solutions, the experimental chemical shift (ppm) was plotted against the salinity (moles NaCl/L) to produce the linear relationship $y=0.1001x - 0.1113$ ($R^2 = 0.9919$). Using this relationship, the salinity of the fluid inclusion signal within each natural halite sample could be interpolated based on its chemical shift (Fig. 3-9).

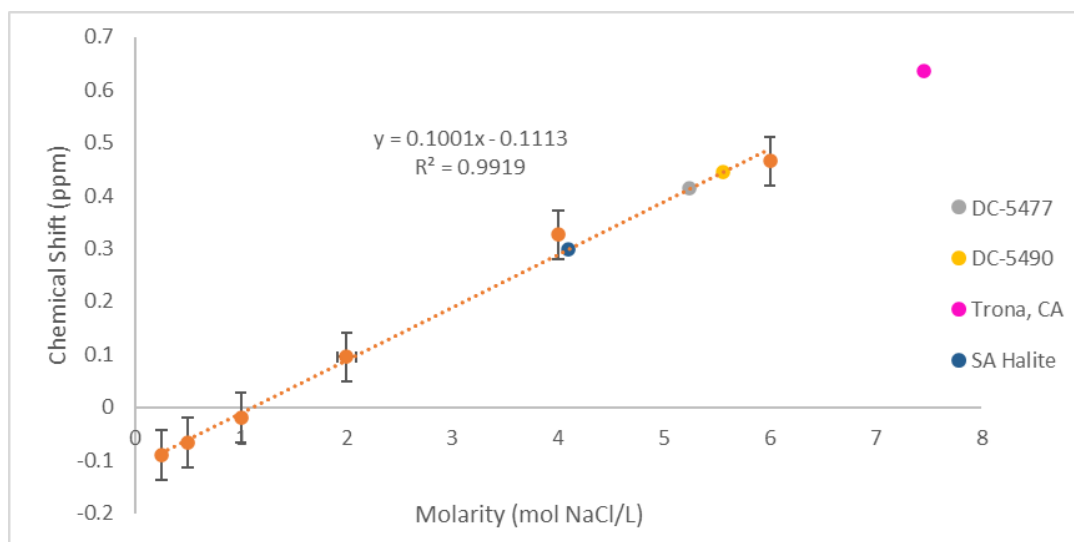


Fig. 3-9: Calibration curve of the NaCl fluid standards from 0.25 M to 6.16 M with halite samples plotted with their estimated salinity.

Because these fluid inclusions are hosted by pure halite, the fluid inside is assumed to be fully saturated and at equilibrium with the surface of the fluid inclusion. With a direct comparison to the calibration standards, the salinity estimated by the linear equation compares quite favourably. All halite samples that exhibited a fluid signal plotted at a concentration of over 5 M NaCl, with the exception of the South African halite sample (and the lab standard before dehydration) which plotted near 4 M NaCl. The sample from Trona, CA appears to be beyond the saturation point expected of halite at ambient conditions if the chemical shift is exclusively attributed to concentration of NaCl within the inclusions. This could be because of the presence of another phase, still unidentified or solvated contaminants causing greater deshielding of the Na in solution. No definitive mineral phases could be identified through pXRD and further investigation is required to determine the cause of such an extreme chemical shift.

One of the unexpected outcomes of this research was an extra signal between 0 ppm and -40 ppm in the Dana 5477 halite sample. In addition to a narrow fluid peak in the spectrum, a group of peaks were identified that could not be attributed to crystalline halite. This extra phase was first seen using ^{23}Na NMR spectroscopy and its identification was made by pXRD analysis, which provided a definitive match to thenardite (Na_2SO_4)

(See XRD section below). This phase contains Na which is strong evidence to suggest that these NMR peaks could be a product of solid thenardite (Na_2SO_4) within the halite sample. Thenardite is a known evaporite product but it is not commonly seen in marine evaporite depositional sequences alongside halite. However, it has been reported in saline lakes in Trona, California (Smith, 1977). To confirm that the NMR signal seen in the Dana 5477 sample was attributable to thenardite, a sample of both anhydrous thenardite and a rehydrated sample, were submitted for NMR analysis using the same method as was used for the halite samples.

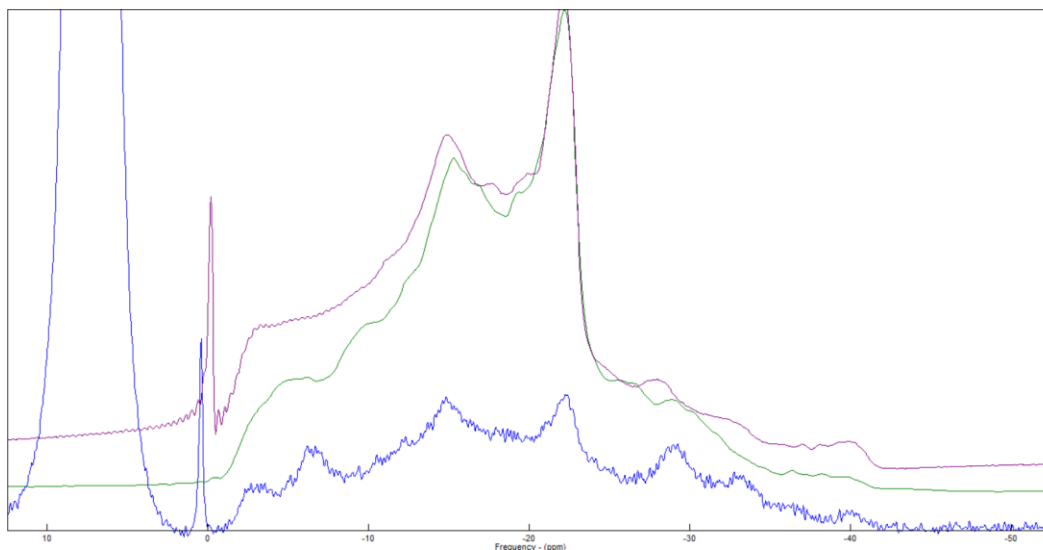


Fig. 3-10: Exaggerated ^{23}Na MAS NMR stack plot of the Dana 5477 halite sample (bottom) versus the thenardite and hydrated thenardite spectra (middle and top, respectively).

This proved to be successful as the resulting spectra from the thenardite samples both produced signals that very closely resembled the peak pattern seen in the Dana 5477 spectrum (Fig. 3-10). The breadth of the signal is approximately 40 ppm (FWHM = \sim 1000 Hz), from 0 – -40 ppm with the two main peaks falling at the same chemical shift as those seen in the halite sample. It appears that the other peaks within the Dana 5477 sample may be a product of quadrupolar line broadening, however the thenardite samples do not show distinct peaks in the same fashion. It is possible that there is thenardite within the Dana 5477 sample creating a compound pattern that is representative of

partially hydrated mineral within the halite. It should also be noted that the fluid signal seen in the hydrated sample is not at the same chemical shift as solvated NaCl signal seen in the halite samples. This indicates that there is likely a fluid component within this sample, perhaps due to uncoordinated H₂O adsorbed on to the sample and causing a liquid signal. The chemical shift is to lower frequency and therefore more shielded than the sodium ions seen in pure NaCl solutions. This may be a result of the sodium ions complexing with molecular sulphates that have been incorporated into solution within the bulk sample, giving further reason to be cautious when attempting to measure NaCl salinity within fluid inclusions using ²³Na NMR. If the chemical shift of the fluid signal in the hydrated thenardite was interpreted as halite in solution, the resulting concentration would be estimated as a negative molarity (approximately -1.1 M NaCl based on the calibration curve equation).

TronaCA had a number of peaks that were only partial matches in the powder X-ray Diffraction (pXRD) diffraction pattern as well as a broad peak on the ²³Na NMR spectrum that couldn't be identified. Since the trace mineral was present in the ²³Na NMR spectrum, we know that at least one mineral contaminant is associated with Na as a main component or as a mineral contaminant/substitution. The minerals trona and natron are both partial matches for the extra peaks (Fig. 3-11)

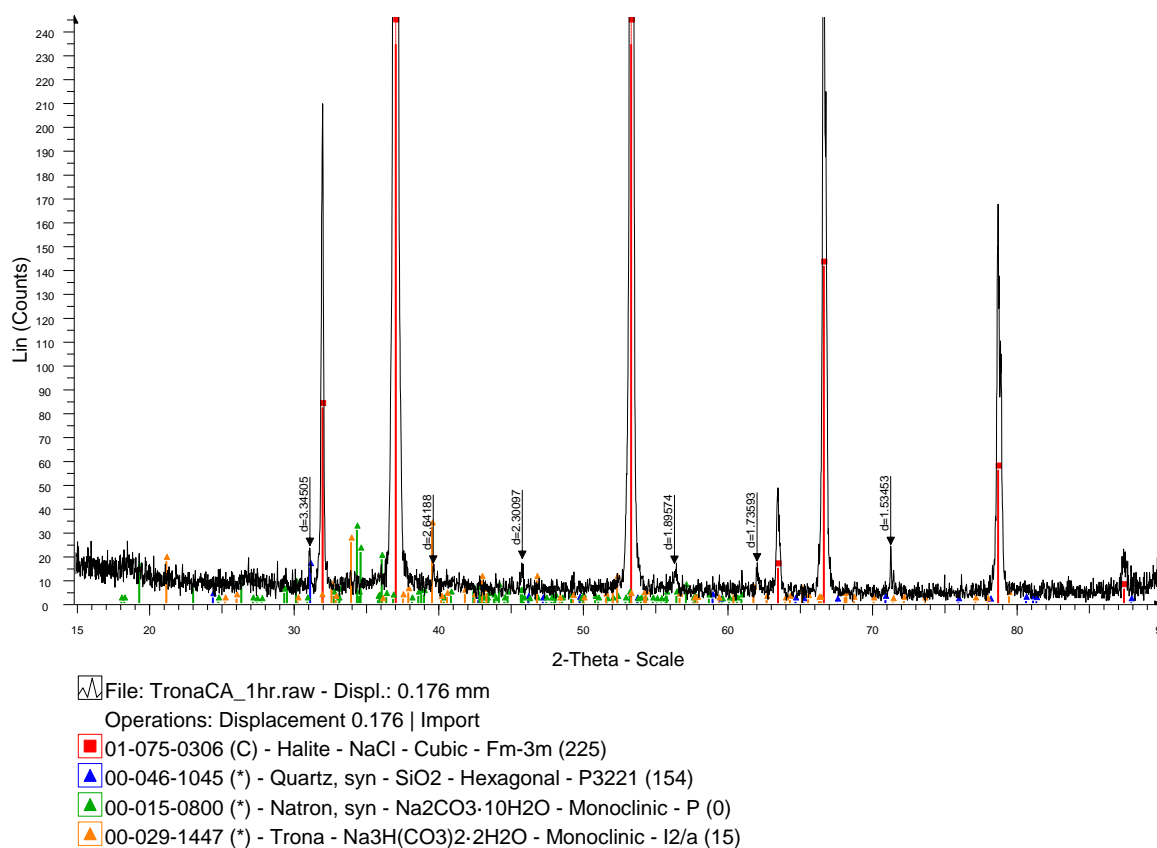


Fig. 3-11: pXRD pattern for TronaCA with partial matches for quartz, trona and natron. The latter two sodium carbonates could contribute to the NMR spectrum.

Trona ($\text{Na}_3\text{H}(\text{CO}_3)_2 \cdot 2\text{H}_2\text{O}$) and natron ($\text{Na}_2\text{CO}_3 \cdot 10\text{H}_2\text{O}$) are both good candidates for this trace mineral because each matches several XRD peaks and we know the extra phase must contain some sodium in its mineral composition to be visible in the NMR Spectrum. The comparatively low proportions may explain the low NMR intensity; because the pXRD intensity is low, a longer scan time could provide more definitive results. Unfortunately, there are no readily available standard ^{23}Na NMR spectra of natron or trona available for comparison. Research by Tambelli et al., (2006) studied alkali-silica reaction (ASR) gels with varying levels of Na_2O (3.2-6.1 mol%) from which the researchers tentatively identified trona mineralization. The published ^{23}Na NMR spectra for their sample set provide a close match to the signal observed in the TronaCA sample, which offers stronger support for the interpretation of this NMR signal as trona (Fig. 3-

12). A mineralogically pure sample of trona studied using ^{23}Na NMR could quickly confirm the identity of these peaks.

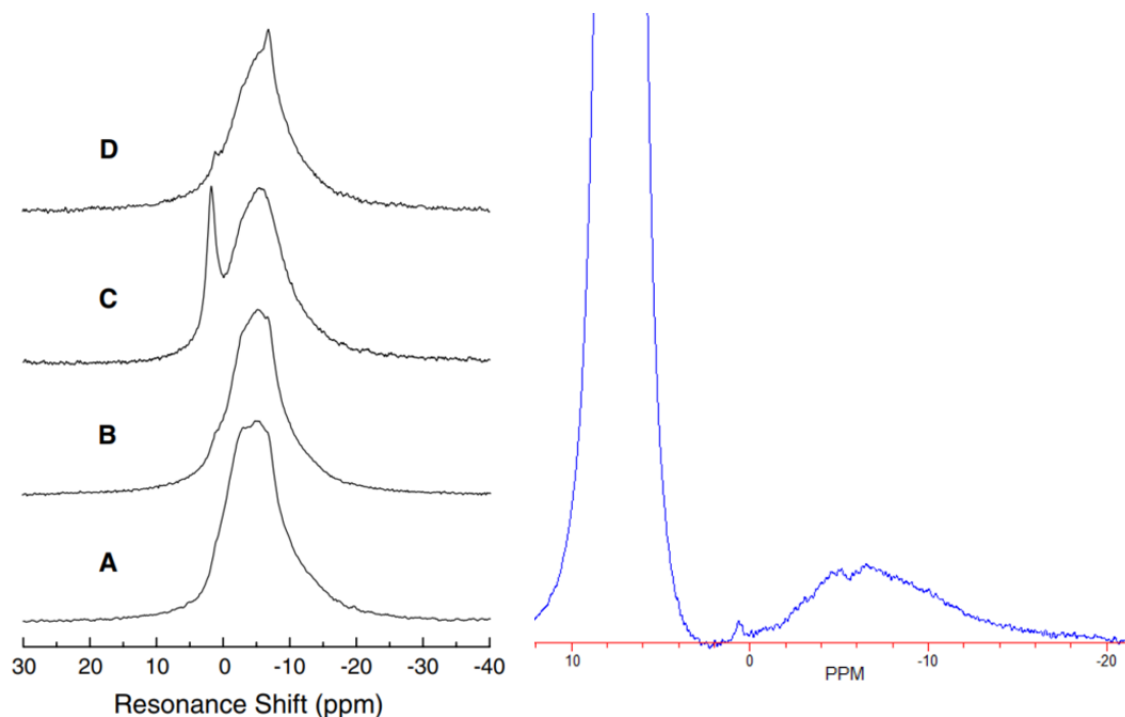


Fig. 3-12: ^{23}Na MAS NMR spectra for the ASR gel sample suite analyzed by Tambelli et al., (2006) (left) in comparison to the signal observed in the TronaCA sample in this research (right).

The town of Trona, California (near where this sample was collected) was so named for its abundance of trona in the adjacent Searles Lake lakebed. It was established as a mining town that is still inhabited today, although mining activity has decreased substantially since its establishment in 1914 (Orr, 2021). It is not surprising that the halite sample from Trona, CA contained traces of mineralized trona.

3.5.2 ICP-MS Discussion

The ICP-MS analysis of the halite was intended to function as supplementary data to identify any trace elements that may have had an influence on the NMR data collected, as well as to gauge the purity of the halite samples. Despite the wide variety across the

samples with respect to provenance, morphology, and colour there was very little variation within the data set in terms of bulk elemental composition. As outlined in the Results section (3.4.3) and Appendix A, there were no instances of any significantly elevated concentrations of any element, with the laboratory grade halite samples (high purity) NaCl producing comparable levels of trace elements such as Mg, Ca, and K. Because the halite standards reported a maximum upper concentration of trace elements at 500 ppm, this value was used as the threshold for discriminating elevated concentrations of common trace elements found in the natural halite samples.

The TronaCA sample reported nearly fourfold the amount of potassium as the laboratory standards with a concentration of 1920 ppm. The TronaCA sample was the only halite sample to fall outside of the calibration curve limits, however when comparing this elevated level of potassium to other halite samples, it can be confidently concluded that the concentration of potassium was not a factor in the increased chemical shift. Elevated levels of potassium can also be seen in DC-5490 (884 ppm), and DC-5477 (1960 ppm) which conveniently allows for a reference to samples with both a greater and lower concentration of potassium, both of which had chemical shifts within the ~0.5 ppm range of the calibration curve. Several samples exhibited elevated levels of Calcium including DC-711 (10800 ppm), DC-730 (3860 ppm), and DC-3137 (2030 ppm), however these elevated levels of Calcium failed to have any associated influence on the NMR signal of any of these samples. Lead was present in only one of the samples (Salton Sea Halite, 525 ppm), and all other trace elements detected across the suite of halite samples were determined to be negligible in terms of influence on NMR spectroscopic analysis. It is noteworthy that the suite of elements analyzed does not include Sulphur (which is too light an element for analysis), so the potential effect of SO₄ can not be ruled out for the TronaCA sample.

Overall, the halite samples showed a very high level of purity, which verified that the concentration of a trace element does not produce any appreciable effects on the sample's NMR spectrum.

Due to the destructive nature of ICP-MS analysis, any fluid that may have been trapped within the halite samples was liberated upon grinding and incorporated into the bulk sample as moisture was driven off. As such, these techniques offer no direct analysis for the composition of the fluid inclusions.

3.5.3 pXRD Discussion

Powder X-Ray Diffraction proved to be very useful in both confirming the chemical purity of the natural halite samples, as well as assisting in identifying extra phases in the NMR spectra that could not be easily identified. Similar to the results produced by NMR spectroscopy, the halite samples were generally found to be predominantly halite with only small traces of contaminant mineral phases in a few of the samples.

The most common contaminant mineral phase identified in the halite sample suite was anhydrite (CaSO_4) which was present in Dana 711, Dana 730, and Dana 3137 (See Fig. 3-8). This finding was also supported by the elevated levels of calcium that were reported in the ICP-MS analysis discussed above. These three samples were the only halite samples to exhibit calcium concentrations greater than 500 ppm, indicating that this increased concentration of calcium is likely due to the presence of anhydrite within the sample. Anhydrite is a common and expected product of evaporite sequences and is usually one of the first minerals to crystallize from a concentrated brine as gypsum before dehydrating to anhydrate under high-salinity conditions (Schreiber & Tabakh, 2000). In solution, the anhydrite would be hydrated to gypsum which exhibits a much lower solubility than halite (maximum saturation range is 0.0147-0.0182 M), prompting rapid deposition from highly concentrated fluids at ambient temperatures (Lebedev & Kosorukov, 2017). Although anhydrite is not syndepositional with halite, the very close relationship between the two minerals leads to a reasonably high probability of co-deposition as the deposits are reworked by multiple instances of fresh water influx and subsequent re-deposition as evaporation reconcentrates the brine (Schreiber & Tabakh, 2000).

Dana 711 also appears to contain a small additional phase which is a reasonable XRD match to giniite, an iron phosphate mineral $((\text{Fe}^{2+}\text{Fe}^{3+})_4(\text{PO}_4)_3(\text{OH})_5 \cdot 2\text{H}_2\text{O})$, (see Fig. 3-

8) although the powder pattern alone is not confirmation of this phase being present. No elevated levels of iron were reported through ICP-MS analysis and the reference pattern is not a perfect match, though it does align well with higher intensity peaks that few other reference mineral cards could match.

Giniite does present as dark grey to nearly black in colour and could explain the smokey grey colouration observed in the halite hand sample, however colouration of a mineral is not analytically diagnostic. The more intensely coloured areas of the Dana 711 sample appeared vitreous and angular/tabular, lending credence to the classification as giniite since these are not typical attributes for halite mineralization (Section 2.5.1 Fig. 2-4). It is uncertain how these two minerals may have hypothetically been co-deposited, but it is likely that the halite would have mineralized after the giniite was deposited. As there is no data on the provenance of Dana 711, it is difficult to establish what geological environment or series of events produced this assemblage. Further analysis would be required to make a definitive mineral identification. Extended pXRD scans may be sufficient to definitively assign the diffraction pattern to giniite. Dana 3137 also showed trace amounts of anhydrite and quartz (Fig. 3-13).

As mentioned in the ^{23}Na NMR discussion section, the most notable finding by pXRD analysis was the presence of thenardite within the Dana 5477 halite sample. The match to thenardite was excellent and accounted for all notable peaks that could not be attributed to the halite diffraction pattern. The sample was analyzed for approximately 14 hours to improve the S/N ratio and more definitively identify peaks against the background signal. This decision was made on the basis of the NMR analysis suggesting the presence of another sodium-containing mineral phase that could not be identified by NMR spectroscopy alone. Based on the low amount of signal produced in the NMR analysis of Dana 5477, it was reasoned that the mineral phase was very low in concentration and would require a longer dwell time while analyzing the sample via pXRD to produce a high enough intensity for the mineral phase to be identified. This proved to be successful as the identification of thenardite could be made definitively, indicating that the broad ^{23}Na signal at low frequency was most likely due to the presence of the sodium within the

sodium sulphate.

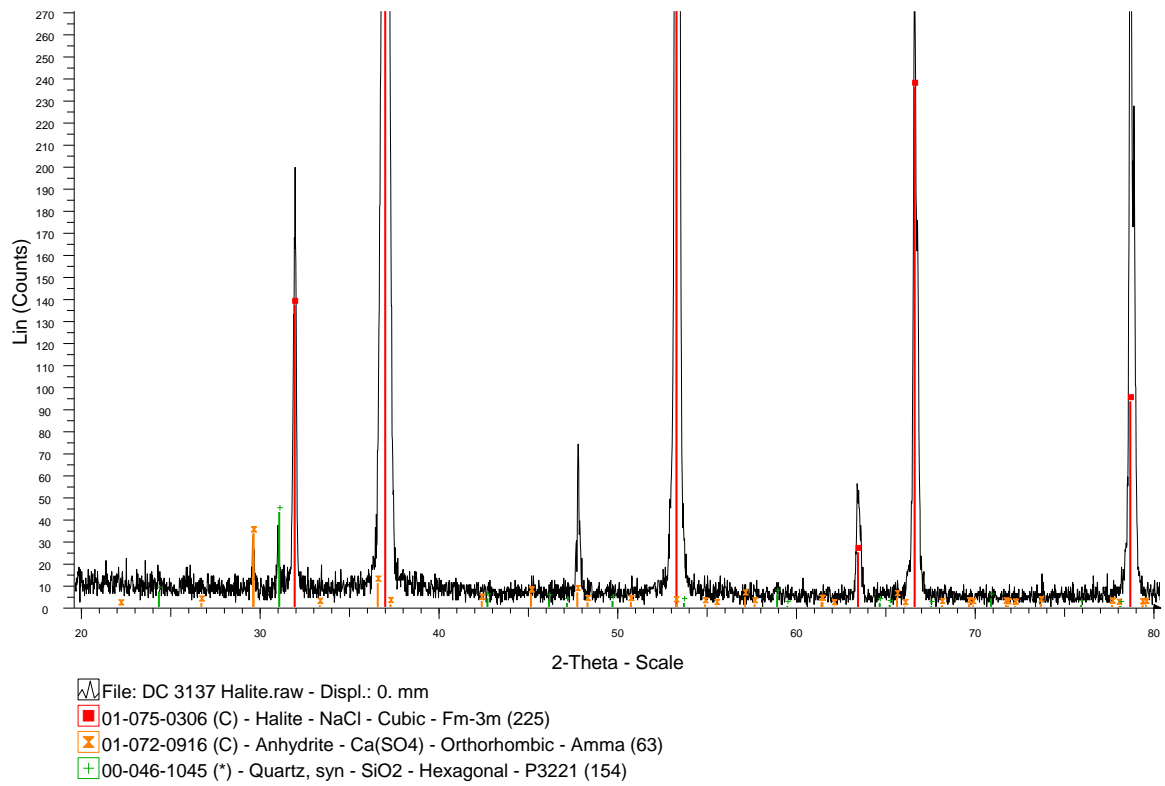


Fig. 3-13: Powder X-ray Diffraction pattern for Dana-3137 halite, zoomed in to show peak mineral assignments.

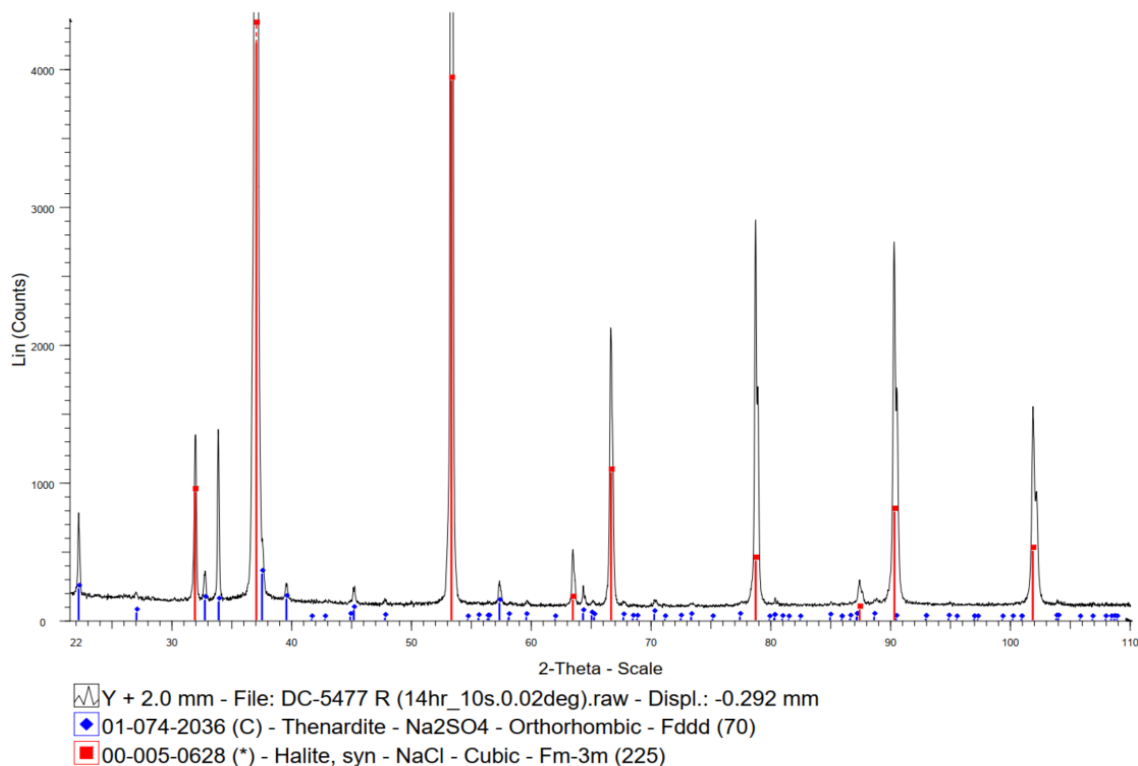


Fig. 3-14: Powder X-ray Diffraction pattern for Dana 5477 halite, with a strong peak match for traces of thenardite (Na₂SO₄).

The presence of thenardite, although unexpected, is not unheard of for evaporite deposits that result from spring-fed evaporite basins. In fact Searles Lake, the location of recovery for the Dana 5477 sample, is known as a major source of naturally occurring mirabilite which can be economically dehydrated to commercially produce Na₂SO₄ (Melvin, 1991). The Searles Lake location is underlain with two discrete crystalline bodies below the modern alkaline brine lake that exists today. The deposition of these crystal strata is attributed to the activity of thermal springs mobilizing evaporites in the late Quaternary period before depositing them on the eastern front of the Sierra Nevada region. Thenardite is readily soluble in water, and through constant reworking of the evaporites in the highly saline brines found in Searles Lake, it is likely that the thenardite was introduced from Long Valley caldera to the north and incorporated into the lake system to be deposited during extended periods of evaporation.

What is notable about the detection of thenardite using ^{23}Na SS NMR spectroscopy is that the total time for analysis of the sample was just over an hour (1 hour 14 minutes), and although the signal was significantly lower in intensity compared to the halite signal, it was still readily identifiable with reference to the standard spectrum collected from the pure thenardite sample (see Fig. 3.9). The maximum intensity for the thenardite peak in the pXRD pattern is approximately 1400 counts after 14 hours of analysis; since pXRD counts scale linearly, a 1-hour scan would produce approximately 100 counts, which would leave many of the smaller peaks lost in the baseline noise. It is possible that the detection of thenardite may not have been certain without the increased dwell time justified by the ^{23}Na NMR spectrum. Confirmation of thenardite by pattern matching of the ^{23}Na NMR spectra (Fig. 3-10) demonstrates the benefit of documenting the characteristic spectra of a variety of reference compounds such as Na_2SO_4 , for reference purposes, similar to the robust archives of standardized ^1H and ^{13}C NMR spectra accumulated through extensive research which have massively improved our ability to interpret those data. This finding is an excellent demonstration of the value in combining multiple analytical techniques to characterize a sample, and with further study of sodium-bearing compounds, ^{23}Na NMR could be extremely useful in efficiently identifying mineral phases in geological samples.

3.6 Conclusion

Overall, it can be concluded that the halite samples, despite their wide array of colours and many different collection sites, were all of relatively high purity. This was confirmed by all three analytical techniques that were used to investigate the samples, but particularly ICP-MS and pXRD which are not as highly selective in their analysis. Four of the naturally occurring samples were confirmed to contain fluid inclusions (Dana 5477, Dana 5490, TronaCA, and South Africa), and ^{23}Na NMR analysis confirmed the presence of thenardite in the Dana 5477 sample with the aid of pXRD analysis. Based on the calibration curve developed with NaCl solution standards, all fluid inclusions plotted at high concentrations of NaCl, but not quite as high as expected at laboratory temperature and pressures. It can be stated with a high degree of certainty that trace elemental contamination is not producing a significant impact on the chemical shift of the

^{23}Na NMR liquid signal. Although it was determined that there was a strong linear correlation between the concentration of NaCl in solution and the chemical shift of the resulting spectrum, it is still uncertain how the internal environment of a fluid inclusion influences the resultant chemical shift. For a higher degree of precision, a stronger field spectrometer is recommended to minimize the uncertainty in the resulting chemical shifts attributed to the change in salinity. This is especially important when working within a 1 ppm chemical shift range where the variability is quite small. If ^{23}Na NMR is to be considered a viable alternative for estimating the salinity of a geological fluid inclusion, further research into effects of internal pressure and contaminant molecular species will need to be conducted.

3.7 References

Aquilano, D., Otálora, F., Pastero, L., & García-Ruiz, J. M. (2016). Three study cases of growth morphology in minerals: Halite, calcite and gypsum. *Progress in Crystal Growth and Characterization of Materials*, 62(2), 227–251.

<https://doi.org/10.1016/j.pcrysgrow.2016.04.012>

Bloss, F. D. (1971). *Crystallography and crystal chemistry*. Holt, Rinehart and Winston.

Handford, C. R. (1990). Halite depositional facies in a solar salt pond: A key to interpreting physical energy and water depth in ancient deposits? *Geology*, 18(8), 691–694.

Herrero, M. J., Escavy, J. I., & Schreiber, B. C. (2015). Thenardite after mirabilite deposits as a cool climate indicator in the geological record: Lower Miocene of central Spain. *Climate of the Past*, 11(1), 1–13. <https://doi.org/10.5194/cp-11-1-2015>

Lebedev, A. L., & Kosorukov, V. L. (2017). Gypsum solubility in water at 25°C. *Geochemistry International*, 55(2), 205–210.

<https://doi.org/10.1134/S0016702917010062>

Melvin, J. L. (Ed.). (1991). *Evaporites, petroleum, and mineral resources*. Elsevier.

Minerals.net: Halite. (2021). Minerals.Net. <https://www.mindat.org/min-1804.html>

Orr, S. by-Patti. (2021, June 28). *History of Trona, California*. Mojave Desert News. http://www.desertnews.com/news/article_e7639c16-d828-11eb-926f-bfb27c1b105a.html

Schreiber, B. C., & Tabakh, M. E. (2000). Deposition and early alteration of evaporites. *Sedimentology*, 47(s1), 215–238. <https://doi.org/10.1046/j.1365-3091.2000.00002.x>

Smith, G. I. (1977). *Subsurface stratigraphy and geochemistry of late Quaternary evaporites, Searles Lake, California* (Vol. 1043). Department of the Interior, Geological Survey.

Smyth, J. R., & Bish, D. L. (1988). *Crystal structures and cation sites of the rock-forming minerals*. Allen & Unwin Boston.

Tambelli, C. E., Schneider, J. F., Hasparyk, N. P., & Monteiro, P. J. M. (2006). Study of the structure of alkali–silica reaction gel by high-resolution NMR spectroscopy. *Journal of Non-Crystalline Solids*, 352(32), 3429–3436. <https://doi.org/10.1016/j.jnoncrysol.2006.03.112>

Warren, J. K. (2016). *Evaporites*. Springer International Publishing. <https://doi.org/10.1007/978-3-319-13512-0>

Wyckoff, R. W. G. (1963). *Crystal structures* (Vol. 1). Interscience publishers New York.

Chapter 4

4 Analysis of Fluorite

In the following chapter, the analysis of Hansonburg and Gonzales fluorite will be introduced and the results from powder X-ray Diffraction (pXRD), ^{23}Na Solid State Magic Angle Spinning Nuclear Magnetic Resonance (SS MAS NMR) spectroscopy, and variable temperature NMR will be discussed.

4.1 Introduction

In this research, two samples of fluorite (CaF_2) that are known to contain saline fluid inclusions were selected for analysis to complement the suite of halite samples for NMR analysis. Fluorite was chosen due to its simple chemical composition and its lack of sodium in the crystal lattice. Unlike halite samples that were guaranteed to produce an NMR signal, the fluorite samples would only produce an NMR spectrum in the event that there was either saline fluids within the sample or the crystalline component was contaminated by another sodium-containing mineral. The detection of a saline fluid inclusion within these samples would be a positive indication that the NMR methods employed to analyze halite samples could also be used to investigate fluids that are not necessarily at full saturation (with regards to NaCl) and that the method is viable for geological samples that don't contain an abundance of sodium.

4.2 Geological Deposition of Fluorite

The deposition of fluorite within both the Gonzales and Hansonburg regions are the result of very similar mineralization processes, both being designated as a Mississippi Valley-Type (MVT) deposit that characterizes much of the surrounding region in Southwestern New Mexico. MVT deposits are normally characterized by metalliferous saline fluid deposition at moderate temperatures of up to 200°C , depositing lead and zinc-rich minerals such as sphalerite and galena while replacing local deposits of calcite and dolomite (McLemore et al., 1998; Paradis et al., 2005). Many of the mineral deposits found within New Mexico are hosted within the Rio Grande Rift (RGR), which shares many similarities with an MVT deposit. The area is still very rich in lead/zinc deposits,

but the primary mineral within these deposits is fluorite. Coupled with the varying levels of salinity in the RGR that tend to increase over geologic time rather than become more dilute, there has been some debate as to whether these deposits deserve a separate designation as RGR-type deposits (McLemore et al., 1998; Partey et al., 2009; Roedder et al., 1968). Although not widely recognized as a unique mineralization style, the RGR-type deposits are characterized primarily by their high levels of fluorite and barite; the process of enrichment for this mineralization is not yet fully understood, but appears to be sourced from asthenosphere-derived fluids over a period of four distinct mineralization events: 1) Silicification and dolomitization with minor pyrite and sphalerite deposition, 2) galena deposition with minor chalcopyrite, 3) major deposition of fluorite, barite, and later quartz in open spaces, and 4) mineralization of quartz and calcite (McLemore et al., 1998).

Both the Hansonburg and Gonzales mineralization systems occur along faults within Pennsylvanian and Permian age limestones and sandstones within the Magdalena Group, primarily occurring as vein-filling deposits and replacing the marine calcite bedding (Hill et al., 2000; Roedder et al., 1968). Although the two sites share many similarities, the Hansonburg region hosts higher salinity fluid inclusions with an average salinity around 10-18% NaCl equivalent by mass, while the Gonzalez fluorite minerals have been found to vary anywhere between 5-7% NaCl equivalent by mass within the fluid inclusions (Hill, 1994; Roedder et al., 1968). The lower salinity fluid inclusions like those in the Gonzales region are believed to be a result of fluid mixing with meteoric waters, while the higher salinity fluids found in Hansonburg appear to be derived from hydrothermal fluids free from meteoric influence (Hill, 1994).

Both of these fluorite-prominent regions have been previously studied for fluid inclusion data and have been relatively well-documented, prompting their inclusion with this research which focuses primarily on the internal fluid properties and secondarily on the geology of the region which produced them.

4.3 Methods

The analysis of the two fluorite samples was conducted as described in the Methods section (Chapter 2). The following is a summary of the methods used in the fluorite analysis.

The pXRD analysis was performed on a Rigaku powder diffractometer at the University of Western Ontario, with a Co X-ray source (λ Co $K\alpha_1 = 1.78897 \text{ \AA}$) operating at 40kV and 35mA. Both samples were analyzed from $10\text{-}110^\circ 2\theta$ with a step size of 0.02° . The Hansonburg sample was analyzed with a dwell time of 10 seconds per step while the Gonzales fluorite dwell time was reduced to 4 seconds per 0.02° increment.

^{23}Na NMR analyses of both the Gonzales and Hansonburg fluorite samples were completed at the J.B. Stothers NMR facility at the University of Western Ontario. Both samples were analyzed using ^{23}Na MAS NMR on a Varian Infinity Plus 400 spectrometer (9.4 Tesla, γ $^{23}\text{Na} = 105.7 \text{ MHz}$). Prior to analysis the samples were coarsely ground to approximately 1-2 mm in grain size. The samples were referenced to a 1.0 M NaCl standard solution ($\delta(^{23}\text{Na}) = 0.0 \text{ ppm}$) at ambient laboratory conditions with a spectral width of 55 kHz. The 90° pulse width was 1.7 μs followed by a 54.5 ms acquisition time. The recycle delay was set to 45 seconds to maximize the collected ^{23}Na signal. (This was determined by doing a relaxation delay experiment where different time delays were allowed and the smallest delay which reproduced all the signals was used.) Magic angle spinning samples were spun at 12 kHz with the same collection parameters as the static samples.

Only the Hansonburg fluorite sample was analyzed using variable temperature NMR, for which the spin rate was decreased to 11 kHz and the spectral width was reduced to 25 kHz. The acquisition time was set to 40.96 ms, and in the interest of time the recycle delay was reduced to 5 seconds. Spectra were collected at 100°C , 150°C , 175°C , and 185°C in an attempt to observe homogenization of the fluid phases within the fluid inclusions (T_h of approximately $160\text{-}185^\circ\text{C}$ (Norman et al., 1985)). The Hansonburg fluorite sample was also preliminarily analyzed under static conditions with variable collection parameters to test the receptivity of geological samples, in order to develop a

standardized collection protocol; specific analysis parameters are documented below (Table 4-1) and more in-depth documentation can be found in Appendix B.

Table 4-1: ^{23}Na NMR Parameters for acquisition of Hansonburg and Gonzales Fluorite.

Sample	Number of Acquisitions	Spectral Width (kHz)	Pulse Width (μs , $\pi/2$)	Acquisition Time (s)	Recycle Delay (s)	Data Points	MAS Frequency (kHz)
Gonzales MAS	4000	55.0055	1.7	0.01862	45	1024	12
Hansonburg Static	1600	50.0000	2.0	0.012	1	256	NA
Hansonburg 12 kHz	4000	55.0055	1.7	0.03723	45	2048	12
Sample (Variable Temperature)	Number of Acquisitions	Spectral Width (kHz)	Pulse Width (μs , $\pi/2$)	Acquisition Time (s)	Recycle Delay (s)	Data Points	MAS Frequency (kHz)
Hansonburg 22C	2064	25.0000	1.6	0.04096	5	1024	12
Hansonburg 100C	2140	25.0000	1.6	0.04096	5	1024	12
Hansonburg 150C	2140	25.0000	1.6	0.04096	5	1024	12
Hansonburg 175C	2140	25.0000	1.6	0.04096	5	1024	12
Hansonburg 185C	2140	25.0000	1.6	0.04096	5	1024	12

4.4 Results

4.4.1 pXRD Results for Fluorite

Powder X-ray diffraction analysis produced clean diffraction patterns for both fluorite samples that were excellent matches for standard fluorite diffraction pattern (ICDD pattern card # 01-077-2094). Both samples exhibited other peaks on the diffraction pattern that matched to contaminant mineral traces; analysis of Gonzales fluorite identified trace amounts of gypsum ($\text{CaSO}_4(\text{H}_2\text{O})_2$) while the Hansonburg fluorite (Fig. 4-1) shows evidence of quartz mineralization.

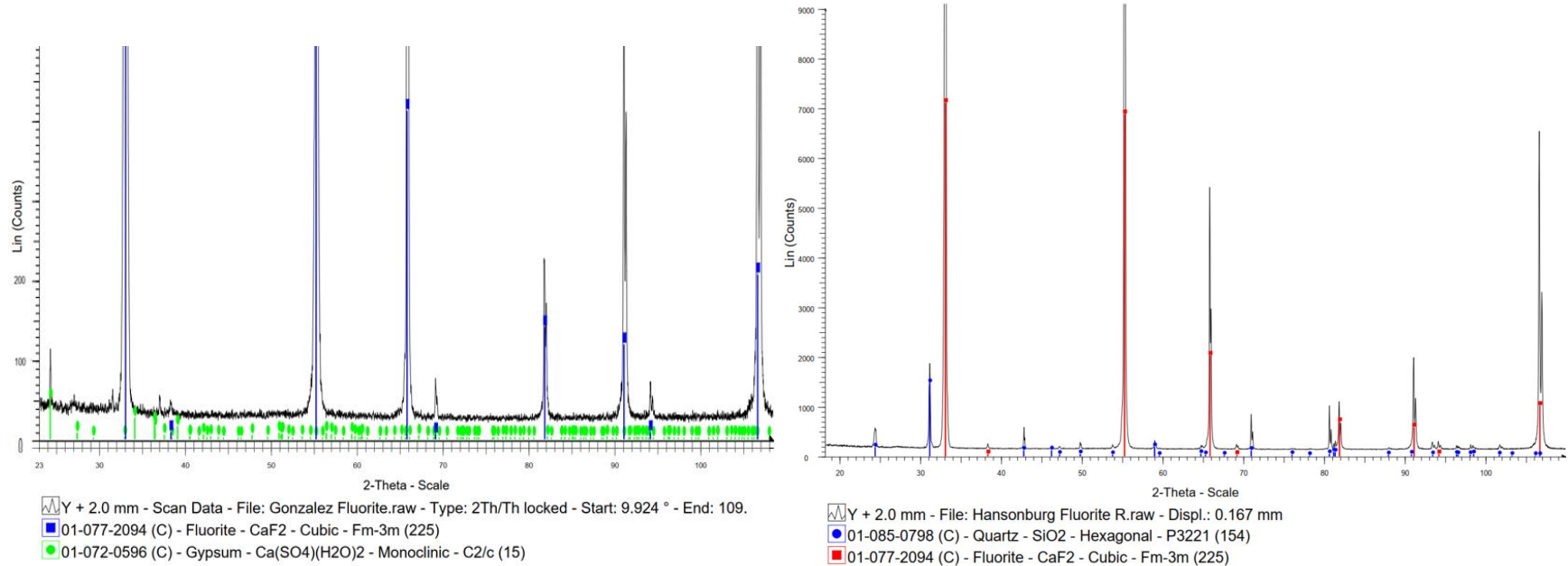


Fig. 4-1: Powder X-ray Diffraction pattern of the Gonzales fluorite sample with matching ICDD mineral cards for fluorite and gypsum applied (left) and a powder X-ray Diffraction pattern for the Hansonburg fluorite sample exhibiting excellent ICDD card matches for fluorite and quartz mineralization (right).

4.4.2 ^{23}Na NMR Results for Fluorite

The Gonzales fluorite sample did not produce any signal when analyzed with ^{23}Na NMR spectroscopy (Fig. 4-2). There is no identifiable signal that exceeds baseline noise across the breadth of the processed spectrum.

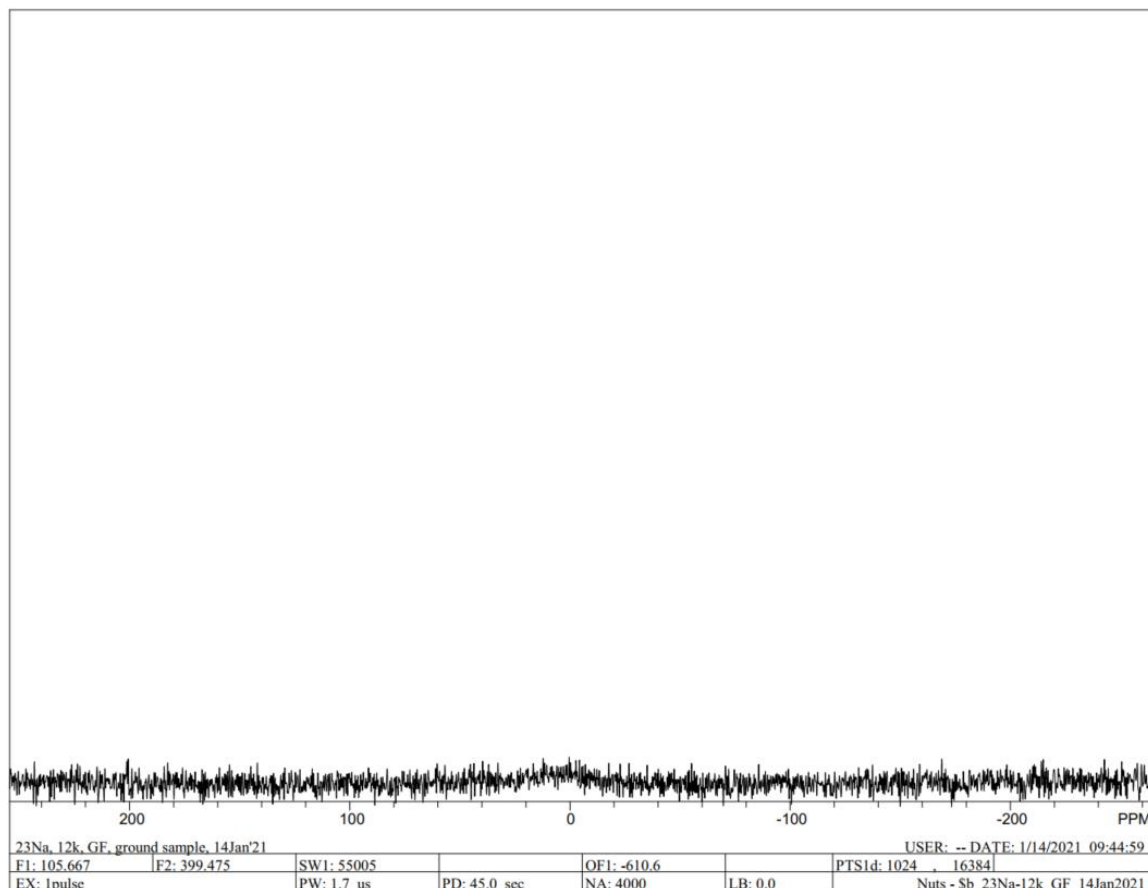


Fig. 4-2: ^{23}Na MAS NMR spectrum for the Gonzales fluorite sample. There is evidence of a small, broad peak developing between -10 and 10 ppm, but no clear signal was collected above baseline noise.

Interpretation of the processed Gonzales fluorite data could support some elevated baseline signal about 0 ppm, but this offers very little useful information. This broad peak might indicate a very low level of NaCl within the Gonzales fluorite, but it is not diagnostic. This sample was not analyzed under static NMR conditions.

The Hansonburg fluorite showed promising results after primary analysis despite initial scans exhibiting interference from borosilicate glass NMR tubes used for static analysis. Once an efficient protocol was developed and ZrO_2 rotors were used for analysis, distinct peaks could be identified in the Hansonburg sample (Fig. 4-3).

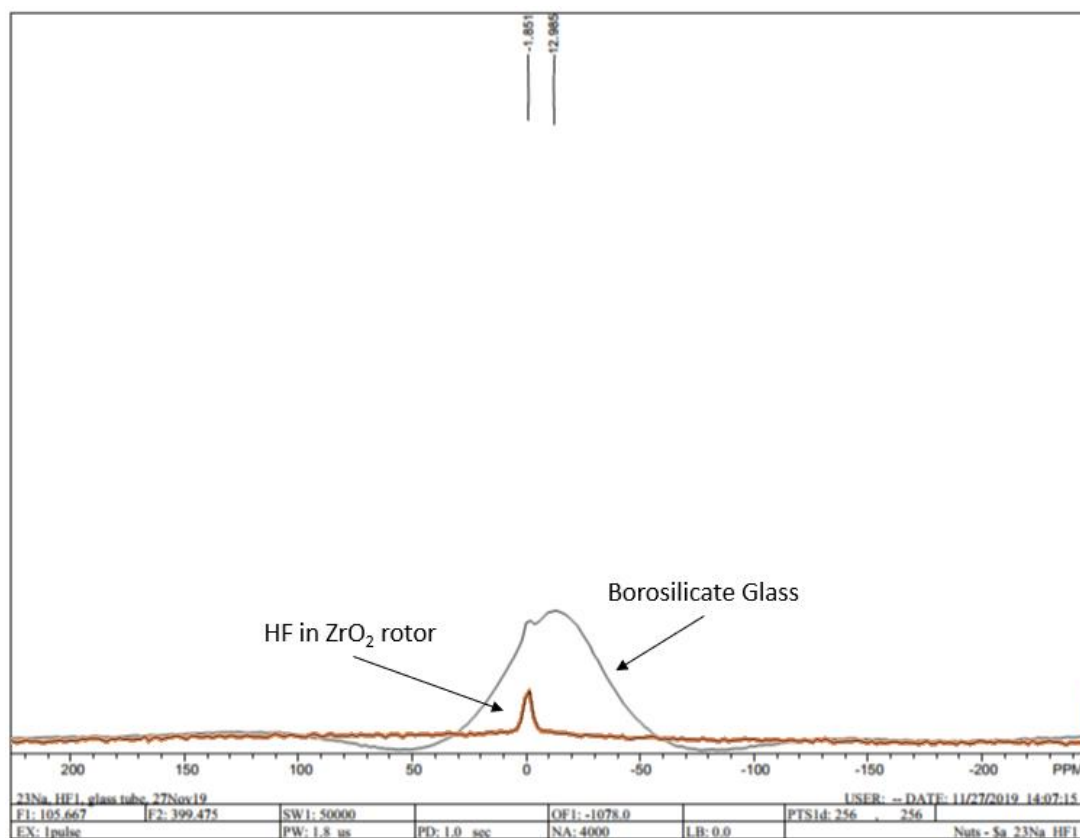


Fig. 4-3: Static ^{23}Na NMR spectra of Hansonburg fluorite. Initial spectrum collected in a borosilicate rotor without MAS compared to a similar static acquisition in a ZrO_2 rotor. Extreme line broadening in borosilicate spectrum is caused by Na in the glass tube, peak near 0 ppm is from the sample.

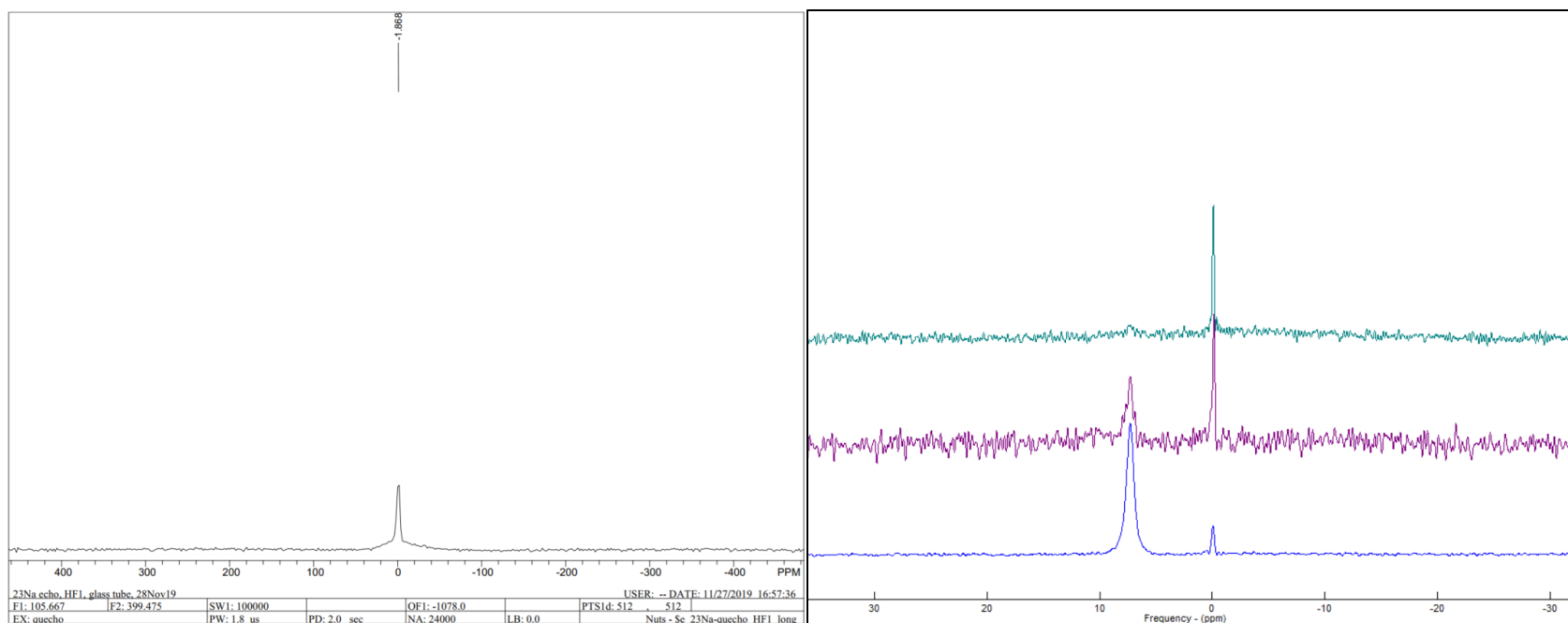


Fig. 4-4: Static ^{23}Na NMR of the Hansonburg fluorite in a ZrO_2 rotor with a relatively narrow peak atop a very broad peak near -2 ppm, 24000 scans overnight (left). Zoomed and exaggerated MAS ^{23}Na NMR stack plot of the Hansonburg fluorite sample under various scan parameters (right). Bottom is 8 kHz/ 7808 acquisitions, middle is 12 kHz/1600 acquisitions, and top is 11 kHz/ 2064 acquisitions.

Static ^{23}Na NMR analysis of the Hansonburg sample produced a single peak around -2 ppm, with minor peak broadening (FWHM = ~400 Hz) (Fig. 4-4 (left)). Upon MAS analysis at 12 kHz, two distinct peaks were identified with narrower peak widths and less distortion of the peak shape (FWHM = ~ 80 Hz). These two peaks tended to appear at around 7 ppm and 0 ppm across three separate scans (Fig. 4-4 (right)). The first two MAS scans produced a small signal at 82 ppm (Fig. 4-5(left)) that was not present on the later scans that used the standardized scan parameters outlined in the methods chapter (Chapter 2). This peak is attributed to contamination of the sample that was used for analysis and was not considered a legitimate signal from the fluorite. Subsequent analysis of the Hansonburg sample using standardized NMR parameters revealed a spectrum dominated by a fluid signal without the contaminant signal at 82 ppm (Fig. 4-5 (right)). This was taken to be the characteristic spectrum for Hansonburg fluorite in all subsequent analysis.

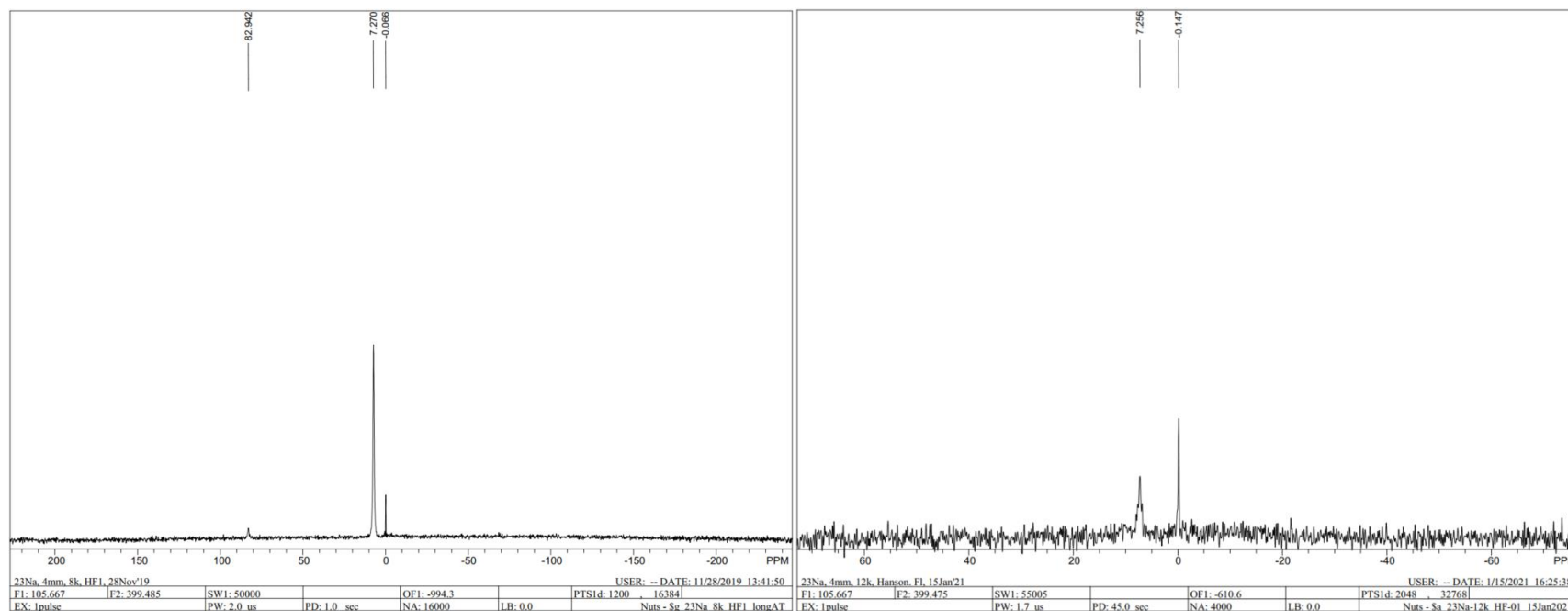


Fig. 4-5: Left, ^{23}Na NMR spectrum of Hansonburg fluorite spinning at 8 kHz. The signal near 83 ppm is considered a contaminant. Legitimate peaks from the fluorite are found near 7 and 0 ppm. Right, 12 kHz MAS spectrum of Hansonburg fluorite acquired with standardized collection parameters.

The Hansonburg fluorite sample was also submitted for Variable Temperature ^{23}Na MAS NMR analysis at elevated temperatures of 100°C, 150°C, 175°C, and 185°C, as well as at room temperature. A stacked plot of the spectra can be seen in Fig. 4-6. These spectra have not been shifted in X for plotting purposes, the change in chemical shift is a function of temperature.

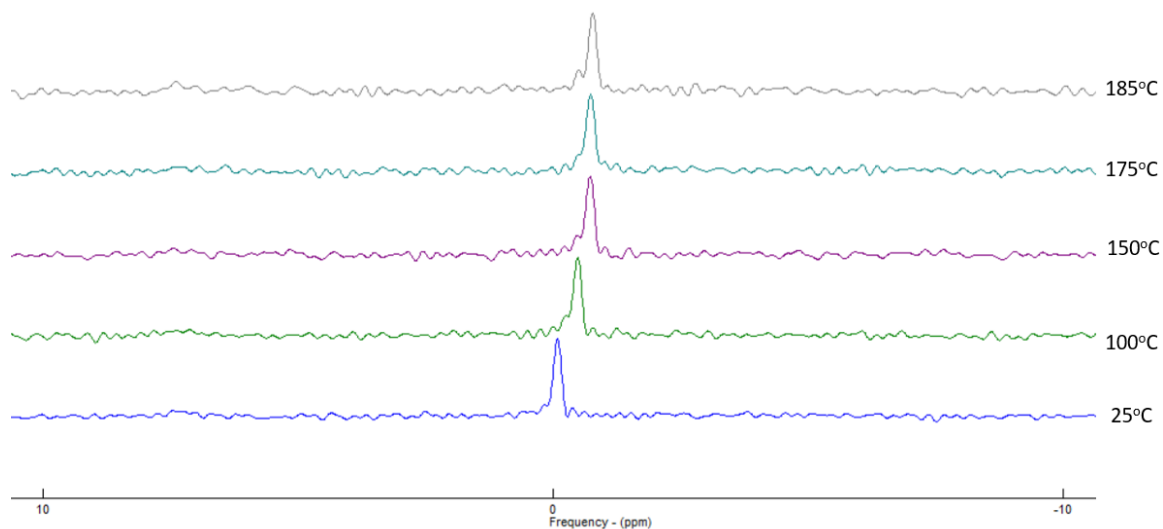


Fig. 4-6: Variable temperature ^{23}Na MAS NMR zoomed stack plot for Hansonburg fluorite. The peak shape around 7 ppm is no longer visible in this series of scans, but the signal near 0 ppm remains and is shifted with elevated temperatures.

4.5 Discussion

4.5.1 ^{23}Na NMR Discussion

The NMR analysis of the Gonzales fluorite shows that there is no significant concentration of sodium within the sample. This does not eliminate the possibility of the Gonzales sample hosting fluid inclusions, but it rules out the possibility of studying them using ^{23}Na NMR. It may be possible to probe these fluid inclusions using ^{19}F NMR spectroscopy, although the solubility of CaF_2 at ambient conditions is low with a $K_{\text{sp}} = 3.12 \times 10^{-11}$ under ambient conditions (Garand & Mucci, 2004). This low level of solubility in comparison to NaCl means that the concentrations of fluoride ions in solution may be too low to see when compared to the solid state CaF_2 signal. Proton

NMR may be the best option for obtaining any fluid data from the Gonzales fluorite sample, but presence of hydrocarbons and organic contaminants may greatly impact the effectiveness of this approach.

In contrast to the Gonzales fluorite results, the Hansonburg fluorite produced definitive results for both solid and solvated sodium within the sample. Based on results that were obtained from the halite analysis (see Chapter 3: Halite) we can confidently assign the peak at 7.26 ppm as a solid halite peak, while the peak at -0.15 ppm is best described as a fluid peak despite the deviation from the calibration curve standards of pure NaCl in solution. It is notable that the fluid signal is not only visible in this sample but is also more intense than the solid signal. Unlike the halite samples which were predominantly solid NaCl with minor amounts of fluid, the Hansonburg fluorite sample actually appears to contain more sodium in solution than it does in the solid state. With the pulse delay set to 45 seconds we see full relaxation of sodium in both solid and fluid environments between pulses so the slower relaxation of the solid-state sodium should not artificially reduce the relative intensity of the signal around 7 ppm. The low signal to noise (S/N) ratio of ~4.5 reflects the overall low concentration of sodium within the sample. Equivalent scans of halite produced S/N ratios of approximately 2000:1 based on max peak intensity measurements with respect to the background signal. The low intensity signal produced by the Hansonburg sample is not a concern when evaluating chemical shift, however it does represent a fundamental limit of detection for geological samples with a low natural abundance of sodium-bearing components.

Although successful in detecting fluid signal, we cannot verify the fluid signal present in the Hansonburg fluorite as a saline fluid inclusion despite its presence in the ^{23}Na spectrum. Based on the calibration curve established for our suite of NMR samples, the expected range of chemical shift attributed to pure NaCl in solution lies within the region of -0.01 ppm and 0.5 ppm (Fig. 4-7). The higher frequency shift seen with the Hansonburg fluid peak appears closer to -0.16 ppm, nearly a 30% deviation from the expected range of saline fluid chemical shifts. The estimated salinity of the Hansonburg fluid signal corresponds to a negative concentration of approximately -0.35 mol/L NaCl,

suggesting further influence beyond salinity affecting the chemical shift.

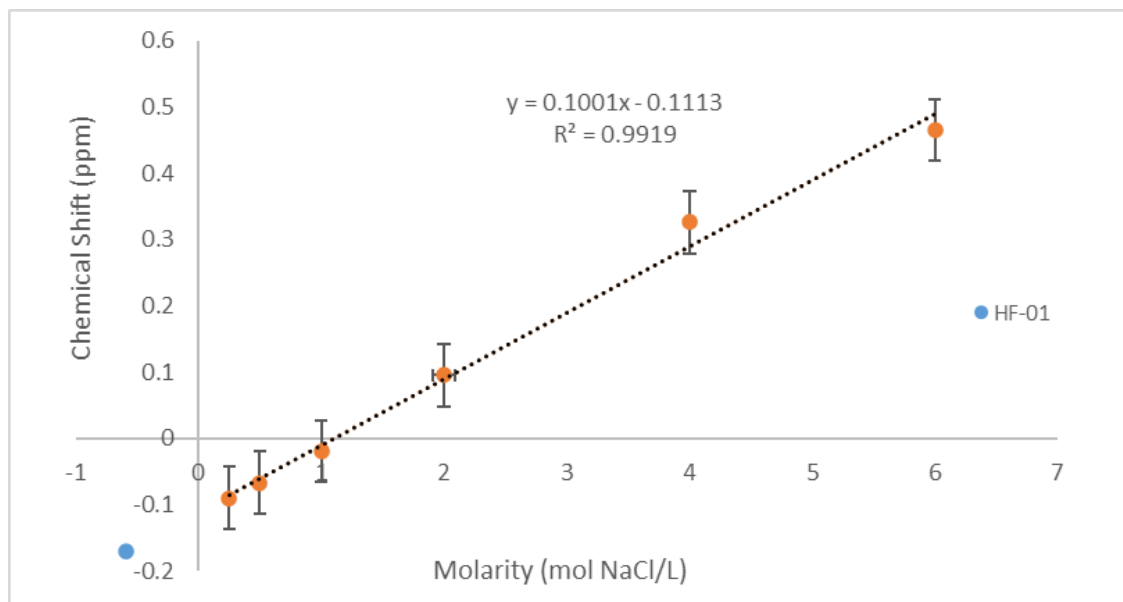


Fig. 4-7: Hansonburg fluorite observed ^{23}Na MAS NMR liquid peak plotted using the solvated NaCl calibration curve to extrapolate molarity; this reports a concentration of approximately -0.36mol/L NaCl.

The variable temperature analysis of Hansonburg fluorite revealed a barely discernible solid peak and a slight shift in the fluid peak with increasing temperature. The signal from the peak around 7 ppm, although still present, is not as easily visible and might be missed if not explicitly looked for and interpreted as an expected peak. This is likely a product of the pulse delay time used in the variable temperature analysis to ensure all scans could be collected in a timely fashion. Since the variable temperature NMR probe cannot be left running unattended, all analyses must be finished during regular laboratory hours so scan times were shortened to accommodate this. The pulse delay time was reduced from 45 seconds in the ambient temperature acquisition down to 5 seconds for the variable temperature analysis, which likely did not allow the signal from solid halite phase sufficient time to relax before the next pulse was initiated. This results in less signal being collected from the slowly decaying solid signal while the liquid signal was relatively unaffected by the shortened delay between pulses. The liquid peak does appear to become more shielded and move to lower frequency as the temperature increases (Fig. 4-8).

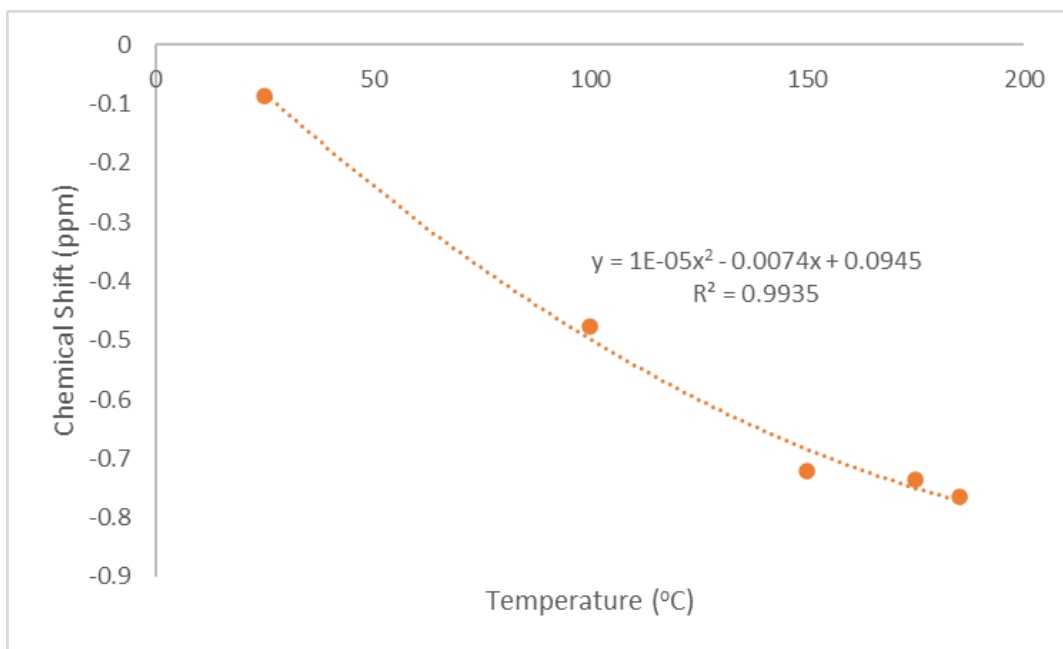


Fig. 4-8: Change in Hansonburg fluorite liquid peak chemical shift with increasing temperature, modelled with a quadratic approximation.

This shift is likely attributable strictly to the increase in temperature within the sample, as the associated pressure increase caused by the rising temperatures is likely to be very small before the homogenization temperature is reached. Despite reaching the maximum expected homogenization temperature of the Hansonburg sample (approximately 140-185°C, Roedder (1968)) no abrupt change was observed in the peak position or shape at 185°C (Fig. 4-6).

The fluids involved in forming the New Mexico RGR-type deposits are complicated, especially in contrast to the fluids involved in the deposition of simple halite evaporites studied in Chapter 3. As a result of this more complex fluid composition, it is possible that the progression toward lower frequency (more shielded) chemical shift may be related to the internal composition of the fluid inclusions, particularly in terms of sulphate concentrations. The RGR region (and other MVT-type deposits) are known to be rich in sulphides such as galena and sphalerite, as well as sulphates such as barite, which could result in elevated levels of sulphates in the brine solution trapped within the fluid inclusions. From previous study in the Halite chapter (chapter 3), the hydrated thenardite

standard sample ($\text{Na}_2\text{SO}_4 \cdot 0.445 \text{H}_2\text{O}$) exhibited a fluid signal in the ^{23}Na NMR analysis similar to the chemical shift exhibited by the Hansonburg sample which may indicate a link between aqueous SO_4^{2-} molecules and the chemical shift of solvated Na^+ ions in solution (Fig. 4-9).

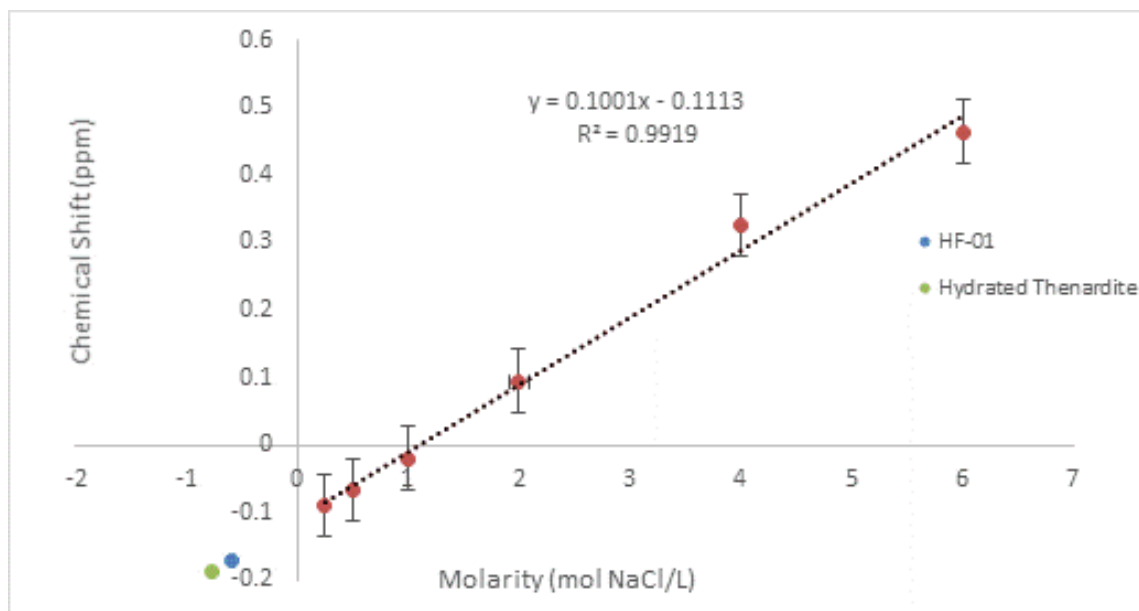


Fig. 4-9: Hansonburg fluorite plotted on the linear regression to estimate salinity of the fluid signal produced by ^{23}Na MAS NMR. The hydrated thenardite fluid signal is also plotted for reference, indicating a possible relationship between sulphate concentration and ^{23}Na chemical shift.

No fluorite samples were submitted for elemental analysis, so further research into the possibility of sulphate influence on the chemical shift is required to form any conclusions.

4.5.2 pXRD Discussion

X-ray diffraction analysis confirmed that both samples were predominantly fluorite with minor trace minerals found in both of them. The Gonzales fluorite exhibited traces of gypsum, which is expected from the RGR-style deposits as a replacement product of the calcite bedding in the presence of sulphur-rich fluids (Böhlke & Irwin, 1992; Lueth et al., 2005).

The Hansonburg fluorite diffraction data indicated a small amount of quartz in the sample, which is also expected for the mineralization of the region. In the Hansonburg area, fluorite is believed to have been one of the primary precipitants, followed by galena, barite, and lastly quartz within open voids and veins throughout the host limestone lithology (Lasky, 1932; Roedder et al., 1968). The interesting result from pXRD analysis is that there were no detectable levels of halite within the sample, despite clear evidence of solid-state and solvated halite from the NMR results. All sample processing was completed under anhydrous ethanol wash to avoid loss of sample while grinding and smearing for the pXRD analysis. It is possible that halite was lost in this process, however the solubility of halite is very low in anhydrous ethanol (0.055wt. % at 25°C compared to 26.483wt. % in H₂O) but this possibility can't be discounted (Pinho & Macedo, 2005). It is perhaps possible that by finely powdering the sample, the trace amounts of halite that were present were dispersed so widely throughout the powder that their diffraction patterns were too weak to be seen above the baseline, or that the amount of halite was so small, that it was lost to the ethanol wash. Halite is not known to mineralize in the Hansonburg region, and the saline fluids were found to mostly result in included fluids, rather than mineralize into discrete halite-rich mineral zones. The fluid inclusions found within the Hansonburg region have been documented to be between 10.5% - 17% NaCl equivalent by weight which is not high enough to produce daughter halite crystals under ambient conditions (Roedder et al., 1968). The same sub-sample was used for NMR and pXRD analysis to ensure there was no sampling bias between instruments, so it is uncertain why there is such a glaring discrepancy.

4.6 Conclusions

Powder X-ray diffraction analysis confirmed the identity of the Gonzales and Hansonburg fluorite mineral species, as well as identified some minor trace minerals that were also present in the samples. The Gonzales fluorite showed trace amounts of gypsum while the Hansonburg sample exhibited minor amounts of quartz present. Neither of these trace minerals pose any risk for producing complications regarding ²³Na NMR analysis, as they don't contain any sodium in their crystal structure.

Despite the failure to detect fluid inclusions within the Gonzales fluorite sample using ^{23}Na NMR, a small and broad peak shape of low intensity was shown in the Gonzales NMR analysis. This ultimately produced no usable results but is still notable. There was still success to be had in studying the Hansonburg fluorite sample which produced an NMR spectrum indicating the presence of both solid and solvated NaCl. This result is not entirely surprising, because the Hansonburg region is known to host fluids of a much higher salinity than those found in the Gonzales region.

The identification of a fluid and solid NaCl signal from the ^{23}Na MAS NMR analysis of the Hansonburg fluorite is an extremely positive result for proving the potential of identifying fluid inclusions within host mineralogy that is free from sodium in the crystal lattice, especially in a mineral that was naturally produced. The complex nature of the fluids trapped in the Hansonburg fluorite are the likely cause for the chemical shift to fall outside the expected saline region of the spectrum, and there is some evidence that the cause may be related to sulphate concentration within the fluids. Evidence from the DC-5470 halite (section 3.5.1) sample suggests that there may be a deshielding effect on sodium ions when there are sulphates in the solution. Further study into the effects of sulphates in solution as well as the effect of internal pressure of fluid inclusions on ^{23}Na NMR spectroscopy are required to fully qualify the unique fluid signal observed in the Hansonburg fluorite sample.

4.7 References

Böhlke, J. K., & Irwin, J. J. (1992). Brine history indicated by argon, krypton, chlorine, bromine, and iodine analyses of fluid inclusions from the Mississippi Valley type lead-fluorite-barite deposits at Hansonburg, New Mexico. *Earth and Planetary Science Letters*, *110*(1–4), 51–66. [https://doi.org/10.1016/0012-821X\(92\)90038-W](https://doi.org/10.1016/0012-821X(92)90038-W)

Garand, A., & Mucci, A. (2004). The solubility of fluorite as a function of ionic strength and solution composition at 25°C and 1 atm total pressure. *Marine Chemistry*, *91*(1–4), 27–35. <https://doi.org/10.1016/j.marchem.2004.04.002>

Hill, G. T. (1994). *Geochemistry of southwestern New Mexico fluorite deposits: Possible base and precious metals exploration significance* [Master's Thesis]. New Mexico Institute of Mining and Technology Socorro, New Mexico.

Hill, G. T., Campbell, A. R., & Kyle, P. R. (2000). Geochemistry of southwestern New Mexico fluorite occurrences implications for precious metals exploration in fluorite-bearing systems. *Journal of Geochemical Exploration*, 68(1–2), 1–20.
[https://doi.org/10.1016/S0375-6742\(99\)00047-3](https://doi.org/10.1016/S0375-6742(99)00047-3)

Lasky, S. G. (1932). *The ore deposits of Socorro county, New Mexico*. New Mexico School of Mines.

Lueth, V. W., Rye, R. O., & Peters, L. (2005). “Sour gas” hydrothermal jarosite: Ancient to modern acid-sulfate mineralization in the southern Rio Grande Rift. *Chemical Geology*, 215(1–4), 339–360. <https://doi.org/10.1016/j.chemgeo.2004.06.042>

McLemore, V. T., Giordano, T. H., Lueth, V. W., & Witcher, J. C. (1998). *Origin of barite-fluorite-galena deposits in the southern Rio Grande rift, New Mexico*. 16.

Norman, D. I., Ting, W., Putnam, B. R., & Smith, R. W. (1985). Mineralization Of The Hansonburg Mississippi-Valley-Type Deposit, New Mexico: Insight From Composition of Gases in Fluid Inclusions. *The Canadian Mineralogist*, 17.

Paradis, S., Dewing, K., & Hannigan, P. (2005). Mineral Deposits of Canada. Mississippi Valley-type Lead–Zinc Deposits (MVT). *Natural Resources Canada*.

Partey, F., Lev, S., Casey, R., Widom, E., Lueth, V. W., & Rakovan, J. (2009). Source of Fluorine and Petrogenesis of the Rio Grande Rift-Type Barite-Fluorite-Galena Deposits. *Economic Geology*, 104(4), 505–520. <https://doi.org/10.2113/gsecongeo.104.4.505>

Pinho, S. P., & Macedo, E. A. (2005). Solubility of NaCl, NaBr, and KCl in Water, Methanol, Ethanol, and Their Mixed Solvents. *Journal of Chemical & Engineering Data*, 50(1), 29–32. <https://doi.org/10.1021/je049922y>

Roedder, E., Heyl, A. V., & Creel, J. P. (1968). Environment of ore deposition at the Mex-Tex deposits, Hansonburg District, New Mexico, from studies of fluid inclusions. *Economic Geology*, 63(4), 336–348. <https://doi.org/10.2113/gsecongeo.63.4.336>

Chapter 5

5 Analysis of Quartz

The following chapter summarizes the analysis of Snowbird quartz via ^{23}Na Magic Angle Spinning Nuclear Magnetic Resonance spectroscopy (MAS NMR), Variable Temperature MAS NMR, and powder X-ray Diffraction (pXRD). The results and their implications for the study of geological samples using NMR spectroscopy are discussed.

5.1 Introduction to the Study of Snowbird Quartz

A sample of quartz from the Snowbird region in Northwestern Montana was selected for this research due to its simple crystal composition (SiO_2 , which is invisible in ^{23}Na NMR) and the highly saline fluids that influenced mineralization in the region. High salinity within the fluid inclusions offers the best opportunity for detecting fluid inclusions using ^{23}Na NMR when small volumes of fluid are involved. Quartz samples from the Snowbird region have also been known to host daughter halite crystals at room temperature within their fluid inclusions, which offers the chance to detect crystalline halite as well as solvated NaCl using NMR spectroscopy (Samson et al., 2004). The mineralization in the region has been fairly well studied, so formation conditions such as temperature and pressure, as well as general fluid compositions have already been established for many parts of the region. Although the underlying geology of the region isn't essential for the study of this quartz sample, a summary is provided below.

5.2 Geological Context for the Snowbird Region

The Snowbird pegmatite is found on the northern border between Montana and Idaho, U.S.A., and is closely tied to the Coeur d'Alene mining district that characterizes much of the greater region. This area is underlain by the Belt Supergroup series which is a collection of six discrete sedimentary lithologies, all of which can briefly be summarized as hosting argillite, quartzite, calcite, and dolomite. The individual formations are distinguished by relative composition, mineral colour, and grain size and have been dated as mid-Proterozoic in age for the oldest Prichard formation (Cressman, 1985; Gott & Cathrall, 1980; Hobbs et al., 1965). The Snowbird deposit is hosted within a quartz-

carbonate unit that intruded into the Wallace Formation, a 1300- 2000 meter thick assemblage of argillite and quartzite that resides just below the uppermost Striped Peak Formation in the Belt assemblage (Hobbs et al., 1965; Metz et al., 1985). Snowbird is primarily considered as a fluorite deposit, but it has notable quartz mineralization as well. Despite the deposit being hydrothermal in origin, mineralization of calcite and quartz often appear pegmatitic; euhedral hexagonal quartz crystals from the area have been reported to be as large as 2 feet (61 cm) in diameter and up to 6 feet (183 cm) in length (Sahinen, 1962). Work by Metz et al., (1985) established that there were two distinct stages of mineralization within the Snowbird deposit, the first of which (stage I) was responsible for the pegmatitic-style mineralization and zoning of quartz and calcite while the second stage (stage II) lacked calcite and produced smaller grain sizes while filling veins and replacing some stage I mineralization. Stage II mineralization may be the result of the same mineralization source as Stage I, but depleted in calcite and with a notably lower salinity (Metz et al., 1985). Both stages of mineralization were accompanied or preceded by brecciation of the host rock. The formation of the Snowbird deposit is strongly associated with the emplacement of the Idaho batholith which likely supplied the hydrothermal fluids responsible for the mineralization. Temperatures of mineralization are estimated to be between 400 and 600°C with pressures exceeding 200 MPa (Metz et al., 1985; Samson et al., 2004). Salinities for the first and second stages of mineralizing fluids are estimated to be 33-50 wt.% NaCl and approximately 29 wt.% NaCl, respectively.

5.3 Methods

The methods used for this study have been documented in depth in Chapters 1 (Introduction) and 2 (Methods) above. These methods are summarized below for ease of reference.

5.3.1 pXRD Methods

The sample of Snowbird quartz was finely powdered to a grain size of approximately 5 μm under an anhydrous ethanol. The powdered sample was thinly smeared onto a recessed glass sample plate and analyzed with a Rigaku powder diffractometer in the

Powder X-ray Diffraction and Micro X-ray Diffraction Laboratory at the University of Western Ontario. The diffractometer used a Cobalt X-ray source (λ Co $K\alpha_1 = 1.78897 \text{ \AA}$) set at 40 kV and 35 mA and was programmed to scan from $10 - 110^\circ 2\theta$ in 0.02° increments with a dwell time of 10 seconds per step. The total scan time for the sample was about 14 hours.

5.3.2 ^{23}Na NMR Methods

The Snowbird quartz sample was coarsely ground to a grain size of approximately 1-2 mm under an anhydrous ethanol in preparation for loading into the 4.0 mm diameter ZrO_2 NMR rotor. The sample was rinsed again with anhydrous ethanol prior to analysis to ensure no contaminants remained on the surface of the sample grains from the grinding procedure. The Snowbird quartz sample was analyzed using a Varian Infinity Plus 400 NMR spectrometer in the J.B. Stothers NMR lab at the University of Western Ontario. For both MAS and variable temperature analysis, a 4.0 mm HXY MAS probe was used; the spectrometer was calibrated using 1.0 M aqueous NaCl solution set to 0 ppm ($\delta(^{23}\text{Na}) = 0.0 \text{ ppm}$). The magic angle spinning spectra were collected with a 55 kHz spectral width, a $1.7 \mu\text{s}$ 90° pulse, with a 54.5 ms acquisition time. The sample was allowed to relax for 45 seconds between RF pulses. MAS analysis was carried out at 12 kHz spin rate while the spin rate was lowered to 11 kHz for variable temperature analysis. Spectra were collected as FIDs in the time domain, and zero filled to a minimum 4096 points before being Fourier Transformed to produce spectra in the frequency domain. The variable temperature MAS NMR parameters are summarized below:

Table 5-1: Acquisition parameters for Variable Temperature ^{23}Na MAS NMR spectroscopy of the Snowbird Quartz sample.

Sample Temperature ($^\circ\text{C}$)	Number of Acquisitions	Pulse Delay (Seconds)	Pulse Width (90° pulse, μs)	Acquisition Time (Seconds)
22 (Ambient)	404	5.000	2.0000	0.0256
50	1032	10.000	2.0000	0.0256
100	808	10.000	2.0000	0.0300

150	800	10.000	2.0000	0.0300
200	800	10.000	2.0000	0.0300

5.4 Results

5.4.1 ^{23}Na NMR Results for Quartz

Spectroscopic data returned from the MAS analysis of Snowbird quartz revealed an intense peak near 7 ppm and a complex signal around 0.5 ppm.

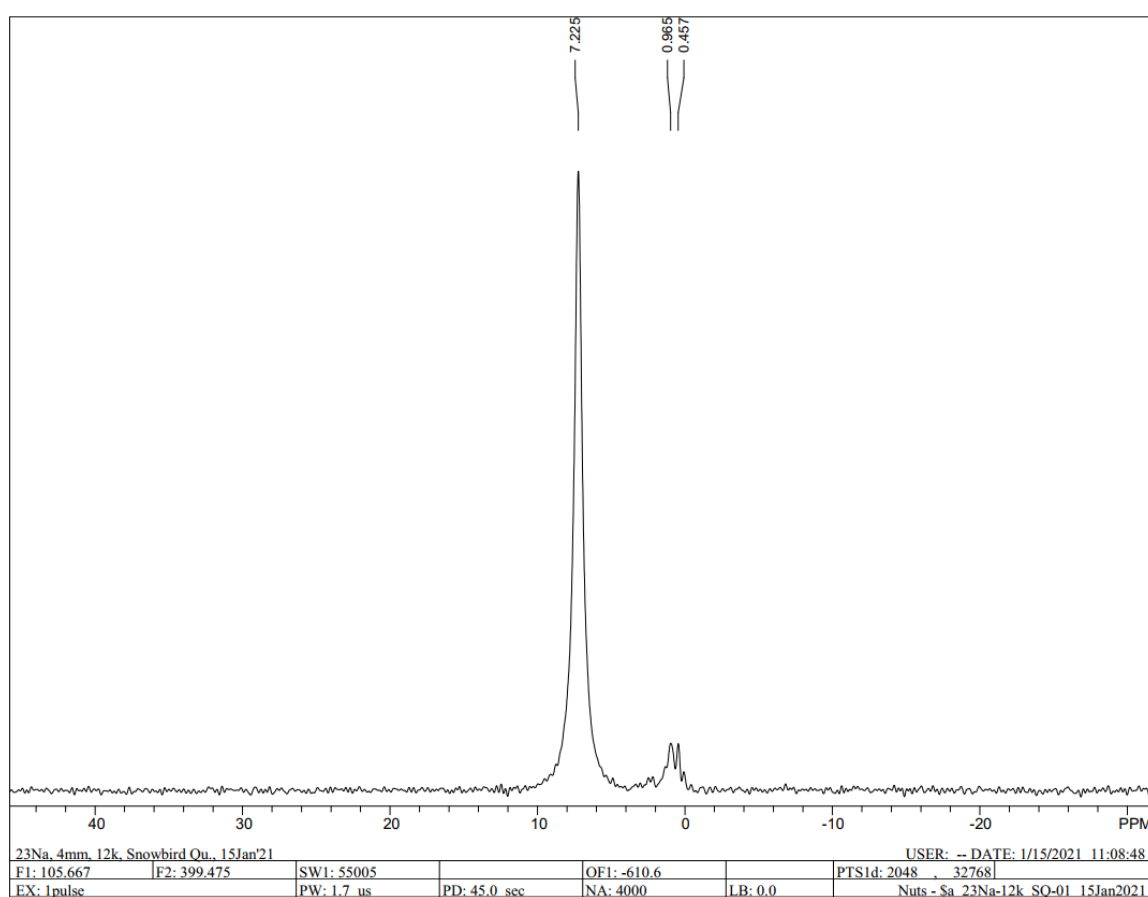


Fig. 5-1: ^{23}Na MAS NMR spectrum of the Snowbird quartz sample at ambient temperature in the laboratory. A single peak is shown at ~7 ppm and a complex peak is shown at ~0.5 ppm.

The variable temperature NMR generally replicated this spectrum, despite heating of the sample up to 200°C. A stack plot of the variable temperature spectra can be seen below (Fig. 5-2).

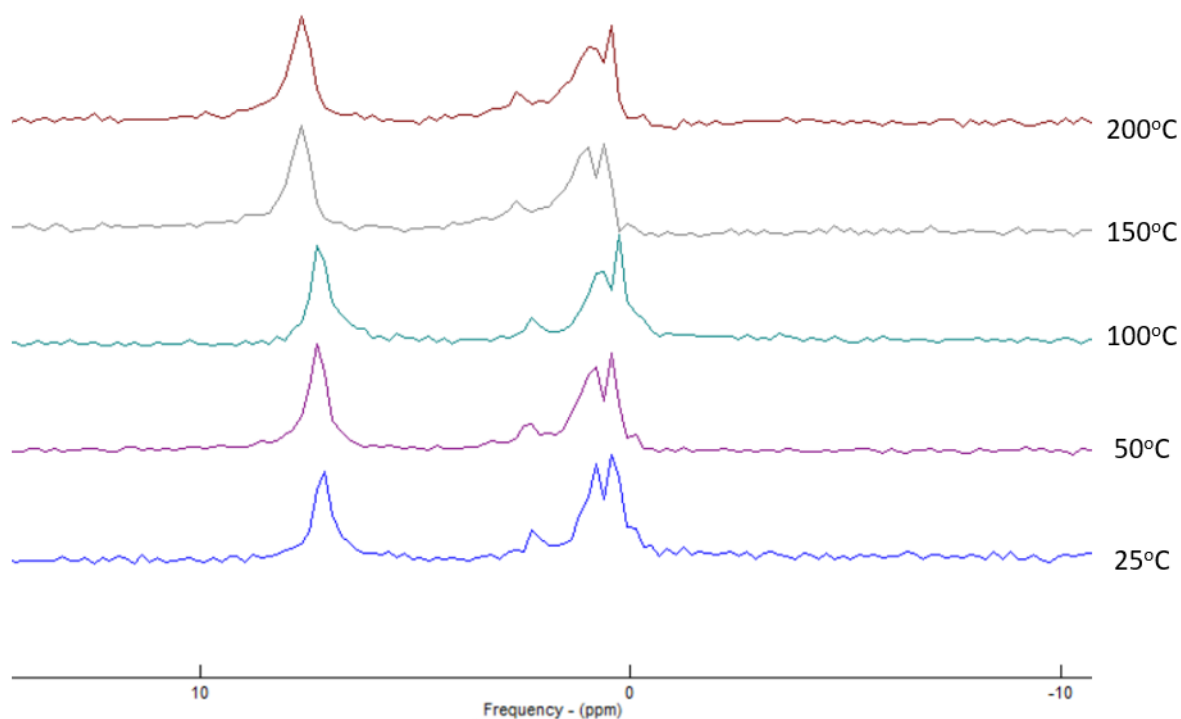


Fig. 5-2: Stack plot of the Snowbird Quartz sample acquired using Variable Temperature ^{23}Na MAS NMR.

Some minor changes in peak position and shape can be seen as the temperature changes from ambient temperature to 200°C, although general peak shape appears to be retained throughout.

5.4.2 pXRD Results

The Snowbird quartz sample produced a clean diffraction pattern matching quartz, with only one small peak around $34^\circ 2\theta$ that remained unaccounted for.

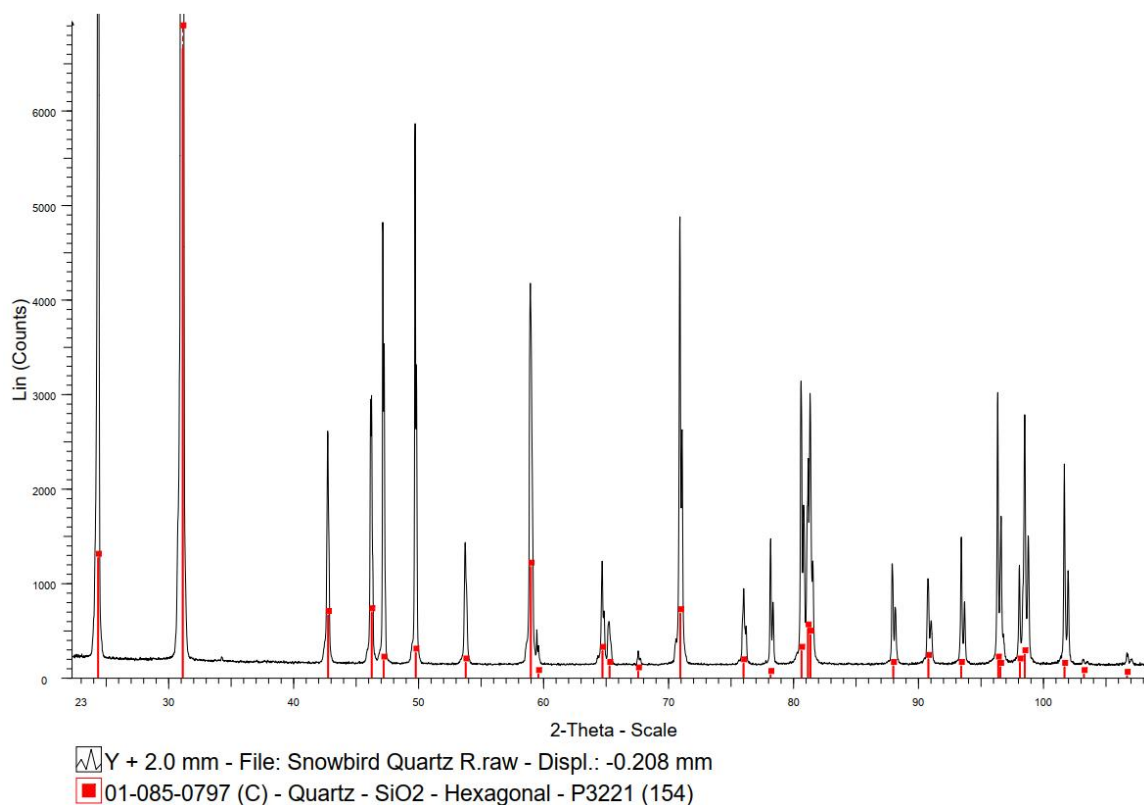


Fig. 5-3: Powder X-ray Diffraction pattern for Snowbird quartz with mineral match for quartz (ICDD Card #01-085-0797).

This peak alone is not enough to definitively identify a mineral phase and does not align with any diffraction peaks that are typical of halite samples. It appears that the Snowbird sample is purely quartz in composition and is devoid of any contaminant mineral phases.

5.5 Discussion

Between both the NMR and pXRD analysis, the Snowbird quartz sample raises more questions than any other sample analyzed over the course of this research. The pXRD pattern was matched to ICDD card #01-085-0797, indicating the sample is quartz in composition with a distinct lack of other mineral patterns present in the data. Apart from a small peak found around $34^\circ 2\theta$ (which was not enough to make a positive mineral identification) the Snowbird sample appears to be pure quartz (Fig. 5-3). The peak position does not correspond with major peaks found in either halite or fluorite diffraction patterns. This is particularly notable, since the Snowbird quartz sample

exhibited clear signals for both solid NaCl and liquid state solvated NaCl in the NMR analysis. It is uncertain why the halite phase was not identified, even with the extended scan time of nearly 14 hours which was intended to pick up minute amounts of mineral within the sample. The same sample that was used for NMR spectroscopy was also powdered for pXRD analysis, so there is no variation that can be attributed to differences in sampling. The pXRD powder was prepared anhydrously, eliminating the possibility that the halite was lost to solvation during preparation for pXRD analysis, and all fluid inclusion-bound halite should have been retained as the sample dried. It is most likely that the halite was too low in concentration within the bulk sample to be detected by the diffractometer, which has a lower detection limit of about 1 %. As with the Hansonburg fluorite sample, it is possible the halite was so minimal a significant amount was lost to ethanol solvation and not retained when the ethanol evaporated.

Unlike the Hansonburg fluorite which produced an NMR peak around 0 ppm that resembles the fluid peak observed in halite samples, the Snowbird sample produced a complex multi-peak lineshape that suggests that the signal may have been produced by a solid compound (Fig. 5-4). These complex peaks either suggest the presence of another sodium-bearing mineral within the sample, or the presence of multiple generations of fluid within the quartz. Because the pXRD pattern failed to detect any other mineral phases, it is unknown what this solid compound could be.

If it is assumed that these peaks correspond to different generations of fluid inclusion, significantly different internal environments in each population would be required to produce such large chemical shifts. The Snowbird deposit is known to have undergone two discrete mineralization stages with fluids of considerably different NaCl concentrations, however, it is unclear whether the variation between 20 wt.% NaCl could be resolved from 50 wt.% NaCl via NMR analysis, especially with the low fluid volumes that are present within fluid inclusions.

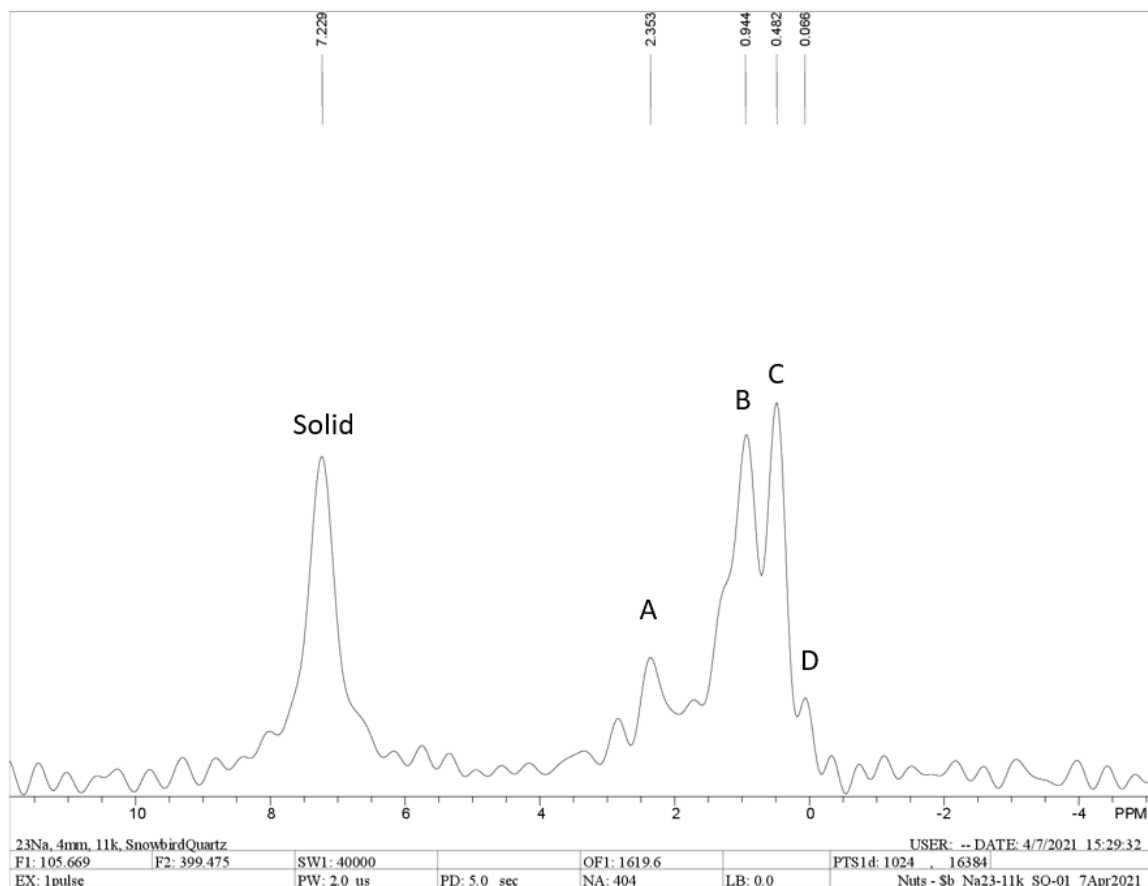


Fig. 5-4: Zoomed in portion of the Snowbird quartz ^{23}Na MAS NMR spectrum spinning at 11 kHz. Spectrum was collected at room temperature before Variable temperature analysis. Note the solid peak at 7 ppm and complex peaks at around 0.5 ppm.

Variable temperature NMR analysis of Snowbird quartz didn't offer any further insight into the nature of the sample. Some peak shifting was observed as the temperature was increased, but when plotting the chemical shift over the change in temperatures, the changes appear to be systematic. All peaks experience equivalent shifting across the different temperatures, and there is no definitive correlation as the temperature increases (Fig. 5-5).

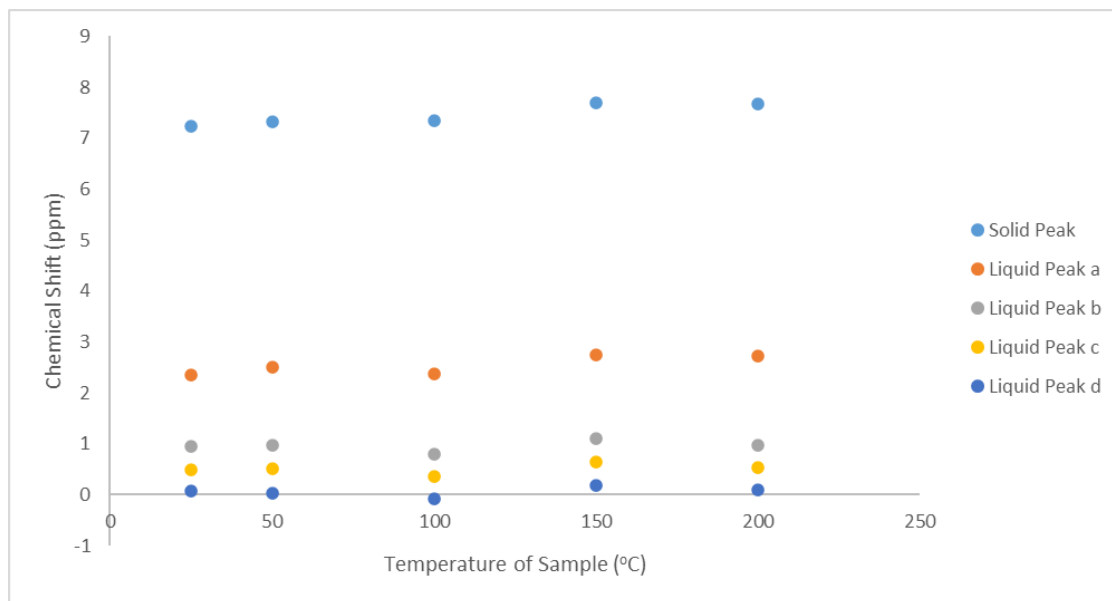


Fig. 5-5: Plot of each peak present in the Snowbird quartz sample and the relative shift with increasing temperature.

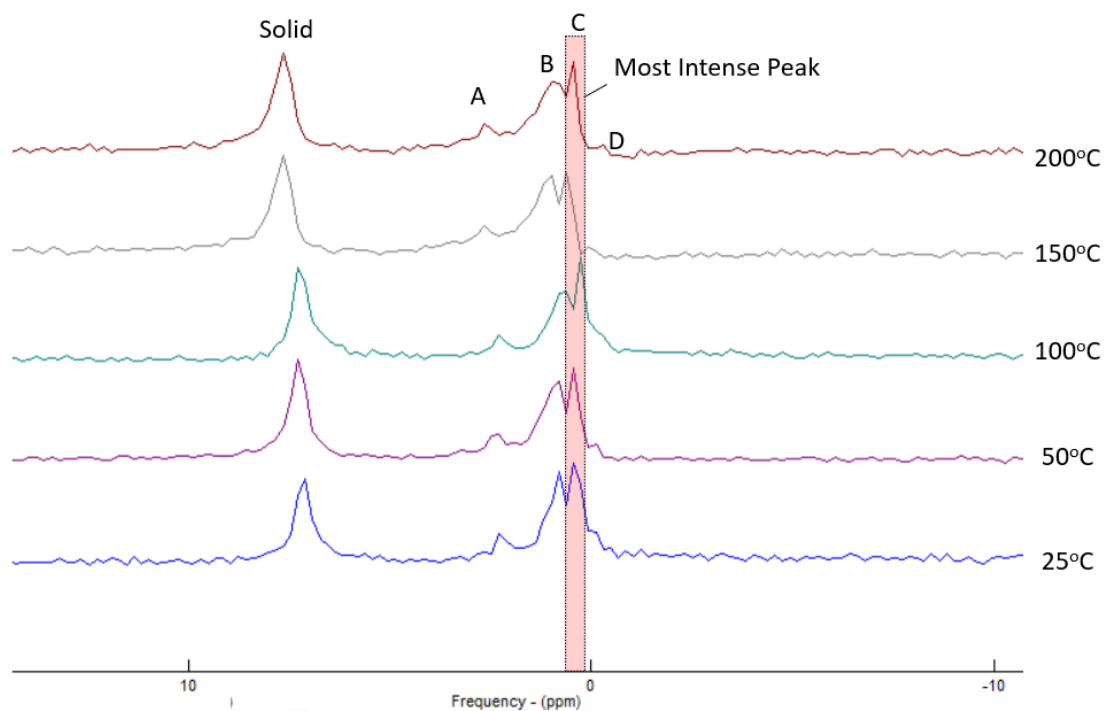


Fig. 5-6: Stacked plot of the Snowbird quartz VT ^{23}Na MAS NMR spectra highlighting the most intense ‘fluid’ peak used for estimating salinity.

If the assumption that the complex Snowbird quartz peaks were derived from a saline fluid is maintained, the most intense and narrowest peak could be taken as the chemical shift for the fluid signal. This was done for all analyses of the Snowbird quartz to estimate the hypothetical salinity. In every case, the central right peak was the most intense and used for salinity estimates (Fig. 5-6).

The result of the salinity calculations can be seen below (Fig. 5-7). Salinity estimates fell between 5 and 8 mol/L NaCl, or approximately 21-30 wt.% NaCl.

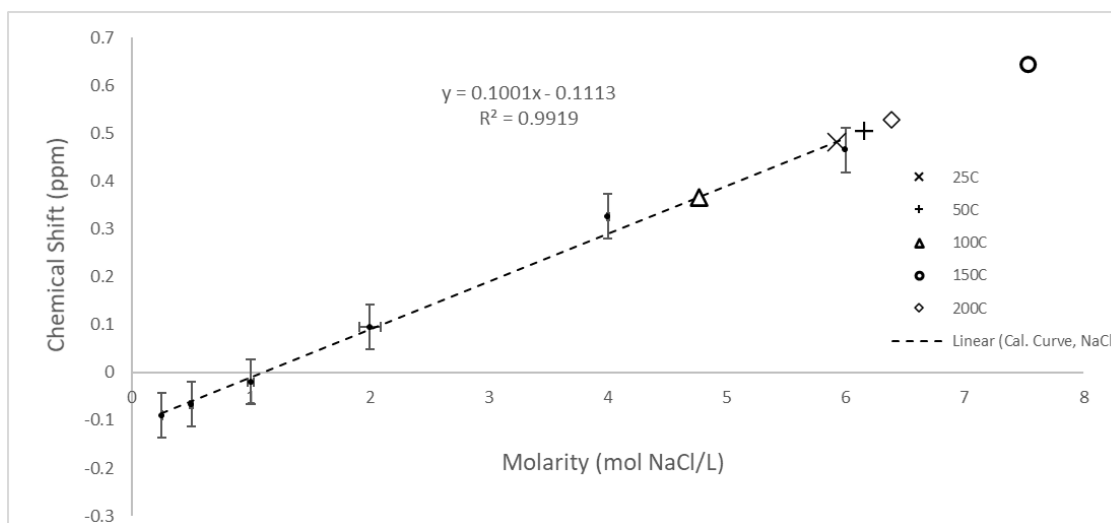


Fig. 5-7: Estimated salinity of the Snowbird quartz fluid signal at varying temperatures based on the standard NaCl calibration curve. There is no systematic chemical shift evident for the increase in temperature.

With Snowbird fluid salinity estimates ranging from 33 wt.% NaCl equivalent up to 50 wt.% NaCl equivalent in Stage I and approximately 29 wt.% equivalent NaCl in Stage II (Samson et al., 2004), the NMR estimates fall at the low end of the scale for estimated salinity for Stage I but overlaps with Stage II. It should be kept in mind, however, that the salinities acquired from microthermometry data are reported as equivalent weight percent of NaCl. Since NMR analysis does not rely on phase changes to estimate salinity, it is possible that the quantification of NaCl is differently influenced by other dissolved salts in solution. More research is required to understand how ^{23}Na NMR is affected by other ions in solution and the degree to which solvated ions influence the resultant signal. Also of note is that the salinity estimates varied wildly with increasing temperatures of

the same sample. Estimates of salinity should be made by analyzing the sample at the same temperature at which the calibration curve was established. The room temperature ^{23}Na NMR analysis of this Snowbird sample indicates a salinity of ~ 5.9 M NaCl, or 25.72 wt.% NaCl equivalent extrapolated from the linear regression of our calibration curve.

It has been shown that changes in both temperature and pressure produce different chemical shifts in NMR, especially for hydrogen-bonded species such as liquid water (Trainor et al., 2020). Increased temperature is known to shift proton chemical shifts to a higher frequency increase their shielding as the extra thermal energy loosens hydrogen bonds and localizes the electrons closer to the proton. Increased pressure on liquid water followed the same effects as temperature until 2-3 kbars of pressure was exceeded, after which the effect appears to act in direct opposition to temperature, causing a deshielding effect on the protons (Linowski et al., 1976). Although the effects of pressure and temperature are relatively well understood for ^1H NMR (Gottlieb et al., 1997; Linowski et al., 1976; Malinowski et al., 1966), the relationship between pressure/temperature and chemical shift is not as well documented for ^{23}Na NMR.

With this in mind, internal pressures for Snowbird quartz fluid inclusions are believed to be in the range of 2-3 kbars (Samson et al., 2004). It is possible that multiple instances of hydrothermal activity could have resulted in populations of fluid inclusions that are different enough in pressure and salinity to produce many peaks around 0.5 ppm, each corresponding to a different range of internal pressures and concentrations. Increasing temperature and increasing pressure both manifest differently in NMR spectroscopy and these effects need to be studied in isolation before the influence of pressure can be considered with respect to sodium chemical shifts. Synthesis of saline fluid inclusions over a range of pressures would be ideal for accurately modelling changes resulting from high-pressure sodium inclusions, isolated from any temperature changes.

Despite the possibility of these peaks being attributable to varying generations of fluid inclusions, another likely explanation must be kept in mind, that there is a sodium-bearing mineral within the Snowbird sample on the same order of concentration as the solid halite. The concentration of the unknown mineral was likely too low to be detected

by pXRD analysis but just high enough to be detected as a low-intensity signal in the NMR spectra. Unfortunately, no NMR match could be found for a similar spectral pattern in the literature that might suggest what compound would cause such a peak distribution. As far as determining the source of the complex NMR signal in Snowbird quartz, no definitive identification can be made until further research is performed on the sample, such as chemical analysis.

5.6 Conclusion

The ^{23}Na MAS NMR analysis of Snowbird quartz successfully identified solid halite and a sodium-associated signal at 7 ppm and 0.5 ppm, respectively. The solid halite signal appears to agree strongly with prior analyses of solid halite, but pXRD could not confirm the presence of solid NaCl within the Snowbird sample. The complex collection of peaks around 0.5 ppm are within the expected range for solvated sodium, however the multiple peaks cannot be adequately accounted for. It is possible it is a product of multiple generation of fluid inclusions, but an equally likely explanation is that the signal is caused by a sodium-bearing mineral that (like the halite) has evaded detection by pXRD. The variable temperature NMR experiment did little in the way of elucidating any new information about the sample but confirms that chemical shifts are not consistent with changes in temperature. Calibration curves for NMR spectroscopy, as with most analytical techniques, only function properly under the conditions they were established under. The estimated average salinity for the Snowbird quartz fluid inclusions was determined to be approximately 25 wt.% NaCl at ambient temperature using ^{23}Na NMR spectroscopy.

5.7 References

Cressman, E. R. (1985). The Prichard Formation of the lower part of the Belt Supergroup (Middle Proterozoic), near Plains, Sanders County, Montana. In *The Prichard Formation of the lower part of the Belt Supergroup (Middle Proterozoic), near Plains, Sanders County, Montana* (USGS Numbered Series No. 1553; Bulletin, Vol. 1553). U.S. Geological Survey. <https://doi.org/10.3133/b1553>

- Gott, G. B., & Cathrall, J. B. (1980). *Geochemical-Exploration Studies in the Coeur d'Alene District, Idaho and Montana*. 69.
- Gottlieb, H. E., Kotlyar, V., & Nudelman, A. (1997). NMR Chemical Shifts of Common Laboratory Solvents as Trace Impurities. *The Journal of Organic Chemistry*, 62(21), 7512–7515. <https://doi.org/10.1021/jo971176v>
- Hobbs, S. W., Campbell, A. B., Griggs, A. B., & Wallace, R. E. (1965). *Geology of the Coeur d'Alene district, Shoshone county, Idaho*.
- Linowski, J. W., Liu, N., & Jonas, J. (1976). Pressure dependence of the proton NMR chemical shift in liquid water. *The Journal of Chemical Physics*, 65(8), 3383–3384. <https://doi.org/10.1063/1.433473>
- Malinowski, E. R., Knapp, P. S., & Feuer, B. (1966). NMR Studies of Aqueous Electrolyte Solutions. I. Hydration Number of NaCl Determined from Temperature Effects on Proton Shift. *The Journal of Chemical Physics*, 45(11), 4274–4279. <https://doi.org/10.1063/1.1727486>
- Metz, M. C., Brookins, D. G., Rosenberg, P. E., & Zartman, R. E. (1985). Geology and geochemistry of the Snowbird Deposit, Mineral County, Montana. *Economic Geology*, 80(2), 394–409. <https://doi.org/10.2113/gsecongeo.80.2.394>
- Sahinen, U. M. (1962). *Fluorspar deposits in Montana*. Montana School of Mines.
- Samson, I. M., Wood, S. A., & Finucane, K. (2004). Fluid Inclusion Characteristics and Genesis of the Fluorite-Parisite Mineralization in the Snowbird Deposit, Montana. *Economic Geology*, 99(8), 1727–1744. <https://doi.org/10.2113/gsecongeo.99.8.1727>
- Trainor, K., Palumbo, J. A., MacKenzie, D. W. S., & Meiering, E. M. (2020). Temperature dependence of NMR chemical shifts: Tracking and statistical analysis. *Protein Science*, 29(1), 306–314. <https://doi.org/10.1002/pro.3785>

Chapter 6

6 Overview of Research and Suggested Future Work

This chapter has been included to summarize the findings from the research and integrate the results from the previous chapters (3. Halite, 4. Fluorite, and 5. Quartz) to form a generalized and coherent conclusion about the prospects of using ^{23}Na Nuclear Magnetic Resonance (NMR) spectroscopy to study geological samples. Although many valuable insights were gained from this study, there is much more work that can be done to understand and utilize NMR spectroscopy in a geological context. A few ideas will be outlined for possible future work.

6.1 Studying Fluid Inclusions with NMR Spectroscopy

The initial idea and inspiration for attempting to study fluid inclusions began with a paper by Sherriff et al. (1987), wherein sharp fluid peaks were noted on the ^{23}Na NMR spectrum of a synthetic beryl sample. Their research concluded that it was possible to detect fluid inclusions in mineral samples despite the small amount of fluid that is contained in them. Since then, other research has employed fluid inclusions to study high pressure systems and interpret organic content using proton (^1H) NMR (Brodholt & Wood, 1994; Dereppe et al., 1994; Withers et al., 2000), and ^{13}C NMR has also been used to detect hydrocarbons within synthetic samples (Kim et al., 2016; Yesinowski et al., 1988). Proton NMR was used to probe the effects of salinity as early as 1966 (Malinowski et al., 1966), and research applications continue to grow to this day.

This research began by determining whether the same relationship between chemical shift and salinity found in proton NMR (Malinowski et al., 1966) existed for ^{23}Na NMR spectroscopy as well. The experimental calibration curve determined that there was indeed a linear relationship between NaCl concentration in solution and the observed chemical shift in ^{23}Na NMR. Similar research was conducted for solvation of sodium iodide (NaI) using ^{23}Na NMR in various solvents and at various concentrations (Bloor & Kidd, 1968), but no definitive correlation between Na concentration and ^{23}Na chemical shifting was formally established.

The dilution scheme outlined in Chapter 2 was used to produce a calibration curve associating the chemical shift with the concentration of NaCl in deionized water. The relationship was subsequently used to extrapolate an estimated salinity for fluids trapped within geological samples of halite, fluorite, and quartz (see Chapters 3, 4, and 5, respectively) to determine the viability of this approach to determining salinity in situ. In halite samples, where the fluid is assumed to be at saturation and in equilibrium with the host crystal, chemical shifts plotted towards the high end of estimated salinity. These results were promising but they don't appear to possess a high degree of analytical power due to the small range of concentrations reported across the halite samples. The main drawback to using NMR spectroscopy for measurements such as salinity is that the chemical shift range over the breadth of salinities is not very large, thus discriminating between a 1 M NaCl solution and a 4 M NaCl solution may come down to a difference of a few decimal points. A higher field spectrometer would be required to establish a more reliable measure of salinity via chemical shift; even though the difference in chemical shift would remain small, the resolution between peaks would become much higher (i.e. much smaller gradations on the "scale") and a higher certainty can be achieved with a smaller margin of error.

In principle, measuring the salinity of a fluid inclusion using NMR spectroscopy (^{23}Na or ^1H) becomes more difficult when considering confounding variables that are all too common in natural samples. Components such as internal pressure, temperature of analysis, and mineral/chemical contaminants can all play a role in influencing the signal obtained through NMR. With systematic research on how each of these aspects contribute to the NMR signal, it may be possible to determine internal pressure, salinity, and the rough composition of a mineral's fluid inclusion with a few scans in an NMR spectrometer. The potential for each of these aspects has been proven in isolation, but they lack integration and do not produce a coherent understanding of how these parameters act concurrently.

6.2 Potential Future Work

Interactions between different geologically relevant contaminants could be investigated using a spiked calibration liquid scheme; this is a fundamental and essential step towards

applying ^{23}Na NMR spectroscopy to any naturally occurring mineral sample. There is some evidence that the presence of SO_4^{2-} in solution creates a shielding effect on sodium ions in solution, but this is unconfirmed and would be interesting to investigate. By varying the relative concentrations of both sodium other cations/anions in solution, systematic changes can be documented and used to interpret the spectra of novel samples. In this manner, ions with less impact on the NMR signal could be neglected while those that have a larger impact could be factored into the interpretation of the NMR data.

The effect of pressure could be investigated using synthetic fluid inclusions with a controlled brine composition and probed with ^{23}Na NMR. Pure water has been used to measure H_2O density at extreme pressures using proton NMR (Withers et al., 2000), but the effects of pressure have not been observed using ^{23}Na NMR. The scale of the chemical shift using proton NMR is less than 1 ppm over the span of 2.6 GPa of pressure (1.4 GPa to 4 GPa), but without experimental data, the change in ^{23}Na NMR is still unknown. The effect may be negligible, or it could be highly indicative depending on what influence it has on the solvated sodium ions.

We understand how the concentration of NaCl affects the chemical shift in ^{23}Na NMR spectroscopy; higher concentrations of NaCl in solution will cause deshielding of the sodium nuclei and induce a positive chemical shift (to higher frequency). This is only one part of the equation, however, and it contributes approximately 1 ppm to the chemical shift of the ^{23}Na NMR signal. By integrating various dimensions of influence on the signal observed from a fluid inclusion, NMR analysis of fluid inclusions can become much more analytically powerful. The signal that is observed from a sample should be considered as a summation of multiple effects (both macro- and microscopic) acting on the nucleus, we now need to quantify the magnitude of each component.

Once the magnitude of influence is known for changes in internal pressure and for different combinations of common solutes, the overall change in signal can be broken down by component (Fig. 6-1).

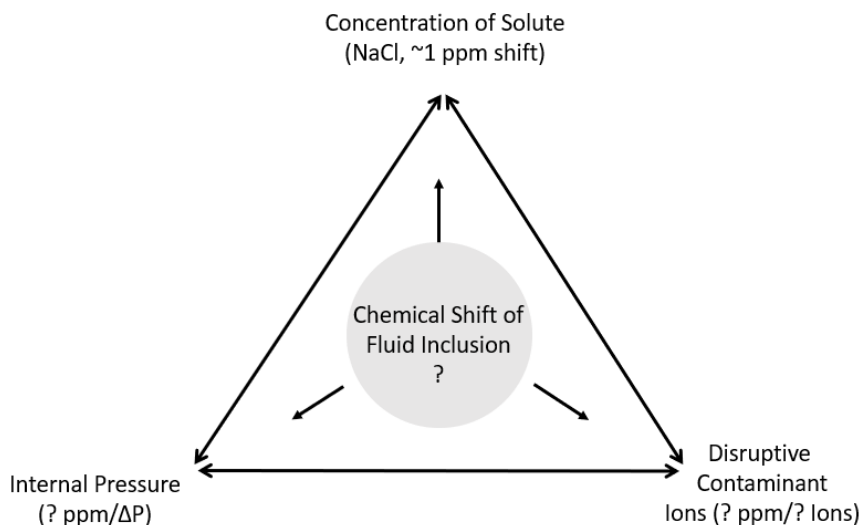


Fig. 6-1: Potential factors influencing the ^{23}Na NMR chemical shift of geological fluid inclusions, as well as shift range if known.

The possibility of discerning two separate generations of fluid inclusions was introduced within the Quartz chapter (Chapter 5), suggesting that it may be possible to differentiate between two discrete phases of mineralization and/or hydrothermal activity using a single NMR analysis. This is heavily speculative and would require further experimental evidence to prove the concept. Perhaps two different coarsely ground crystalline samples in the same sample rotor could determine whether the two fluid inclusion populations can be distinguished or if they appear as one signal on the spectrum. Synthetic fluid inclusions could even be used as internal standards while analyzing novel samples, allowing quantitative integration of NMR peaks and provide absolute concentration of Na nuclei within a sample with a high degree of precision. This would require carefully synthesized samples with very precise volumes of fluid, but it is possible in theory.

In order for NMR to be a viable tool in the geologist's toolkit, foundational information needs to be established to give predictive power to these new techniques and provide context for analytical results they provide.

6.3 Unexplained Results

Over the course of the research, a number of observations were made that still do not have a definitive interpretation. These are outlined briefly below.

6.3.1 X-ray Burn on Powder X-ray Diffraction Samples

Every sample that was analyzed using pXRD came out of the diffractometer with a distinctive ‘burn’ pattern across the powder where the X-rays contacted the sample (Fig. 6-2). This is not a unique occurrence; virtually all samples that are exposed to the X-ray diffractometer produce this distinctive patina that persists indefinitely.



Fig. 6-2: X-ray burn on a selection of samples after pXRD analysis. From left to right: DC-5477, Salton Sea, DeLaval Blue, 99.9% AnalR, Gonzales Fluorite.

No subsequent analysis was performed on any processed samples; however, it would be interesting to uncover what the cause is behind this phenomenon. The crystal structure does not appear to be affected, since the diffraction pattern does not change over the course of the scan time, and there is no apparent change to the sample otherwise. Each sample slide post-pXRD can be found in Appendix C, with the exception of Snowbird quartz and Hansonburg fluorite. Images were not collected of these slides post-processing.

6.3.2 Complex NMR Peaks in Snowbird Quartz

There is still no definitive conclusion about the identity of the peaks between -1 and 5 ppm that were observed on the Snowbird quartz ^{23}Na MAS NMR spectrum. Similar to the TronaCA sample, the signal appears predominantly in a region where we do not

expect to see multiple peaks, only a single fluid peak is expected (Fig. 6-3). The lowest frequency signal nearest to 0 ppm falls on the high end of the salinity calibration curve at approximately 5.7 M NaCl. This is a reasonable value for the Snowbird sample, but the peak shape is not the same narrow singlet observed in the other halite samples that had fluid signals.

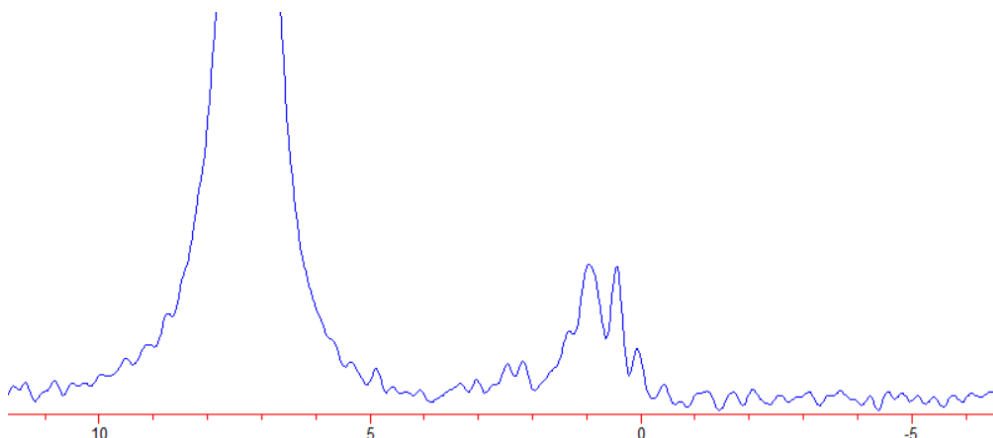


Fig. 6-3: Exaggerated and zoomed Snowbird quartz ^{23}Na NMR spectrum showing the unidentified peak shape between -1 and 3 ppm.

Unlike TronaCA, however, there were no reasonable matches for any contaminant minerals from the pXRD data so there is no indication as to what may be producing the extra peaks. If it is a solid mineral phase, it must contain sodium; as stated in Chapter 5 there is a possibility that these peaks are a product of different fluid inclusion populations. It is also possible that the deshielding that is shifting the peaks to high frequency may be attributable to sulphates or other dissolved contaminants effecting the local chemical environment around the solvated sodium ions. Establishment of a ^{23}Na MAS NMR database for Na-bearing minerals is required to definitively assign these peaks empirically.

6.4 References

- Bloor, E. G., & Kidd, R. G. (1968). Solvation of sodium ions studied by ^{23}Na nuclear magnetic resonance. *Canadian Journal of Chemistry*, *46*(22), 3425–3430.
<https://doi.org/10.1139/v68-569>
- Brodholt, J. P., & Wood, B. J. (1994). Measurements of the PVT properties of water to 25 kbars and 1600°C from synthetic fluid inclusions in corundum. *Geochimica et Cosmochimica Acta*, *58*(9), 2143–2148. [https://doi.org/10.1016/0016-7037\(94\)90292-5](https://doi.org/10.1016/0016-7037(94)90292-5)
- Dereppe, J.-M., Pironon, J., & Moreaux, C. (1994). Characterization of the composition of fluid inclusions in minerals by ^1H NMR. *American Mineralogist*, *79*(7–8), 712–718.
- Kim, E. J., Fei, Y., & Lee, S. K. (2016). Probing carbon-bearing species and CO_2 inclusions in amorphous carbon-MgSiO₃ enstatite reaction products at 1.5 GPa: Insights from ^{13}C high-resolution solid-state NMR. *American Mineralogist*, *101*(5), 1113–1124.
<https://doi.org/10.2138/am-2016-5563>
- Malinowski, E. R., Knapp, P. S., & Feuer, B. (1966). NMR Studies of Aqueous Electrolyte Solutions. I. Hydration Number of NaCl Determined from Temperature Effects on Proton Shift. *The Journal of Chemical Physics*, *45*(11), 4274–4279.
<https://doi.org/10.1063/1.1727486>
- Sherriff, B. L., Grundy, H. D., & Hartman, J. S. (1987). Analysis of fluid inclusions using nuclear magnetic resonance. *Geochimica et Cosmochimica Acta*, *51*(8), 2233–2235.
[https://doi.org/10.1016/0016-7037\(87\)90273-0](https://doi.org/10.1016/0016-7037(87)90273-0)
- Withers, A. C., Kohn, S. C., Brooker, R. A., & Wood, B. J. (2000). A new method for determining the P-V-T properties of high-density H₂O using NMR: Results at 1.4–4.0 gpa and 700–1100°C. *Geochimica et Cosmochimica Acta*, *64*(6), 1051–1057.
[https://doi.org/10.1016/S0016-7037\(99\)00318-X](https://doi.org/10.1016/S0016-7037(99)00318-X)
- Yesinowski, J. P., Eckert, Hellmut., & Rossman, G. R. (1988). Characterization of hydrous species in minerals by high-speed proton MAS-NMR. *Journal of the American Chemical Society*, *110*(5), 1367–1375. <https://doi.org/10.1021/ja00213a007>

Appendices

Appendix A: Inductively Coupled Plasma – Mass Spectrometry Data

Results

Activation Laboratories Ltd.

Report: A21-03310

Analyte Symbol	Ag	Al	As	Au	Ba	Be	Bi	Br	Ca	Cd	Ce	Cl	Co	Cr	Cs	Cu	Dy	Er	Eu	Fe	Ga	Gd	Ge
Unit Symbol	ppb	ppm	ppb	ppb	ppb	ppb	ppb	ppb	ppm	ppb	ppm	ppb	ppb	ppb									
Lower Limit	0.1	0.5	0.1	0.005	0.5	0.1	0.5	1	5	0.1	0.01	1000	0.2	3	0.01	1	0.01	0.01	0.01	1	0.3	0.01	0.05
Method Code	Deioniz ed-MS																						
TRONA, CA HALITE	< 10	< 50	7360	< 0.5	130	13.0	< 50	88500	< 500	< 10	3.55	760000000	< 20	< 300	1.39	833	< 1	< 1	< 1	< 100	< 30	< 1	< 5
BONAIRE HALITE	< 10	< 50	25.5	< 0.5	< 50	16.6	< 50	195000	< 500	< 10	< 1	816000000	< 20	< 300	1.31	< 100	< 1	< 1	< 1	< 100	< 30	< 1	< 5
DC-3137	< 10	< 50	41.4	< 0.5	58.5	< 10	< 50	77800	2030	< 10	2.97	799000000	< 20	< 300	10.8	< 100	< 1	< 1	< 1	< 100	< 30	1.04	< 5
DC-1922	< 10	< 50	18.1	< 0.5	457	< 10	< 50	112000	< 500	36.5	4.52	745000000	< 20	< 300	10.0	145	< 1	< 1	< 1	< 100	< 30	< 1	< 5
DC-5490	< 10	< 50	6130	< 0.5	< 50	< 10	< 50	73600	< 500	< 10	< 1	831000000	< 20	< 300	< 1	< 100	< 1	< 1	< 1	< 100	151	< 1	109
DC-730	< 10	< 50	33.3	< 0.5	428	27.8	< 50	183000	3860	27.6	1.78	806000000	< 20	< 300	< 1	< 100	< 1	< 1	< 1	< 100	< 30	< 1	< 5
SALTON SEA HALITE	2990	< 50	139	< 0.5	250000	12.0	< 50	10200	< 500	35700	4.14	826000000	115	< 300	101	365	< 1	< 1	2.09	< 100	< 30	< 1	< 5
DC-711	34.5	< 50	52.5	< 0.5	8640	19.8	< 50	45000	10800	46.7	1.12	706000000	20.9	< 300	20.0	343	< 1	< 1	< 1	< 100	< 30	< 1	< 5
DB-001	< 10	< 50	22.8	< 0.5	< 50	12.5	< 50	26300	< 500	< 10	< 1	849000000	< 20	< 300	< 1	152	< 1	< 1	< 1	< 100	71.3	< 1	36.6
STANDARD HALITE	< 10	< 50	23.6	< 0.5	< 50	20.9	< 50	25800	< 500	< 10	< 1	855000000	< 20	< 300	< 1	< 100	< 1	< 1	< 1	< 100	< 30	< 1	< 5
DC-5477	< 10	< 50	17600	< 0.5	< 50	16.7	< 50	129000	< 500	< 10	< 1	778000000	< 20	< 300	< 1	319	< 1	< 1	< 1	< 100	< 30	< 1	< 5
NMR LAB HALITE	< 10	< 50	26.8	< 0.5	< 50	< 10	< 50	49800	< 500	< 10	< 1	850000000	< 20	< 300	< 1	< 100	< 1	< 1	< 1	< 100	32.3	< 1	< 5

Results

Activation Laboratories Ltd.

Report: A21-03310

Analyte Symbol	Hf	Hg	Ho	I	In	K	La	Li	Lu	Mg	Mn	Mo	Na	Nb	Nd	Ni	Pb	Pd	Pr	Pt	Rb	Re	Ru
Unit Symbol	ppb	ppb	ppb	ppb	ppb	ppm	ppb	ppb	ppb	ppm	ppb	ppb	ppm	ppb									
Lower Limit	0.01	0.1	0.01	1	0.01	5	0.01	0.5	0.01	2	0.4	0.1	5	0.1	0.01	1	0.1	0.5	0.01	0.5	0.1	0.005	0.5
Method Code	Deioniz ed-MS																						
TRONA, CA HALITE	< 1	24.5	< 1	544	< 1	1920	< 1	3020	< 1	< 200	259	21.1	447000	< 10	< 1	< 100	162	< 50	< 1	< 50	542	< 0.5	< 50
BONAIRE HALITE	< 1	< 10	< 1	< 100	< 1	< 500	< 1	51.6	< 1	< 200	159	< 10	458000	< 10	< 1	< 100	74.6	< 50	< 1	< 50	< 10	< 0.5	< 50
DC-3137	< 1	< 10	< 1	< 100	< 1	< 500	1.52	70.6	< 1	< 200	267	< 10	444000	< 10	1.88	< 100	121	< 50	< 1	< 50	50.0	< 0.5	< 50
DC-1922	< 1	< 10	< 1	< 100	< 1	< 500	1.74	64.3	< 1	< 200	483	< 10	413000	< 10	3.71	< 100	< 10	< 50	< 1	< 50	230	< 0.5	< 50
DC-5490	< 1	13.3	< 1	121	< 1	884	< 1	1700	< 1	< 200	204	< 10	457000	< 10	< 1	< 100	12.0	< 50	< 1	< 50	239	< 0.5	< 50
DC-730	< 1	< 10	< 1	< 100	< 1	< 500	< 1	495	< 1	< 200	269	< 10	430000	< 10	1.53	< 100	630	< 50	< 1	< 50	53.0	< 0.5	< 50
SALTON SEA HALITE	< 1	< 10	< 1	< 100	< 1	< 500	3.87	390	< 1	< 200	61700	< 10	444000	< 10	1.13	< 100	525000	< 50	< 1	< 50	246	< 0.5	< 50
DC-711	< 1	< 10	< 1	< 100	< 1	< 500	< 1	103	< 1	< 200	588	< 10	377000	< 10	< 1	< 100	119	< 50	< 1	< 50	88.5	< 0.5	< 50
DB-001	< 1	< 10	< 1	< 100	< 1	< 500	< 1	< 50	< 1	< 200	146	< 10	452000	< 10	< 1	< 100	161	< 50	< 1	< 50	< 10	< 0.5	< 50
STANDARD HALITE	< 1	< 10	< 1	< 100	< 1	< 500	< 1	< 50	< 1	< 200	62.4	< 10	457000	< 10	< 1	< 100	48.5	< 50	< 1	57.4	< 10	< 0.5	< 50
DC-5477	< 1	53.5	< 1	2000	< 1	1960	< 1	4770	< 1	< 200	96.0	51.9	442000	< 10	< 1	< 100	36.4	< 50	< 1	< 50	795	< 0.5	< 50
NMR LAB HALITE	< 1	< 10	< 1	< 100	< 1	< 500	1.22	62.6	< 1	< 200	49.7	< 10	451000	< 10	< 1	< 100	42.9	< 50	< 1	< 50	< 10	< 0.5	< 50

Results

Activation Laboratories Ltd.

Report: A21-03310

Analyte Symbol	Sb	Sc	Se	Sm	Sn	Sr	Ta	Tb	Te	Th	Ti	Tl	Tm	U	V	W	Y	Yb	Zn	Zr
Unit Symbol	ppb																			
Lower Limit	0.01	10	1	0.01	0.2	0.1	0.02	0.01	0.5	0.01	10	0.005	0.01	0.01	0.1	0.1	0.05	0.01	5	0.1
Method Code	Deioniz ed-MS																			
TRONA, CA HALITE	420	< 1000	< 100	< 1	< 20	129	< 2	< 1	< 50	44.1	< 1000	1.96	< 1	546	24.4	2380	< 5	< 1	1560	89.8
BONAIRE HALITE	< 1	< 1000	< 100	< 1	< 20	510	< 2	< 1	< 50	< 1	< 1000	1.66	< 1	< 1	18.0	< 10	< 5	< 1	< 500	< 10
DC-3137	< 1	< 1000	< 100	< 1	< 20	6400	< 2	< 1	< 50	< 1	< 1000	6.09	< 1	< 1	14.0	< 10	< 5	< 1	< 500	< 10
DC-1922	14.3	< 1000	< 100	< 1	< 20	1840	< 2	< 1	< 50	< 1	< 1000	33.2	< 1	< 1	20.2	< 10	< 5	< 1	< 500	< 10
DC-5490	14.5	< 1000	< 100	< 1	114	60.9	< 2	< 1	< 50	< 1	< 1000	1.69	< 1	78.3	18.5	1320	< 5	< 1	< 500	< 10
DC-730	2.45	< 1000	< 100	< 1	< 20	116000	< 2	< 1	< 50	< 1	< 1000	1.51	< 1	< 1	14.0	< 10	< 5	< 1	< 500	< 10
SALTON SEA HALITE	23.3	< 1000	< 100	< 1	< 20	37300	< 2	< 1	< 50	< 1	< 1000	15.0	< 1	< 1	14.5	< 10	5.52	< 1	2240	< 10
DC-711	17.1	< 1000	< 100	< 1	< 20	209000	< 2	< 1	< 50	< 1	< 1000	9.78	< 1	4.04	19.2	< 10	< 5	< 1	< 500	< 10
DB-001	9.48	< 1000	< 100	< 1	35.9	36.6	< 2	< 1	< 50	< 1	< 1000	1.54	< 1	< 1	17.6	< 10	7.16	< 1	1150	< 10
STANDARD HALITE	< 1	< 1000	< 100	< 1	< 20	1070	< 2	< 1	< 50	< 1	< 1000	1.72	< 1	< 1	16.6	< 10	< 5	< 1	< 500	< 10
DC-5477	52.4	< 1000	< 100	< 1	88.4	346	< 2	< 1	< 50	5.75	< 1000	1.22	< 1	219	21.7	5340	< 5	< 1	< 500	< 10
NMR LAB HALITE	< 1	< 1000	< 100	< 1	< 20	497	< 2	< 1	< 50	< 1	< 1000	1.22	< 1	< 1	24.6	10.9	< 5	< 1	< 500	< 10

QC

Activation Laboratories Ltd.

Report: A21-03310

Analyte Symbol	Ag	Al	As	Au	Ba	Be	Bi	Br	Ca	Cd	Ce	Cl	Co	Cr	Cs	Cu	Dy	Er	Eu	Fe	Ga	Gd	Ge
Unit Symbol	ppb	ppm	ppb	ppb	ppb	ppb	ppb	ppb	ppm	ppb	ppm	ppb	ppb	ppb									
Lower Limit	0.1	0.5	0.1	0.005	0.5	0.1	0.5	1	5	0.1	0.01	1000	0.2	3	0.01	1	0.01	0.01	0.01	1	0.3	0.01	0.05
Method Code	Deioniz ed-MS																						
TILL-1 Meas			22.0	0.064	153	0.3		509		18.0			5.3	9	0.22	200		1.39	0.72	5			
TILL-1 Cert			18000	13	702000	2400.0		6400.0		71000			18000	65000	1000.0	47000		3600.0	1300.0	48100.00			
TILL-2 Meas			18.9	< 0.005	253	0.8		1290		58.5			5.8	12	1.50	238		3.27	1.57	2			
TILL-2 Cert			26000	2	540000	4000.0		12200.0		98000			15000	74000	12000	150000		3700.0	1000.0	38400.00			
Method Blank	< 10	< 50	< 10	< 0.5	< 50	< 10	< 50	< 100	< 500	< 10	< 1	< 100000	< 20	< 300	< 1	< 100	< 1	< 1	< 1	< 100	< 30	< 1	< 5

QC

Activation Laboratories Ltd.

Report: A21-03310

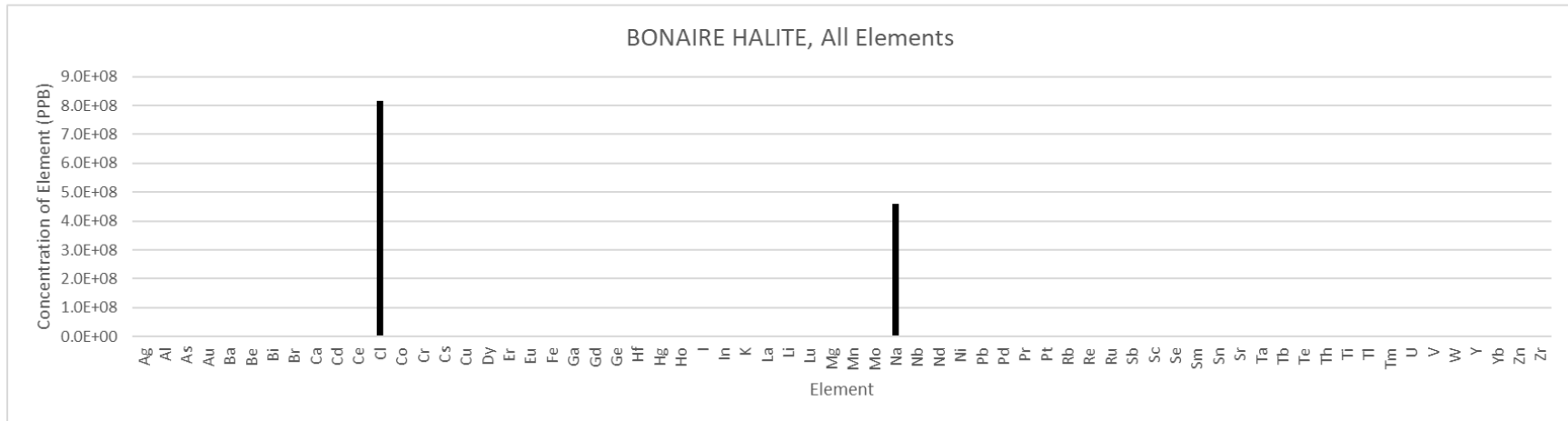
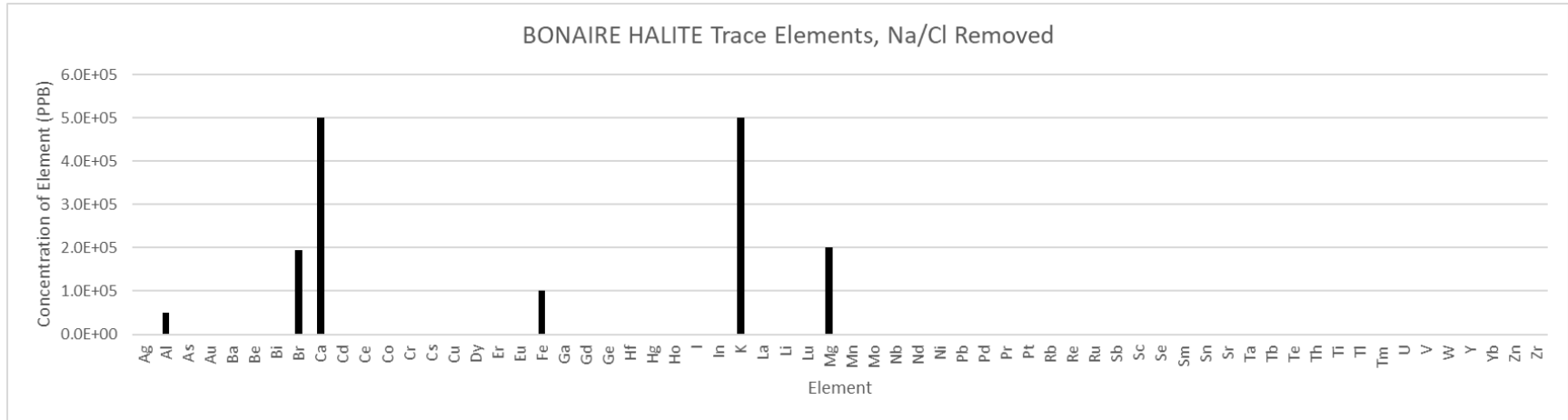
Analyte Symbol	Hf	Hg	Ho	I	In	K	La	Li	Lu	Mg	Mn	Mo	Na	Nb	Nd	Ni	Pb	Pd	Pr	Pt	Rb	Re	Ru
Unit Symbol	ppb	ppb	ppb	ppb	ppb	ppm	ppb	ppb	ppb	ppm	ppb	ppb	ppm	ppb									
Lower Limit	0.01	0.1	0.01	1	0.01	5	0.01	0.5	0.01	2	0.4	0.1	5	0.1	0.01	1	0.1	0.5	0.01	0.5	0.1	0.005	0.5
Method Code	Deioniz ed-MS																						
TILL-1 Meas	0.28	< 0.1					11.3	1.4	0.22		4800	3.1		0.2	14.7	11	4.3				35.9		
TILL-1 Cert	13000	90.0					28000	15000	600.0		142000	2000		10000	26000	24000	22000				44000		
TILL-2 Meas	0.89	< 0.1					26.8	4.7	0.46		2400	14.6		< 0.1	33.4	9	1.8				122		
TILL-2 Cert	11000	70.0					44000	47000	600.0		780000	14000		20000	36000	32000	31000				143000		
Method Blank	< 1	< 10	< 1	< 100	< 1	< 500	< 1	< 50	< 1	< 200	< 40	< 10	< 500	< 10	< 1	< 100	< 10	< 50	< 1	< 50	< 10	< 0.5	< 50

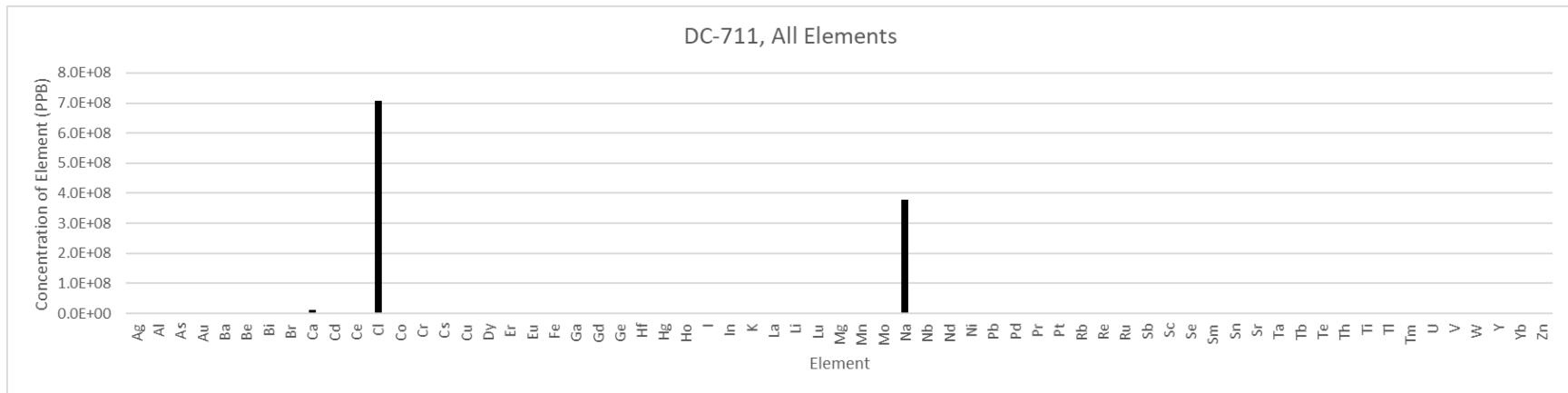
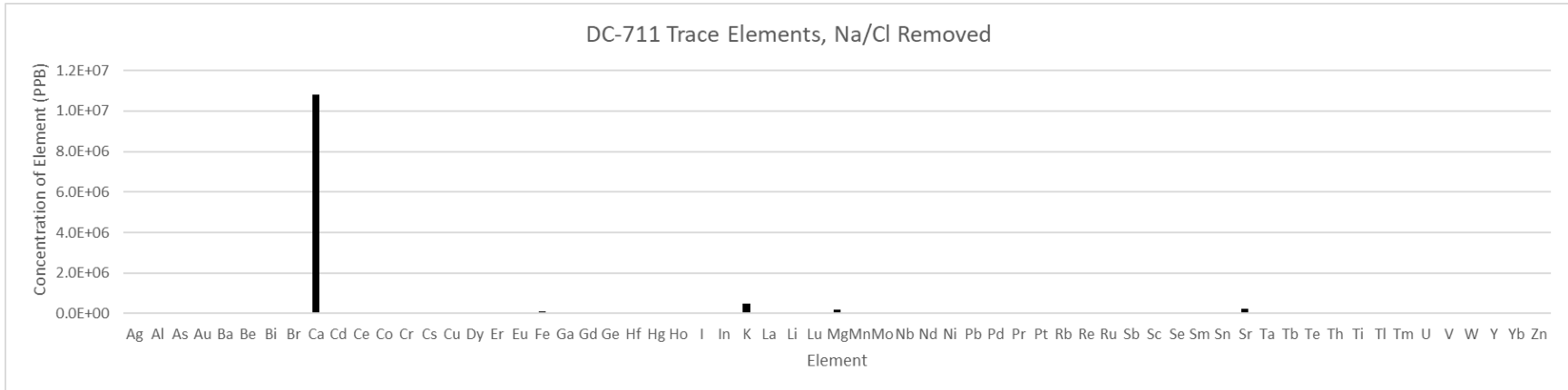
QC

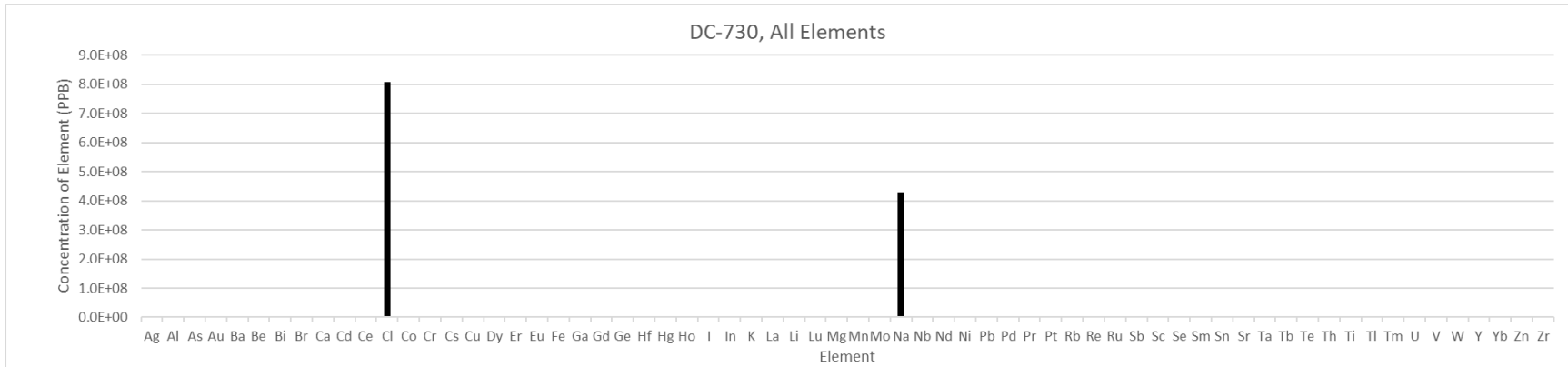
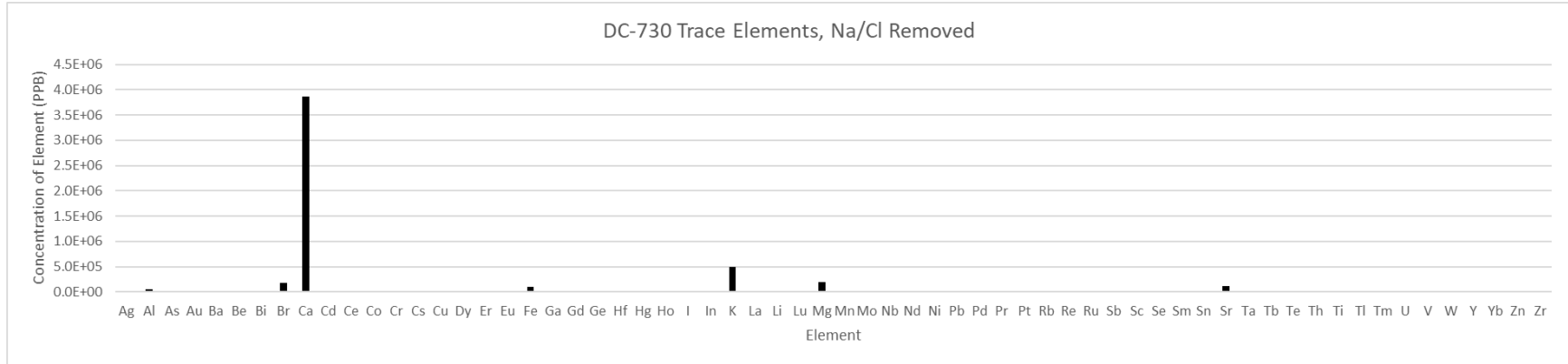
Activation Laboratories Ltd.

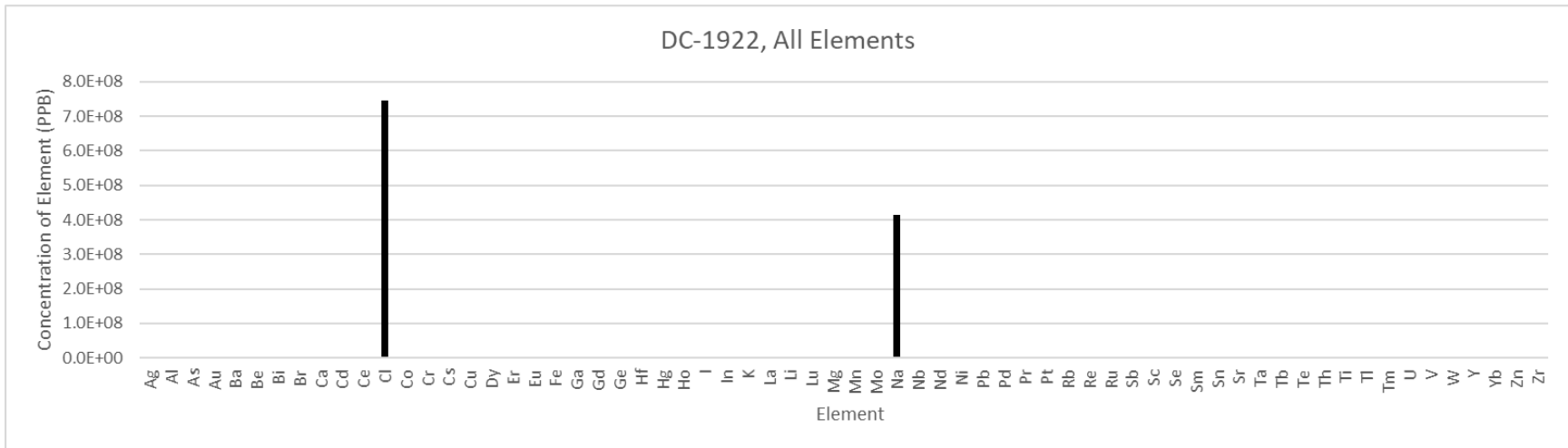
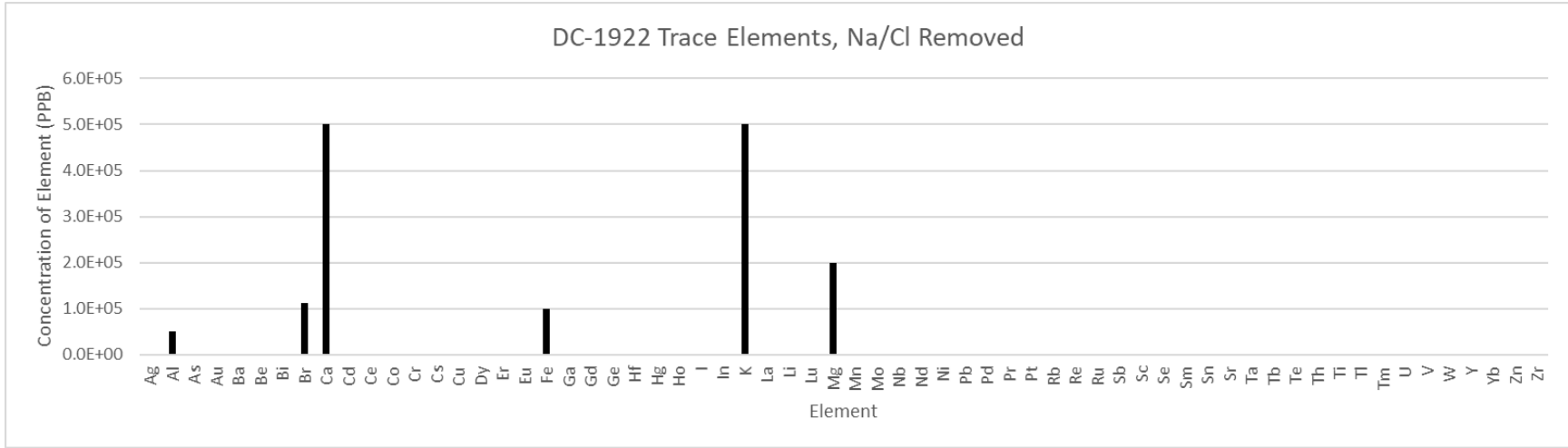
Report: A21-03310

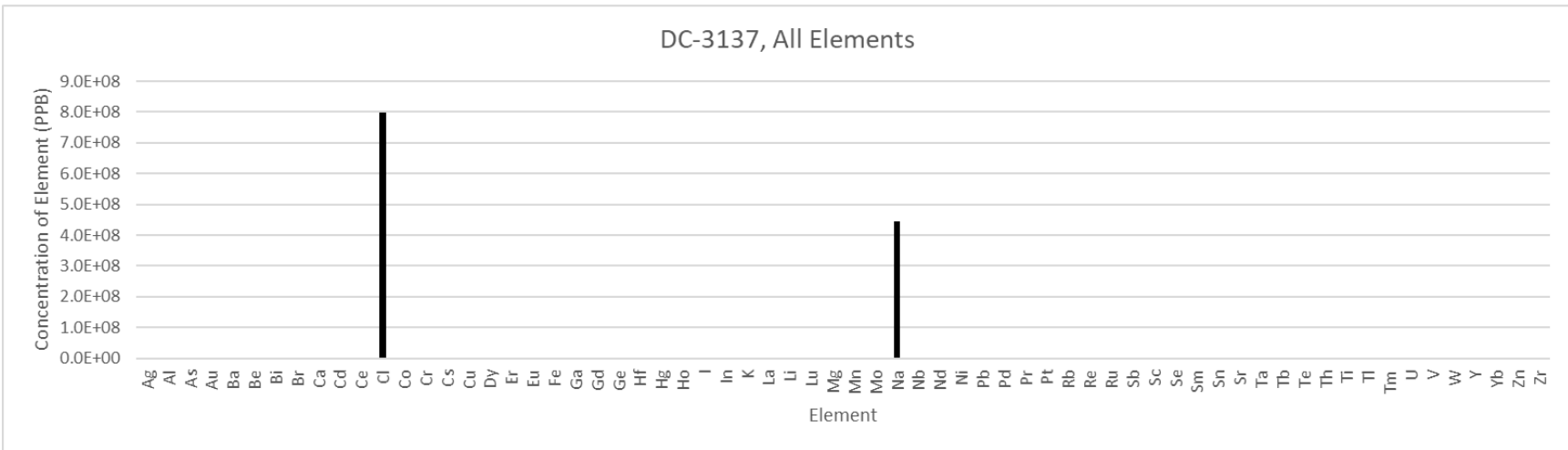
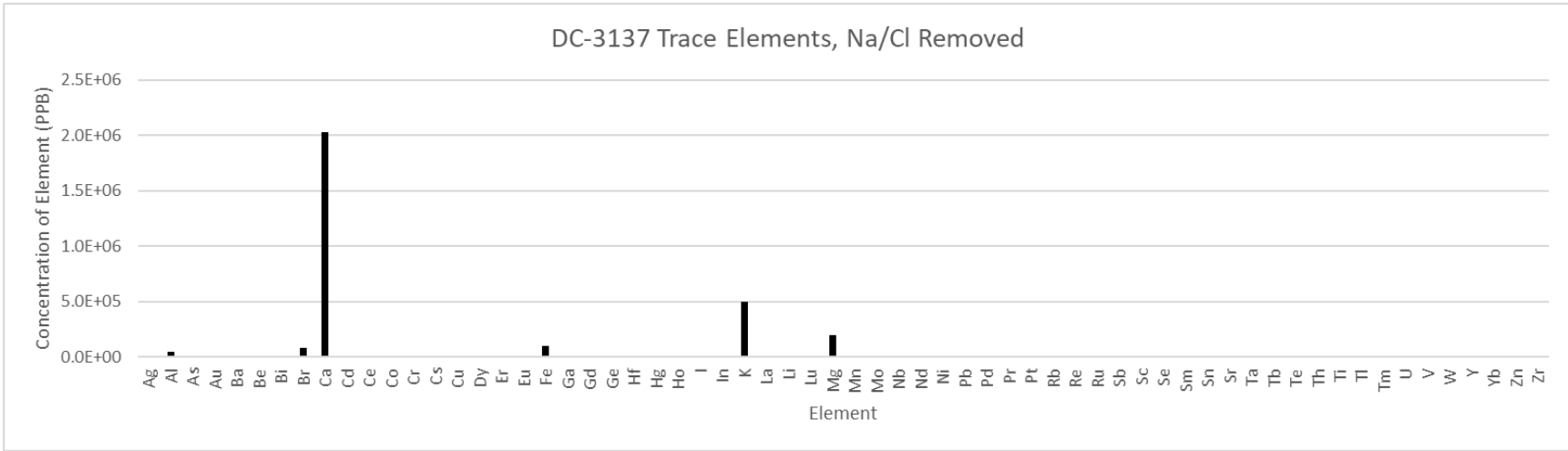
Analyte Symbol	Sb	Sc	Se	Sm	Sn	Sr	Ta	Tb	Te	Th	Ti	Tl	Tm	U	V	W	Y	Yb	Zn	Zr	
Unit Symbol	ppb																				
Lower Limit	0.01	10	1	0.01	0.2	0.1	0.02	0.01	0.5	0.01	10	0.005	0.01	0.01	0.1	0.1	0.05	0.01	5	0.1	
Method Code	Deioniz ed-MS																				
TILL-1 Meas	33.7	< 10		3.09		144	0.03	0.47		1.42	240			2.74	18.4		12.9	1.28	36	7.1	
TILL-1 Cert	7800.0	13000		5900.0		291000	700.0	1100.0		5600.0	599000			2200.0	99000		38000	3900.0	98000	502000	
TILL-2 Meas	1.32	< 10		7.10		238	0.02	1.07		5.10	110			11.2	9.3	1.1	32.4	2.90	40	22.5	
TILL-2 Cert	800.0	12000		7400.0		144000	1900.0	1200.0		18400.0	530000			5700.0	77000	5000	40000	3700.0	130000	390000	
Method Blank	< 1	< 1000	< 100	< 1	< 20	< 10	< 2	< 1	< 50	< 1	< 1000	< 0.5	< 1	< 1	< 10	< 10	< 5	< 1	< 500	< 10	

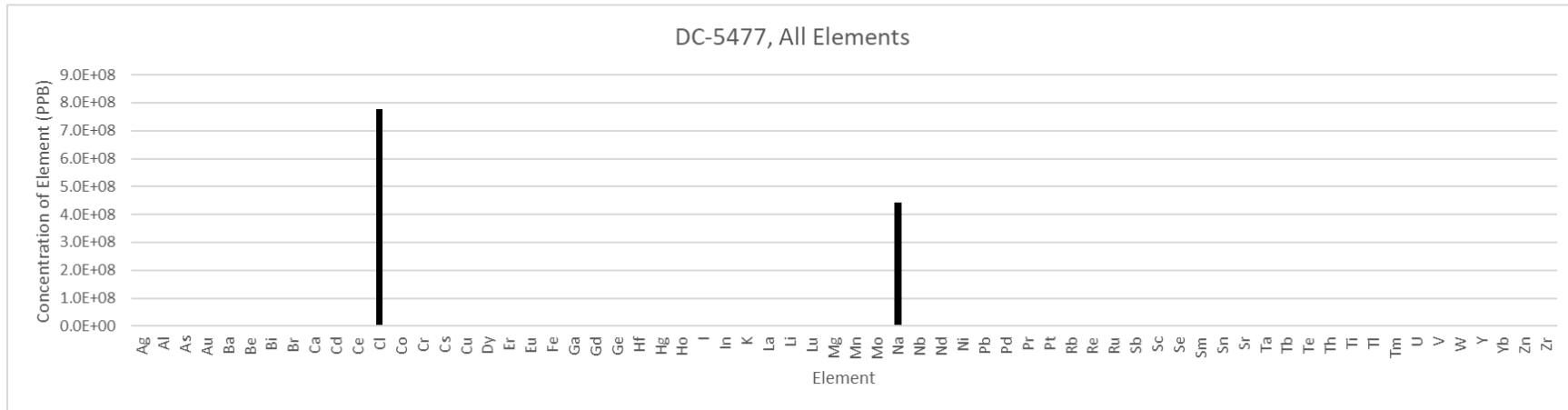
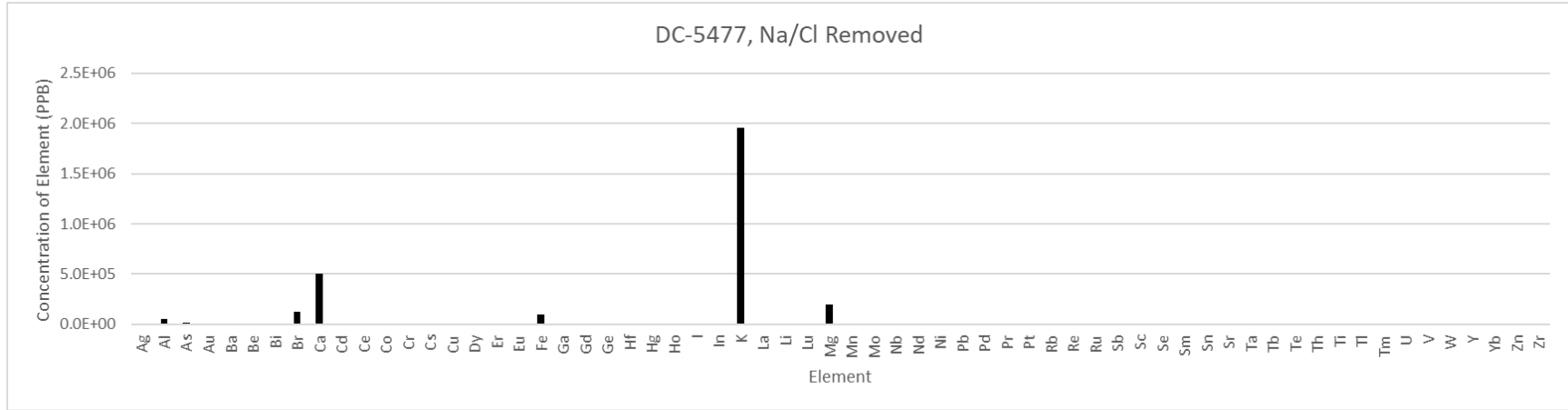


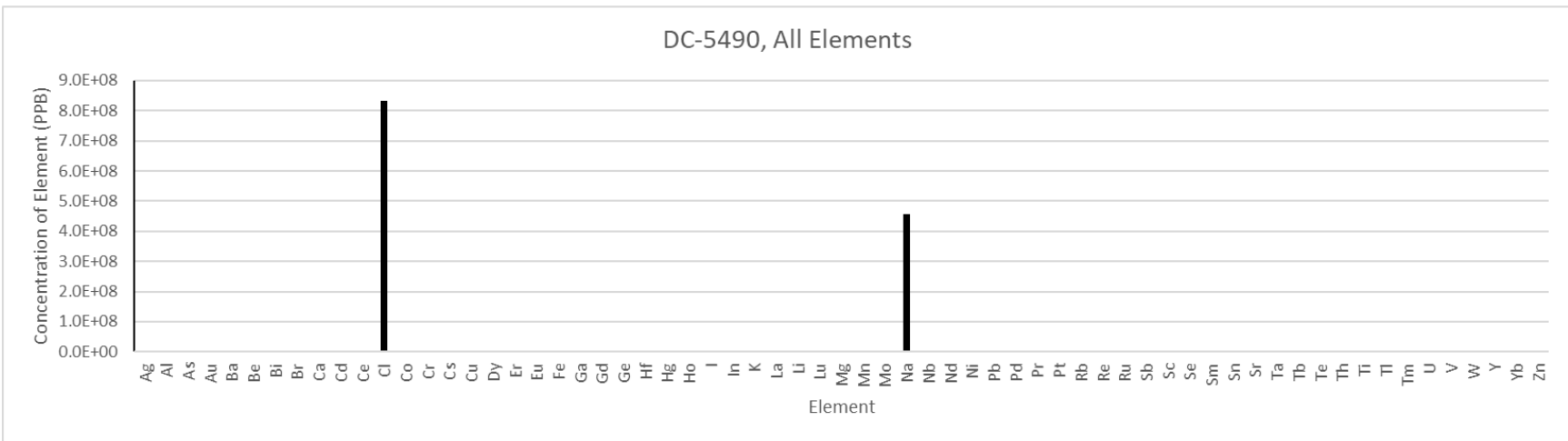
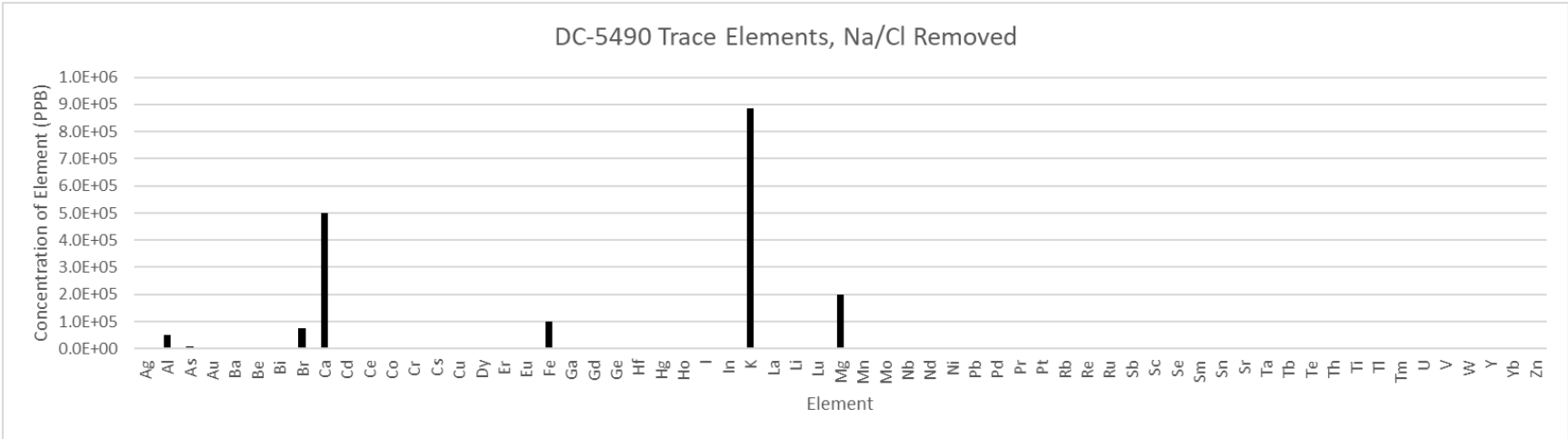


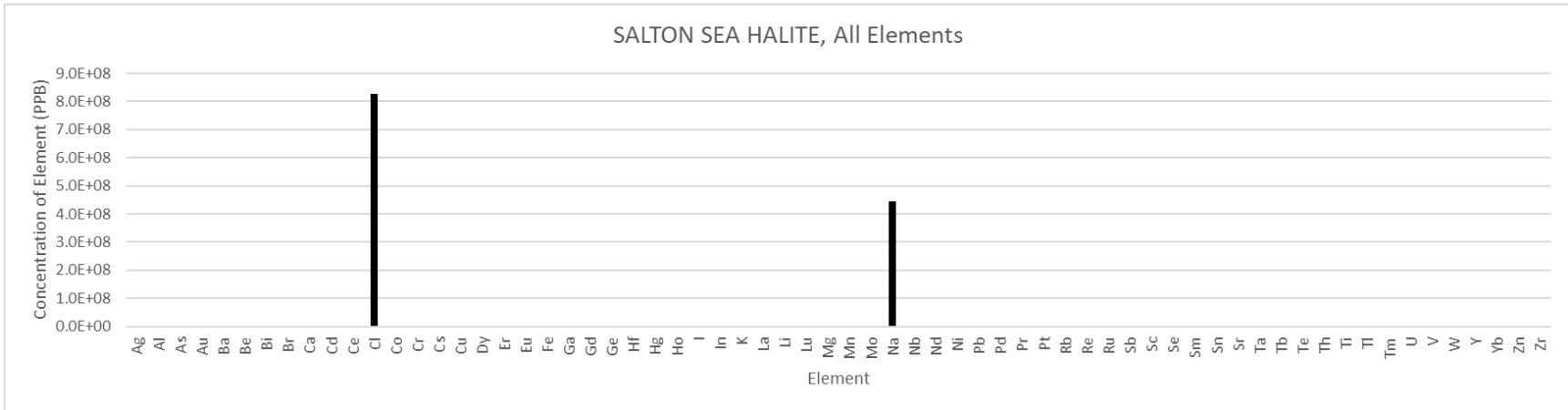
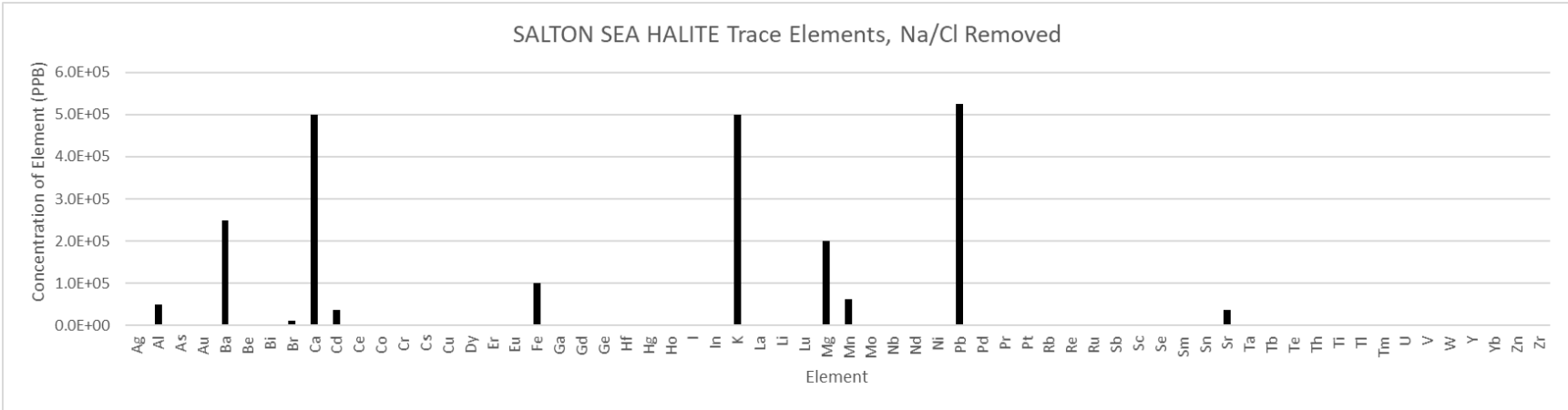




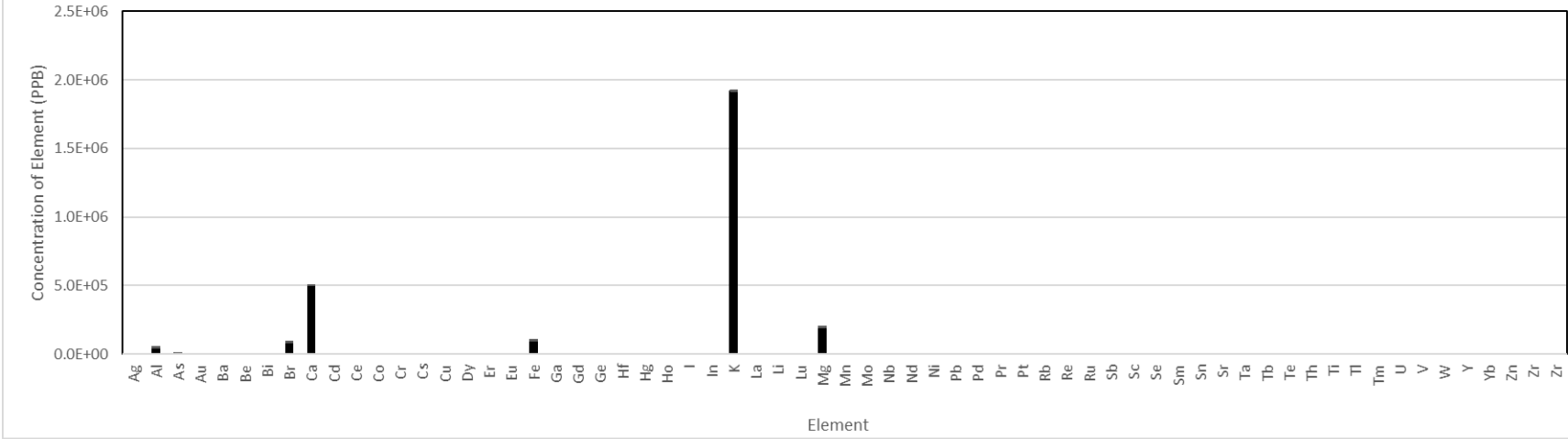




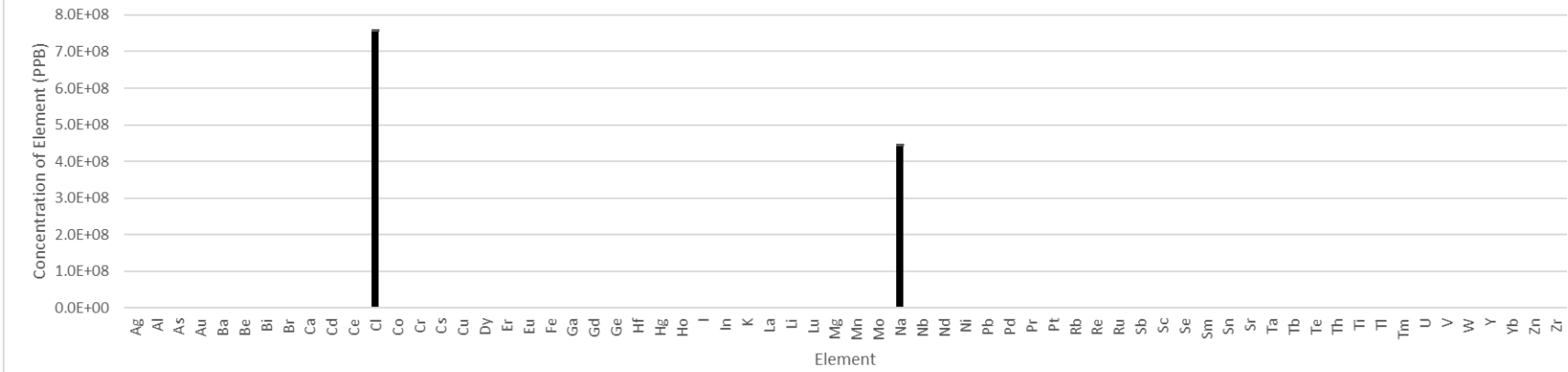


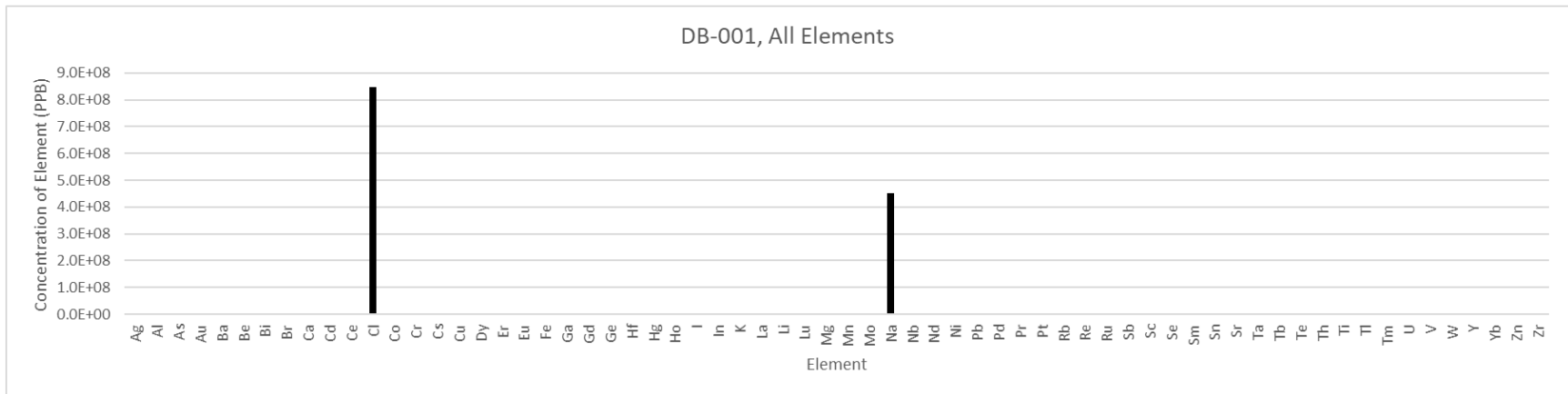
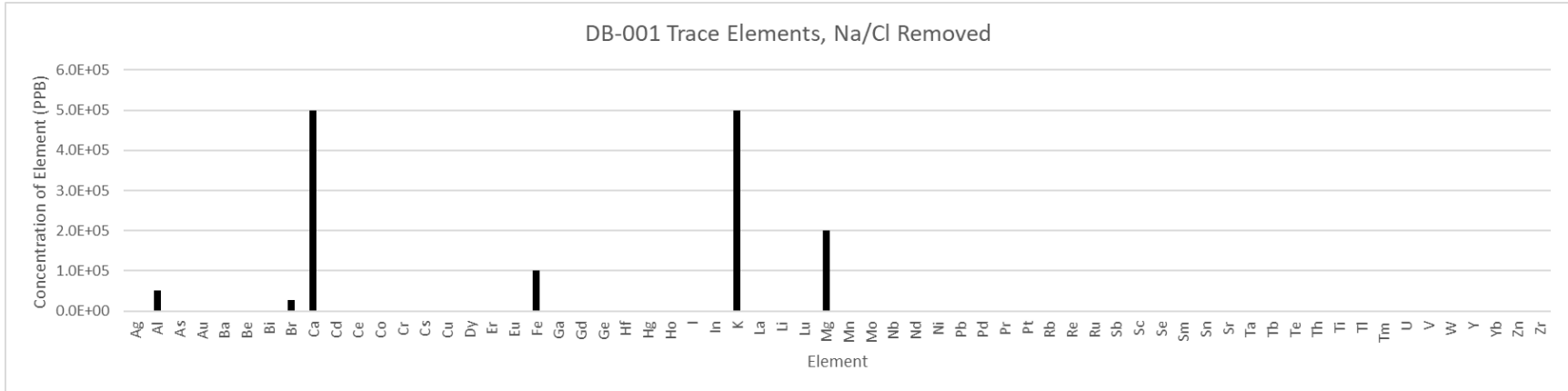


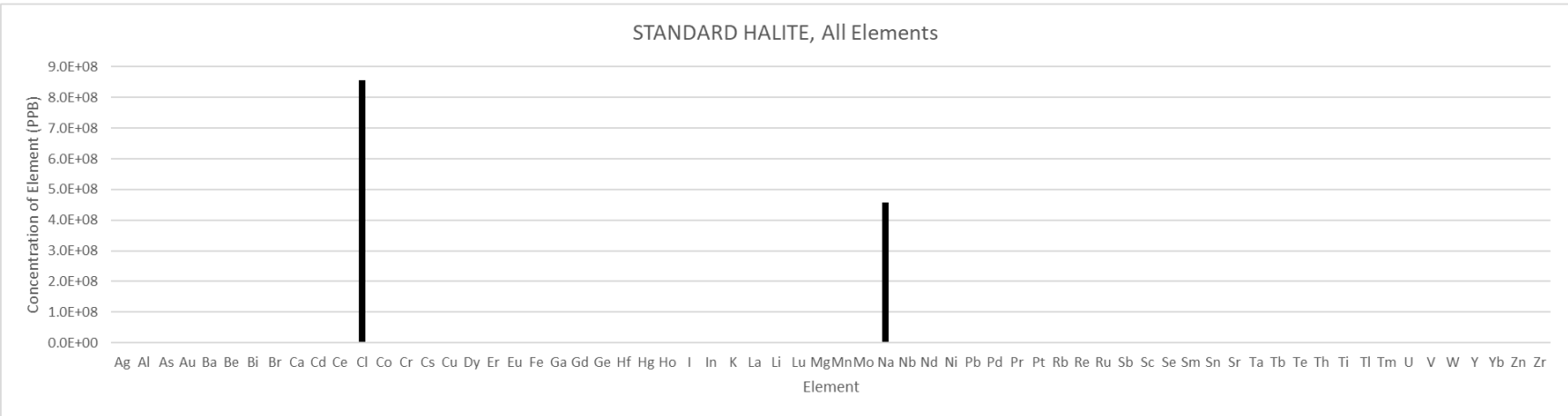
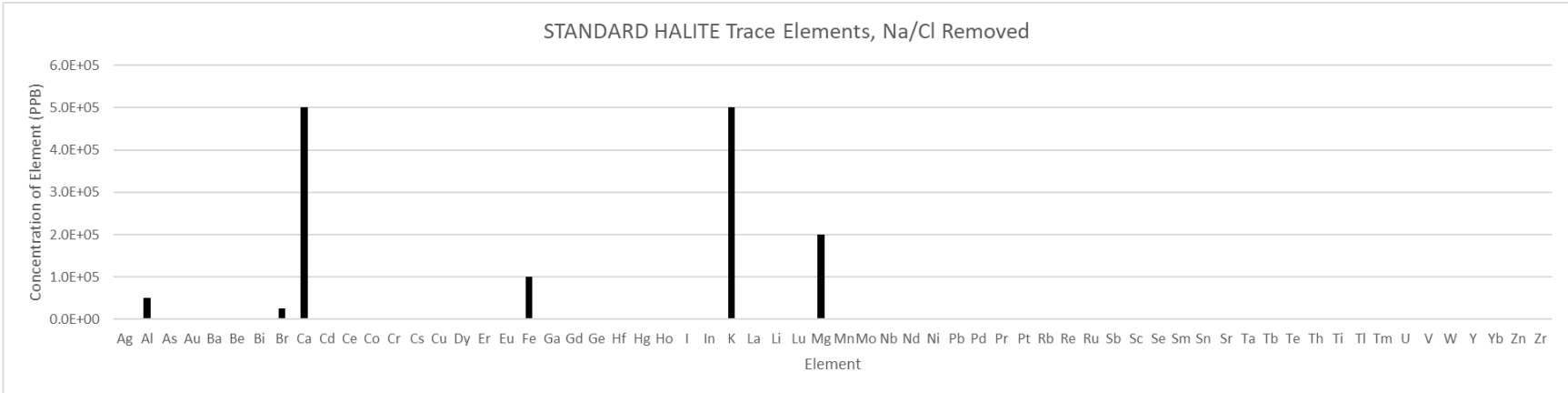
TRONA, CA HALITE Trace Elements

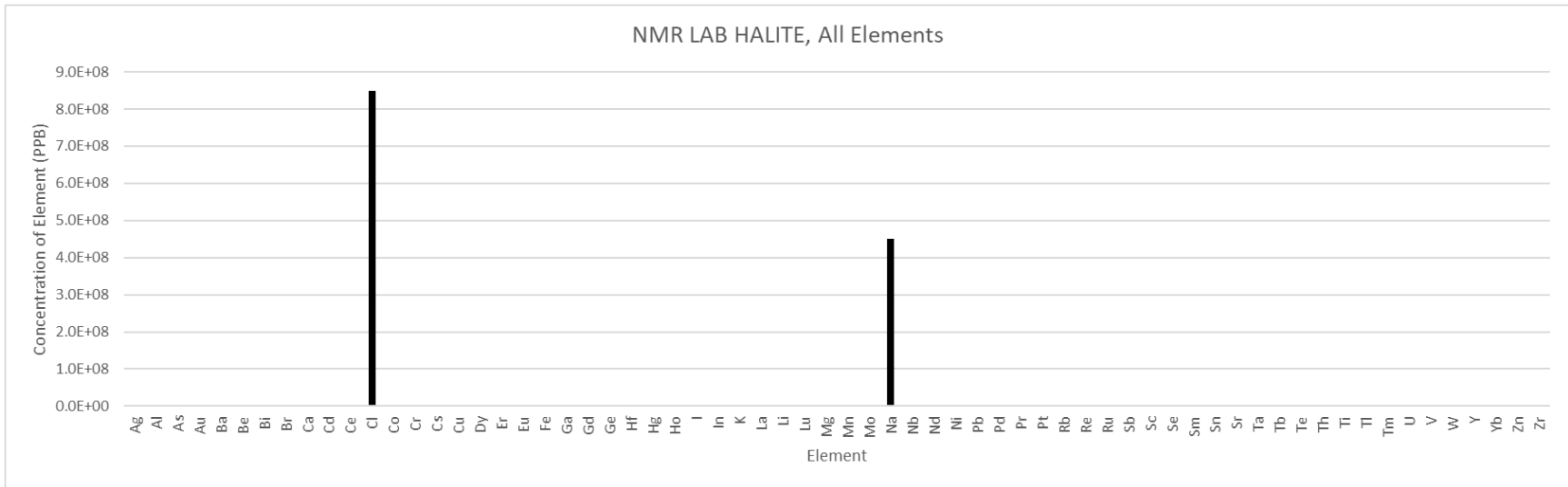
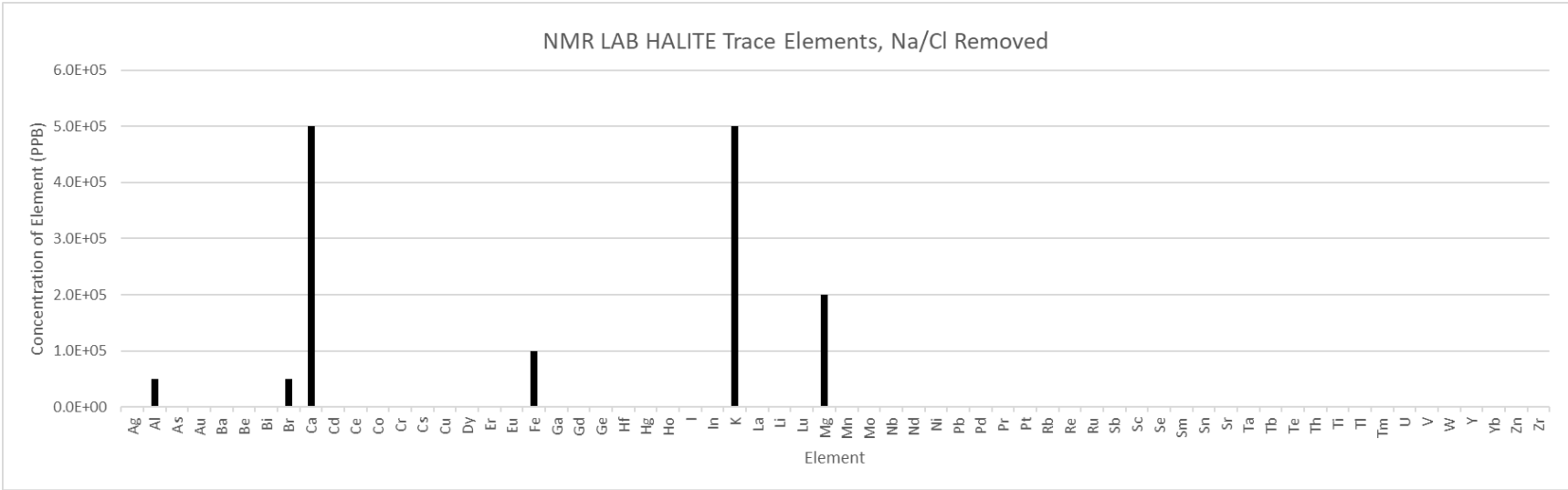


TRONA, CA HALITE, All Elements









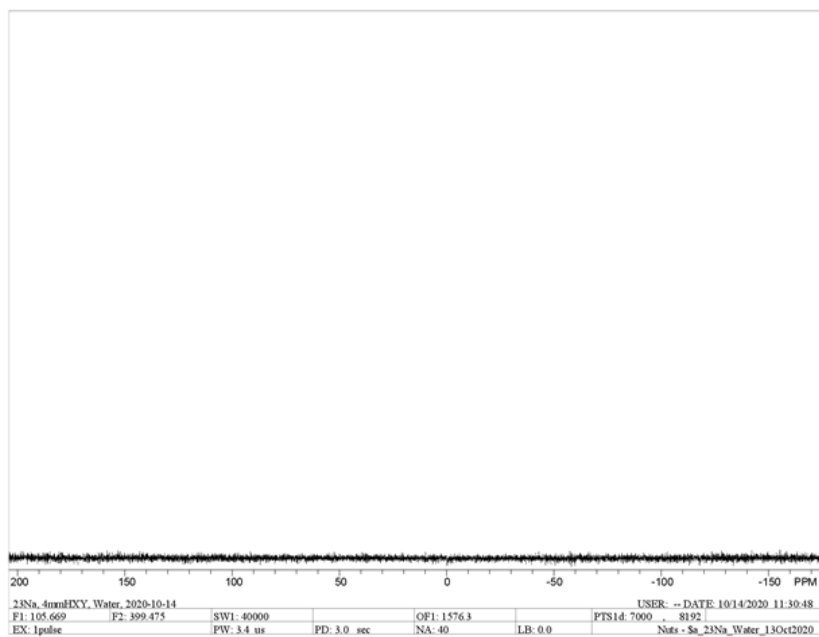
Appendix B: ²³Na Nuclear Magnetic Resonance Spectroscopy Data

Sample	Number of Acquisitions	Spectral Width (kHz)	Pulse Width (μs , $\pi/2$)	Acquisition Time (s)	Recycle Delay (s)	Data Points	MAS Frequency (kHz)	Temperature ($^{\circ}\text{C}$)	FWHM of Solid Peak (Hz)
Calibration Standards									
DI H ₂ O Blank	40	40	3.4	0.175	3	7000	NA	22	--
0.25 M NaCl	40	40	3.4	0.175	3	7000	NA	22	21.3
0.5 M NaCl	40	40	3.4	0.175	3	7000	NA	22	22.6
1.0 M NaCl	40	40	3.4	0.175	3	7000	NA	22	19.4
1.000 M NaCl	40	40	3.4	0.175	3	7000	NA	22	21.3
2.0 M NaCl	40	40	3.4	0.175	3	7000	NA	22	22.5
4.0 M NaCl	40	40	3.4	0.175	3	7000	NA	22	25.8
Saturated NaCl	40	40	3.4	0.175	3	7000	NA	22	27.6
Halite Samples (Static)									

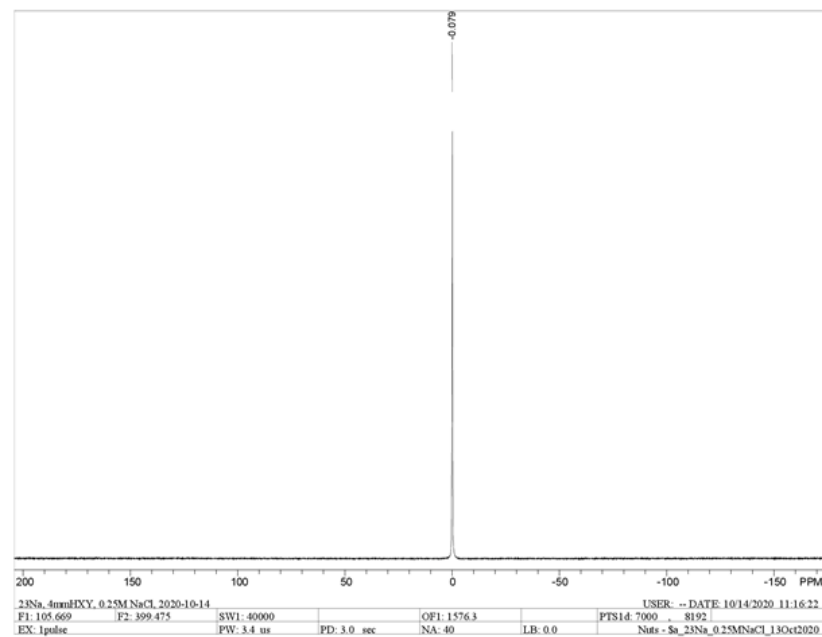
Bonaire Halite	40	55.005	1.7	0.00465	45	256	NA	22	2649.7
Dana 1922	40	55.005	1.7	0.00465	45	256	NA	22	2786.1
Dana 711	40	55.005	1.7	0.00465	45	256	NA	22	2631.4
Dana 730	40	55.005	1.7	0.00465	45	256	NA	22	2824.6
Dana 3137	40	55.005	1.7	0.00465	45	256	NA	22	2698.6
Dana 5477	40	55.005	1.7	0.00465	45	256	NA	22	2698.0
Dana 5490	40	55.005	1.7	0.00465	45	256	NA	22	2650.1
DeLaval Blue Halite	40	55.005	1.7	0.00465	45	256	NA	22	2717.0
99.9% Reagent NaCl, AnalR	40	55.005	1.7	0.00465	45	256	NA	22	2551.1
Salton Sea Halite	40	55.005	1.7	0.00465	45	256	NA	22	2716.9
TronaCA Halite	40	55.005	1.7	0.00465	45	256	NA	22	2652.3
MAS Halite Samples									
Bonaire Halite	20	55.005	1.7	0.05097	45	2800	12	22	53.4
Dana 1922	20	55.005	1.7	0.05454	45	2800	12	22	54.5
Dana 711	20	55.005	1.7	0.05454	45	2800	12	22	58.6

Dana 3137	20	55.005	1.7	0.05454	45	2800	12	22	53.7
Dana 5477	20	55.005	1.7	0.05090	45	2800	12	22	50.6
Dana 5490	20	55.005	1.7	0.05090	45	2800	12	22	51.2
DeLaval Blue Halite	20	55.005	1.7	0.05090	45	2800	12	22	58.1
99.9% Reagent NaCl, AnalR	16	55.005	1.7	0.05120	45	2800	12	22	47.3
Salton Sea Halite	20	55.005	1.7	0.05454	45	2800	12	22	48.8
TronaCA Halite	20	55.005	1.7	0.05090	45	2800	12	22	51.8
South African Halite	20	55.005	1.7	0.05454	45	3000	12	22	51.6
Fluorite Samples									
Hansonburg Static	1600	50	2	0.01200	1	256	NA	22	418.2
Hansonburg 12 kHz	4000	55.0055	1.7	0.03723	45	2048	12	22	97.7
Hansonburg 22C	2064	25	1.6	0.04096	5	1024	12	22	20.1
Hansonburg 100C	2140	25	1.6	0.04096	5	1024	12	100	20.7
Hansonburg 150C	2140	25	1.6	0.04096	5	1024	12	150	20.9
Hansonburg 175C	2140	25	1.6	0.04096	5	1024	12	175	22.0

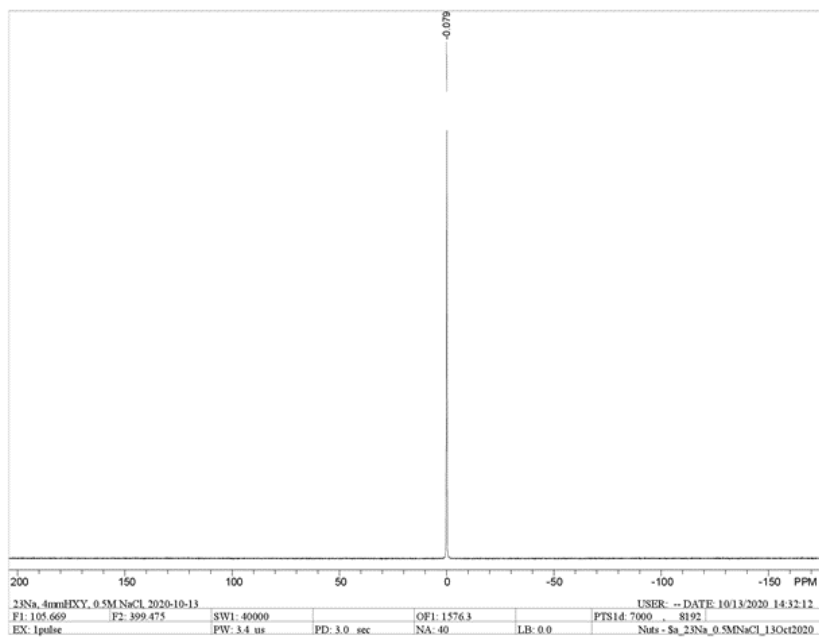
Hansonburg 185C	2140	25	1.6	0.04096	5	1024	12	185	20.7
Gonzales MAS	4000	55.0055	1.7	0.01862	45	1024	12	22	--
Quartz Samples									
Snowbird MAS	4000	55.0055	1.7	0.01862	45	2048	12	22	63.5
Snowbird 22C	404	40	2.0	0.02560	5	1024	11	22	48.6
Snowbird 50C	1032	40	2.0	0.02560	10	1024	11	50	51.4
Snowbird 100C	808	40	2.0	0.03000	10	1200	11	100	48.3
Snowbird 150C	800	40	2.0	0.03000	10	1200	11	150	56.1
Snowbird 200C	800	40	2.0	0.03000	10	1200	11	200	56.6
Sulphate Samples									
Thenardite	200	80	1.7	0.0128	10	1024	11	22	1004.2
Hydr. Thenardite	344	80	1.7	0.0256	10	2048	11	22	979.6



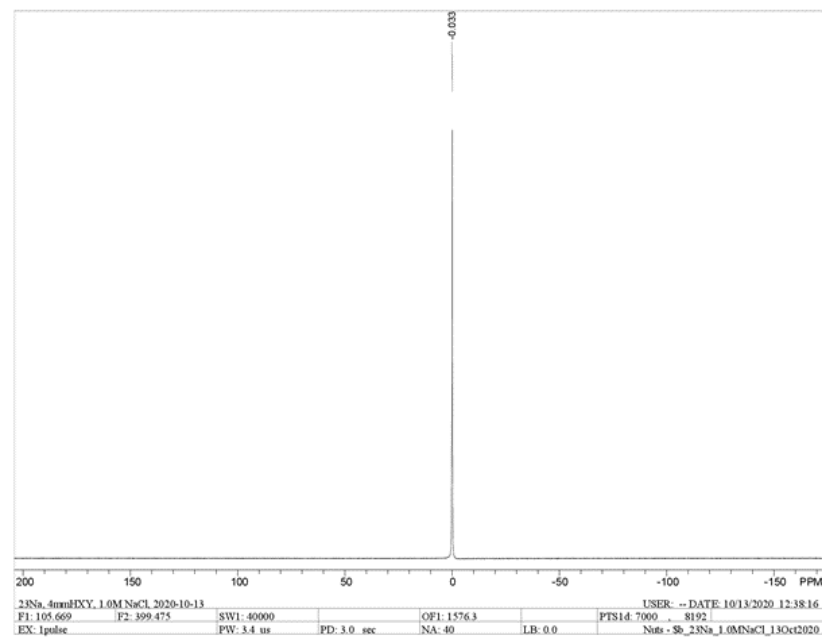
MAS Sample: Deionized Water Blank Standard



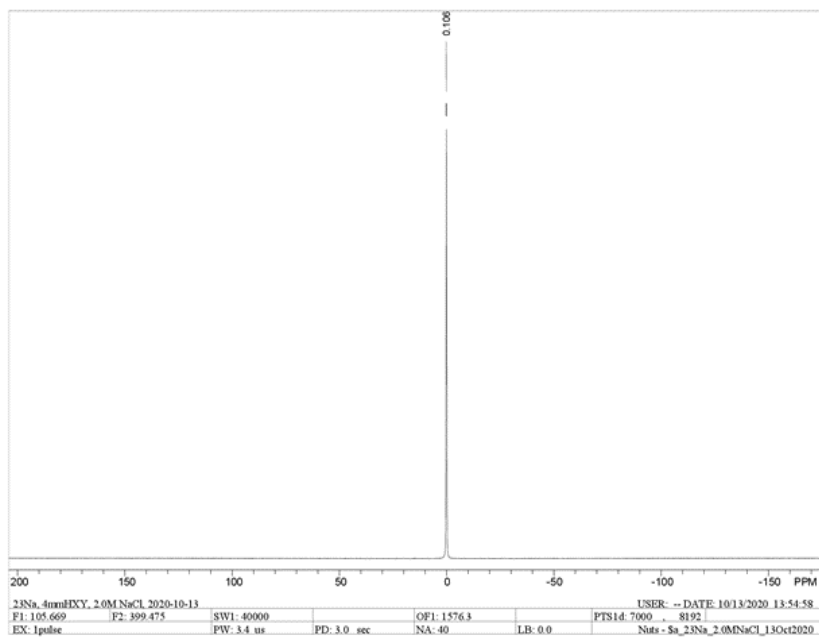
MAS Sample: 0.25 M NaCl



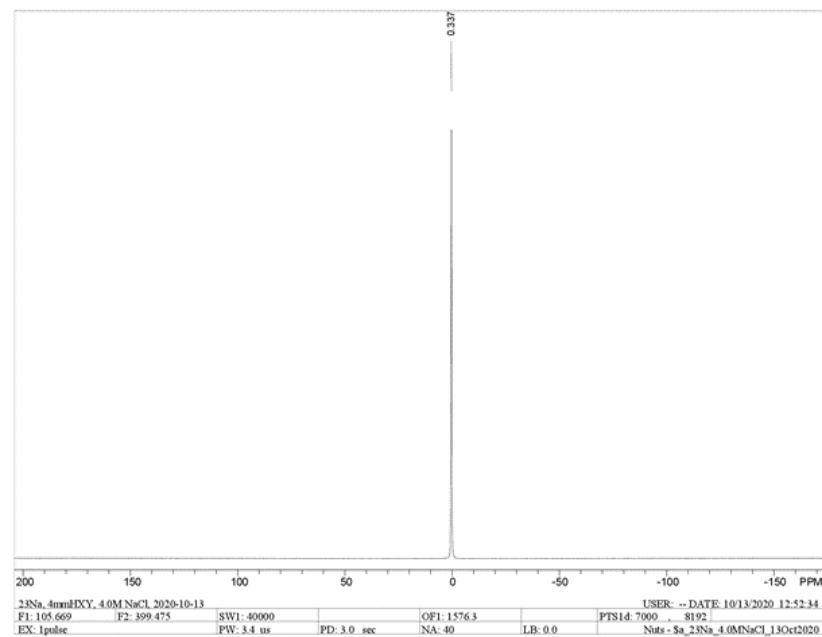
MAS Sample: 0.50 M NaCl



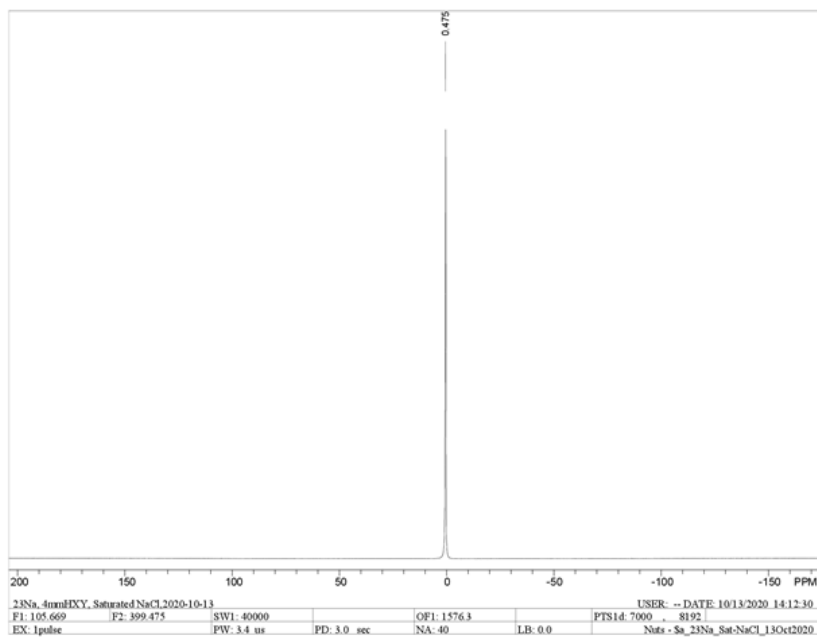
MAS Sample: 1.00 M NaCl



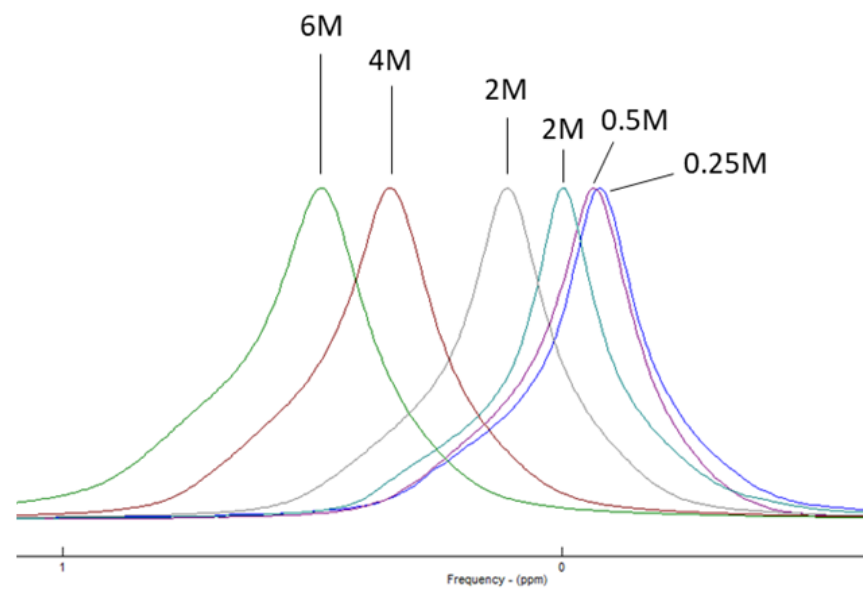
MAS Sample: 2.00 M NaCl



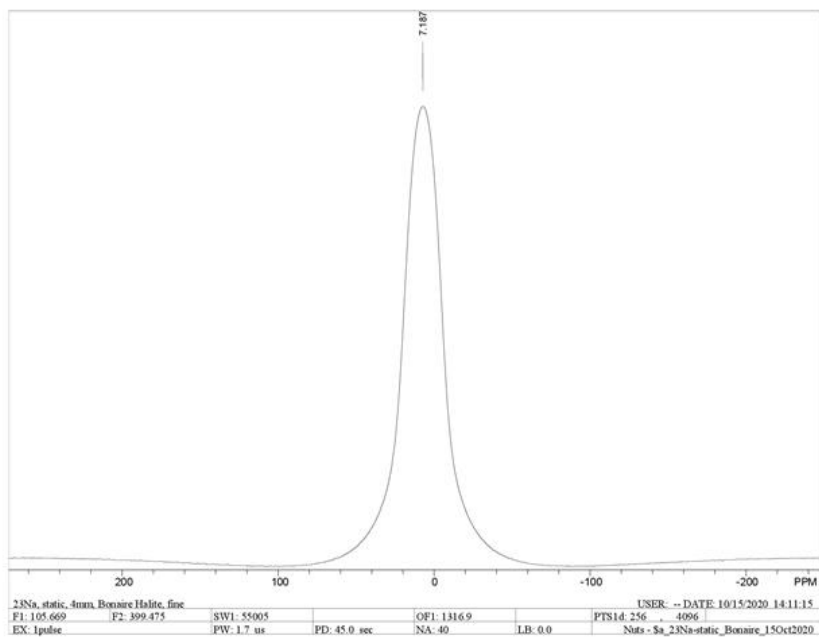
MAS Sample: 4.00 M NaCl



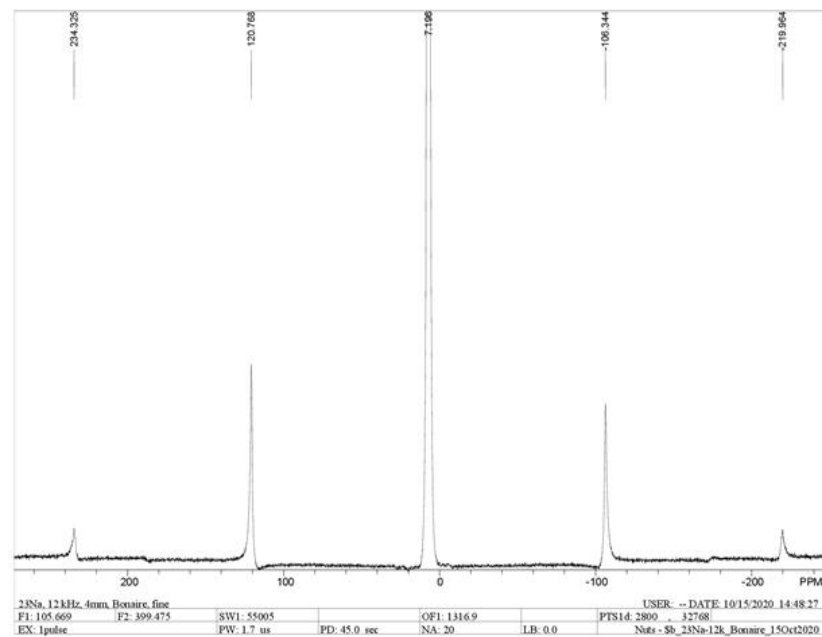
MAS Sample: Fully Saturated NaCl (6M ambient)



MAS Sample: Stack plot of saline standard spectra

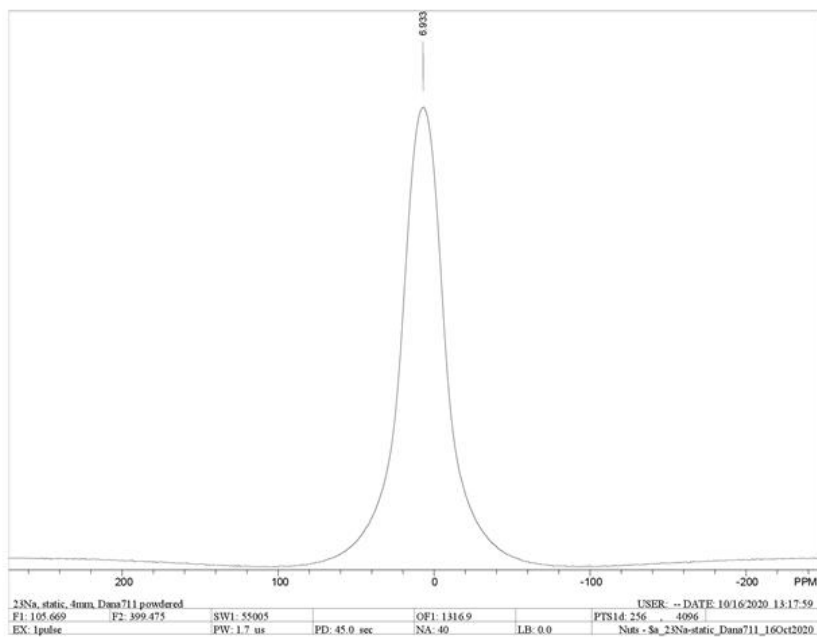


Static Sample: Bonaire Halite

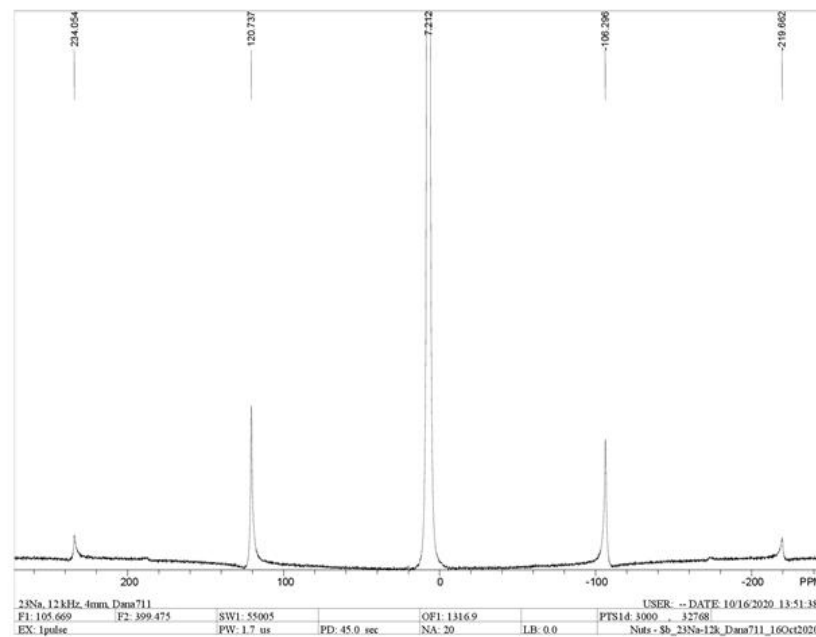


MAS Sample: Bonaire Halite

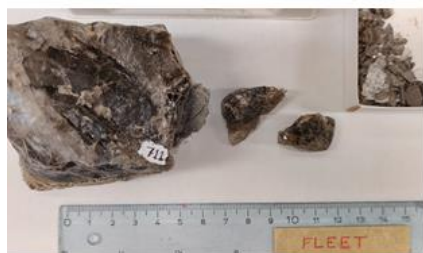


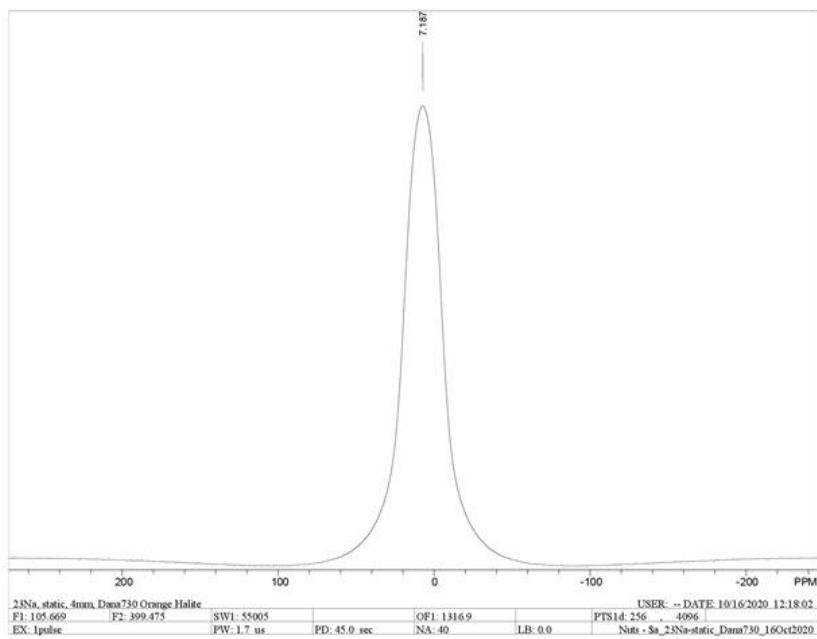


Static Sample: Dana 711



MAS Sample: Dana 711



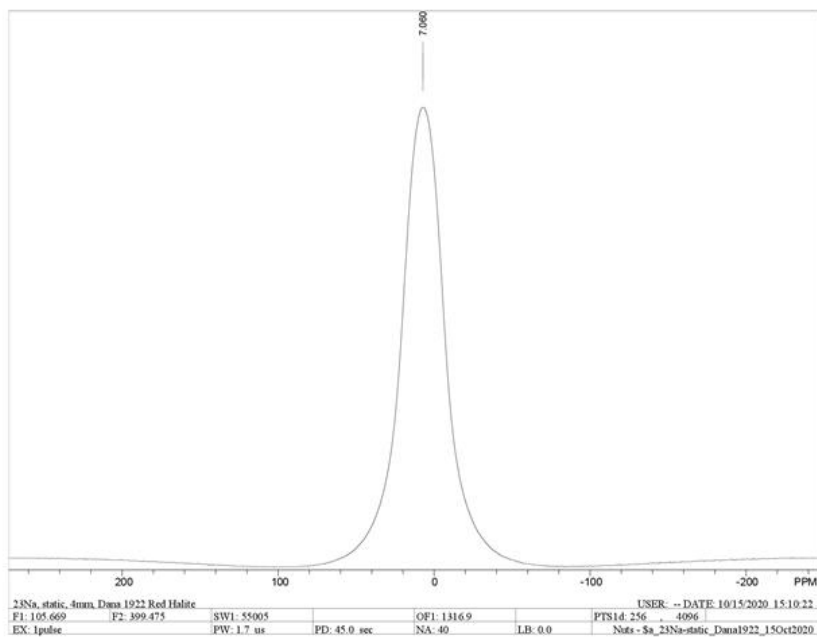


Static Sample: Dana 730

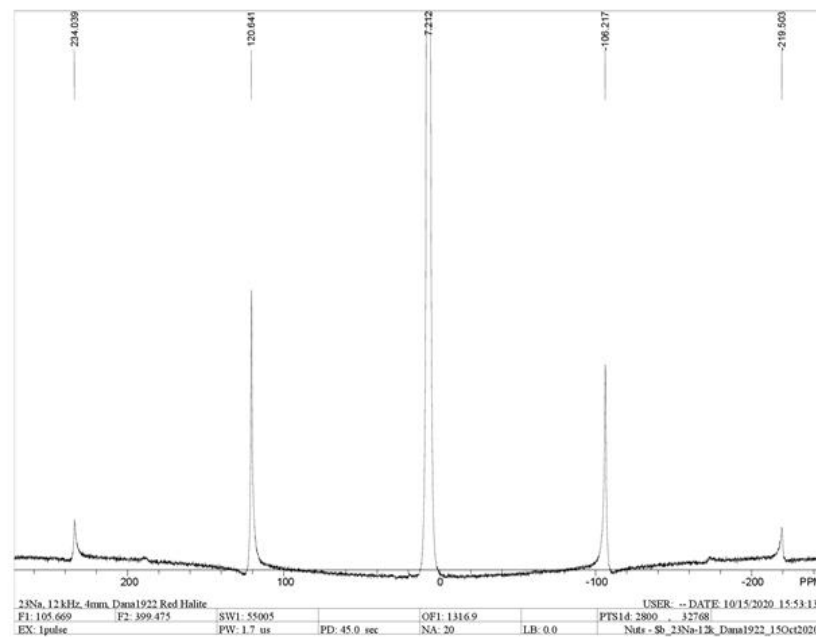


MAS Sample: No Spectrum Collected



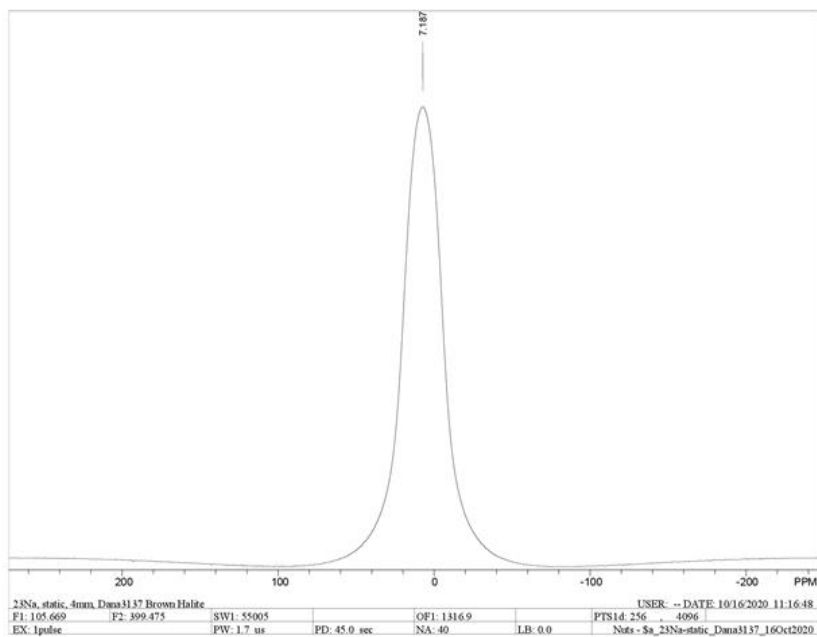


Static Sample: Dana 1922

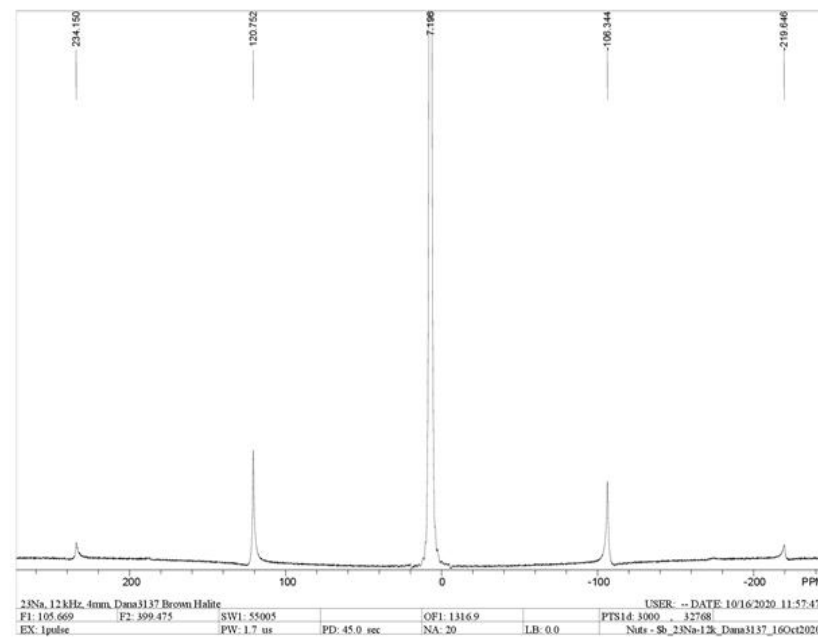


MAS Sample: Dana 1922



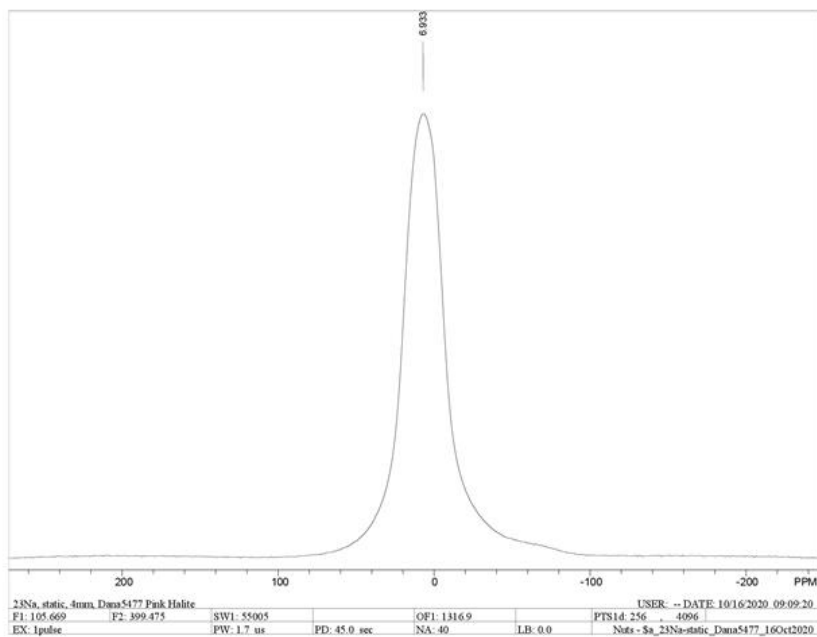


Static Sample: Dana 3137

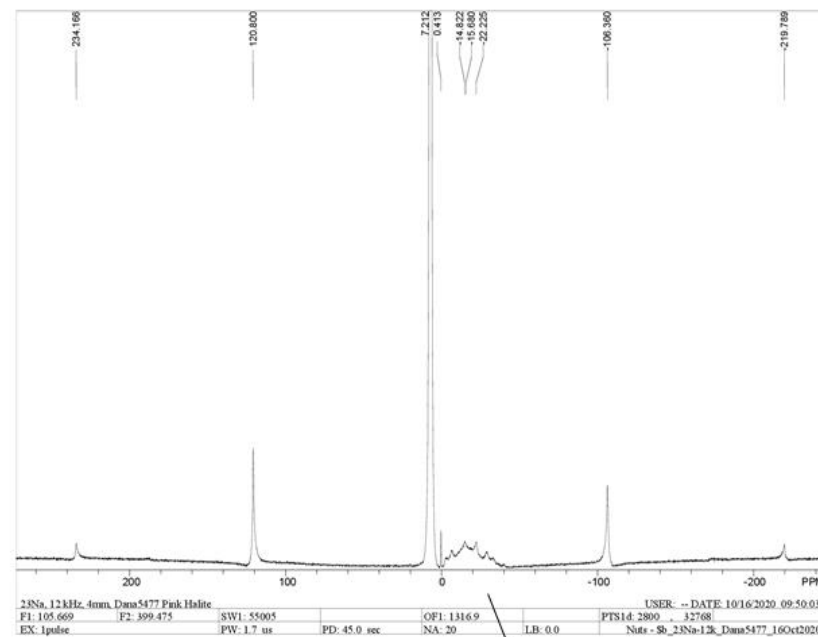


MAS Sample: Dana 3137

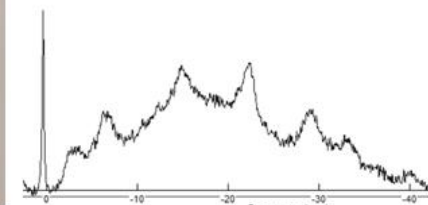


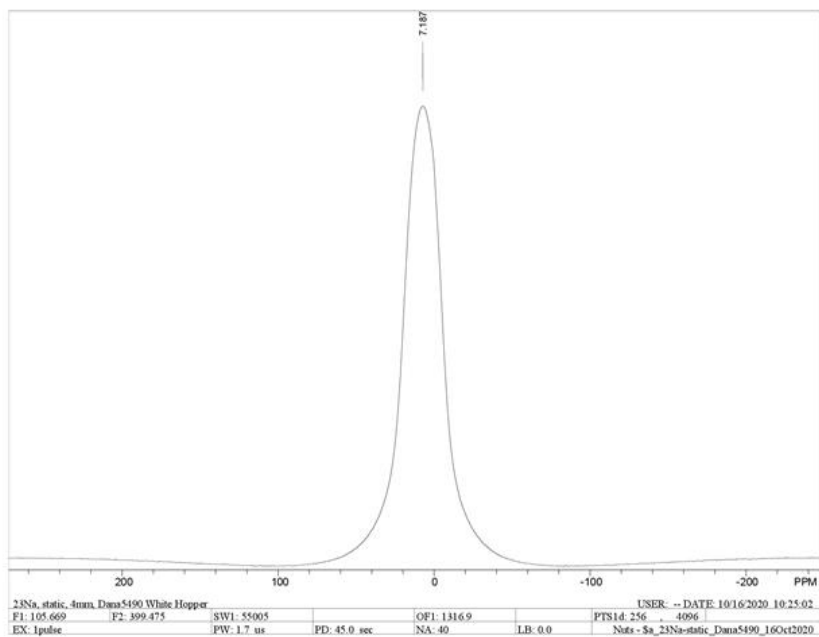


Static Sample: Dana 5477

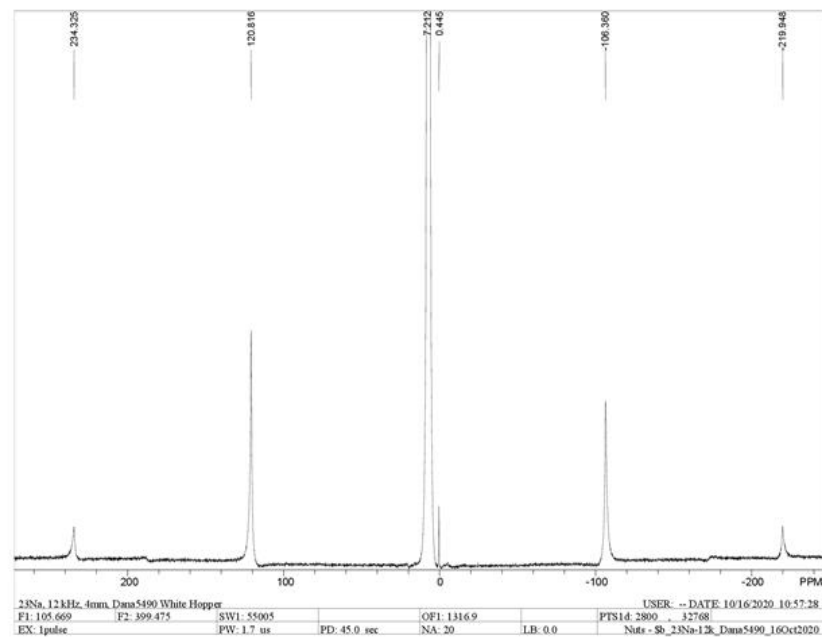


MAS Sample: Dana 5477

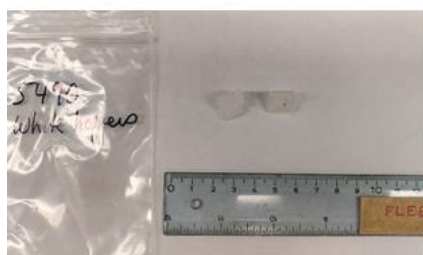


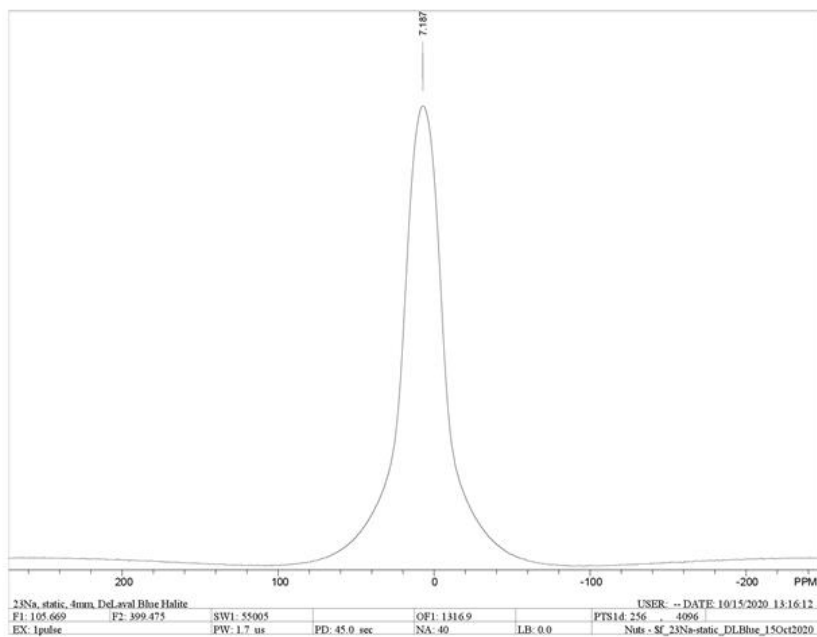


Static Sample: Dana 5490

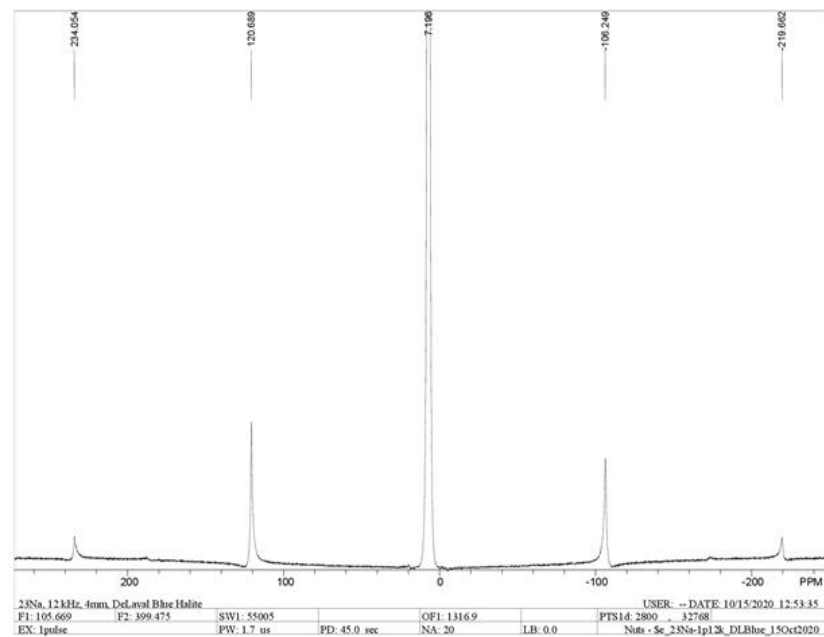


MAS Sample: Dana 5490



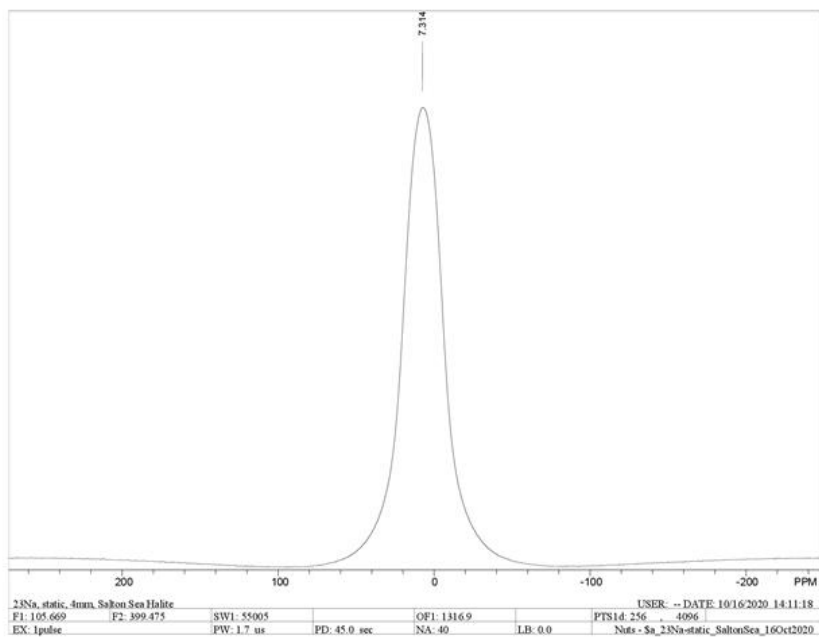


Static Sample: DeLaval Blue Halite

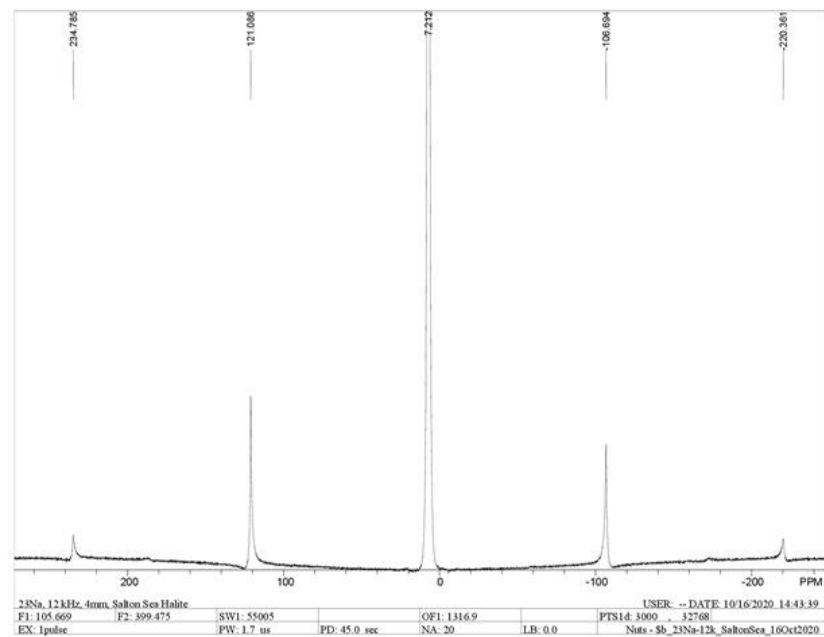


MAS Sample: DeLaval Blue Halite



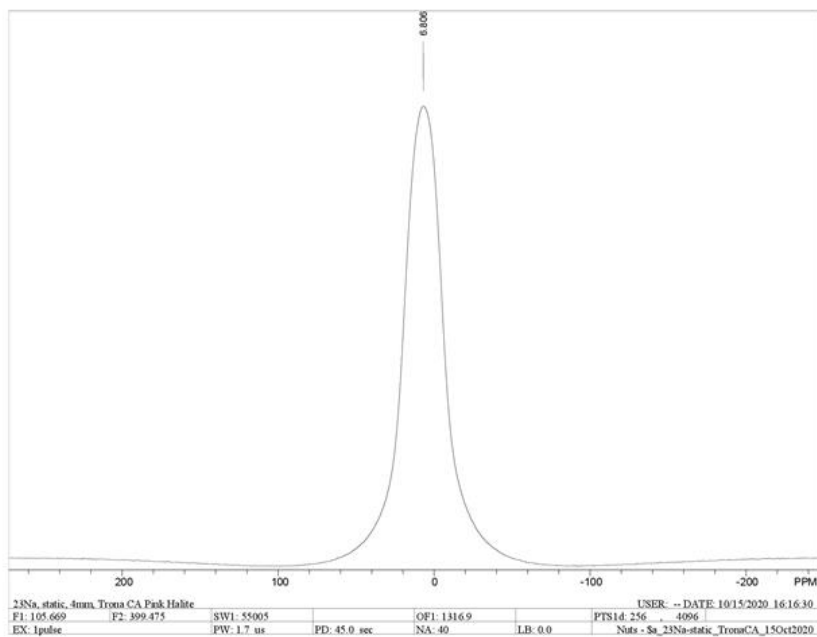


Static Sample: Salton Sea Halite

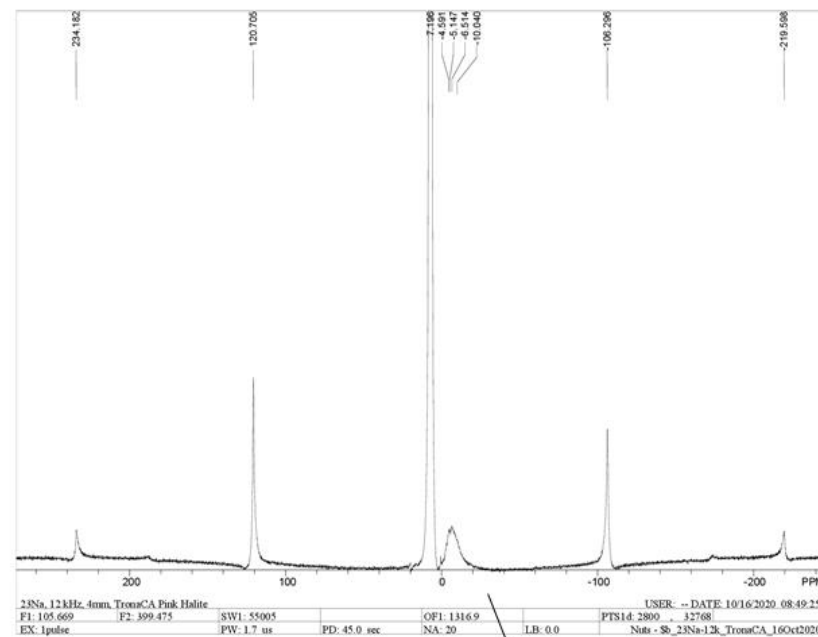


MAS Sample: Salton Sea Halite

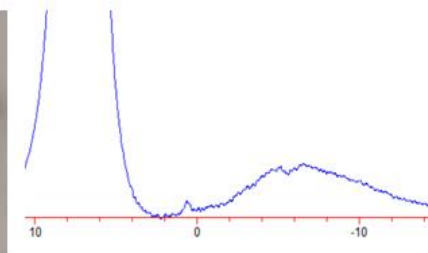


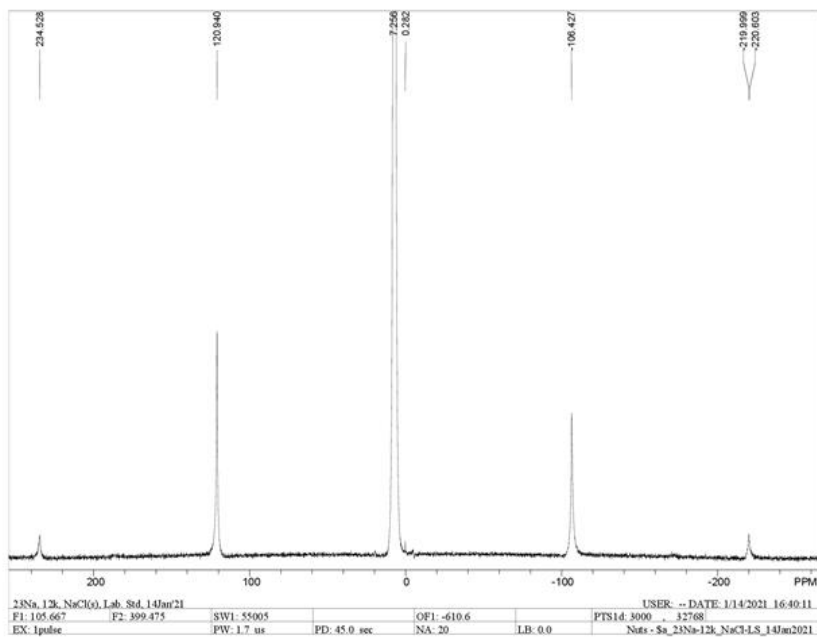


Static Sample: TronaCA Halite

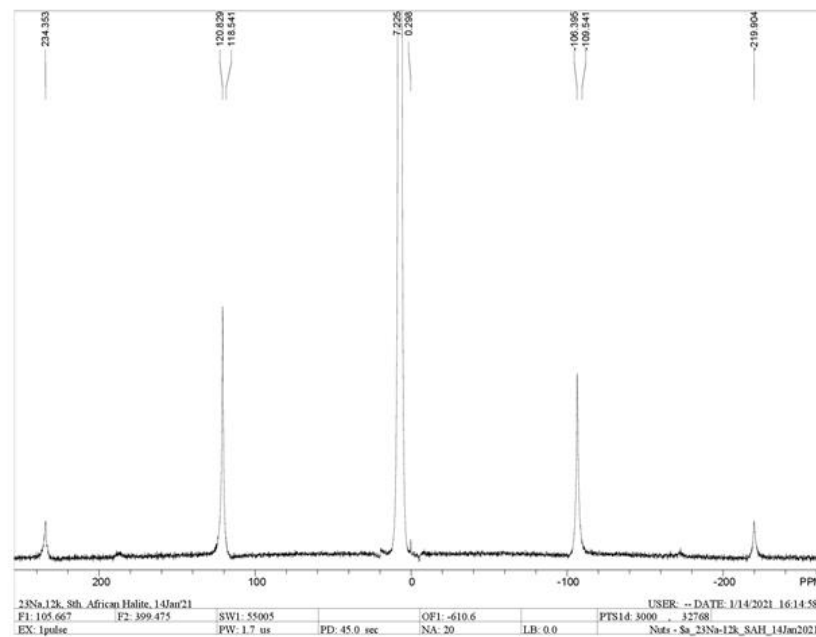


MAS Sample: TronaCA Halite



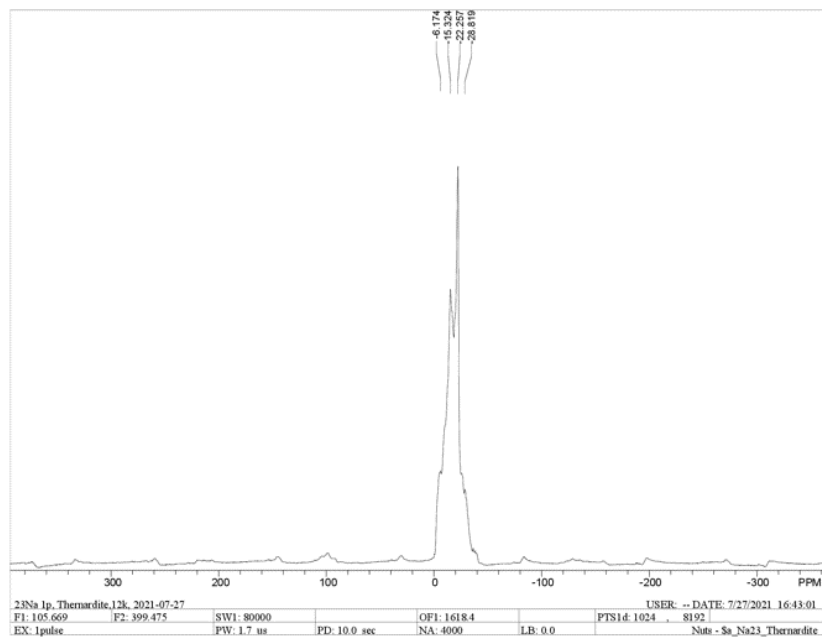
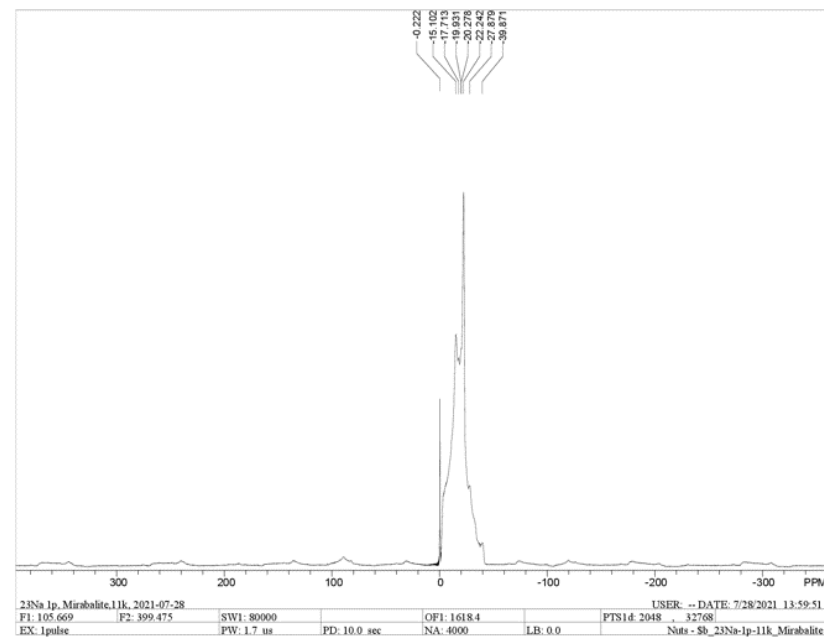
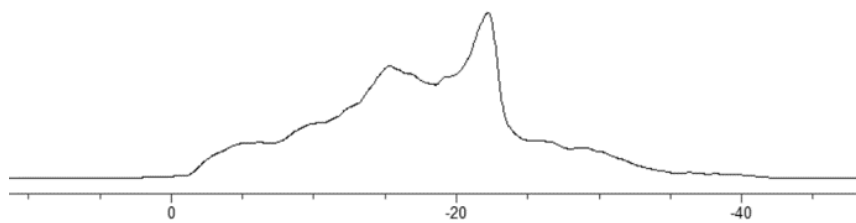
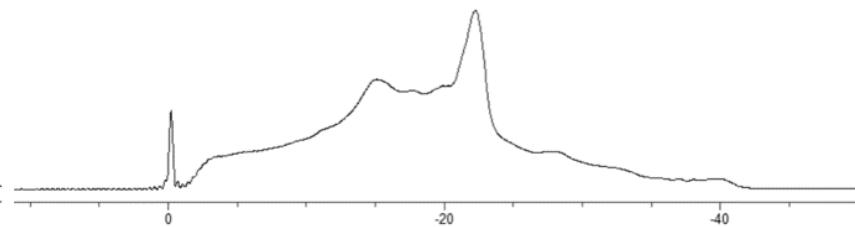


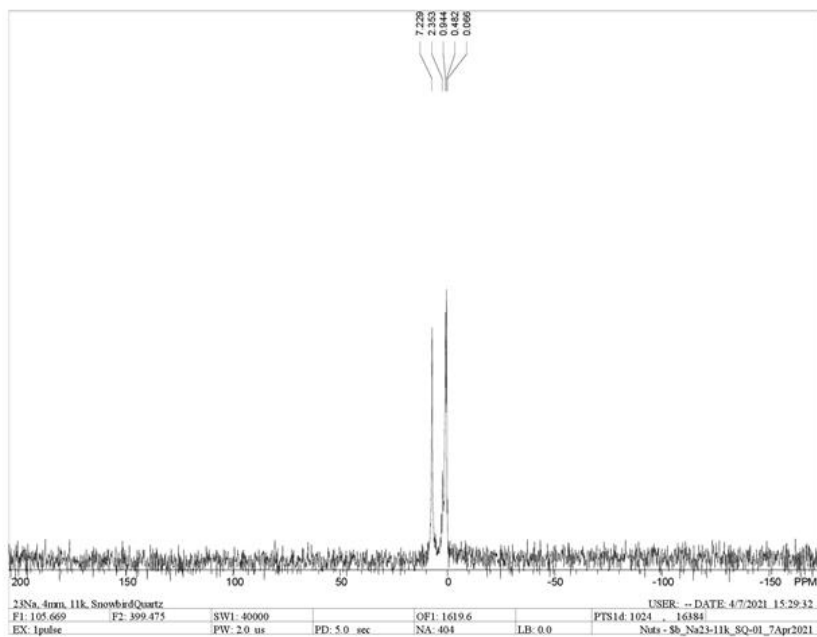
Static Sample: 99.9% AnR Reagent NaCl



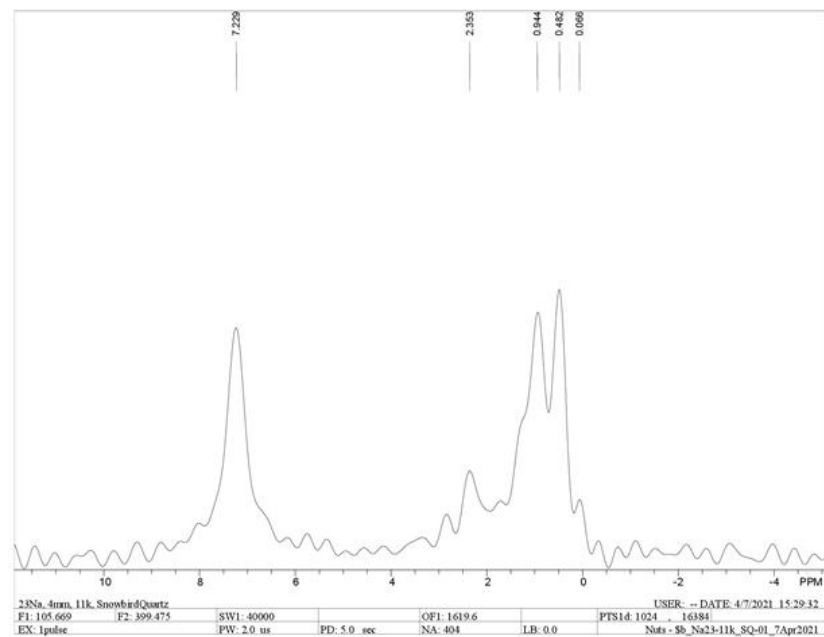
MAS Sample: 99.9% AnR Reagent NaCl



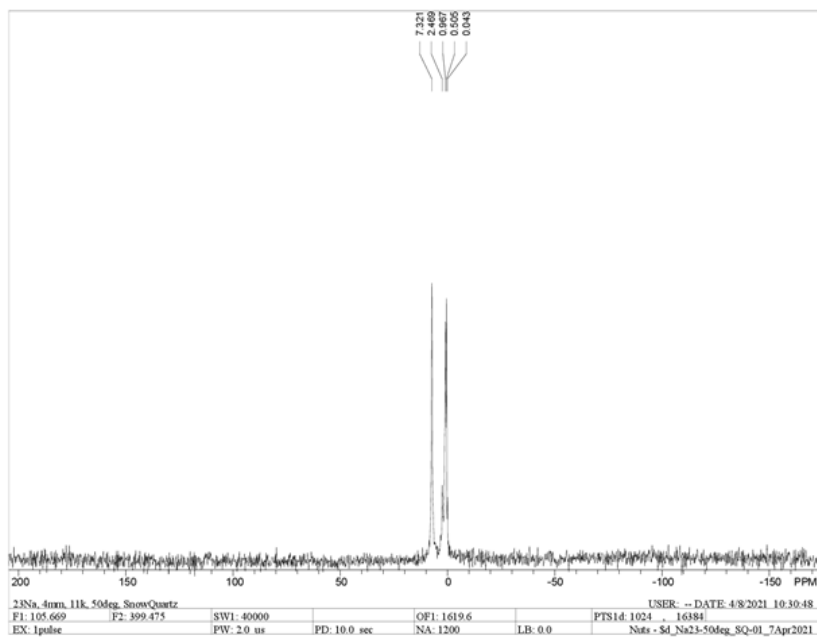
MAS Sample: Thenardite (Na_2SO_4)MAS Sample: Hydrated Thenardite ($\text{Na}_2\text{SO}_4 \cdot 0.445 \text{H}_2\text{O}$)



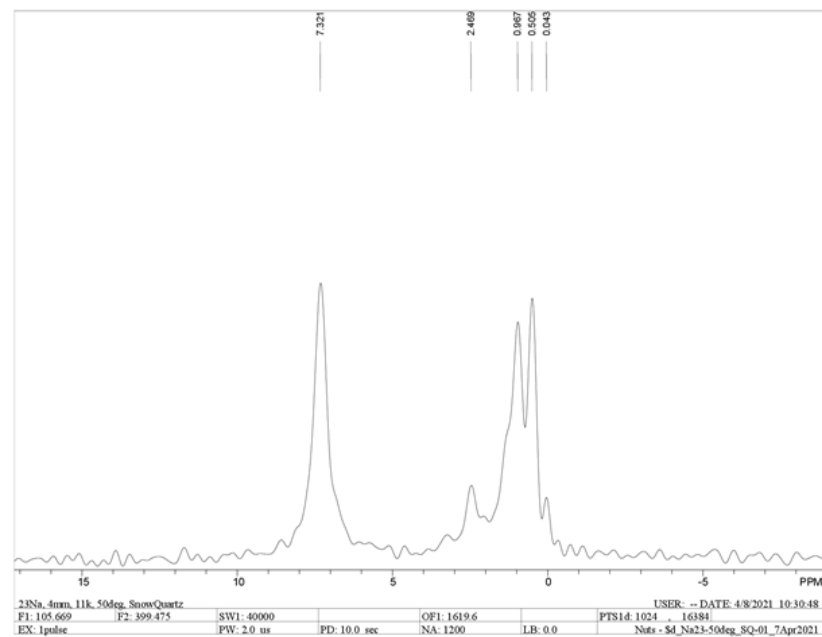
MAS Sample: Snowbird Quartz Ambient Temperature



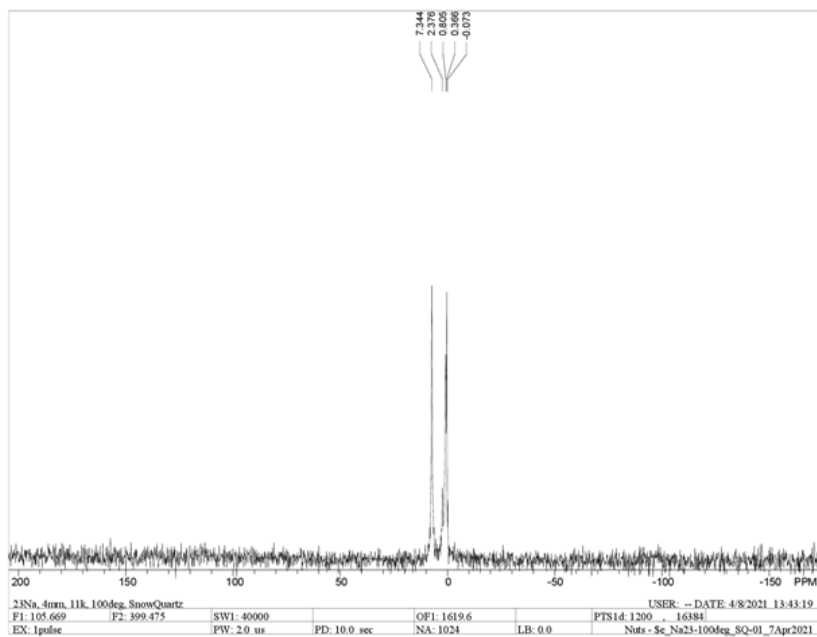
MAS Sample: Snowbird Quartz Ambient Zoom



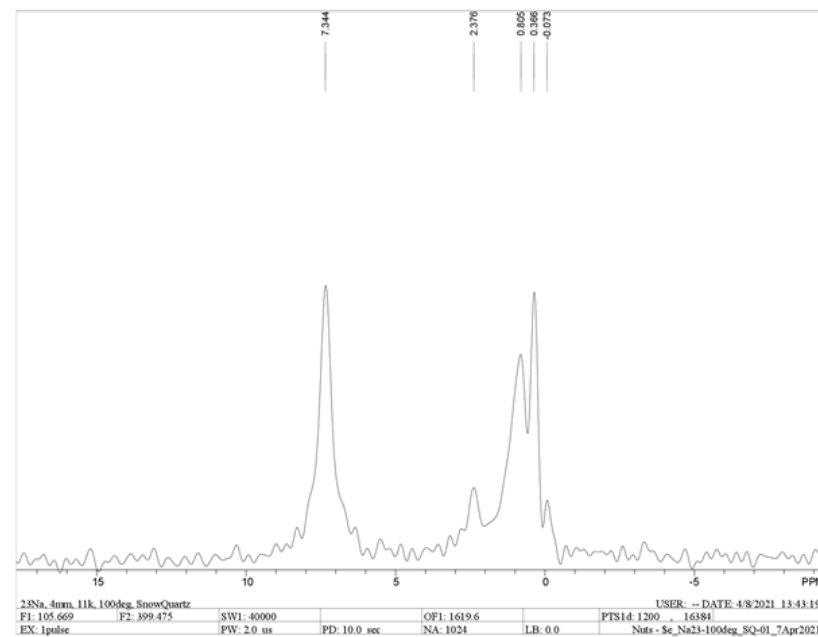
MAS Sample: Snowbird Quartz 50°C



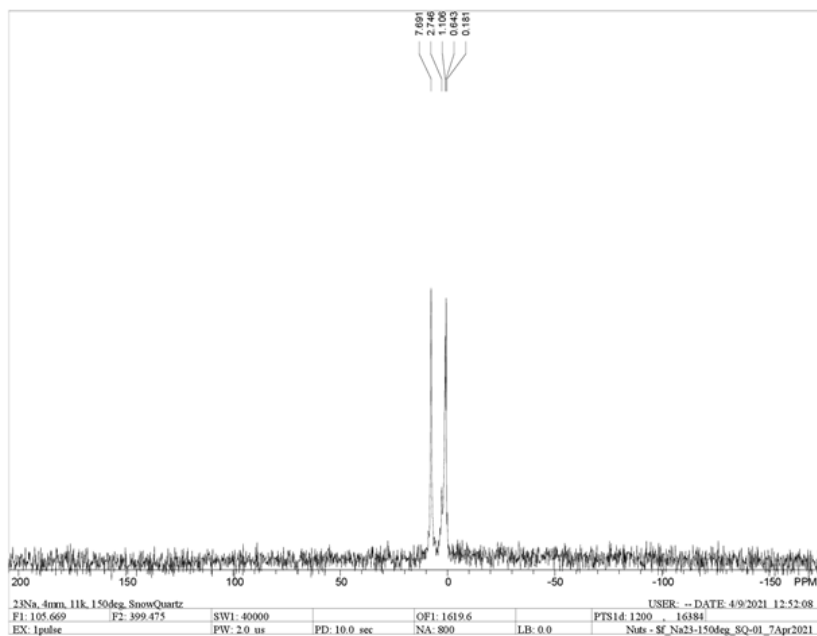
MAS Sample: Snowbird Quartz 50°C Zoom



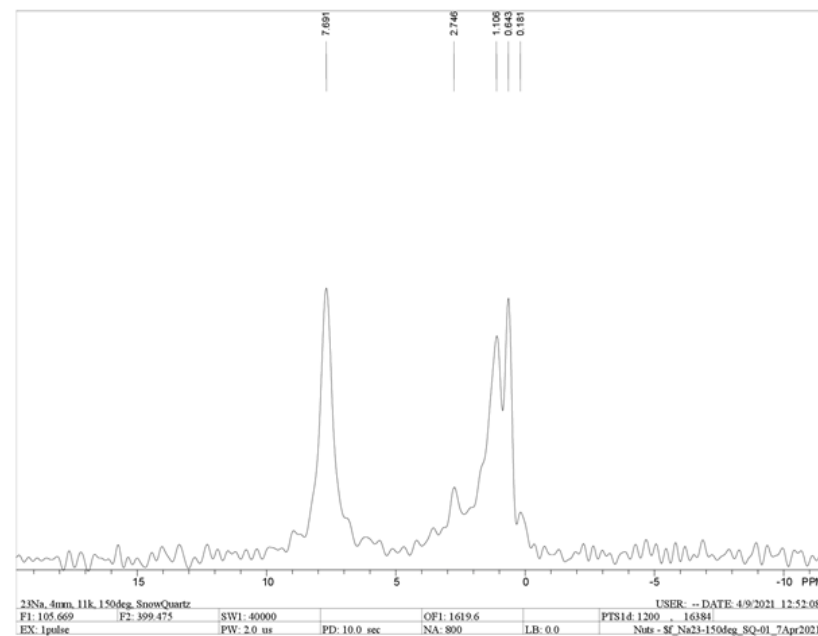
MAS Sample: Snowbird Quartz 100°C



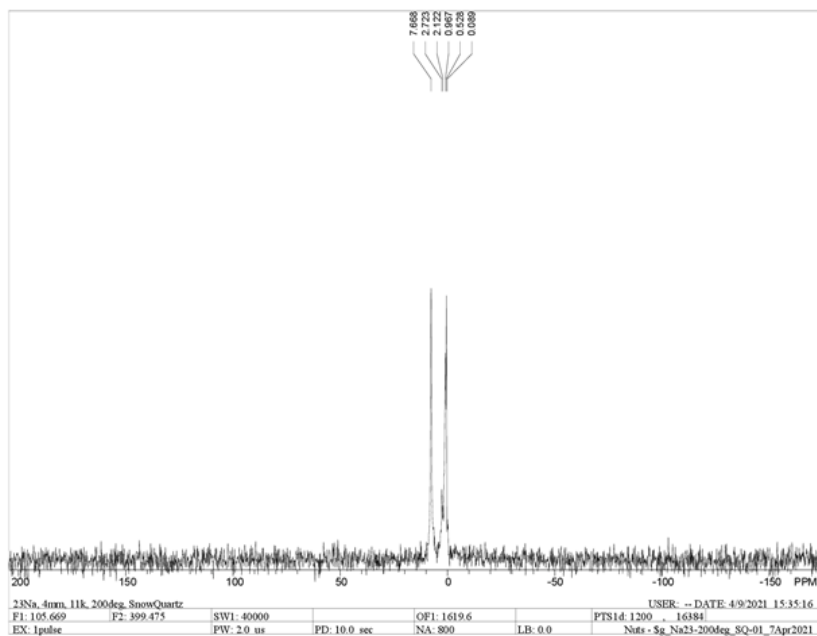
MAS Sample: Snowbird Quartz 100°C Zoom



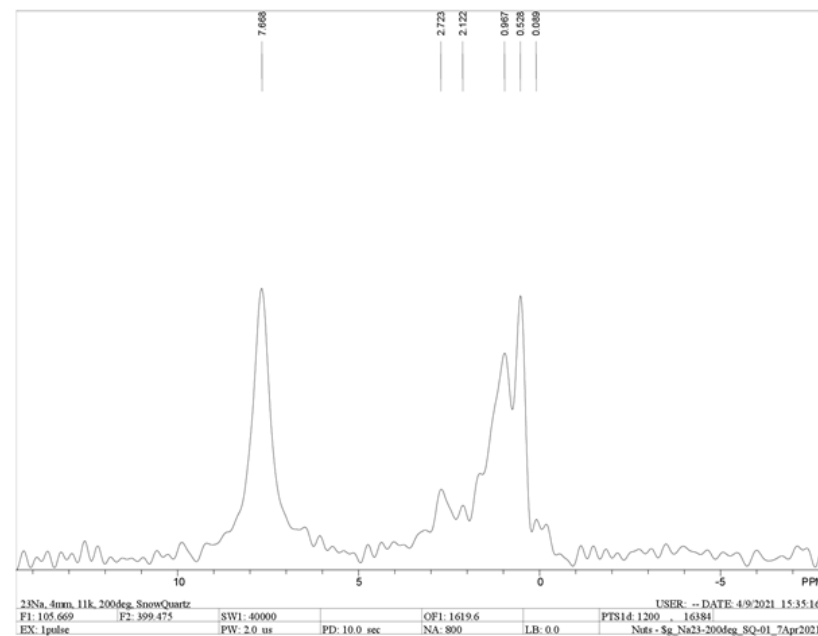
MAS Sample: Snowbird Quartz 150°C



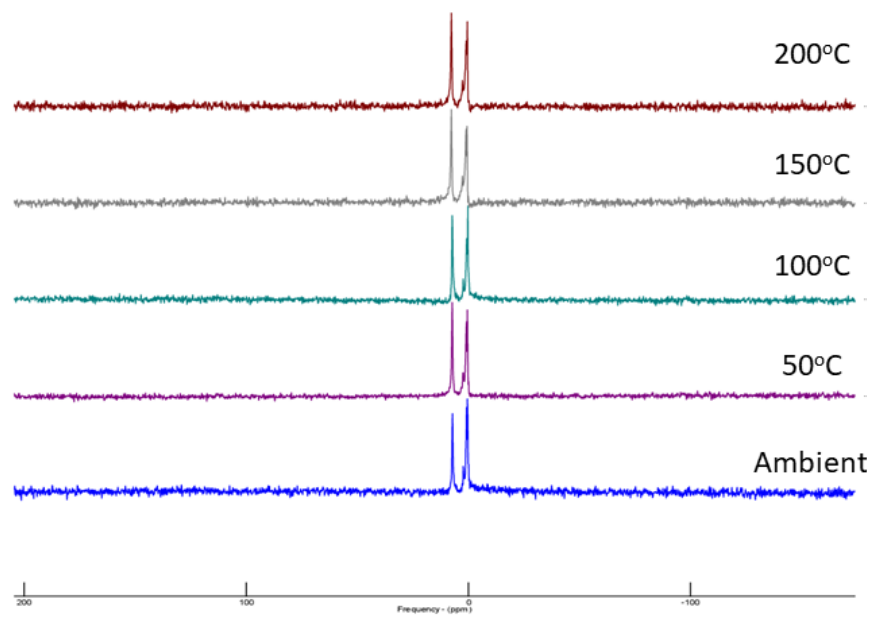
MAS Sample: Snowbird Quartz 150°C Zoom



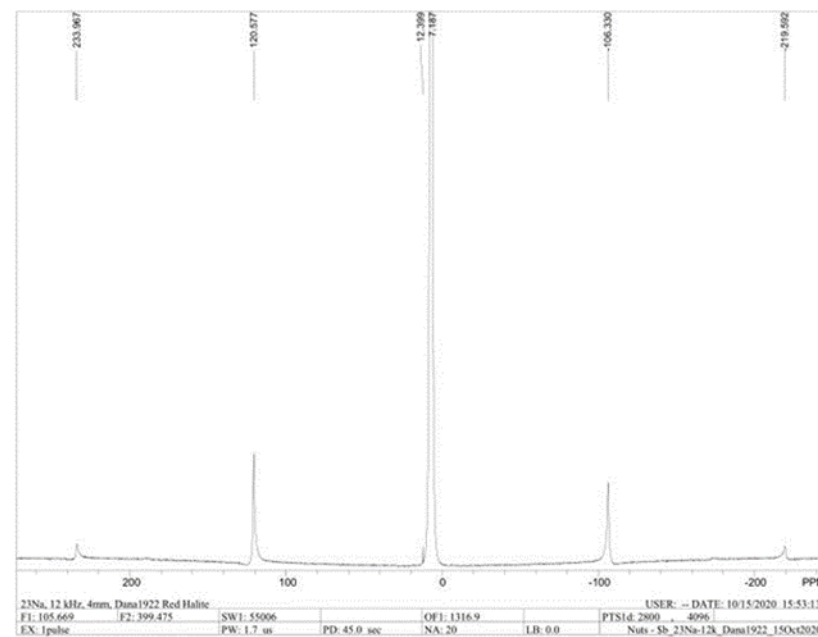
MAS Sample: Snowbird Quartz 200°C



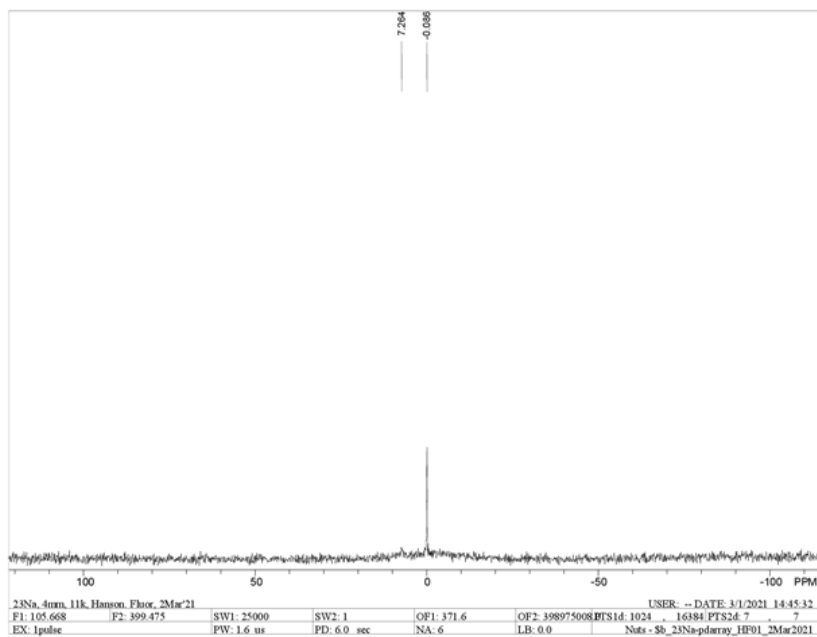
MAS Sample: Snowbird Quartz 200°C Zoom



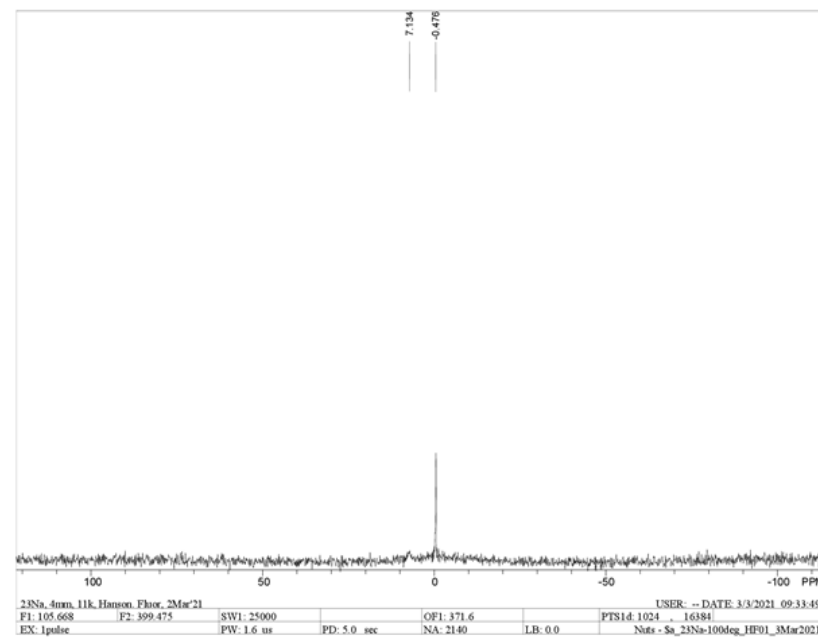
MAS Sample: Stack Plot of all Snowbird VT Spectra



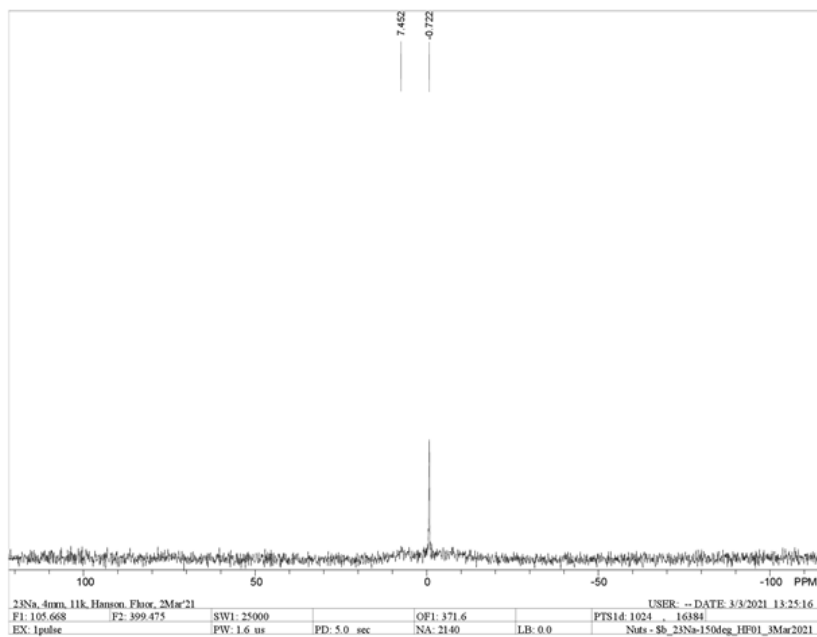
MAS Sample: Dana 1922 w/ errant liquid peak



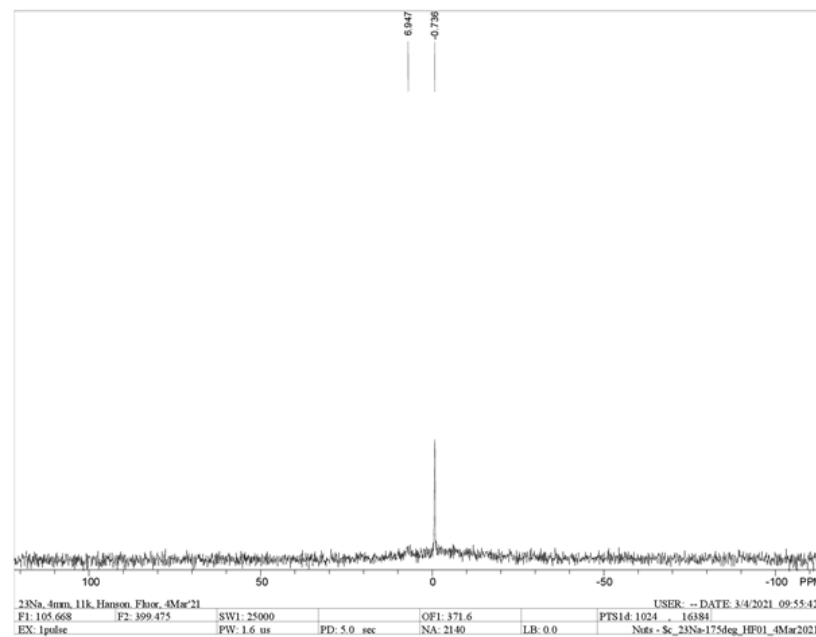
MAS Sample: Hansonburg Fluorite Ambient Temperature



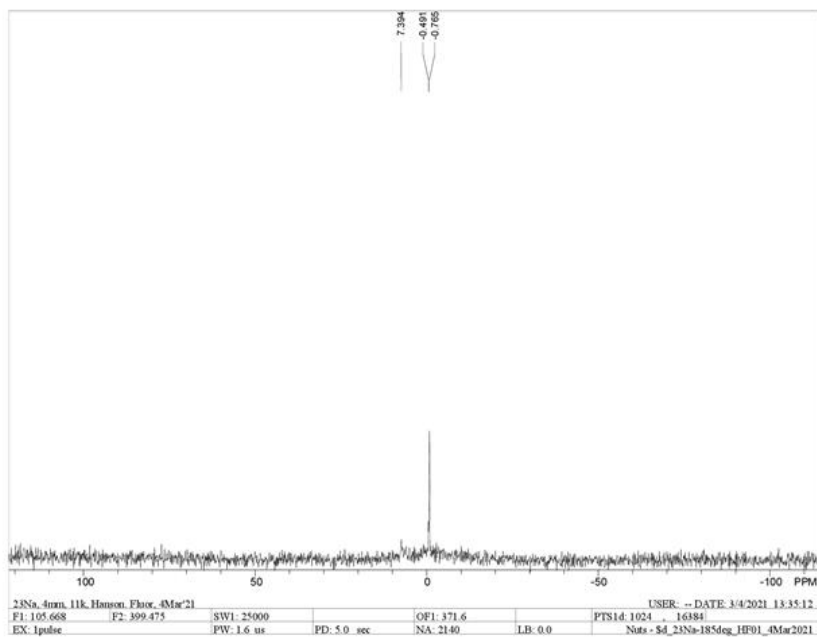
MAS Sample: Hansonburg Fluorite 100°C



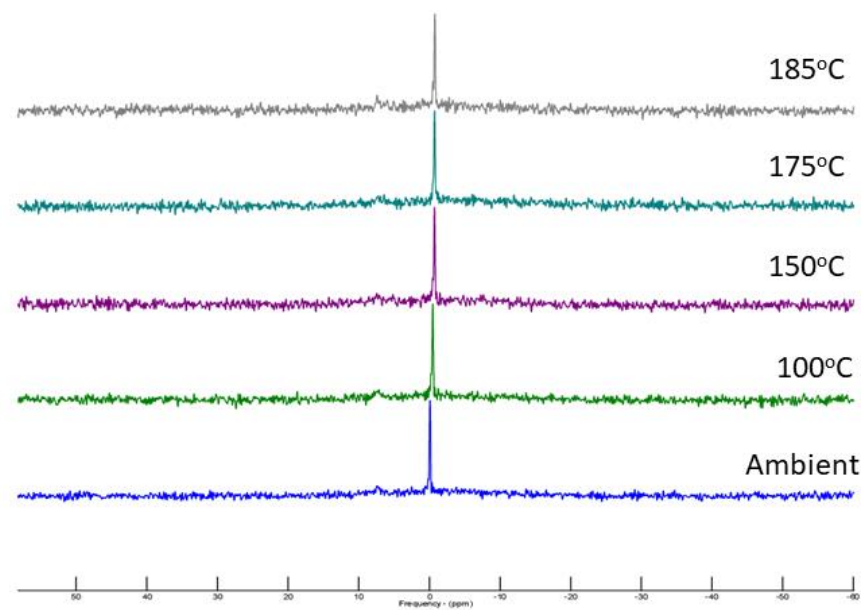
MAS Sample: Hansonburg Fluorite 150°C



MAS Sample: Hansonburg Fluorite 175°C



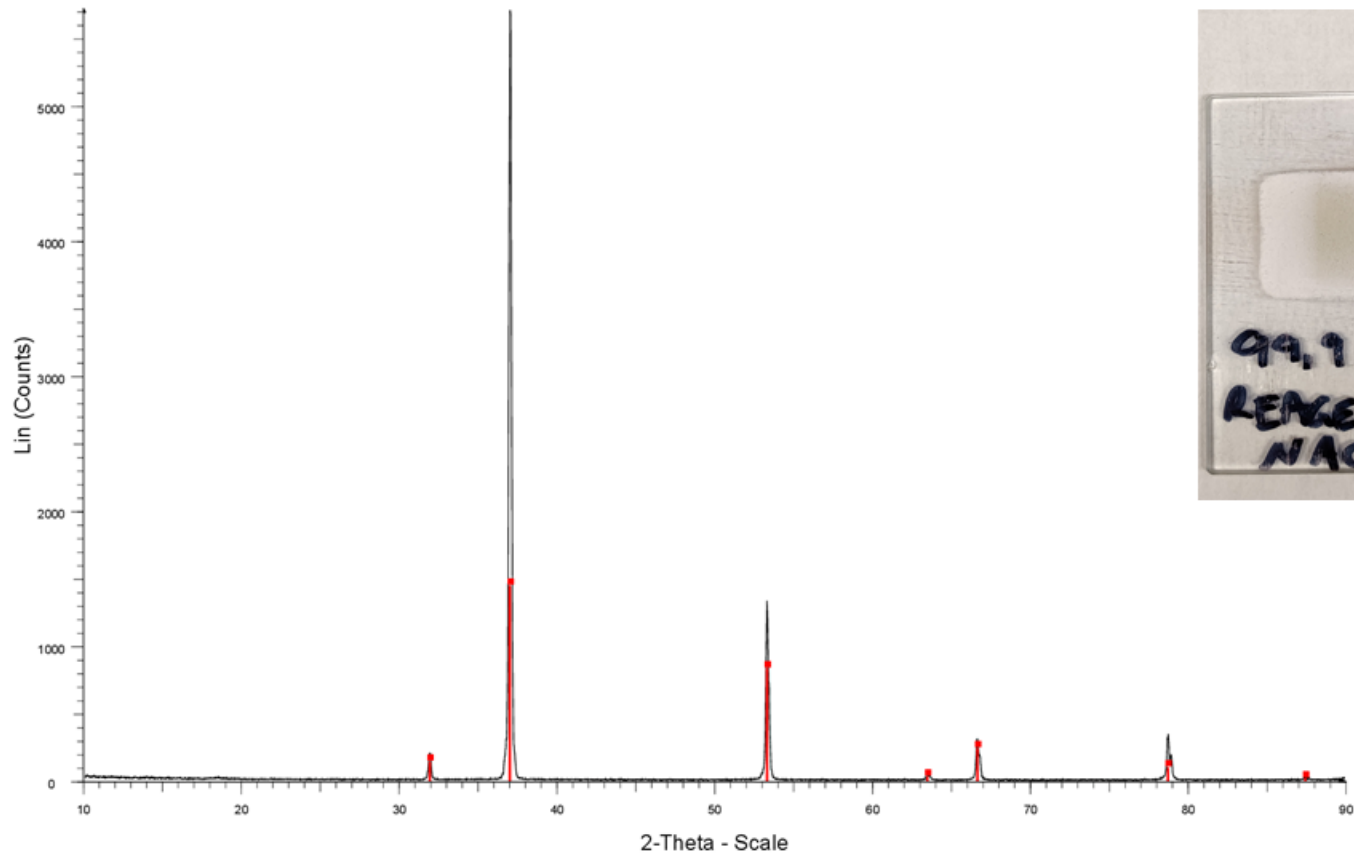
MAS Sample: Hansonburg Fluorite 185°C



MAS Sample: Stack plot of all Hansonburg VT Spectra

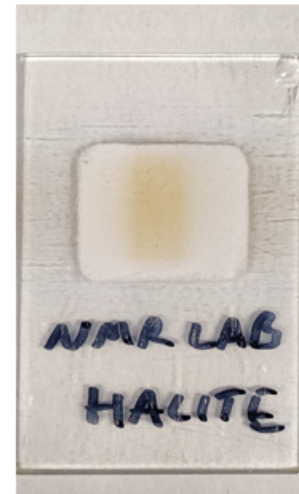
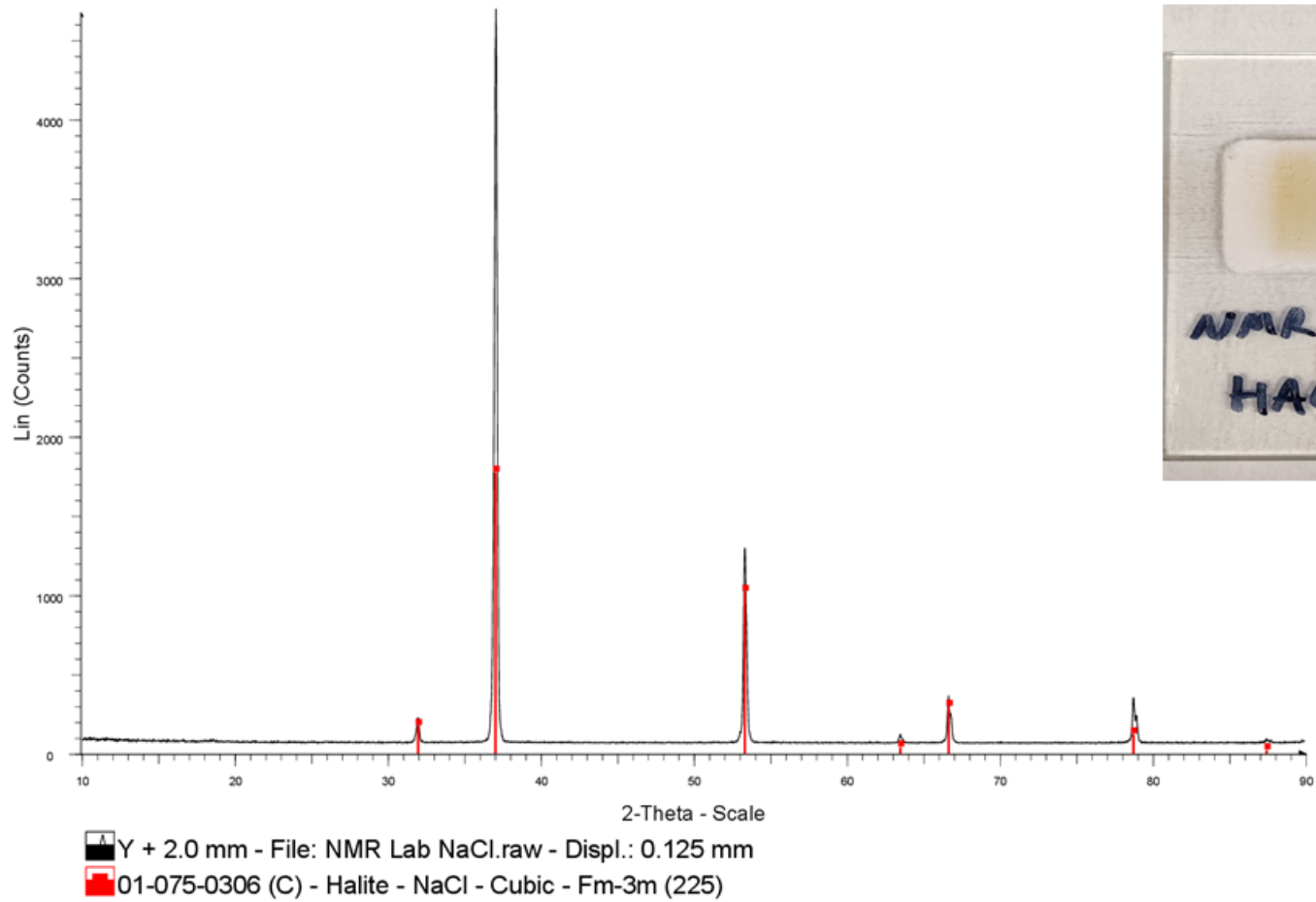
Appendix C: Powder X-ray Diffraction Data

Sample ID: AnalR 99.9% Reagent NaCl

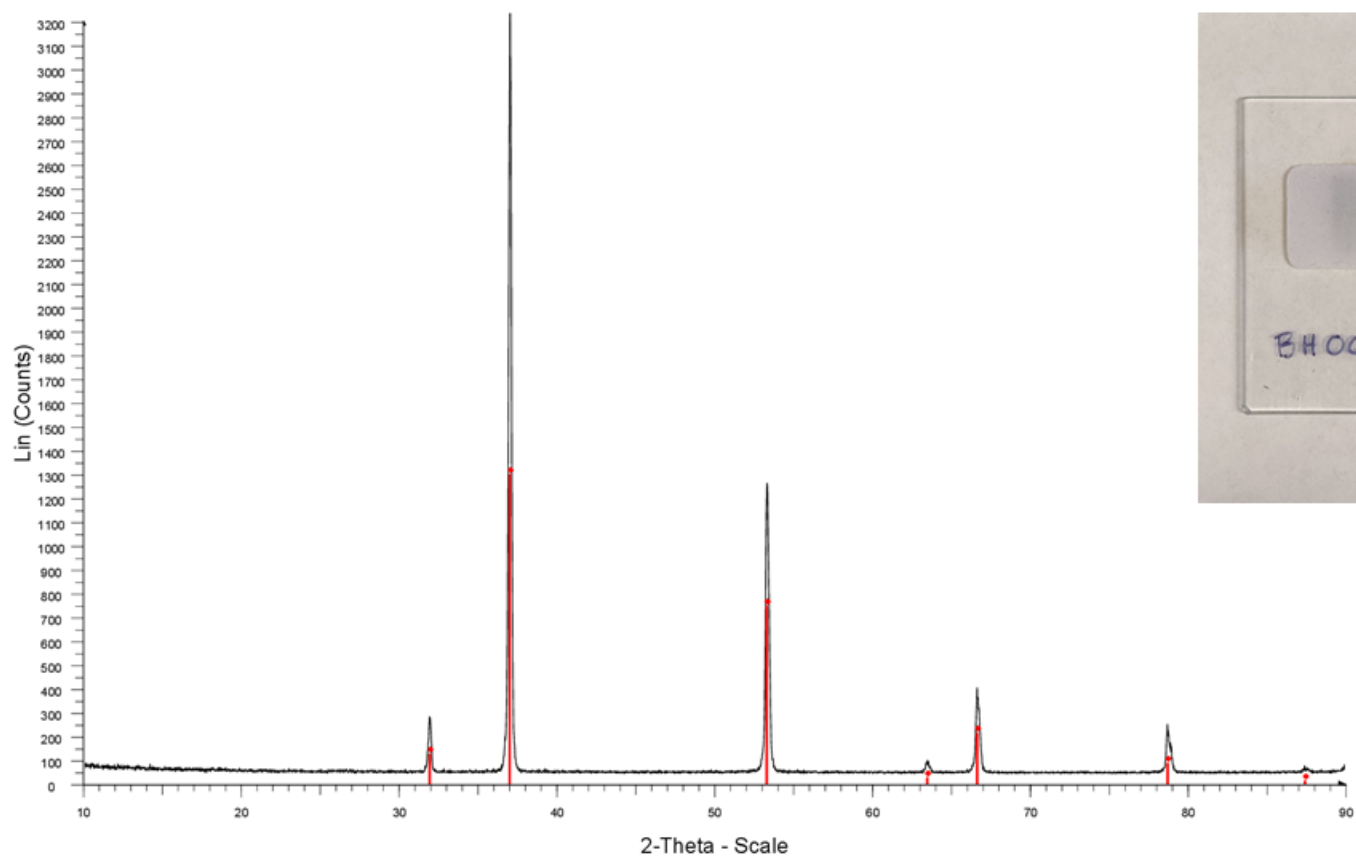


File: 99,9 Reagent Halite.raw - Displ.: 0. mm
01-075-0306 (C) - Halite - NaCl - Cubic - Fm-3m (225)

Sample ID: NMR Lab Grade NaCl

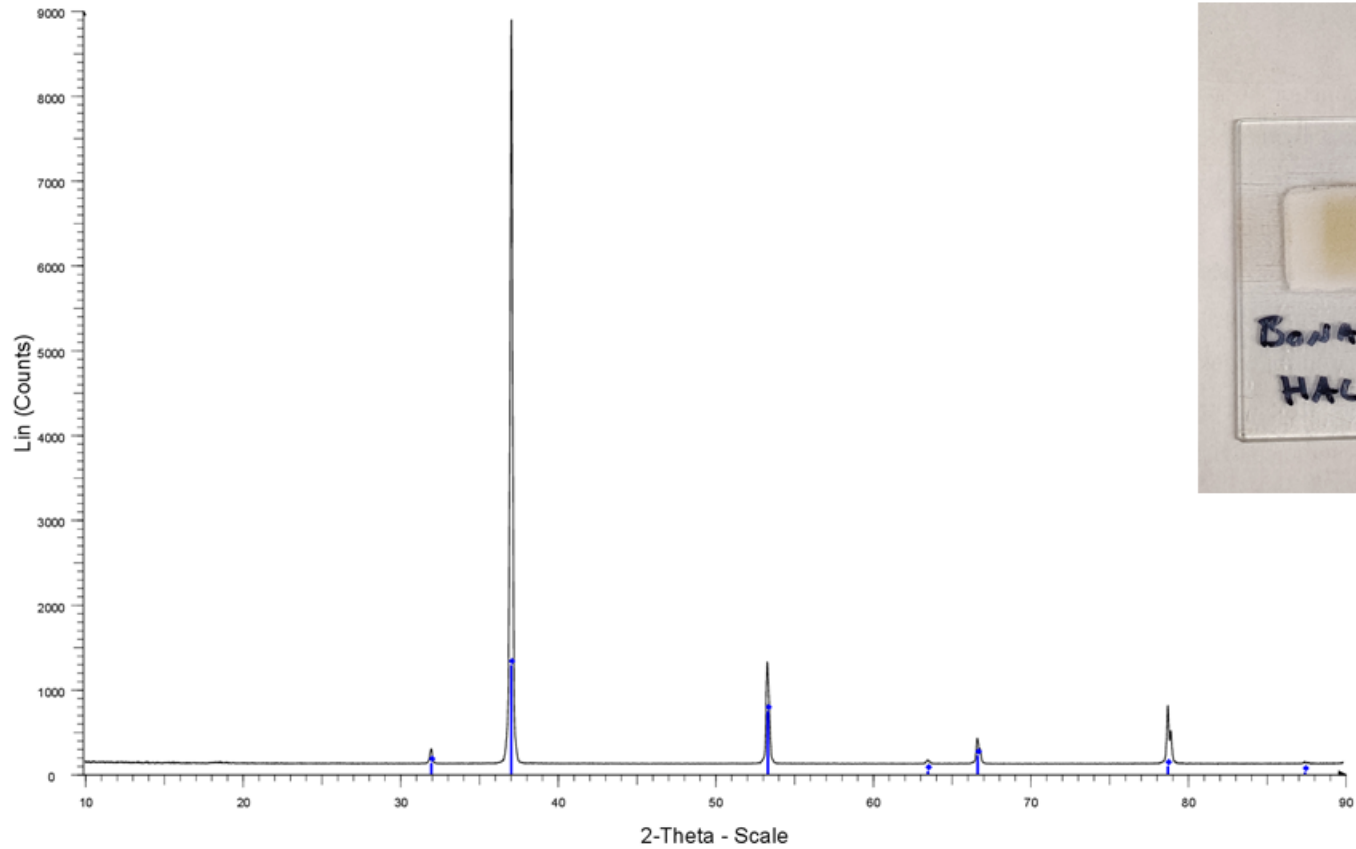


Sample ID: DeLaval Blue Halite



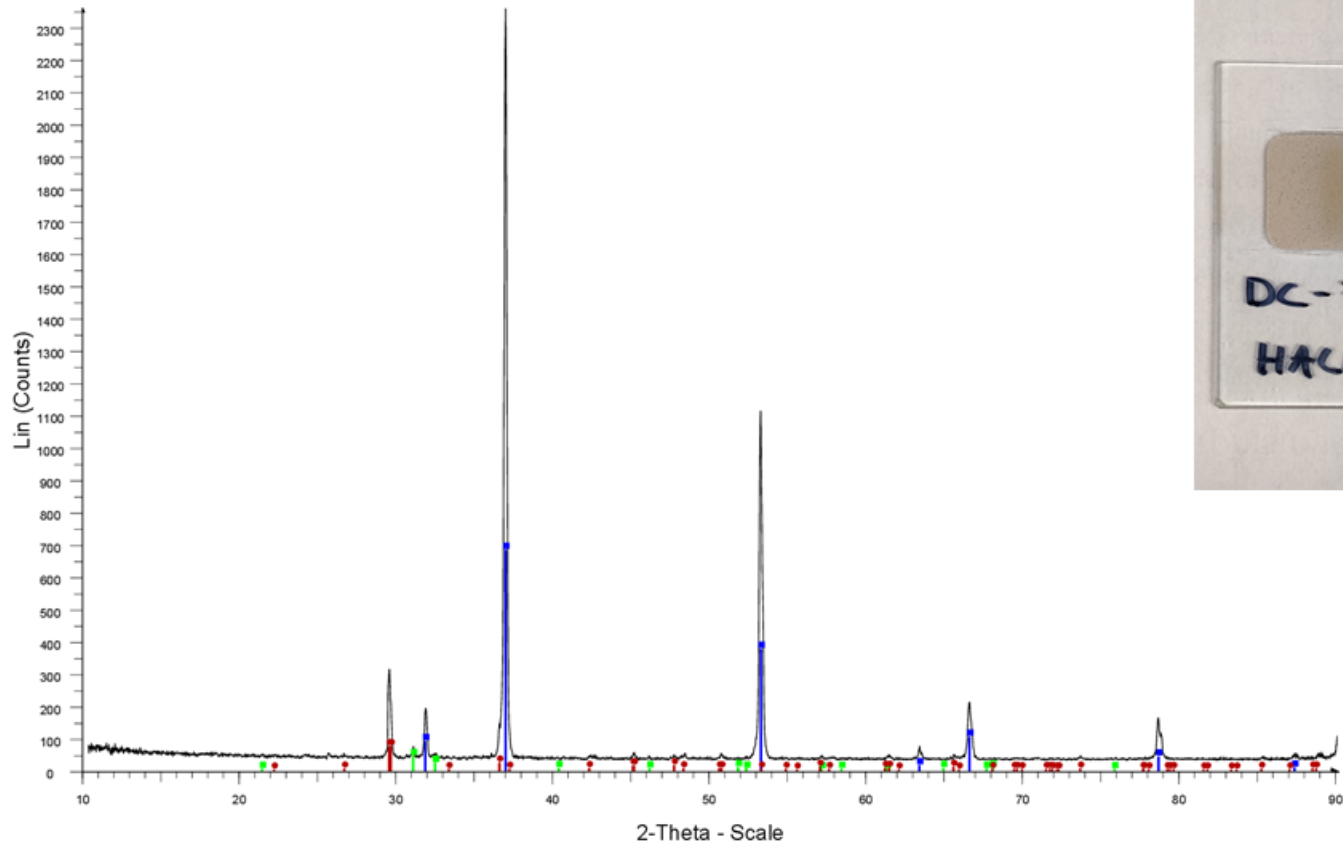
Y + 2.0 mm - File: Blue Halite pXRD 1h_(10_902Theta).raw
01-075-0306 (C) - Halite - NaCl - Cubic - Fm-3m (225) - a 5.64000

Sample ID: Bonaire Halite



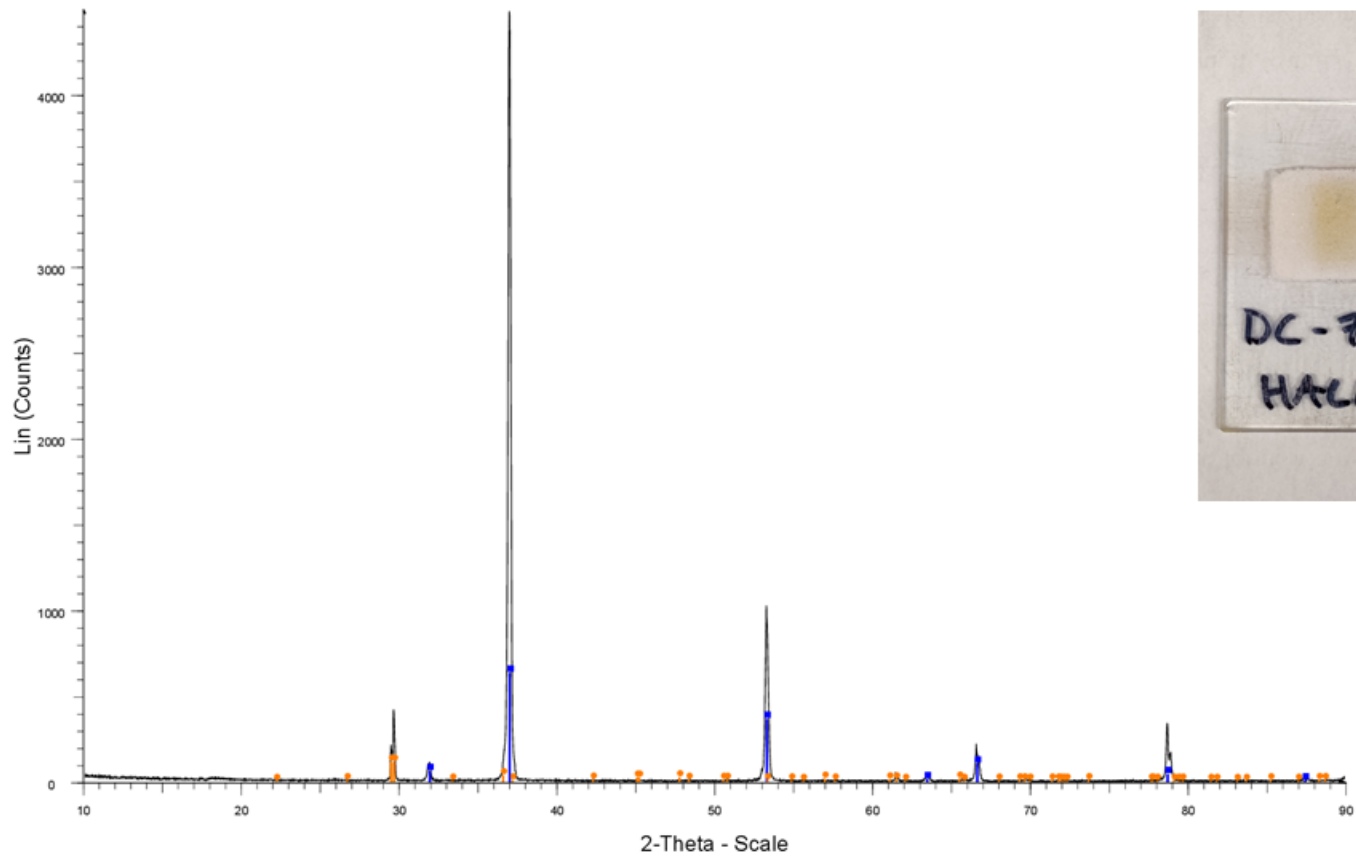
Y + 2.0 mm - File: BonaireHalite.raw - Displ.: 0.208 mm
01-075-0306 (C) - Halite - NaCl - Cubic - Fm-3m (225)

Sample ID: DC-711



- Y + 2.0 mm - File: DC 711 Halite.raw - Displ.: -0.429 mm
- 00-005-0628 (*) - Halite, syn - NaCl - Cubic - Fm-3m (225)
- 00-045-1436 (I) - Giniite, Fe-rich, syn - Fe₅(PO₄)₄(OH)₃·2H₂O - Orthorhombic -

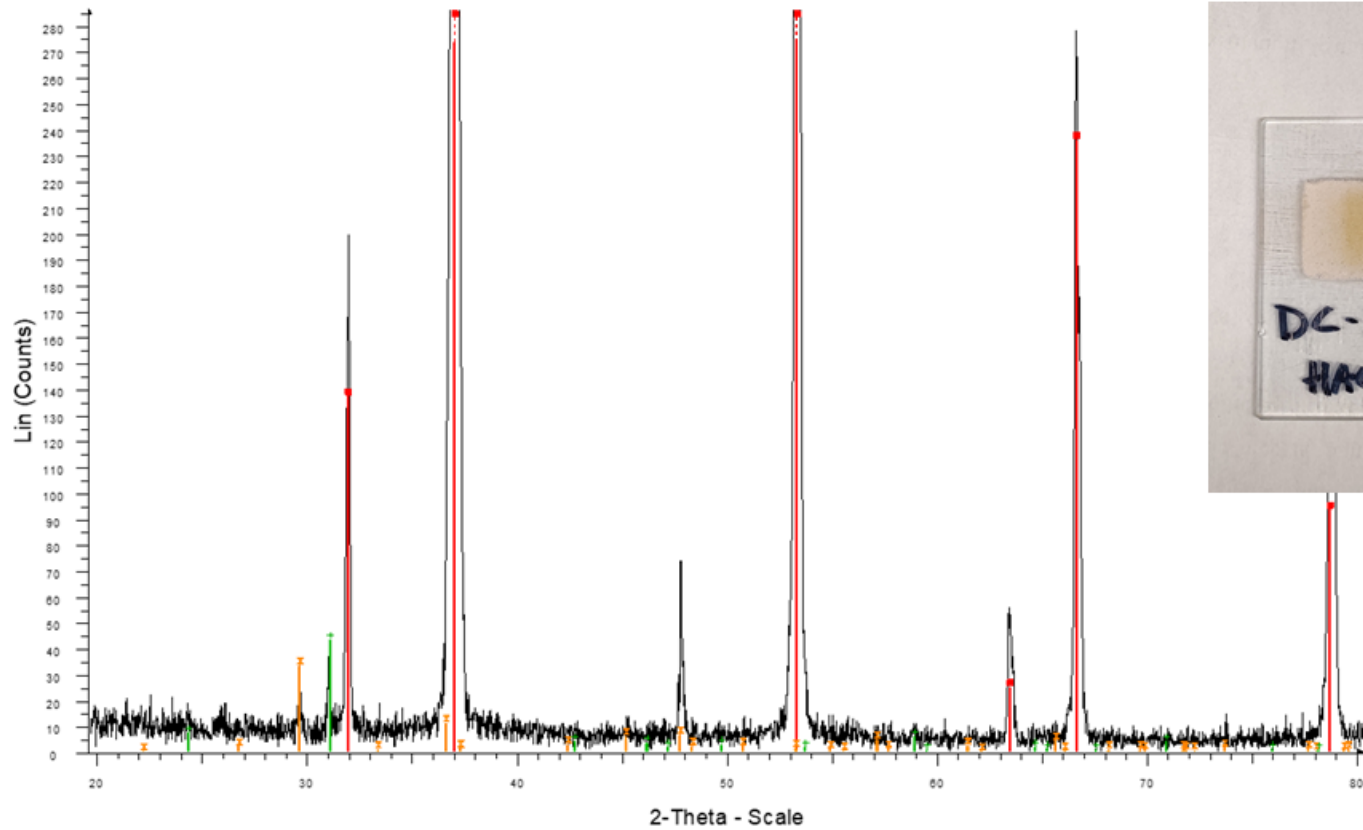
Sample ID: DC-730



- File: DC 730 Halite.raw - Displ.: 0. mm
- 01-075-0306 (C) - Halite - NaCl - Cubic - Fm-3m (225)
- 01-072-0503 (C) - Anhydrite - Ca(SO₄) - Orthorhombic - Amma (63)



Sample ID: DC-3137

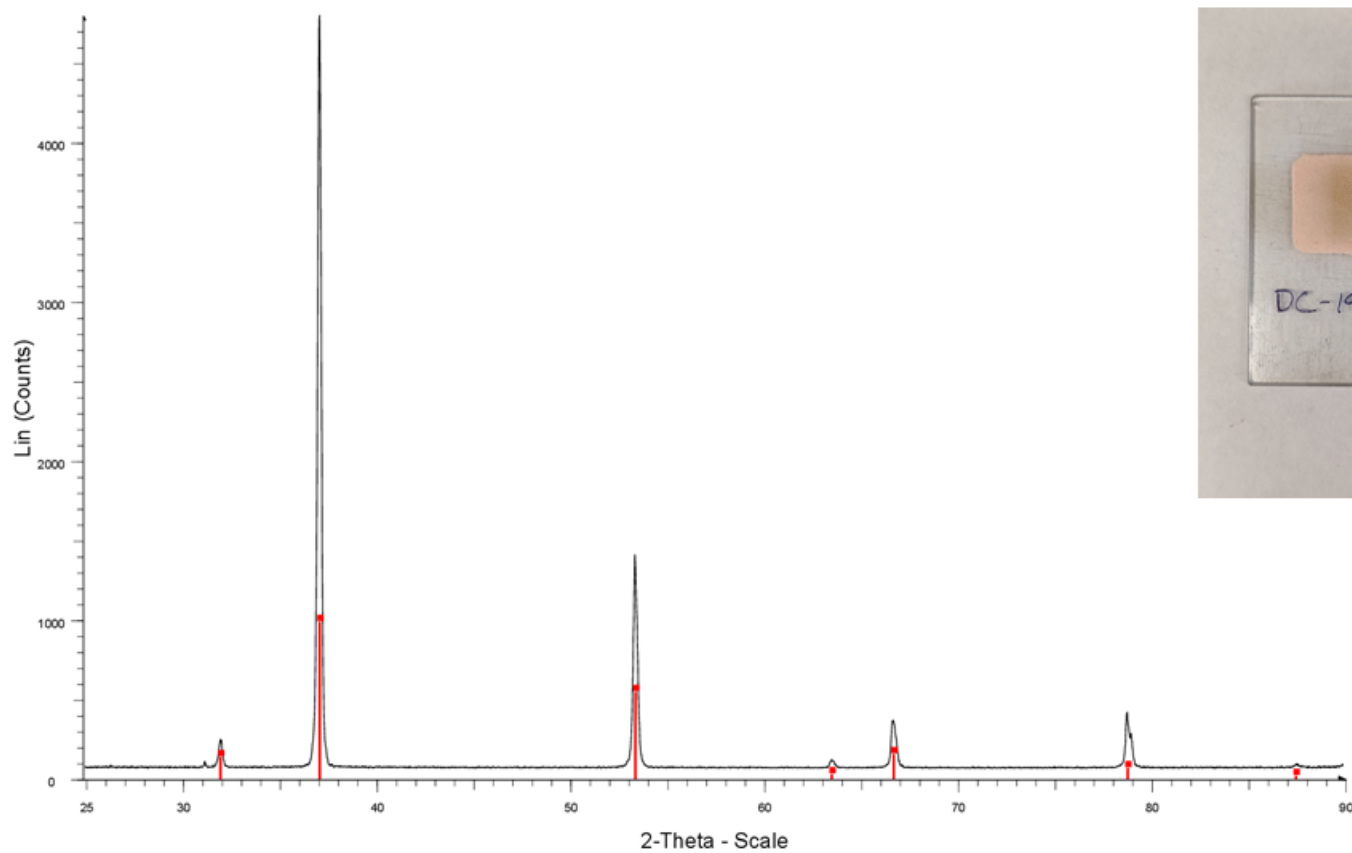


File: DC 3137 Halite.raw - Displ.: 0. mm

01-075-0306 (C) - Halite - NaCl - Cubic - Fm-3m (225)

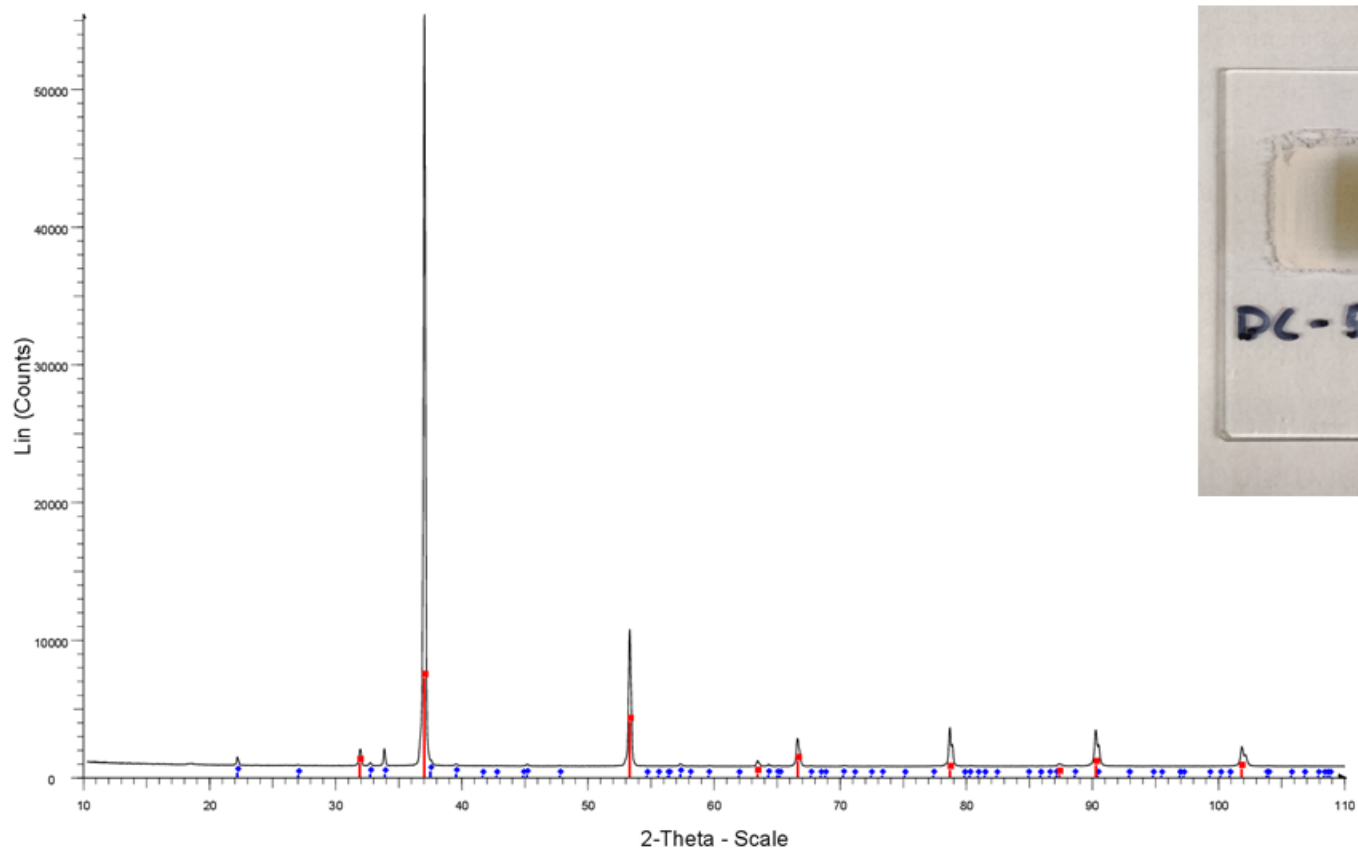
01-072-0916 (C) - Anhydrite - Ca(SO₄) - Orthorhombic - Amma (63)00-046-1045 (*) - Quartz, syn - SiO₂ - Hexagonal - P3221 (154)

Sample ID: DC-1922



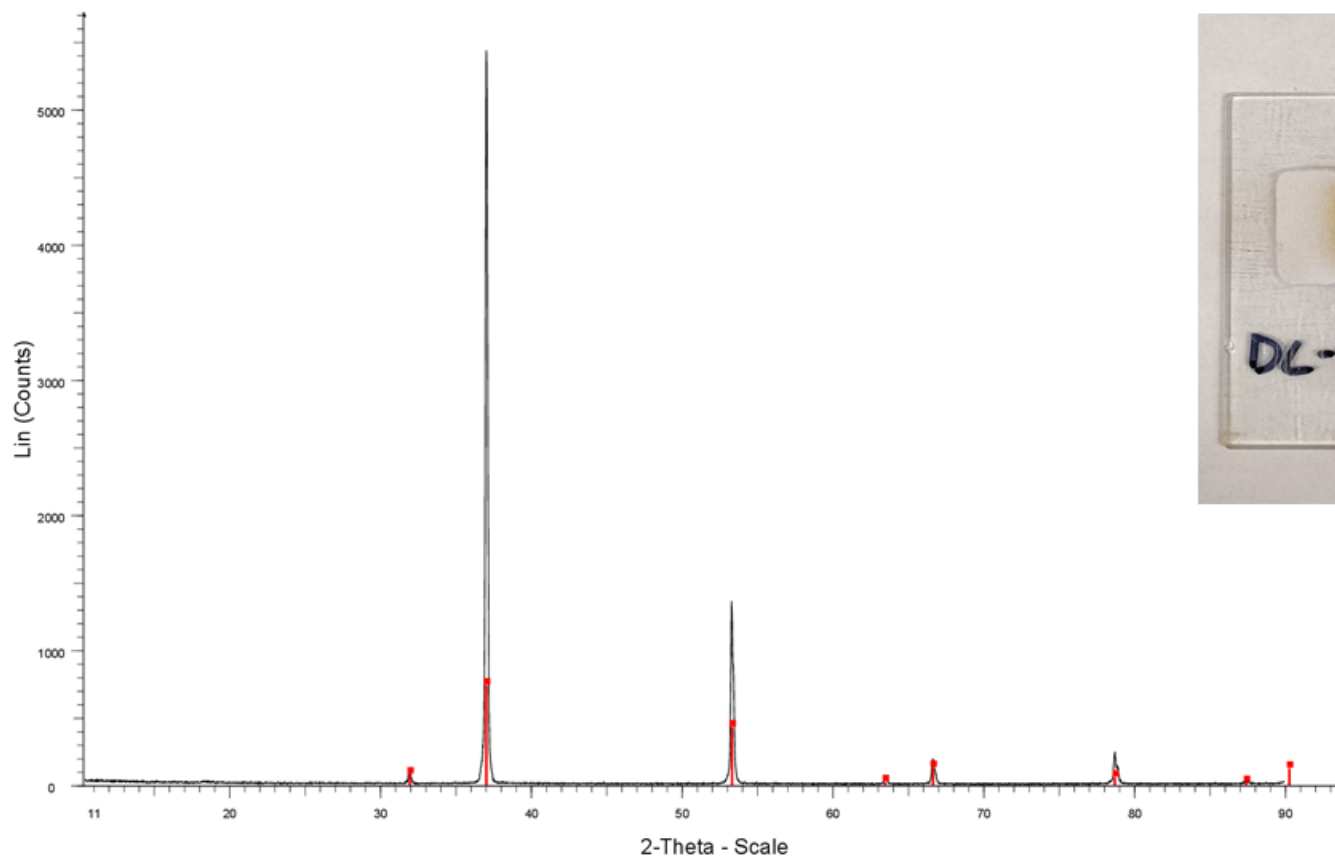
Y + 2.0 mm - File: DC-1922.raw - Displ.: 0.25 mm - Humidity: n.a.
00-005-0628 (*) - Halite, syn - NaCl - Cubic - Fm-3m (225)

Sample ID: DC-5477



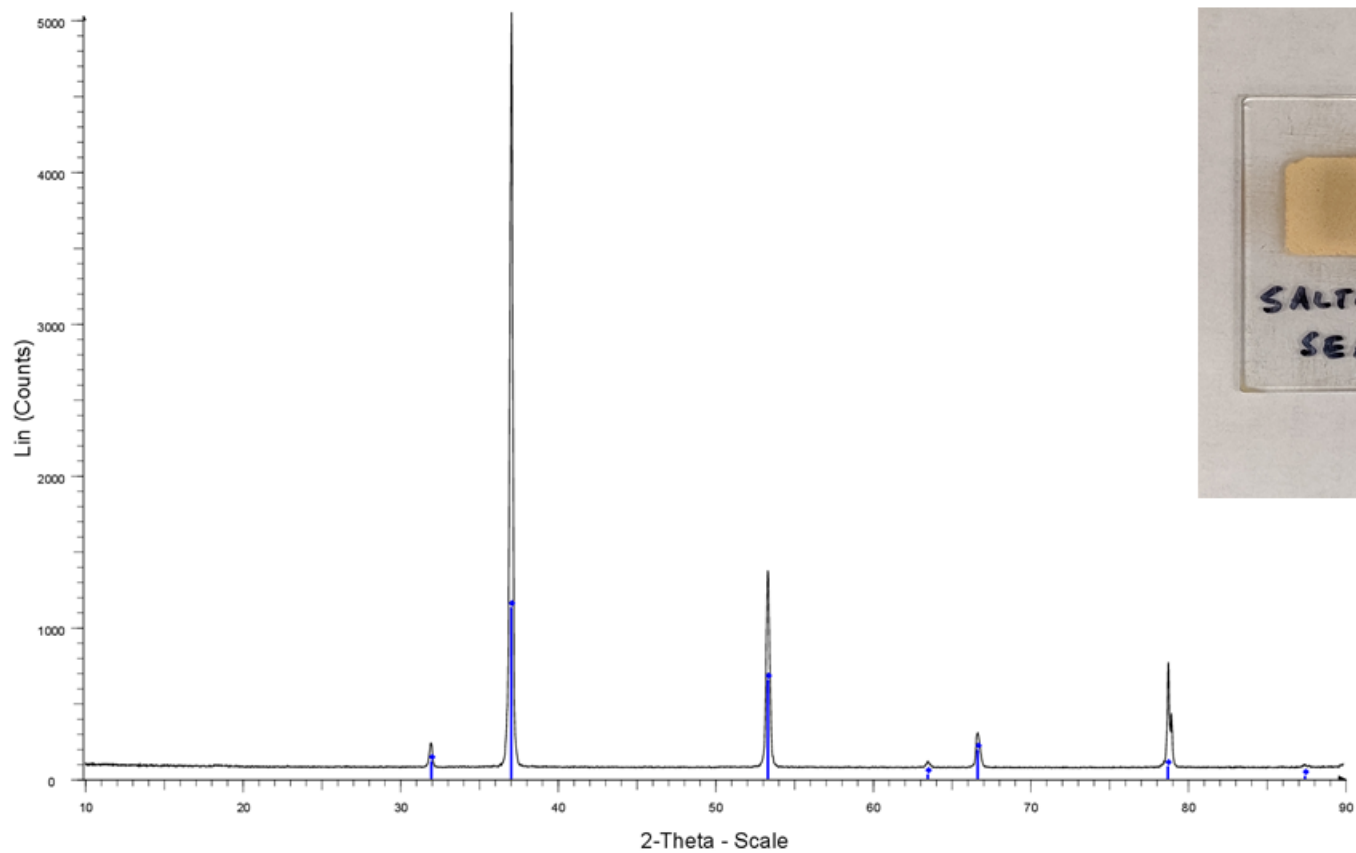
- Y + 2.0 mm - File: DC-5477 R (14hr_10s.0.02deg).raw - Displ.: -0.292 mm
- 01-074-2036 (C) - Thenardite - Na₂SO₄ - Orthorhombic - Fddd (70)
- 00-005-0628 (*) - Halite, syn - NaCl - Cubic - Fm-3m (225)

Sample ID: DC-5490



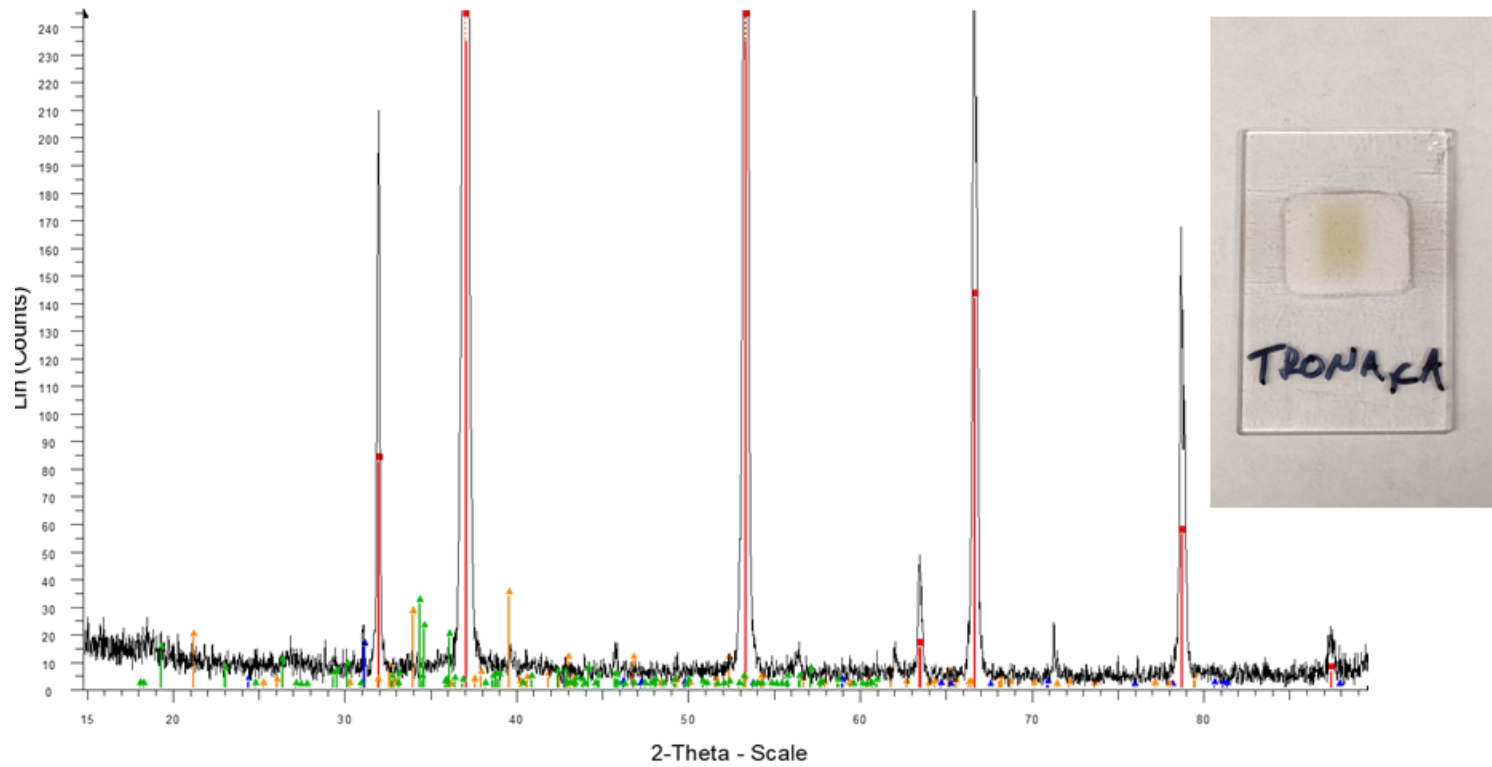
File: DC-5490_1hr_(10-90_0.02_1s).raw - Displ.: 0. mm
01-075-0306 (C) - Halite - NaCl - Cubic - Fm-3m (225)

Sample ID: Salton Sea Halite



Y + 2.0 mm - File: SaltonSea.raw - Displ.: 0.208 mm
01-075-0306 (C) - Halite - NaCl - Cubic - Fm-3m (225)

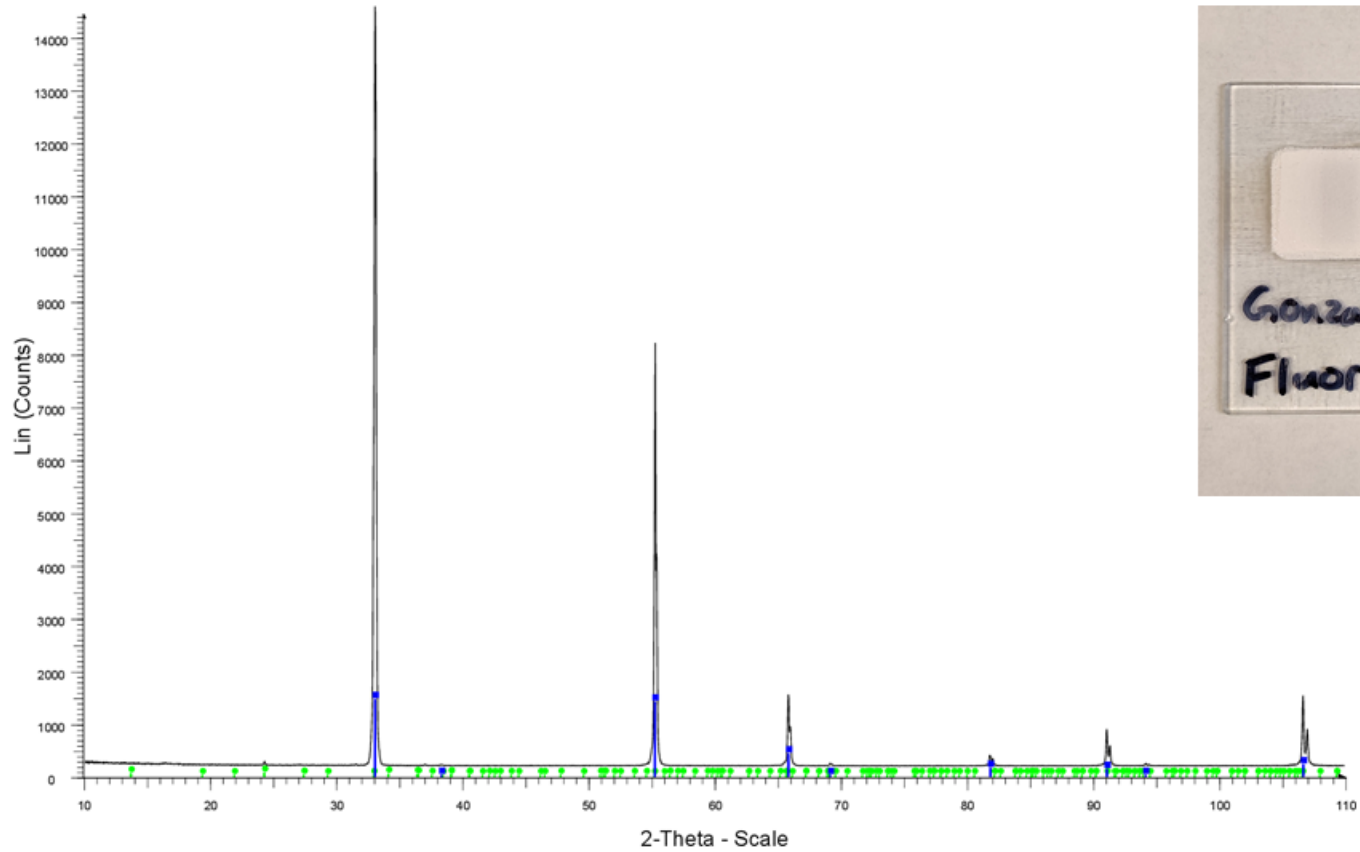
Sample ID: TronaCA



File: TronaCA_1hr.raw - Displ.: 0.176 mm

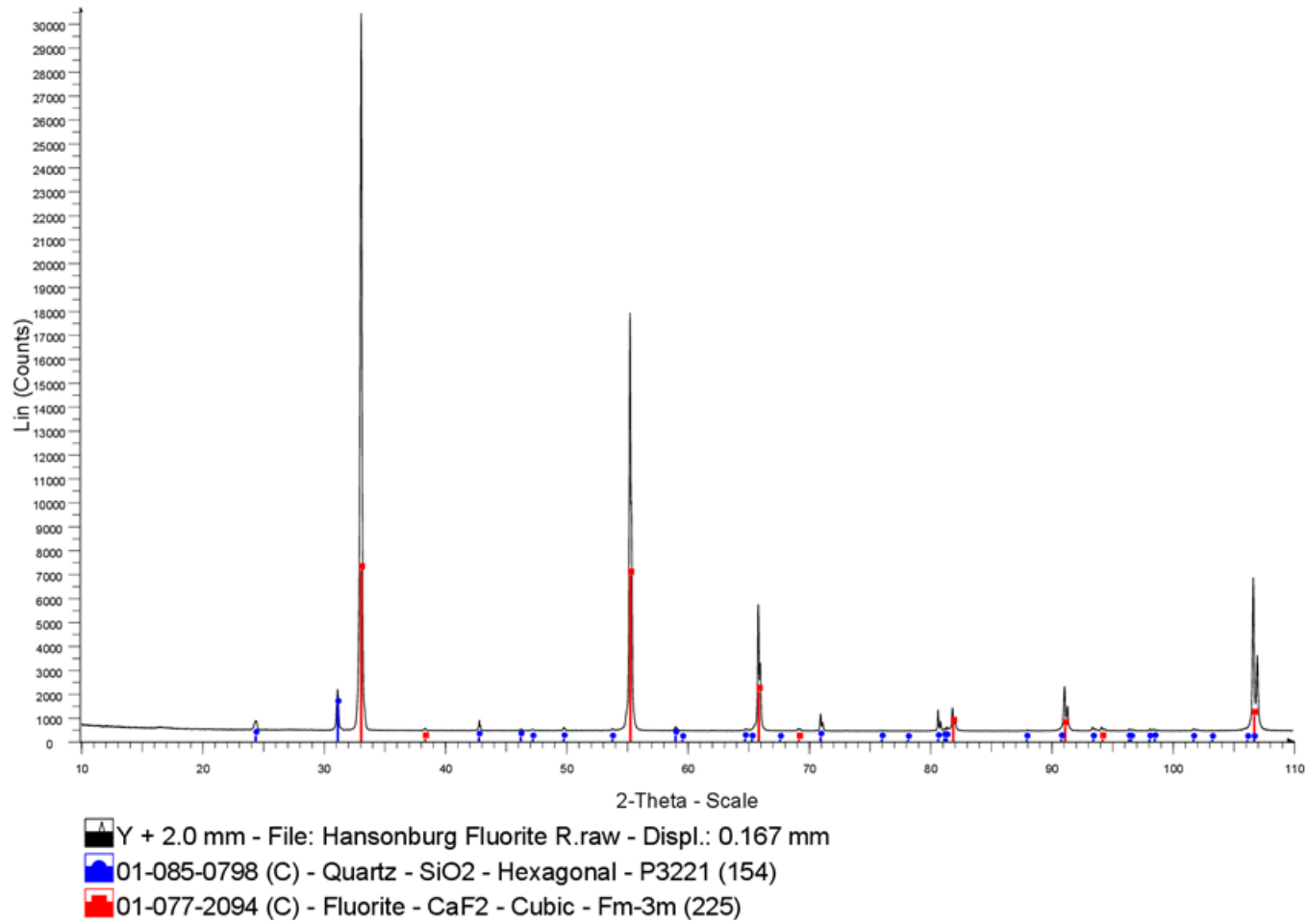
- 01-075-0306 (C) - Halite - NaCl - Cubic - Fm-3m (225)
- ▲ 00-046-1045 (*) - Quartz, syn - SiO₂ - Hexagonal - P3221 (154)
- ▲ 00-015-0800 (*) - Natron, syn - Na₂CO₃·10H₂O - Monoclinic - P (0)
- ▲ 00-029-1447 (*) - Trona - Na₃H(CO₃)₂·2H₂O - Monoclinic - I2/a (15)

Sample ID: Gonzalez Fluorite

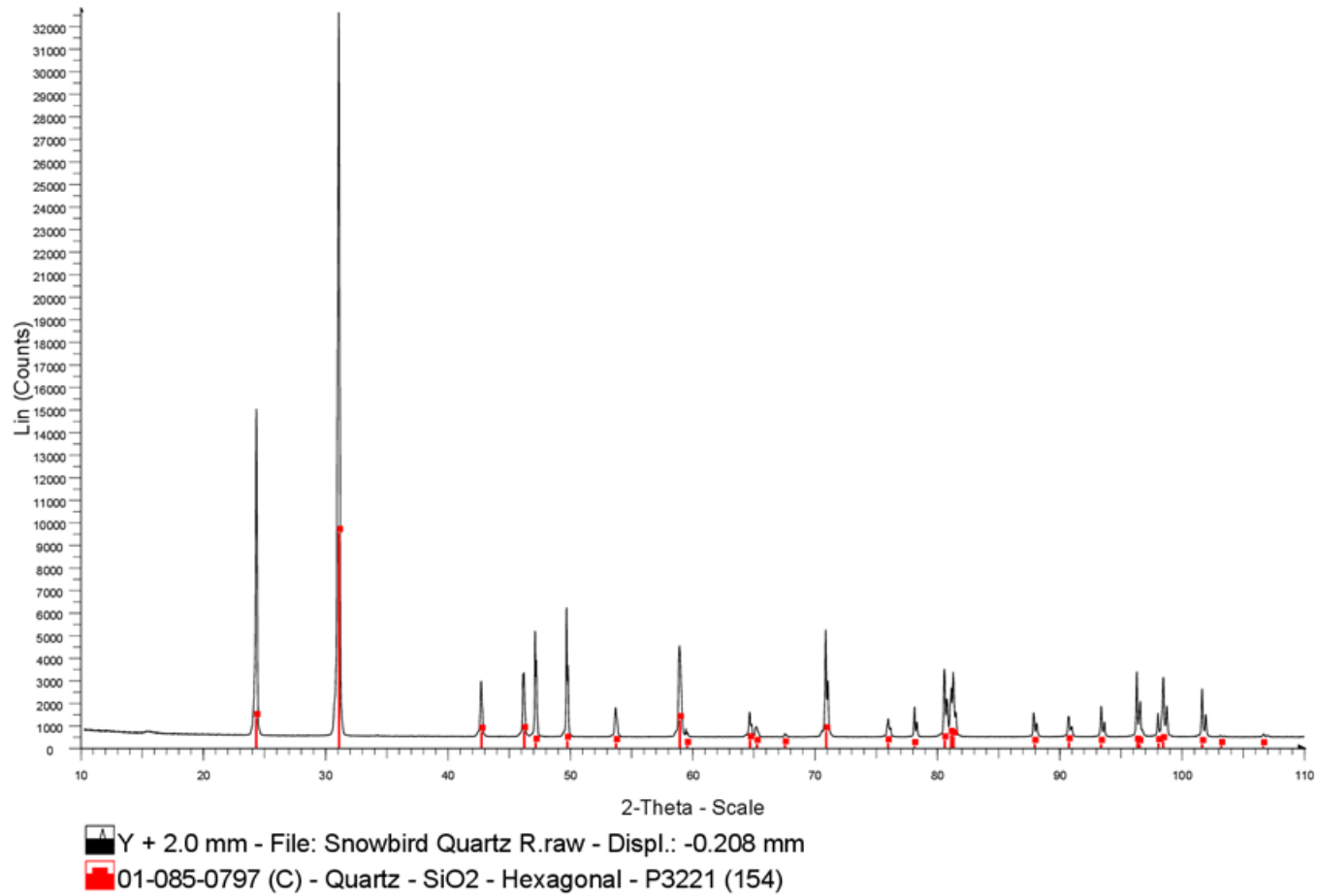


- Y + 2.0 mm - Scan Data - File: Gonzalez Fluorite.raw - Type: 2Th/Th locked - Start: 9.924 ° - End: 109.
- 01-077-2094 (C) - Fluorite - CaF₂ - Cubic - Fm-3m (225)
- 01-072-0596 (C) - Gypsum - Ca(SO₄)(H₂O)₂ - Monoclinic - C2/c (15)

Sample ID: Hansonburg Fluorite



Sample ID: Snowbird Quartz



Curriculum Vitae

Stephen Pilar

Education

B.Sc. Major in Chemistry, Minors in Geology/Psychology

The University of Western Ontario, London, Ontario

2014-2019

M.Sc. Candidate, Geology

The University of Western Ontario, London, Ontario

2019-Present

Under the supervision of:

Dr. Roberta Flemming and Dr. Nigel Blamey

Honors and Awards

Robert W. Hodder Travel Bursary

2019

The University of Western Ontario, London, Ontario

Employment

Teaching Assistant, University of Western Ontario

2019-2021

ES 2232: Exploring the Planets

ES 2240: Catastrophic Events of the Earth's History

Research Assistant, Mining Industry Human Resources

2019

Part of interdisciplinary group of researcher students

finding solutions to problems in the mining industry

Posters and Presentations

Geological Study of Fluid Inclusions Using Solid State

2021

Nuclear Magnetic Resonance Spectroscopy

IUPAC CCCE, Abstract and Poster Presentation